

OPTIMIZATION OF AN AXIALLY COMPRESSED RING AND STRINGER STIFFENED CYLINDRICAL SHELL WITH A GENERAL BUCKLING MODAL IMPERFECTION

David Bushnell,* Fellow, AIAA, Retired
 775 Northampton Drive, Palo Alto, CA 94303
 email: bush@sonic.net

ABSTRACT

PANDA2, a computer program for the minimum-weight design of elastic perfect and imperfect stiffened cylindrical panels and shells under multiple sets of combined loads, is used to obtain optimum designs of uniformly axially compressed elastic internal T-ring and external T-stringer stiffened cylindrical shells with initial imperfections in the form of the general buckling mode. The optimum designs generated by PANDA2 are verified by STAGS elastic and elastic-plastic finite element models produced automatically by a PANDA2 processor called STAGSUNIT. Predictions from STAGS agree well with those from PANDA2. Improvements to PANDA2 during the past year are summarized. Seven different optimum designs are obtained by PANDA2 under various conditions. The most significant condition is whether or not PANDA2 is permitted automatically to make the initial user-specified amplitude of the general buckling modal imperfection directly proportional to the axial halfwavelength of the critical general buckling mode. A survey is conducted over (m,n) space to determine whether or not the critical general buckling modal imperfection shape computed by PANDA2 with (m,n) critical (m =axial, n =circumferential) halfwaves is the most harmful imperfection shape. It is found that indeed (m,n) critical is, for all practical purposes, the most harmful imperfection mode shape if PANDA2 is permitted automatically to make the general buckling modal imperfection amplitude directly proportional to the axial halfwavelength of the critical general buckling mode (inversely proportional to m). It is concluded that for axially compressed, stiffened, globally imperfect cylindrical shells the optimum designs obtained with the condition that PANDA2 is NOT allowed to change the initial user-specified imperfection amplitude are probably too heavy. One of the cases investigated demonstrates that the optimum design of a perfect shell obtained via the commonly used condition that a likely initial imperfection be replaced by an increase in the applied load by a factor equal to the inverse of a typical knockdown factor is too heavy. A new input index, ICONSV, is introduced into PANDA2 by means of which optimum designs of various degrees of conservativeness can be generated. Optimum designs are obtained with $\text{ICONSV} = -1, 0,$ and $+1$, which represent increasing degrees of conservativeness in the PANDA2 model. It is concluded that, when obtaining optimum designs with PANDA2, it is best to allow PANDA2 to enter its branch in which local postbuckling behavior is determined, thereby avoiding the generation of designs that may be unsafe because of excessive local bending stresses in the panel skin and stiffener parts. In most cases both nonlinear static and nonlinear dynamic analyses are required in order to obtain collapse loads with STAGS. A table is included that demonstrates how to use STAGS to evaluate an optimum design obtained by PANDA2. In most cases the elastic STAGS models predict collapse in one of the ring bays nearest an end of the cylindrical shell. With the effect of elastic-plastic material behavior included in the STAGS models, collapse most often occurs in an interior ring bay where the finite element mesh is the most dense.

TABLE OF CONTENTS

1.0 INTRODUCTION	2
2.0 PURPOSE OF THIS PAPER.....	3
3.0 BRIEF DESCRIPTION OF PANDA2	4
4.0 DESCRIPTION OF STAGS [18-21].....	4

* Copyright © 2007 by David Bushnell. Published by the American Institute of Aeronautics and Astronautics, Inc, with permission

5.0 WHY MUST STAGS OR SOME OTHER GENERAL-PURPOSE CODE BE USED TO CHECK OPTIMUM DESIGNS FROM PANDA2?	6
6.0 HOW TO USE STAGS FOR THE ANALYSIS OF IMPERFECT STIFFENED CYLINDRICAL SHELLS	6
7.0 TWO MAJOR EFFECTS OF A GENERAL BUCKLING MODAL IMPERFECTION	8
8.0 DIFFERENCES IN THIS PAPER FROM [1K]	9
9.0 IMPROVEMENTS IN PANDA2 SINCE [1K] WAS WRITTEN	9
10.0 TYPICAL PANDA2 RUNSTREAM TO OBTAIN A "GLOBAL" OPTIMUM DESIGN.....	17
11.0 OPTIMUM DESIGNS OBTAINED UNDER VARIOUS CONDITIONS.....	17
12.0 DETAILS FOR AN EXAMPLE: CASE 2 IN TABLE 4	20
12.1 PANDA2 phase of the computations.....	20
12.1.1 PANDA2 runstream and files.....	20
12.1.2 Item 659 in the file .../panda2/doc/panda2.news. July 2006	22
12.1.3 Results from surveys of (MUSER, NUSER) for the most critical margins in Table 6.....	24
12.2 STAGS phase of the computations (including some results from BIGBOSOR4 [14F])	25
12.2.1 Finding the buckling loads of the perfect shell and the best STAGS model	26
12.2.2 Results from linear buckling analyses with BIGBOSOR4 [14F].....	29
12.2.3 Results from the nonlinear static and dynamic STAGS runs	30
13.0 SELECTED DETAILS FROM SOME OF THE OTHER CASES LISTED IN TABLE 4.....	32
13.1 Some results from Case 1, the perfect shell	32
13.2 Some results from Case 4.....	33
13.3 Some results from Case 5.....	36
13.4 Some results from Case 6.....	38
13.5 Some results from Case 7.....	39
14.0 THE EFFECTS OF ELASTIC-PLASTIC MATERIAL BEHAVIOR IN STAGS MODELS	41
14.1 STAGS elastic-plastic results from Case 2	41
14.2 STAGS elastic-plastic results from Case 4	42
14.3 STAGS elastic-plastic results from Case 5	42
14.4 STAGS elastic-plastic results from Case 7	43
15.0 IMPERFECTION SENSITIVITY STUDY CORRESPONDING TO THE DESIGN IN CASE 5	44
16.0 SUMMARY, CONCLUSIONS, SUGGESTIONS FOR FURTHER WORK.....	45
16.1 Summary.....	45
16.2 Conclusions	46
16.3 Suggestions for further work	46
17.0 DEDICATION.....	47
18.0 ACKNOWLEDGMENTS.....	48
19.0 REFERENCES	48

1.0 INTRODUCTION

Local and overall buckling and optimization of panels can be determined with the PANDA2 [1], POSTOP [2], VICONOPT [3], and PASCO [4] computer programs. These four programs are capable of obtaining optimum designs, and PANDA2, POSTOP, and VICONOPT can do so including the effect of local postbuckling of the panel skin and/or parts of the stringers.

Other contributions to the field of buckling of axially compressed stiffened cylindrical shells (and other loadings on other thin-walled structures) include the books, reports, and papers by Brush and Almroth [5], Jones [6], Singer, Arbocz, and Weller [7], Bushnell [8], Weingarten, Seide, and Peterson [9], Koiter [10], Hutchinson and Amazigo [11], and Baruch and Singer [12], to identify but a few in a vast literature. In [1K] is given an abbreviated survey of the recent literature on the buckling and optimization of stiffened panels and shells. For brevity most of the references listed there are not repeated here. They apply equally well to the subject of this paper.

In [1K] is described the optimization of an externally T-stringer and externally T-ring stiffened cylindrical shell under combined axial compression, external pressure, and torque. The computer program PANDA2 [1, 13-17, 22, 23] was used for the optimization. Details about PANDA2 are given in [1K]. They will not be repeated here. In

[1K] the optimum design obtained by PANDA2 is evaluated with the use of STAGS [18–21], a general-purpose finite element computer program. Because of the nature of the combined loading described in [1K] the general buckling mode of the optimized shell featured in that paper has a critical axial half-wave with wavelength equal to the length of the shell (Fig. 56 of [1K], for example). Because of the presence of torque there are no planes of symmetry in the general buckling mode. The results given in [1K] were obtained for a fictional material with a very, very high stress allowable. Hence, stress constraints were never active during optimization.

2.0 PURPOSE OF THIS PAPER

In the work leading to this paper PANDA2 and STAGS are used as before. PANDA2 is used to obtain the optimum design and STAGS is used to evaluate (test) the optimum design derived by PANDA2. The cylindrical shell has **different overall dimensions** (listed in Table 1) from those in [1K], the **stress constraints are active**, and the two sets of stiffeners are on opposite sides of the shell wall: **internal T-rings** and **external T-stringers**. The loading is **pure axial compression**, an important loading case that leads to certain behavior that sometimes causes difficulties during optimization cycles and during evaluation of the optimum design by a general-purpose computer code such as STAGS. These difficulties arise mainly because the critical buckling mode of the optimized shell usually has several axial half-waves rather than just one axial half-wave, as was the case in the study described in [1K].

Figures 1a,b,c and 2 show the configuration treated in this paper, a typical general buckling mode (Fig. 1), and the cylindrical shell with a general buckling modal imperfection as deformed under the design load (Fig. 2).

Because of the absence of in-plane shear loading (torque) and the absence of anisotropy in the cases explored here, there are multiple planes of symmetry in the general buckling mode of the perfect shell and hence in the imperfect shell with a general buckling modal imperfection shape derived from a linear bifurcation buckling analysis of the perfect shell. See Fig. 1b, for example. Therefore, STAGS models of the imperfect shell that include much less than 360 degrees of circumference are valid provided the symmetry planes at the two straight edges (generators) bound a circumferential sector that permits an integral number of circumferential half-waves with circumferential wavelength equal to that of the **critical** general buckling mode of the perfect, complete optimized cylindrical shell. For reasons described below, in most of the cases examined here the most refined models span a circumferential arc of one **full** circumferential wave of the critical general buckling mode, not just one half circumferential wave.

It is emphasized that in this paper the **stress constraints are active**. They therefore influence the evolution of the design during optimization cycles. The shell material is aluminum with an allowable effective (von Mises) stress of 60 ksi. In all the PANDA2 runs the material remains elastic. PANDA2 cannot handle elastic-plastic material behavior. Most STAGS runs are with elastic models. **Some STAGS models are processed in which elastic-plastic material behavior is accounted for (Figs. 81–95).**

Figure 2 displays a typical distribution of effective (von Mises) stress in a STAGS model of an elastic imperfect cylindrical shell previously optimized by PANDA2 and subjected to the design load, axial compression $N_x = -3000$ lb/in.

Improvements to PANDA2 implemented since [1K] was written are briefly described in Section 9.

In this paper **several optimum designs are obtained for the same system**: an elastic, imperfect, uniformly axially compressed, internal T-ring and external T-stringer stiffened, simply-supported aluminum cylindrical shell 75 inches long and 50 inches in diameter (Tables 1 and 2 and Figs. 1 and 2). Optimum designs are obtained with respect to **three types of model choice**:

1. Model choice type 1: Optimum designs are obtained for three values of a “conservativeness index”, $ICONSV = -1, 0,$ and 1 , which governs how conservative the PANDA2 model is (Item 676 in Section 9.0):

a. with respect to knockdown factors to compensate for the inherent unconservativeness of smearing stringers and smearing rings,

- b. with respect to a knockdown factor for imperfection sensitivity computed from equations given by Arbocz in [1D], and
- c. with respect to a knockdown factor to compensate for truncation error in the double trigonometric series expansion of the alternative solution for general buckling [1G].

2. Model choice type 2: Optimum designs are obtained for two strategies with respect to the modeling of a general buckling modal imperfection [1K]:

- a. **Strategy 1:** the initial user-specified **amplitude, W_{imp}** , of the imperfection in the shape of the critical (lowest eigenvalue) general buckling mode of the perfect shell **remains fixed** during optimization cycles, and
- b. **Strategy 2:** the initial user-specified **amplitude, W_{imp}** , of the critical general buckling modal imperfection is changed during optimization cycles such that **W_{imp} becomes proportional to the axial wavelength of the critical general buckling mode**. This strategy is based on the assumption that general buckling modal imperfections with many axial waves are more detrimental than those with fewer axial waves, given the amplitude, **W_{imp}** . Imperfections with short axial wavelengths are probably easier to detect than those with long axial wavelengths, given the amplitude, **W_{imp}** . Therefore, fabricated shells with short-wavelength imperfections would more likely be discarded or repaired than fabricated shells with long-wavelength imperfections, given the amplitude, **W_{imp}** .

3. Model choice type 3: Optimum designs are obtained for two models of local postbuckling [1C]:

- a. Local postbuckling **IS allowed** to occur, and
- b. Local postbuckling **is NOT allowed** to occur.

Not all combinations of these three types of model choices are explored, just enough to learn what the effect of one type of model choice is while the other two types of model choice remain the same.

Many examples are provided to give the reader a “feel” for the behavior of axially compressed, stiffened, imperfect cylindrical shells. Predictions of the behavior of shells optimized by PANDA2 are validated by STAGS [18-21] and BOSOR4 [14] models.

3.0 BRIEF DESCRIPTION OF PANDA2

See [1A] and [1K] for more details. PANDA2 is a computer program for the minimum weight design of elastic, ring and stringer stiffened, composite, flat or cylindrical, perfect or imperfect panels and cylindrical shells subjected to multiple sets of combined in-plane loads, normal pressure, edge moments, and temperature. For most configurations the panels can be locally postbuckled [1C]. Previous work on PANDA2 is documented in [1A-L, 22, 23]. PANDA2 incorporates the theories of earlier codes PANDA [1B,13] and BOSOR4 (called “BIGBOSOR4” in this paper) [14]. The local postbuckling analysis [1C] is based on a model by Koiter [15] (different from Koiter’s “classical” asymptotic imperfection sensitivity theory in [10]). The optimizer used in PANDA2 is called ADS [16,17]. Panels are optimized subject to buckling and stress constraints and certain inequality constraints (Table 1). Details about PANDA2 are given in the recent references listed under [1] (see especially [1K]). Therefore, these details will not be repeated here. Only the most significant improvements in PANDA2 since the publication of [1K] are briefly enumerated in Section 9 of this paper.

4.0 DESCRIPTION OF STAGS [18-21]

In most of the PANDA2 references listed under [1] and in [22, 23] and in this paper optimum designs obtained by PANDA2 are evaluated later via STAGS models.

STAGS (STructural Analysis of General Shells [18–21]) is a finite element code for **general-purpose nonlinear**

analysis of stiffened shell structures of arbitrary shape and complexity. Its capabilities include stress, stability, vibration, and transient analyses with both material and geometric nonlinearities permitted in all analysis types. STAGS includes enhancements, such as a higher order thick shell element, more advanced nonlinear solution strategies, and more comprehensive post-processing features such as a link with STAPL, a postprocessor used to generate many of the figures in this paper: figures that display the STAGS model, such as Figs. 1a-c and 2, for example.

Research and development of STAGS by Rankin, Brogan, Almroth, Stanley, Cabiness, Stehlin and others of the Computational Mechanics Department of the Lockheed Martin Advanced Technology Center has been under continuous sponsorship from U.S. government agencies and internal Lockheed Martin funding for the past 40 years. During this time particular emphasis has been placed on improvement of the capability to solve difficult nonlinear problems such as the prediction of the behavior of axially compressed stiffened panels loaded far into their locally postbuckled states. STAGS has been extensively used worldwide for the evaluation of stiffened panels and shells loaded well into their locally postbuckled states. See [21], for example.

A large rotation algorithm that is independent of the finite element library has been incorporated into STAGS [20B]. With this algorithm there is no artificial stiffening due to large rotations. The finite elements in the STAGS library do not store energy under arbitrary rigid-body motion, and the first and second variations of the strain energy are consistent. These properties lead to quadratic convergence during Newton iterations.

Solution control in nonlinear problems includes specification of load levels or use of the **advanced Riks-Crisfield path parameter** [21] that enables traversal of limit points into the post-buckling regime. Two load systems with different histories (Load Sets A and B) can be defined and controlled separately during the solution process. Flexible restart procedures permit switching from one strategy to another during an analysis, including shifts from bifurcation buckling to nonlinear collapse analyses and back and shifts from static to transient and transient to static analyses with modified boundary conditions and loading. STAGS provides solutions to the generalized eigenvalue problem for **buckling and vibration from a linear (Fig. 24) or nonlinear (Figs. 26, 27) stress state**.

Quadric surfaces can be modeled with minimal user input as individual substructures called "**shell units**" in which the analytic geometry is represented exactly. "Shell units" can be connected along edges or internal grid lines with partial or complete compatibility. In this way complex structures can be assembled from relatively simple units. Alternatively, a structure of arbitrary shape can be modeled with use of an "element unit".

Geometric imperfections can be generated automatically in a variety of ways, thereby permitting imperfection-sensitivity studies to be performed. For example, **imperfections can be generated by superposition of several buckling modes determined from previous linear and nonlinear STAGS analyses of a given case**. (See Parts 4-7 of Table 9 and Figs. 24, 26, and 27, for example).

A variety of material models is available, including both plasticity and creep. STAGS handles isotropic and anisotropic materials, including composites consisting of up to 60 layers of arbitrary orientation. Four plasticity models are available, including isotropic strain hardening, the White Besseling (mechanical sublayer model), kinematic strain hardening, and deformation theory.

Two independent load sets, each composed from simple parts that may be specified with minimal input, define a spatial variation of loading. Any number of point loads, prescribed displacements, line loads, surface tractions, thermal loads, and "live" pressure (hydrostatic pressure which remains normal to the shell surface throughout large deformations) can be combined to make a load set. For transient analysis the user may select from a menu of loading histories, or a general temporal variation may be specified in a user-written subroutine.

Boundary conditions (B.C.) may be imposed either by reference to certain standard conditions or by the use of single- and multi-point constraints. Simple support, symmetry, anti-symmetry, clamped, or user-specified B.C. can be defined on a "shell unit" edge. Single-point constraints that allow individual freedoms to be free, fixed, or a prescribed non-zero value may be applied to grid lines and surfaces in "shell units" or "element units". A useful feature for buckling analysis allows these constraints to differ for the prestress and eigenvalue analyses. Langrangian constraint equations containing up to 100 terms may be defined to impose multi-point constraints.

STAGS has a variety of finite elements suitable for the analysis of stiffened plates and shells. Simple four node quadrilateral plate elements with a cubic lateral displacement field (called "410" and "411" elements) are effective and efficient for the prediction of postbuckling thin shell response. A linear (410) or quadratic (411) membrane interpolation can be selected. For thicker shells in which transverse shear deformation is important (**and for the thin-shell cases described in this paper**), STAGS provides the **Assumed Natural Strain (ANS) nine node element (called "480" element)**. A two node beam element compatible with the four node quadrilateral plate element is provided to simulate stiffeners and beam assemblies. Other finite elements included in STAGS are described in the STAGS literature [18-21].

5.0 WHY MUST STAGS OR SOME OTHER GENERAL-PURPOSE CODE BE USED TO CHECK OPTIMUM DESIGNS FROM PANDA2?

PANDA2 uses many approximations and “tricks” in models for stress and buckling. Some of these are described in Sections 8 - 10 of [1K]. For example, knockdown factors are derived to compensate for the inherent unconservativeness of smearing stiffeners [1K] and to account for the effects of transverse shear deformation [1A]. The effect of initial local, inter-ring, and general imperfections in the shapes of critical local, inter-ring, and general buckling modes are accounted for in an approximate manner as described in [1D] and [1E]. The distribution of prebuckling stress resultants in the various segments of a discretized skin-stringer module [1A and Fig. 4 in this paper] and of a “skin”-ring discretized module [1G] of an imperfect and therefore initially bent stiffened shell are approximate. For example, stabilizing (**tensile**) axial and hoop resultants in the panel skin that arise from prebuckling bending of an initially globally imperfect shell are neglected in order to avoid the production of unconservative optimum designs.

PANDA2 has been developed over the years with the philosophy that the use of many relatively simple approximate models will lead to optimum designs that are reasonable and for which no complicated “combined” modes of failure will inadvertently be missed. Because of the approximate nature of these multiple simple PANDA2 models, one **MUST** use STAGS or some other general-purpose finite element code to evaluate optimum designs obtained by PANDA2.

The particular advantage of using STAGS is that there exists a PANDA2 processor called STAGSUNIT [1I] that automatically generates input files, ***.bin** and ***.inp**, for STAGS. As described in [1I], the processor STAGSUNIT is written in such a way that “patches” (sub-domains) of various portions of a complete panel or shell can be analyzed with STAGS. **The correct prebuckled state of a perfect panel is preserved independently of the size of the “patch” to be included in the STAGS sub-domain model.** The minimum size “patch” must contain at least one stiffener spacing in each coordinate direction. In a stringer-stiffened shell stringers are always included along the two straight edges of the “patch”. There may or may not be rings running along the two curved edges of the “patch”, depending on input to STAGSUNIT provided by the user of PANDA2. **Stiffeners that run along the four boundaries of the “patch” have half the stiffness and half the loading of those that lie within the “patch”.** It is primarily this characteristic of the STAGS models produced by STAGSUNIT that preserves the correct prebuckled state of the “patch” independently of its size.

The STAGS models are constructed by the PANDA2 processor, STAGSUNIT, in such a way that all stiffeners are connected only to the panel skin. That is, where stiffeners intersect they simply pass through one another with no constraints between them along their lines of intersection, if any. This is a conservative model with respect to buckling. The same model is used in PANDA2. The STAGSUNIT processor can generate models in which all stiffeners may be composed of shell units, one or more sets of stiffeners may be composed of beams, or one or more sets of stiffeners may be “smeared” as prescribed by Baruch and Singer [12].

6.0 HOW TO USE STAGS FOR THE ANALYSIS OF IMPERFECT STIFFENED CYLINDRICAL SHELLS

In order to use STAGS to evaluate a shell with a general buckling modal imperfection, one must:

1. Obtain an optimum design with PANDA2 via multiple executions of SUPEROPT [1D, 1K, and Fig. 3 and Table 3 in this paper].
2. Use STAGSUNIT [1I] to generate input files, ***.bin** and ***.inp**, for STAGS operating in its linear bifurcation buckling mode (STAGS analysis type index INDIC=1). Generate various ***.inp** files corresponding to various models, as described next.
3. Explore at least two **preliminary linear buckling** models with the STAGS input index ILIN=0 [20C] in each shell unit (Runs 1 and 2 in Part 1 of Table 9). In each model ask for about 8 eigenvalues (*.bin file) so that in the case of closely spaced eigenvalues a general buckling mode shape similar to that determined by PANDA2 will be found. The purpose of these preliminary runs is to obtain good and better estimates of the critical **general** buckling mode shape and load factor (eigenvalue). The most accurate general buckling load factor is to be used as the initial “**eigenvalue shift**” (see Parts 2 and 3 of Table 9 and [20C]) in the *.bin file for models of the type described in the next item (Item 4). Two preliminary models are:
 - a. 1st linear buckling model: **all stiffeners smeared** (Figs. 37 and 38, for example)
 - b. 2nd linear buckling model: **stringers smeared, rings as shell units** (2 shell units per ring for a T-shaped ring, one for the ring web and the other for the outstanding flange of the ring) (Figs. 39 and 40, for example).
4. Decide how much of the shell circumference to include in the most refined STAGS model. The circumferential domain should permit one **full** circumferential wave of the critical general buckling mode determined in Model 3b (previous item), that is, the general buckling mode that most resembles that predicted by PANDA2. Symmetry conditions should be applied to the two opposite straight edges (generators) of the model of the cylindrical shell (Runs 3 and Runs 5-7 in Part 1 of Table 9 and Fig. 21a, for example).
5. Decide how to concentrate nodal points in Model 4 in order accurately to capture all possible buckling modes (local stiffener buckling, local skin buckling, inter-ring buckling, stiffener rolling, and general buckling) (Run 8 in Part 1 of Table 9). One can refer to the margins listed in the PANDA2 output file, ***.OPM**, corresponding to the optimized design in order to establish reasonable nodal point densities to guarantee converged behavior because the phrases that define these margins contain the critical numbers of axial and circumferential halfwaves in the various buckling modes. (See the top part of Table 7 and Figs. 26 and 27, for example).
6. With the use of Model 5, run STAGS multiple times in its **linear bifurcation buckling** branch (INDIC=1) with various “**eigenvalue shifts**” in order to find one or more **general buckling modes**. (See Part 2 of Table 9). One or more of these modes are to be used as imperfection shapes in future nonlinear static and dynamic STAGS runs. The initial “eigenvalue shift” should be close to (perhaps slightly under) that predicted from Model 3b. If the critical general buckling mode is “polluted” by a short-wavelength component, such as that shown in Figs. 23 and 24 of [1I] and in Fig. 75 in this paper, try running again with the STAGS index ILIN = 1 [20C] in every shell unit instead of ILIN= 0. ILIN=1 “filters out” many short-wavelength buckling modes, thus making it easier to find the few general buckling modes “hidden” in the dense eigenvalue spectrum and less likely that a “dirty” general buckling mode such as that displayed in Fig. 75 will occur. See, for example, Fig. 76. If changing ILIN from 0 to 1 does not solve this problem, one can make seemingly insignificant alterations in the nodal point distribution and run again. Experience with numerous STAGS models seems to indicate that “dirty” general buckling modes such as that displayed in Fig. 75 arise when a mode corresponding to short-wavelength buckling is associated with an eigenvalue that is extremely close (the same to five significant figures, for example) to that corresponding to the critical general buckling mode. “Jiggling” the finite element model causes the eigenvalues to shift slightly, those corresponding to a general buckling mode shifting less than those corresponding to short-wavelength buckling modes. **It is important to obtain a “clean” general buckling mode** because short-wavelength components in the initial imperfection shape, such as that displayed if Fig. 75, give rise to significant local bending stresses obtained from future nonlinear STAGS runs, bending stresses of a nature that are extremely unlikely to occur in an actual fabricated shell.
7. Edit the ***.bin** and ***.inp** files (or run STAGSUNIT again with different input) to prepare for a **nonlinear static equilibrium** run with STAGS (STAGS analysis type index INDIC=3). Include at least one general buckling modal imperfection in the ***.inp** file, such as that shown in Fig. 24. (See Part 5 of Table 9 and Fig. 25). Choose carefully **both the amplitude** of the general buckling modal imperfection and its **sign**.

8. Run the nonlinear static (INDIC=3) STAGS case and inspect the results after execution. (See Part 6 in Table 9).

9. Multiple nonlinear static STAGS runs are usually required to obtain a **collapse** load. With each run it may be necessary to **add one or more nonlinear bifurcation buckling modes**, such as those shown in Figs. 26 and 27, as additional imperfection shapes in order to “trigger” collapse or to avoid nonlinear bifurcation points that lie on or near the nonlinear equilibrium path [1H, 22]. (See Sub-section 18.5 of [1K] and Parts 6 – 9 of Table 9 and Figs. 26–29 in this paper).

10. It may be necessary to follow Step 9 with a series of **nonlinear dynamic** STAGS runs [23] in order to determine the maximum load-bearing capability of a shell. This step is used in the STAGS analysis of the “testax3” case in [1K], as described in Section 18.0 of [1K]. This step is used for most of the cases explored in this paper. (See Parts 10 – 13 of Table 9 and Figs. 30-32).

7.0 TWO MAJOR EFFECTS OF A GENERAL BUCKLING MODAL IMPERFECTION

Much of the following appears in Section 11.1 on p. 19 of [1K]. It is repeated here because this section is especially important. It briefly describes the behavior of a **stiffened cylindrical shell** with a **general buckling modal imperfection shape**. This behavior plays a major role in the evolution of the design during optimization cycles in PANDA2. Here it is assumed that the shortest wavelength of the general buckling modal imperfection is greater than the greatest stiffener spacing, as holds in Figs. 1 and 2, for example (disregarding the component of stringer bending-torsional deformation displayed in the expanded insert in Fig. 1a).

A general buckling modal imperfection in a **stiffened shell** has **two major effects**:

1. The imperfect stiffened panel or shell bends as soon as any loading is applied. This **prebuckling bending** causes significant **redistribution of stresses** between the panel skin and the various stiffener parts, thus affecting significantly many local and inter-ring buckling and stress constraints (margins).

2. The **“effective” circumferential curvature** of an imperfect cylindrical panel or shell depends on the amplitude of the initial imperfection, on the circumferential wavelength of the critical buckling mode of the perfect and of the imperfect shell, and on the amount that the initial imperfection grows as the loading increases from zero to the design load. The **“effective” circumferential radius of curvature of the imperfect and loaded cylindrical shell is larger than its nominal radius of curvature** because the larger “effective” radius corresponds to the maximum local radius of the cylindrical shell with a typical **inward circumferential lobe** of the initial and subsequently load-amplified buckling modal imperfection. In PANDA2 this larger local “effective” radius of curvature is assumed to be the governing UNIFORM radius in the buckling equations pertaining to the imperfect shell. For the purpose of computing the general buckling load, the imperfect shell is replaced by a new perfect cylindrical shell with the larger “effective” circumferential radius. By means of this device a complicated nonlinear collapse analysis is converted into a simple **approximate** bifurcation buckling problem - a linear eigenvalue problem. For each type of buckling modal imperfection (general, inter-ring, local [1E]) PANDA2 computes a “knockdown” factor based on the ratio:

$$\frac{(\text{buckling load factor: panel with its “effective” circumferential radius})}{(\text{buckling load factor: panel with its nominal circumferential radius})} \quad (7.1)$$

Figures 1a,b,c show a STAGS model of a typical general buckling modal imperfection shape (amplitude exaggerated) for an optimized “compound” model [1K] of an axially compressed cylindrical shell with external stringers and internal rings (Case 4 in Table 4 in this paper). In this compound model a 45-degree sector has both external stringers and internal rings modeled as branched shell units. A 315-degree sector, the remainder of the cylindrical shell, has smeared stringers and internal rings modeled as branched shell units. Figure 2 shows the deformed state of the imperfect compound model as loaded by the design load, $N_x = -3000$ lb/in axial compression (STAGS load factor PA is close to 1.0). One observes three characteristics:

1. The stresses in the imperfect axially compressed shell have been redistributed as the globally imperfect shell bends under the applied axial compression. The maximum effective (von Mises) stress in this case, $s_{\text{bar}}(\text{max}) =$

66.87 ksi, occurs in the outstanding stringer flanges where the prebuckling deformation pattern of the imperfect shell has a maximum inward lobe.

2. The typical maximum “effective” circumferential radius also occurs where the deformation pattern has a maximum inward lobe. This larger-than-nominal circumferential radius is highlighted most clearly by the in-plane circumferential deformation of the interior ring located one ring spacing in from the right-hand curved edge of the STAGS model shown in Fig. 2. See the right-most expanded insert in Fig. 2.

3. There is an important phenomenon that occurs when **imperfect** cylindrical shells are **optimized**. This phenomenon has been described in previous papers [1K]. It occurs in the case of a stiffened cylindrical shell with an **imperfection in the form of the critical general buckling mode of the perfect shell**. The optimum design of an **imperfect stiffened cylindrical shell has a general buckling load factor that is usually considerably higher than load factors that correspond to various kinds of local and “semi-local” buckling, such as local buckling of the panel skin and stiffener segments, rolling of the stiffeners, and inter-ring buckling**. The general buckling margin of such a shell is usually not critical (near zero). In contrast, when a **perfect** stiffened cylindrical shell is optimized the general buckling load factor is usually very close to at least one local buckling load factor and is usually lower than many other local and “semi-local” buckling load factors. The general buckling margin of an optimized **perfect** shell is usually critical (near zero).

The cases explored in this paper exhibit this characteristic. Take, for example, the optimum designs called Case 1 and Case 2 in Table 4. In Case 1 a **perfect** shell is optimized. The margins for the Case 1 optimum design are listed in Table 10. Several of the margins for local and “semi-local” buckling are essentially equal to or greater than that for general buckling, and the general buckling margin is near zero (critical). In Case 2 a shell with a general buckling modal imperfection is optimized. The margins for the imperfect optimized shell are listed in Table 6 and those for the same optimum configuration but with the amplitude of the general buckling modal imperfection set equal to zero are listed in Table 7. In both Tables 6 and 7 the margin for general buckling is considerably higher than many of the margins corresponding to local and “semi-local” buckling. The general buckling margin of the optimized **imperfect** shell is well above zero (not critical).

Why does this happen? **The general buckling margin of optimized IMPERFECT stiffened shells is forced higher during optimization cycles because PREBUCKLING BENDING OF THE IMPERFECT SHELL increases with applied load approximately hyperbolically as the applied load approaches the general buckling load of the imperfect shell [1E]. If the general buckling load of the optimized imperfect shell were close to the design load, that is, if the general buckling margin were near zero (almost critical), there would be so much prebuckling bending near the design load that LOCAL STRESS AND BUCKLING MARGINS FOR THE STIFFENER PARTS AND FOR THE PANEL SKIN WOULD BECOME NEGATIVE BECAUSE THESE PARTS OF THE STRUCTURE WOULD BECOME HIGHLY STRESSED.**

8.0 DIFFERENCES IN THIS PAPER FROM [1K]

1. The loading is **pure uniform axial compression**
2. There are external T-shaped stringers and **internal** T-shaped rings
3. The stress constraint is active in this paper. **sigbar(allowable) = 60000 psi**.
4. The **dimensions, loading, imperfection amplitude** are listed in Table 1. (Decision variables defined in Table 2.)
5. Since [1K] was written **PANDA2 has been improved** as described in Section 9.0.
6. **Elastic-plastic material behavior** is accounted for in some STAGS models of the optimized shells.

9.0 IMPROVEMENTS IN PANDA2 SINCE [1K] WAS WRITTEN

Bugs have been eliminated and there are some new “wrinkles” in PANDA2 strategy introduced since [1K] was written. These are described in the file called "**panda2.news**" [1L], which has numbered items that date from as early as 1987. For more details about the panda2.news items listed next, and for other less significant items not included in this section, see [1L]. The most significant new items include the following:

Item 626: The strategy used in SUPEROPT [1D] was modified as follows:

1. The maximum constraint gradient of all active constraints for each design iteration is now printed in the *.OPP file. Also printed in the *.OPP file is a new line,
“-----
-----AUTOCHANGE”,
which appears in the *.OPP file for the first design iteration immediately following an execution of AUTOCHANGE [1D] during a SUPEROPT run.
2. **A single execution of SUPEROPT now generates a maximum between 470 and 500 design iterations** rather than between 270 and 300 iterations. This allows a better chance of finding a “global” optimum design.
3. **During a SUPEROPT run the “starting” design is set equal to the best design determined so far at or near Design Iteration Numbers. 150, 300, and 430, and the maximum permitted “move limits” are reduced temporarily from 0.1 to 0.02 at or near each of these same three Iteration Numbers. This new strategy helps PANDA2 “close in” on a FEASIBLE or ALMOST FEASIBLE local minimum-weight design.** The “move limits” are re-expanded to 0.1 at the next execution of AUTOCHANGE [1D].
4. The following classes of optimum designs now exist: “FEASIBLE”, “ALMOST FEASIBLE”, “MILDLY UNFEASIBLE”, “MORE UNFEASIBLE”, “MOSTLY UNFEASIBLE”, and “UNFEASIBLE”, whereas previously only “FEASIBLE”, “ALMOST FEASIBLE”, and “UNFEASIBLE” classes existed. A design is judged to be “FEASIBLE” if all margins exceed -0.01; a design is judged to be “ALMOST FEASIBLE” if all margins exceed -0.05 and the most negative margin is less than or equal to -0.01; a design is judged to be “MILDLY UNFEASIBLE” if all margins exceed -0.10 and the most negative margin is less than or equal to -0.05; a design is judged to be “MORE UNFEASIBLE” if all margins exceed -0.15 and the most negative margin is less than or equal to -0.10; a design is judged to be “MOSTLY UNFEASIBLE” if all margins exceed -0.20 and the most negative margin is less than or equal to -0.15; a design is judged to be “UNFEASIBLE” if the most negative margin is less than -0.20. PANDA2 still accepts as the “best” design that design with the minimum weight that belongs to either the “FEASIBLE” or “ALMOST FEASIBLE” class.

Item 633: The knockdown factor for compensating for the inherent unconservativeness of smearing rings was made less conservative than previously.

Item 634: The factor of safety for buckling of an outstanding flange of a stiffener as a beam on an elastic foundation (in which the web is the “elastic foundation”) was reduced from 3.0 to 1.2. The factor of safety for “rolling” of a stiffener without participation of the panel skin (See Fig. 6b,c in [1B]) was reduced from 1.6 to 1.4.

Item 643: The STAGSUNIT processor (main program stagun.src) was modified to make it relatively easy to generate compound models of the type shown in Figs. 56-60 of [1K] and in Figs. 1, 2 and Figs. 61-63 here. This is a specialized application and not very flexible as of this writing. The compound model must be a closed cylindrical shell and the most complicated section of the compound model must be the first section to be processed. (“most complicated” = both stringers and rings modeled as shell units). The compound model may have only two circumferential sectors. There are no compound models with multiple parts along the axis of a cylindrical shell. Complete directions for setting up compound models are included in Item 643 of [1L].

Item 645: The slope of the buckling nodal lines are sometimes included in the computation of **Wxx**, **Wyy**, **Wxy**. These three quantities are the pre-buckling bending and twisting of the initially imperfect shell that give rise to redistribution of the stresses between panel skin and stiffener parts and that generate an “effective” circumferential radius that is larger than the radius of the perfect cylindrical shell. (See Section 7.0).

Item 646: The user now supplies the number of nodal points across the webs and flanges of the stiffeners in STAGSUNIT.

Item 648: The strategy for computing “fractional” wavenumbers [1K] was modified for low numbers of circumferential waves.

Item 649: "Fractional" wave numbers (See Section 14 and Parts 2, 3, and 7 of Table 10 in [1K]) are set to zero less often than before. NOTE: Axial and circumferential "fractional" wave numbers, \mathbf{dm} and \mathbf{dn} , were introduced to smooth the change in buckling and stress margins with small changes in decision variables, such as occur when gradients of constraint conditions are being computed and from design iteration to design iteration. With the use of only integral numbers of axial and circumferential halfwaves, \mathbf{m} and \mathbf{n} , very large changes in margins might occur especially if \mathbf{m} and/or \mathbf{n} are small and change during successive design iterations.

Item 651: PANDA2 scans the general buckling mode produced by SUBROUTINE ALTSOL [1G]. If the mode resembles a local buckling mode or an inter-ring buckling mode determined earlier in the run, then no corresponding buckling margin is generated. The same holds for the inter-ring buckling mode produced by ALTSOL. This important modification usually leads to less conservative optimum designs. (ALTSOL is the subroutine that computes buckling load(s) via a double trigonometric series expansion of the buckling mode. See [1G] for details.)

Item 656: The effect of PANDA2's changing the imperfection amplitude formerly influenced only \mathbf{Wxx} , \mathbf{Wyy} , \mathbf{Wxy} . This item now also causes PANDA2's change in imperfection amplitude to change the effective circumferential radius of curvature of the bent, imperfect shell.

Item 659: The PANDA2 user may now specify the (\mathbf{m}, \mathbf{n}) combination for the general buckling modal imperfection, in which \mathbf{m} = **number of axial halfwaves** and \mathbf{n} = **number of circumferential halfwaves**. Formerly, PANDA2 only used $(\mathbf{m}, \mathbf{n})_{crit}$ as the general buckling modal imperfection shape, in which $(\mathbf{m}, \mathbf{n})_{crit}$ denotes the computed values of \mathbf{m} and \mathbf{n} that correspond to the minimum general buckling load factor. The user now has a choice: either let PANDA2 determine $(\mathbf{m}, \mathbf{n}) = (\mathbf{m}, \mathbf{n})_{crit}$ or let the user specify (\mathbf{m}, \mathbf{n}) . Accordingly, there exists new input in MAINSETUP (*.OPT file), $\mathbf{m}=\text{MUSER}$ and $\mathbf{n}=\text{NUSER}$, where MUSER and NUSER are specified by the user. (Because of the new input, old *.OPT files will no longer work with the latest version of PANDA2).

Item 660: Now additional boundary constraints are introduced in STAGSUNIT for the bifurcation buckling phase of the STAGS analysis. This eliminates some "phony" buckling modes that were previously possible. (See Fig. 16c of [1I], for example).

Item 662: For pure axial compression PANDA2 uses **WYYAMP=4.0** except when

- 1. $\mathbf{m} = 1$ or
- 2. $C_{44n}/C_{55n} > 2$ or
- 3. $L/m_{crit} > 2.0 * r$

in which **WYYAMP** is the amount by which the original buckling modal imperfection amplitude W_{imp} is amplified when the shell is loaded by the design load, \mathbf{m} = number of axial halfwaves in the buckling mode, C_{44n} = axial bending stiffness about the axial neutral plane, C_{55n} = circumferential bending stiffness about the circumferential neutral plane, L = axial length of the panel, m_{crit} = critical number of axial halfwaves, and r = the radius of the cylindrical panel. If **1** and/or **2** and/or **3** hold, PANDA2 now uses the same strategy as for all other combined loading conditions. (See Table 10 in [1K] for details about that strategy). **This important modification leads to less conservative optimum designs for shells subjected to loads in which applied axial compression dominates.**

Item 663: The inter-ring lateral-torsional buckling load factor computed from the PANDA2 single skin-stringer discretized module model was made less conservative by constraining the in-plane transverse displacement **WSTAR** at mid-stringer-bay.

Item 664: If the user has introduced a very small (or zero) **local imperfection amplitude**, PANDA2 increases this amplitude to only 5 per cent of the panel skin wall thickness rather than to 10 per cent of the wall thickness, as it had previously done.

Item 666: The effect of rings is now included in the "alternate" (double trigonometric series expansion) ALTSOL model of inter-ring buckling [1G]. Formerly, simple support was used where the ring webs intersect the panel skin, and the contribution of the rings to the stiffness and load-geometric matrices was neglected, often generating buckling load factors that were overly conservative.

Item 667: PANDA2 can now generate a STAGS model with STAGSUNIT in which **symmetry conditions** are imposed along the two straight edges (generators of a cylindrical panel). This is an extremely useful modification, valid only for cases in which both the in-plane shear loading and anisotropy, properties that give rise to “skewed” buckling modes, are not significant. Without this modification it would not have been possible to obtain many of the results in this paper. A STAGS model such as that shown in Fig. 1a is fine for predicting general buckling and perhaps even for “semi-local” bending-torsion buckling of the type displayed in Figs 19 and 20a. However, in order to obtain accurate local buckling load factors and mode shapes, such as those shown in Figs. 22 and 23a, one needs a small region with a very high nodal mesh density, as is illustrated in Fig. 22 of this paper and in Figs. 68 and 69 of [1K]. As described in [1K], nodal point distributions of this kind used in connection with a compound finite element model of a complete (360-degree) cylindrical shell did not work with the 480 finite element. Even if they had worked there would have been so many degrees of freedom that cases would have required excessive computer time. It would have taken days to extract the critical general buckling mode and load factor from the “haystack” of local and “semi-local” modes.

Item 668: A bug was eliminated in the computation of the contribution of the stiffeners to the twisting stiffness, C66, of the shell wall with smeared stiffeners. Previously the twisting stiffness had been overestimated.

Item 669: The STAGSUNIT processor (main program STAGUN) was modified to permit the user to select one or more stringers and/or one or more rings the cross sections of which have a higher nodal point density than all the other stiffeners of like kind. (See Figs. 24 - 31 for an example in which the central three stringers have been so modeled).

Item 670: The KOITER branch of PANDA2 [1C] was modified to set FMULT = 1.0 if the skin is **not** a sandwich wall. FMULT is a factor to be applied to the unknown, “**f**”, which is one of the four unknowns in the simultaneous nonlinear algebraic equations that govern the local postbuckling behavior of a stiffened panel [1C, 15].

Item 672: The STAGSUNIT processor (STAGUN) was modified to allow the user to permit constraint of meridional rotation, called “**rv**” in STAGS jargon, along the two curved edges of a cylindrical panel or shell in nonlinear static or dynamic (INDIC = 3 or 6) analyses. This now-possibly-imposed prebuckling constraint is released for the bifurcation buckling phase of the nonlinear analysis. This was done to raise the load level at which shell failure of the type shown in Fig. 73 occurs, a type of shell failure that cannot be predicted by PANDA2 and that is unlikely to occur in actual fabricated shells that are locally strengthened near their curved edges.

Item 676: A new input datum, **ICONSV**, has been introduced into the PANDA2 mainprocessor, MAINSETUP/PANDAOPT (*.OPT file). Therefore, old *.OPT files will no longer work. ICONSV can have values 1 or 0 or -1, the **recommended value being ICONSV = 1**. As set forth in the PROMPT.DAT file (prompting file for interactive PANDA2 input), The three permitted values of ICONSV are defined as follows:

ICONSV = 1 (recommended model) means:

- a. Include the ARBOCZ theory [1D] along with the “PANDA2 theory” [1E] when computing knockdown factors for local, inter-ring, general buckling of imperfect shells.
- b. Use a conservative knockdown factor to compensate for the inherent unconservativeness of smearing stringers for models in which the stringers are smeared (Item 676 in [1L]).
- c. Use the computed (conservative) knockdown factor for smearing rings (Item 605 in [1L]).
- d. The Donnell shell theory is used in SUBROUTINE STRIMP, where imperfection sensitivity is being computed. This is done because the ARBOCZ theory [1D] is based on Donnell theory.
- e. PANDA2 will use the non-zero slope of the buckling nodal lines in the computation of prebuckling bending and twisting, **Wxx**, **Wyy**, **Wxy**, of shells with general, inter-ring, and local buckling modal imperfections. (panda2.news Items 620 and 645 are cancelled).

ICONSV = 0 (less conservative model) means:

- a. Do NOT include the ARBOCZ theory [1D] when computing knockdown factors for local, inter-ring, general buckling of imperfect shells. Use **only** the “PANDA2 theory” [1E].
- b. Use a less conservative knockdown factor for models in which the stringers are smeared (Item 676 in [1L]).
- c. Use the computed knockdown factor for smearing rings (Same as for ICONSV = 1).
- d. The user-selected shell theory is used in SUBROUTINE STRIMP, where imperfection sensitivity is being computed.
- e. Panda2.news Items 620 and 645 are cancelled. (Same as for e. under ICONSV = 1).

ICONSV = -1 (still less conservative model) means:

- a. Do NOT include the ARBOCZ theory [1D] when computing knockdown factors for local, inter-ring, general buckling of imperfect shells. Use **only** the “PANDA2 theory” [1E]. (Same as for ICONSV = 0).
- b. Use a less conservative knockdown factor for models in which the stringers are smeared. (Same as for ICONSV = 0)
- c. Do NOT use the computed knockdown factor for smearing rings (Knockdown factor for smearing rings = 1.0 when ICONSV = -1, EXCEPT when there exists significant local deformation in the outstanding flange of the ring in the “skin”-ring single discretized module general buckling model, in which case the knockdown factor is computed in the same way as for ICONSV = 0 and ICONSV = 1).
- d. Set the knockdown factor for truncated double-trigonometric series expansion (ALTSOL) models [1G] to RFACT = 0.95. (RFACT=0.85 for "ALTSOL" models in which there are smeared stiffeners if ICONSV = 0 or 1).
- e. The user-selected shell theory is used in SUBROUTINE STRIMP, where imperfection sensitivity is being computed. (Same as for d under ICONSV = 0).
- f. Panda2.news Items 620 and 645 are in force, that is, a non-zero slope of buckling nodal lines will probably be set equal to zero for the computation of prebuckling bending and twisting, **Wxx**, **Wyy**, **Wxy**, of an initially imperfect panel. (Different from e. under ICONSV = 0 and ICONSV = 1).

With **ICONSV = 1** a given stiffened cylindrical shell with a given general buckling modal imperfection and given loading experiences more prebuckling bending under application of the design load than is the case with the less conservative options, **ICONSV = 0** or **ICONSV = -1**. With ICONSV = 1 the knockdown factors for compensating for the inherent unconservativeness of smearing stringers and of smearing rings are conservative. Therefore, estimates of the general buckling load factor obtained from PANDA-type models [1B] for both the perfect shell and for the imperfect shell are lower than they would be with the less conservative options, ICONSV = 0 or -1. The amplitude of a general buckling modal imperfection is assumed to grow hyperbolically [1E] as the applied load approaches the general buckling load of the imperfect shell. Therefore, for a given applied load, the lower the general buckling load factor the more overall prebuckling bending of the imperfect shell occurs. With more overall prebuckling bending there is more stress redistribution between panel skin and stiffener segments, with the result that **local** buckling load factors and **bending-torsion** buckling load factors are lower with ICONSV = 1 than they would be with ICONSV = 0 or -1, given the design of the stiffened shell. Also, maximum stresses are higher with ICONSV = 1 than with ICONSV = 0 or -1. Figure 99 shows various stress and buckling margins for the Case 4 design (Table 4) as functions of the “conservativeness” index, ICONSV. All the margins are highest for the least conservative model, ICONSV = -1, because the general buckling load factor (margin) is highest for the least conservative model. To emphasize what has already been stated: the lower the margin for general buckling the more prebuckling bending of the imperfect shell and therefore, because of stress redistribution between panel skin and stiffener parts, the lower the margins for local stress and buckling.

The behavior sometimes changes as a result of changes in ICONSV. For example, with ICONSV = 1 the maximum effective stress in Case 4 in Table 4 occurs in the outstanding flange of a ring. (See Margin No. 6 in Part 1 of Table 11). With ICONSV = -1 the maximum effective stress for the same configuration occurs in the outstanding flange of a stringer. The difference is caused by the different amounts of prebuckling bending with ICONSV = 1 and ICONSV = -1; significantly more circumferential bending occurs with ICONSV = 1 than with ICONSV = -1.

Item 677: The STRUCT library was modified to provide more structure to the *.OPM file in a case in which NPRINT = 1 or 2 (NPRINT=2 especially). The long output file, *.OPM generated with NPRINT = 1 or 2, now has a table of contents and chapter headings to aid the user in learning just what is going on in PANDA2 during the many, many computations for each load set and sub-case.

The table of contents, printed out in the *.OPM file from SUBROUTINE STRUCT if NPRINT = 1 or 2, is as follows:

ENTERING SUBROUTINE STRUCT

***** TABLE OF CONTENTS *****

CHAPTER 1 Compute the 6 x 6 constitutive matrices [C] for individual model segments and various combinations thereof (skin with one or more smeared stiffener sets).

CHAPTER 2 Do PANDA-type [1B] general buckling analysis to get Donnell factors for later use, if appropriate.

CHAPTER 3 Do various PANDA-type [1B] general buckling analyses needed for later computation of effective length of the panel.

CHAPTER 4 Compute axisymmetric prebuckling "hungry-horse" state of the curved panel or cylindrical shell. (See Ref.[1E]).

CHAPTER 5 Get static response of panel to normal pressure.

CHAPTER 6 Do PANDA-type general and inter-ring buckling analyses to permit later computation of amplification of panel bowing.

CHAPTER 7 Compute distribution of loads in panel module skin-stringer segments, neglecting redistribution due to initial buckling modal imperfections.

CHAPTER 8 Do PANDA-type [1B] local, inter-ring, general buckling analyses and PANDA-type stringer web and ring web buckling analyses to get knockdown factors to compensate for lack of in-plane shear loading N_{xy} and anisotropy in discretized BOSOR4-type models (Section 11 in [1A]). See Fig. 4 in this paper for an example of a discretized BOSOR4-type model.

CHAPTER 9 Do BOSOR4-type "skin"-ring buckling analyses to compute a knockdown factor to compensate for the inherent unconservativeness of models with smeared rings (Items 509, 511, 522, 532, and 605 in [1L]). ("Skin" is in quotes because it means "panel skin plus smeared stringers").

CHAPTER 10 Compute knockdown factors and prebuckling bending associated with initial general, inter-ring, local buckling modal imperfections. (See Ref.[1E]).

CHAPTER 10.1 Compute knockdown factor and prebuckling bending associated with a **general** buckling modal initial imperfection.

CHAPTER 10.2 Compute knockdown factor and prebuckling bending associated with an **inter-ring** buckling modal initial imperfection.

CHAPTER 10.3 Compute knockdown factor and prebuckling bending associated with a **local** buckling modal initial imperfection.

CHAPTER 10.4 Present a summary of imperfection sensitivity results.

CHAPTER 11 Get change in stress resultants, N_x , N_y , N_{xy} in various segments of the skin-stringer module during prebuckling bending of the imperfect shell. Also, do PANDA-type [1B] local, inter-ring, general buckling analyses and PANDA-type stringer web and ring web buckling analyses to get knockdown factors to compensate for lack of in-plane shear N_{xy} loading and anisotropy in discretized BOSOR4-type models, such as the BOSOR4-type model

displayed in Fig. 4.

CHAPTER 12 List prebuckled state of the initially imperfect and loaded and bent panel or shell. This section includes the redistribution of N_x , N_y , N_{xy} in the various segments of the stiffened shell structure caused by prebuckling bending of the imperfect shell.

CHAPTER 13 List prebuckling stress resultants, N_x , N_y , needed for the discretized single-module skin-stringer model used for local buckling and bending-torsion buckling (BOSOR4-type model, [1A]; An example of a single discretized skin-stringer module is displayed in Fig. 4 in this paper).

CHAPTER 14 Compute local (high-axial-halfwave- \mathbf{m}) buckling from a BOSOR4-type discretized skin-stringer single module model of the type displayed in Fig. 4.

CHAPTER 15 Compute bending-torsion (low-axial-halfwave- \mathbf{m}) buckling from a BOSOR4-type discretized skin-stringer single module model of the type displayed in Fig. 4.

CHAPTER 16 Compute post-local buckling from the Koiter theory given in Ref.[15]. (See Ref.[1C] and Figs. 4 and 5 in this paper).

CHAPTER 17 Compute stresses in layers and at various locations in skin-stringer module model, including local post-buckling, if any. Compute stringer popoff constraints [1A]. SUBROUTINE STRTHK is used.

CHAPTER 18 Present summary of the state of the loaded imperfect panel and give the effective stiffnesses of the possibly locally postbuckled skin-stringer module. These effective stiffnesses are used later for overall buckling and inter-ring buckling [24]. See Table 12 in this paper.

CHAPTER 19 Do the wide-column inter-ring buckling analysis (if IWIDE=1) with the possibly locally postbuckled skin-stringer module model [1A].

CHAPTER 20 Compute width-wise wide column buckling and lateral-torsional buckling load factors from the possibly locally postbuckled skin-stringer module model (inter-ring buckling modes).

CHAPTER 21 Compute a "skin"-ring buckling load factor for computing knockdown to compensate for the inherent unconservativeness of smeared ring models. (See the bottom row in Fig. 30 of [1G] for examples of the type of buckling and see Item 6 of Section 9.0 of [1K] for the computation of the "smeared ring" knockdown factor.)

CHAPTER 22 Compute "skin"-ring buckling load factors for:

1. medium- \mathbf{n} inter-ring buckling mode (See rightmost three mode shapes in top row of Fig. 30 of Ref.[1G]),
2. high- \mathbf{n} inter-ring buckling mode (See rightmost mode shape in middle row of Fig. 30, Ref.[1G]),
3. low- \mathbf{n} inter-ring buckling mode (See leftmost mode shape in top row of Fig. 30, Ref.[1G]).

CHAPTER 23 Compute stresses in layers and at various locations in modules for both positive and negative imperfection amplitudes from SUBROUTINE STRCON (local postbuckling neglected).

CHAPTER 24 Present short summary of redistribution of stress resultants, N_x , N_y , N_{xy} , caused by prebuckling bending of an initially imperfect shell.

CHAPTER 25 Compute buckling load factors from PANDA-type theory [1B] for the various segments of a stringer and a ring. Typical buckling modes are displayed in Figs. 5 and 6 of Ref.[1B].

CHAPTER 26 Compute local, inter-ring, general buckling load factors from PANDA-type models (Ref.[1B]) and from "alternative" (double-trigonometric series expansion models, Ref.[1G]).

CHAPTER 27 Compute the objective function (e.g. WEIGHT).

CHAPTER 28 Present design, loading, and margins for the current load set and subcase. (See Table 6, for

example).

Each CHAPTER in the *.OPM file now has the typical heading:

```
*****
***** CHAPTER 1 *****
*****
```

Item 684: The STAGSUNIT processor was modified to permit **plasticity** in certain limited types of STAGS models. All model segments must be shell units; no smeared stiffeners are allowed; no beam elements are allowed; only isotropic material is allowed; only one type of material in the entire structure is allowed. This modification was implemented with use of what in STAGS jargon is called “GCP” input format [20C]. For details, see Item 684 in [1L].

Item 686: A less conservative factor of safety is used for local buckling and stringer bending-torsional buckling in panels with blade-shaped stringers.

Item 688: A bug was eliminated concerning use of the **effective radius of curvature** of an initially imperfect and loaded cylindrical panel of nominal radius, R. The effective radius of curvature, RADNEW, is now used instead of the nominal radius, R, in the computation of local buckling of the discretized skin-stringer module of the type shown in Fig. 4 if the PANDA2 user specifies that a curved panel skin (ICURV=1) forms part of this particular model.

Item 694: Previously the Donnell shell theory was **always** used in the section of PANDA2 in which imperfection sensitivity is computed. Now the user-selected shell theory is used (either Donnell or Sanders or Marlowe shell theory) except when ICONSV = 1 (Item 676), for which Donnell shell theory is still used in the imperfection sensitivity branch of PANDA2 (SUBROUTINE STRIMP) no matter what shell theory is selected by the user.

Item 695: Different factors of safety can now be used for general buckling obtained from the PANDA-type [1B] theory and general buckling obtained from the “alternative” theory [1G]. The reasons for this increased flexibility are rather complex. An explanation is given in Item 695 in [1L].

Item 696: STAGSUNIT was modified to create a STAGS input file, *.inp, in either the “GCP” format or the “older” format. The “GCP” format applies to STAGS input data relating to material properties and shell wall fabrication.

Item 697: The wrong factor of safety was being applied to the “alternative” [1G] buckling load factor for inter-ring buckling. This bug was corrected. Now the inter-ring buckling factor of safety (called FSPAN) is applied.

Item 698: The buckling load factor for stringer segment buckling as computed from PANDA-type theory [1B] is now superseded by the buckling load factor as computed from the single discretized skin-stringer module model [1A] if the critical number of axial halfwaves between rings is less than or equal to 2.

Item 700: A bug was found in SUBROUTINE SEGCIJ that caused the ring faying flange to be omitted in the PANDA-type model [1B] of general buckling and in STAGS models generated by STAGSUNIT.

Item 701: It was decided never to use “fasteners” (STAGS jargon) in STAGS models generated by STAGSUNIT. The use of “fasteners” significantly increases the computer time and storage required without adding significantly to the accuracy of the result.

Item 702: The eccentricity of stringer and ring faying flanges relative to the panel skin reference surface was previously incorrect in STAGS models generated by STAGSUNIT in the case when either the middle surface or the inner surface was designated as the reference surface of the panel skin.

Item 703: STAGSUNIT previously did not work correctly for a flat plate under uniform axial compression. The boundary conditions did not permit enough freedom for proper transverse Poisson ratio expansion, with the result that transverse compression developed near the top and bottom edges of the plate.

Item 709: The strategy used for determining an appropriate knockdown factor to compensate for the inherent unconservativeness of smearing rings was modified to account for local deformation of the outstanding flange of a ring in the general buckling mode as generated with use of a single “skin”/ring discretized module model. (“Skin” in quotes means “skin + smeared stringers”).

Item 711: A bug was found in SUBROUTINE BUCPAN, which computes buckling load factors from PANDA-type (closed form) theory [1B] and from the alternate buckling theory in which the buckling mode is expanded in a double trigonometric series with undetermined coefficients. [1G]. The wrong prebuckling hoop resultant was being used for some of the alternate domains, including that governing general instability. This wrong hoop resultant did not include the additional prebuckling hoop compression in the panel skin caused by bending of an initially imperfect shell.

Item 718: A bug was found in the STAGSUNIT processor concerned with compound STAGS models [1K]. Too much in-plane shear loading, N_{xy} , was being introduced into the first part of the two-part compound model.

10.0 TYPICAL PANDA2 RUNSTREAM TO OBTAIN A "GLOBAL" OPTIMUM DESIGN

A sample PANDA2 runstream to produce a "global" optimum design is listed in Table 3. The case name is "test2". "Global" is in quotes because there is no guarantee that the optimum is truly a **global** optimum design. The more sets of "superopt/chooseplot/diplot" the user executes, the more likely it is that a truly global optimum design or a design the weight of which is very close to the global minimum weight will result. During the "global" optimization in the case listed in Table 3, there are four executions of the sequence SUPEROPT/CHOOSEPLOT/DIPLOT. Each execution of SUPEROPT [1D, 1K] must be followed by an execution of CHOOSEPLOT [1K] because CHOOSEPLOT is where the total number of design iterations gets reset to zero between executions of SUPEROPT. Therefore, **CHOOSEPLOT must always be executed before the next execution of SUPEROPT**.

Figure 3 shows a typical plot of an objective function versus design iterations after a first execution of SUPEROPT. Each “spike” in the plot corresponds to a **new starting design**, which (as explained in [1D, 1K]) is **generated randomly** in a manner consistent with all linking and inequality constraints.

11.0 OPTIMUM DESIGNS OBTAINED UNDER VARIOUS CONDITIONS

The optimum designs obtained in this study are listed in Table 4. **Table 4 is the most important item in this paper.** Seven cases are listed in order of increasing weight of half (180 degrees, see Table 1) of each of the optimized cylindrical shells. In Table 4 there appear variables, words, and phrases that must be defined:

1. “**perfect**” and “**imperfect**” have obvious meanings. All of the “imperfect” shells have a general buckling modal imperfection with **initial** amplitude, $W_{imp} = +/- 0.25$ inch specified by the PANDA2 user (and possibly changed later by PANDA2 as described in Item 4 below).
2. “**As if perfect**” (Case 6) means that the shell is optimized as if it were perfect (general buckling modal imperfection amplitude, $W_{imp} = 0$) and the applied load and maximum allowable stress **are doubled** to compensate for initial imperfections. This doubling is derived from the assumption for this particular configuration that the effect of a maximum allowable general buckling modal imperfection with amplitude W_{imp} equal to one per cent of the shell diameter (typical ASME allowable: $W_{imp} = 0.25$ inch in the other cases explored here) is to cause the shell to fail at half the load that its perfect equivalent would fail at.
3. “**No Koiter**” and “**yes Koiter**” refer to local “postbuckling” (or more generally, local bending perhaps without any instability) of the panel skin between adjacent stiffeners and local bending of the stringer parts. “No Koiter” means that the “Koiter” branch of PANDA2 [1C, 15] is skipped (Koiter branch is turned **off** in the *.OPT file) and the factor of safety for local buckling is set to unity (actually 0.999 in order to prevent PANDA2 from automatically raising the factor of safety to from 1.0 to 1.1). “Yes Koiter” means that the “Koiter” branch of PANDA2 is entered (Koiter branch is turned **on** in the *.OPT file), that is, local “postbuckling” (bending) states are computed; **the factor**

of safety for local buckling is set equal to a small number (0.1 in this case, which causes the evolution of the design to be unconstrained by local bifurcation buckling margins); and the shell is optimized accounting for local bending deformation between adjacent stiffeners and local bending deformation of the stringer parts. **Local buckling (bending) at or below the design load raises the maximum effective stress** because of short-wavelength bending of the skin between stiffeners and of the stringer parts. (See Fig. 7, for example). Local buckling (bending) lowers inter-ring and general buckling load factors because a locally buckled (bent) skin is less stiff in an average sense than an unbuckled (unbent) skin ([24], and see Table 12 in this paper). Corresponding to the optimum design in Case 5 (“yes Koiter”) the skin-stringer module (similar to that shown in Fig. 4 but with different cross section dimensions) has not actually buckled locally in the sense that its local buckling load factor is less than the design load, $N_x = -3000$ lb/in. Indeed, in Case 5 the local buckling load factor is about 1.3 times the design load (approximately $N_x = -4000$ lb/in). For the Case 4 design with use of the “yes Koiter” option, a very small initial local buckling modal imperfection (equal to five per cent of the shell skin thickness) grows under application of the design load as displayed in Figs. 4 and 5, giving rise to significant local bending stress in the skin and stringer parts at the design load. This local bending stress adds to the overall membrane compression, causing the stress constraints to become critical with “yes Koiter” sooner than with “no Koiter”. That is why the “yes Koiter” optimum design (Case 5) is heavier than the “no Koiter” optimum design (Case 4) for this particular configuration, material, and loading. **The additional stress generated by local bending/buckling of the sort depicted in Figs. 4 and 23a, for example, is accounted for with the “yes Koiter” option and ignored with the “no Koiter” option.**

Figures 4 – 7 demonstrate the local bending phenomenon and its effect on stress margins. These figures correspond to the optimum configuration identified as Case 4 in Table 4, the shell optimized with “no Koiter”. However, Figs. 4 and 5 are derived from an analysis of the Case 4 configuration with the Koiter branch turned on in the *.OPT file, that is, with the “yes Koiter” option. Figure 4 shows a single skin-stringer discretized module and its local bending deformation at four levels of the applied axial compression N_x (amplitude of bending deformations greatly exaggerated). Figure 5 shows the maximum normal displacement w midway between stringers as a function of applied axial compression. Figure 6 demonstrates the effect of omitting (NO KOITER) and including (YES KOITER) the contribution of local bending to the total maximum effective (von Mises) stress in the Case 4 stiffened shell. The optimum design obtained with “no Koiter” (Case 4) is no longer feasible if the Koiter branch of PANDA2 is turned on (“yes Koiter”) for this configuration. At the design load, $N_x = -3000$ lb/in, four of the YES KOITER stress margins are significantly negative. Figure 7 shows a STAGS model of the Case 4 configuration with nodal points concentrated where global bending of the imperfect shell is maximum inward. The effect of local bending of the panel skin in the region of highest nodal mesh density is clearly visible, and the maximum effective stress, $s_{bar(max)} = 68.22$ ksi, significantly exceeds the maximum allowable effective stress, $s_{bar(allowable)} = 60$ ksi.

Typically, designs in which local postbuckling is permitted during optimization are lighter than those in which it is not, especially if in-plane shear N_{xy} is a significant component of the applied loading. Such “typical” designs are more lightly loaded shells in which in-plane shear loading N_{xy} may be significant and/or shells made of a material with a higher allowable stress than is so for the cases included in this paper. For the cases in this paper (Case 4 and Case 5) the “yes Koiter” option (Case 5) leads to a heavier optimized shell than does the “no Koiter” option (Case 4).

4. **“Yes change imperfection”** means that **Strategy 2** is followed in the PANDA2 main processor. (See Section 15.1 and Table 13 in [1K] for the definition of “Strategy 2”). In **Strategy 2** the **initial (user specified) amplitude** of the general buckling modal imperfection is multiplied by the ratio,

$$(\text{axial wavelength of actual critical general buckling mode}) / (\text{user-specified length of general buckling mode}) \quad (11.1)$$

during all computations. This strategy is derived from the assumption that imperfections of given amplitude with shorter axial wavelengths are easier to detect than those with longer axial wavelengths. They are therefore easier to control during manufacture. Here it is assumed that what is detected in an initially imperfect cylindrical shell is actually the error in **axial slope** of the imperfect generators. For a **given** (specified) allowable error in axial slope of an imperfect generator, that is, the minimum detectable error in axial slope, the **amplitude** of that same initial imperfection shape is proportional to its axial wavelength (inversely proportional to the number of axial halfwaves m in the imperfection shape). **With Strategy 2 “turned on” (“yes change imperfection”) the shorter the axial wavelength of the initial general buckling modal imperfection the smaller its amplitude.** For axially compressed cylindrical shells the critical general buckling mode usually has several axial halfwaves m . If the

PANDA2 user chooses the specified axial length of the initial general buckling modal imperfection to be equal to the axial length of the shell, which is in the range of the recommended input in the *.OPT file for the particular cylindrical shells featured in this paper (Table 1), PANDA2 will reduce the user-specified imperfection amplitude by a factor equal to the ratio defined above (Expression 11.1) if Strategy 2 is chosen. **Strategy 2 is based on the assumption that one general buckling modal imperfection is approximately equivalent to another if their maximum axial slopes are equal.**

Notice that the previous paragraph does not mention PANDA2 automatically changing the initial user-specified general buckling modal imperfection amplitude based on possibly easily detectable errors in **circumferential slope** of the wall of the imperfect shell. Only an error in **axial slope** is mentioned. It turns out that, for the particular cases explored in this paper, the error in axial slope is less than that in circumferential slope. For example, if the critical general buckling mode has $(m,n)_{\text{critical}} = (4 \text{ axial}, 6 \text{ circumferential})$ halfwaves, then the axial halfwavelength is $75.0/4.0 = 18.75$ inches and the circumferential halfwavelength is $\pi r / 6.0 = \pi \times 25.0 / 6.0 = 13.09$ inches. For a given user-specified amplitude of general buckling modal imperfection, the error in axial slope is $13.09/18.75 = 0.698$ or about 70 percent as large as the error in circumferential slope for $(m,n) = (4,6)$.

A more systematic way to approach **Strategy 2** (allowing PANDA2 to change the imperfection amplitude based on wavelength of the imperfection) would be to have the PANDA2 user supply **two** new input data: 1. minimum detectable error in axial slope and 2. minimum detectable error in circumferential slope. Then PANDA2 would compute the amplitude of the general buckling modal imperfection. This computed amplitude would depend on $(m,n)_{\text{critical}}$. The amplitude would be that which causes the imperfection to be at the threshold of detectability for either axial or circumferential error in slope, whichever barely detectable error in slope leads to the smallest amplitude. The PANDA2 user would supply two new inputs, one for minimum detectable error in axial slope and the other for minimum detectable error in circumferential slope, because the threshold of detectability of error in axial slope might be different from that of error in circumferential slope. It is logical to assume that an error in axial slope would be easier to detect than the same error in circumferential slope because the axial slope of the perfect cylindrical shell is zero and the quality control engineer is looking for deviations from zero.

The maximum axial slope corresponding to a general buckling modal imperfection of the form, $W_{\text{imp}}(x,\theta) = A \sin(m\pi x/L) \sin(n\theta)$, is $A \cdot m\pi/L$. The minimum **detectable** non-zero axial slope in the cases explored in this paper is given by **0.25.pi/L radians** because the user-specified initial amplitude of the general buckling modal imperfection is 0.25 inch and the user-specified axial halfwavelength is 75 inches, the length of the cylindrical shell, that is, $m = 1$. **The writer does not know what is a reasonable minimum detectable error in axial slope in practice. Hence, the results in this paper labeled “yes change imperfection” in Table 4 are presented for the purpose of demonstration only, not as a guideline for the reader to use in the actual fabrication of shells.**

“No change imperfection” means that **Strategy 1** [1K] is followed; the **user-specified imperfection amplitude is not modified**. Unless the PANDA2 user specifies an initial general buckling modal imperfection with a very small amplitude, optimum designs obtained with the “no change imperfection” option are probably too conservative (too heavy) because the optimum design thus obtained by PANDA2 usually ends up with an imperfection (general buckling mode with several axial halfwaves) with an amplitude that could easily be detected. Therefore such an imperfect shell would have to be repaired or a shell with such an imperfection would have to be discarded. Also, with “no imperfection change” specified in the *.OPT file, design margins often change drastically from design iteration to iteration, a phenomenon described in Section 15.1 and Fig. 20 of [1K] that makes it difficult to find a “global” optimum design.

5. The index, **ICONSV**, is defined above in **Item 676** of Section 9.0. **ICONSV = -1** denotes the least conservative model and **ICONSV = 1** denotes the most conservative model. See Fig. 99 for an example of how several of the margins in Case 4 vary with **ICONSV = -1, 0, and +1**.

6. The critical margins from PANDA2, enumerated in the row in Table 4 just below that which lists the shell weights, are defined in **Table 5**. The string, “**SANDERS**” in Table 5 indicates that Sanders’ shell equations [25] are used in the computations. In Table 5 “M” or “m” is the number of axial halfwaves; “N” or “n” is the number of circumferential halfwaves except in Margins 6 and 23 where “n” means nodal point number in a module; “slope” is the slope of the buckling nodal lines as shown in Fig. 9 of [1B]; “FS” is the factor of safety; “STR” = stringer; “SKN” = panel skin; “RNG” = ring; “Dseg” = segment number in the discretized skin-stringer single module model

(Fig. 4): Dseg=1 = panel skin in left-hand part of Fig. 4; Dseg=2 = base under the stringer where the stringer web root intersects the panel skin; Dseg=3 = stringer web; Dseg=4 = outstanding stringer flange; Dseg=5 = panel skin in right-hand part of Fig. 4. “z” is the thickness coordinate in a shell wall or stiffener segment wall; “MID” means “midway between rings” (same as Sub-case 1); “RNGS” means “at ring stations” (same as Sub-case 2); “Iseg” means skin-stringer or skin-ring single module segment number (PANDA-type model [1B], not discretized module [1A]): Iseg=1 = panel skin; Iseg=2 = base under the stiffener (either stringer or ring); Iseg=3 = stiffener web; Iseg=4 = stiffener outstanding flange. “ROOT” means “at web root” (where a stiffener web intersects the panel skin); “allnode” means “at all nodal points in the panel skin”; “C=0” means “slope of buckling nodal lines=0”; “NOPO” means “neglecting local postbuckling effects”. “V(i)” is the ith variable. See Table 2 for definitions of the variables, V(i), i = 1 to 13.

7. The quantity “PA” that appears in the row in Table 4 pertaining to STAGS predictions is the applied load factor. PA = 1.0 corresponds to the design load, that is, the applied load specified in the PANDA2 input file, *.OPT. The design load is Nx = -3000 lb/in axial compression in all cases except Case 6, for which the design load is Nx = -6000 lb/in.

8. The (-) and (+) that occur in Case 7 immediately following the collapse load factors PA predicted by STAGS, PA= 1.22(-) and PA= 1.15(+), refer to the sign of the amplitude of the buckling modal imperfection, Wimp = - or + 0.25 inch.

9. The string, “stringer sidesway”, means “bending-torsional” buckling or “stringer rolling” [1B] of the type shown in Fig. 20a.

10. All the PANDA2 and STAGS models for which results are listed in Table 4 are based on the assumption that the **material remains elastic**. Therefore, the collapse load factors, PA, listed in Table 4 in the row pertaining to STAGS predictions would be somewhat lower if plastic flow were included. See Section 14 for a discussion of the effects of accounting for elastic-plastic material behavior in STAGS models of some of the shells optimized by PANDA2 (Cases 2, 4, 5, 7).

12.0 DETAILS FOR AN EXAMPLE: CASE 2 IN TABLE 4

The results are summarized in Column 3 of Table 4. The information in this section generally applies to all the cases listed in Table 4, especially those cases in which an initial general buckling modal imperfection exists.

In this paper the phrases, “**design load**”, “**buckling load factor**”, “**buckling margin**”, and “**stress margin**” appear many times. The following definitions apply:

$$\text{Design load} = \text{applied load (the load or combination of loads that is specified by the PANDA2 user)} \quad (12.1)$$

$$\text{Buckling load factor} = \text{eigenvalue} = (\text{load that causes buckling}) / (\text{applied load}) \quad (12.2)$$

$$\text{Buckling margin} = (\text{buckling load factor}) / (\text{factor of safety}) - 1.0 \quad (12.3)$$

$$\text{Stress margin} = \{(\text{allowable stress}) / [(\text{actual stress}) \times (\text{factor of safety})]\} - 1.0 \quad (12.4)$$

12.1 PANDA2 phase of the computations

Tables 6, 7, and 8 and Figs. 8 – 15 pertain to this sub-section.

12.1.1 PANDA2 runstream and files

The optimum design is obtained from PANDA2 via the following sequence of commands. In the following, “*” denotes the user-selected name for the case. Here, “*” = “test2”.

COMMAND	PURPOSE OF THE COMMAND
panda2log	Activate the PANDA2 set of commands.
begin	Supply the starting design, material properties, and boundary conditions.

setup	PANDA2 sets up templates of stiffness matrices, data base files, etc.
decide	Choose decision variables, upper and lower bounds, linking relations, inequality relations.
mainsetup	Choose loading, factors of safety, imperfections, model types, strategies, shell theory, type of analysis (e.g. ITYPE = 1 means “optimization”).
superopt	Launch the first attempt to find a “global” optimum design. Stiffener spacings can change.
chooseplot	Choose what to plot. Usually the PANDA2 user will want to plot only the objective. (See Fig. 3).
diplot	Obtain the plot(s). The plot of the objective function vs. design iterations will be in the file, *.5.ps .
change	Change the ring spacing and the stringer spacing to the nearest values suitable for a later analysis by STAGS. The new stiffener spacings must be such that an integral number of equally spaced stringers spans the circumferential domain and an integral number of equally spaced rings spans the axial domain of the STAGS model, the input data for which are to be generated later by STAGSUNIT.
setup	PANDA2 sets up templates of stiffness matrices, data base files, etc.
decide	Choose decision variables, etc., this time omitting the stiffener spacings, which are to be fixed.
superopt	Launch the second attempt to find a “global” optimum design with the stiffener spacings now fixed.
chooseplot	Choose what to plot versus design iterations. Choosing only the objective is usually best after a “superopt” run.
diplot	Obtain the plot(s). See Fig. 3, for example.
mainsetup	Use the same input file as for the previous “mainsetup”, except choose the analysis of a fixed design (ITYPE=2) rather than optimization (ITYPE=1). The fixed design is automatically the optimized design, provided the previous optimization was via a successfully completed “superopt” execution .
pandaopt	Obtain the margins and values of all variables for the optimized design. See Table 6, for example.

Input files, ***.bin** and ***.inp**, for STAGS are obtained via the following command:

stagsunit Obtain the input files, ***.bin** and ***.inp**, for STAGS.

Input files, ***.ALL**, for BOSOR4 (or BIGBOSOR4) [14] are obtained via the following commands:

panel	Obtain the input file, *.ALL , for BOSOR4 or BIGBOSOR4 [14F] for local and inter-ring buckling from models such as those shown in Figs. 33 and 34, for examples.
panel2	Obtain the input file, *.ALL , for BOSOR4 or BIGBOSOR4 for general buckling from models such as those shown in Figs. 35 and 36, for examples.

The PANDA2 commands just listed create the following files:

COMMAND	INPUT FILE	OUTPUT FILE(S)
begin	*.BEG	*.OPB
setup	no input files	several data base output files used “internally” by PANDA2 processors
decide	*.DEC	*.OPD
mainsetup	*.OPT	no output files
superopt	no file created	*.OPP
chooseplot	*.CPL	*.OPL
diplot	no file created	*.i.ps (i postscript files, i = 1,2,3.. The objective (Fig. 3) is in *.5.ps).
change	*.CHG	*.OPC
pandaopt	no file created	*.OPM
stagsunit	*.STG	*.bin, *.inp (input files for STAGS)
panel	*.PAN	*.ALL (input file for BIGBOSOR4 [14F])
panel2	*.PAN	*.ALL (input file for BIGBOSOR4 [14F])

The input files, ***.BEG**, ***.DEC**, ***.OPT**, ***.CPL**, ***.CHG**, ***.STG**, and ***.PAN**, created during the interactive sessions initiated by the commands, **begin**, **decide**, **mainsetup**, **chooseplot**, **change**, **stagsunit**, and **panel** or **panel2**, respectively, are convenient because they serve as documentation for the case and because they can be used again in

the future (with or without editing) in order to bypass possibly tedious interactive sessions. Examples of these input files for the cases described in this paper are listed in the directory, ...**panda2/case/sdm48**. NOTE: It is very useful to create a *.CHG file for each “global” optimum design obtained. By doing this the PANDA2 user can easily re-establish optimum designs generated in the past by executing **begin** immediately followed by **change**. The seven optimum designs listed in Table 4 are stored in seven files, called “case1.chg”, “case2.chg”, etc., located in the ...**panda2/case/sdm48** directory.

The optimum design obtained by PANDA2 is listed as Case 2 in Column 3 of Table 4. The critical margins corresponding to the two load sets (Table 1) and two sub-cases for each load set are listed in Table 6. The critical and near-critical margins are in bold font. **Sub-case 1 means “conditions midway between rings”; Sub-case 2 means “conditions at a typical ring station” or “at rings”.** These conditions differ because a perfect axially compressed cylindrical shell bends axisymmetrically with an axial wavelength equal to the ring spacing due to the Poisson effect. Poisson radial expansion is retarded at ring stations more than it is midway between rings. The maximum axial compressive stress in the outstanding **external stringer flange** is higher at the ring locations (Sub-case 2) than midway between rings (Sub-case 1) because of this Poisson effect. There is more than nominal axial compression of the outstanding flanges of the external stringers at the rings and less than nominal axial compression of the outstanding flanges of the external stringers midway between the rings. (Had the stringers been internal the reverse would have held: the maximum axial compression of the stringer flanges would have been midway between rings and the minimum axial compression would have been at the ring stations). **The differing conditions midway between rings and at the ring stations also influence many of the local buckling margins.** While the prebuckling conditions that prevail in Sub-case 1 differ from those in Sub-case 2, it is assumed in the PANDA2 buckling models that these different prebuckling conditions are locally uniform in the axial coordinate direction in the analyses performed by PANDA2 for each of the two sub-cases. (NOTE: These assumed-to-be-axially-locally-uniform-prebuckling states are different in the two sub-cases).

The first two parts of Table 6 correspond to a **positive** general buckling modal imperfection (Load Case No. 1). The second two parts of Table 6 correspond to a **negative** general buckling modal imperfection (Load Case No. 2).

The general buckling margin (Margin No. 13 in Load Set 1, Sub-case 1 and in Load Set 2, Subcase 1) is computed **only** for Sub-case 1 because it is assumed that the global bending of the imperfect shell has an axial halfwavelength that is very long compared to the ring spacing and that the “worst” (most destabilizing) conditions for general buckling correspond to those midway between adjacent rings. In this example Margin 13 is the same for both Load Set 1 and Load Set 2 because the applied loads are the same in these two load cases. Only the sign of the amplitude of the general buckling modal imperfection changes. This sign does not influence the general buckling margin of the imperfect shell. Note, however, that the sign of the amplitude of the general buckling modal imperfection **does** influence the inter-ring and local buckling margins.

Although the optimum design is listed in column 3 of Table 4, it is repeated near the end of Table 6 in a form that also provides the lower and upper bounds of the decision variables. These bounds are not listed elsewhere in this paper.

Table 7 lists the margins obtained for the same design with the amplitude, Wimp, of the general buckling modal imperfection set equal to zero. Some of these margins are compared later to those obtained by STAGS for the perfect shell with Case 2 dimensions.

With the relatively new strategy introduced into PANDA2, that is, the strategy described in Item 595 of [1L], in Section 15.1 and Table 13 of [1K], and above in connection with the “**yes change imperfection**” notation in Table 4 (see Item 4 in Section 11.0), it is no longer certain that the “worst” general buckling modal imperfection is that associated with the smallest general buckling load factor, that is, with the mode shape $(m,n) = (m,n)_{crit}$ (axial, circumferential) halfwaves, in which $(m,n)_{crit}$ are computed by PANDA2. Therefore, it is beneficial to be able to check the feasibility of the optimized design with general buckling modal imperfections that have **user-specified** mode shapes, $(m, n) = (MUSER, NUSER)$ as described briefly in **Item 659** in Section 9.0 above. This is a significant new PANDA2 capability. Hence the description of it included in [1L] is reproduced next.

12.1.2 Item 659 in the file .../panda2/doc/panda2.news. July 2006

This is a rather important news item involving a significant modification to PANDA2. The subject is the general

buckling modal imperfection shape. Previously, the general buckling modal imperfection shape was always the **critical** general buckling mode, either of the perfect shell or of the imperfect shell, depending on which PANDA2 judged as the "worst" (most harmful) shape. PANDA2 conducted a thorough search over **(m,n,s)** space to determine the **critical** general buckling mode. (**m** = number of axial halfwaves; **n** = number of circumferential halfwaves; **s** = slope of the buckling nodal lines). The **(m,n,s)** computed by PANDA2 is the general buckling mode that corresponds to the **smallest general buckling load factor** (eigenvalue).

PANDA2 will still do this. However, now the user can choose which values of **(m,n)** PANDA2 **must** use for the general buckling modal imperfection shape. Instead of searching over **(m,n)** to determine what PANDA2 judges to be the most critical general buckling modal imperfection shape, if the user identifies an **(m,n)** pair, **(m,n) = (MUSER, NUSER)**, PANDA2 will use **only** that pair and not search over **(m,n)**. PANDA2 continues to search for the most critical slope **s** of the buckling nodal lines, given the user-specified pair, **(m,n) = (MUSER, NUSER)**.

It is emphasized that this modification affects **only** the section of PANDA2 that deals with **general buckling imperfection sensitivity**, that is, the computations that occur in PART 1 of SUBROUTINE STRIMP (See Table 10 in [1K]).

In order to permit this new choice, I had to add at least one input datum for each load set in the MAINSETUP interactive session. (This interactive session produces the *.OPT file). The additional lines in the PROMPT.DAT file (which contains prompts for the PANDA2 user) are as follows:

367.1 Do you want PANDA2 to find the general imperfection shape?

367.2

Almost always answer Y (yes). PANDA2 will then find the **(m,n,s)** for the general buckling mode, in which

m = number of axial halfwaves

n = number of circumferential halfwaves

s = slope of the buckling nodal lines.

The imperfection shape is assumed to be the same as the general buckling mode shape.

If you for some reason should answer N (no), then you must next supply values of **(m,n)**, called MUSER and NUSER. In the section of PANDA2 that computes general buckling imperfection sensitivity, PANDA2 will not search over **(m,n)** space to find the critical general buckling modal imperfection shape, but instead will use only the values (MUSER,NUSER) that you will next supply. PANDA2 will continue to search over "s-space" (**s** = slope of buckling nodal lines) for a minimum general buckling load factor with respect to **s** for given and fixed **(m,n) = (MUSER, NUSER)**.

368.1 Number of axial halfwaves over the length of the panel, MUSER

368.2

MUSER must be greater than zero. PANDA2 will use ONLY this number of axial halfwaves in the section on general buckling imperfection sensitivity.

369.1 Number of circumferential halfwaves over the panel, NUSER

369.2

NUSER must be greater than zero. PANDA2 will use ONLY this number of circumferential halfwaves in the section on general buckling imperfection sensitivity.

There is some new output in the *.OPM file, as follows:

General instability.

NOTE: The user has chosen to fix (MWAVEX,NWAVEX) at the values (MUSER,NUSER) = 1 3

EIGMNC= 2.95E+00 1.00E+17 1.00E+17 1.00E+17 1.00E+17 1.00E+17 1.00E+17

SLOPEX= 0.00E+00 0.00E+00 0.00E+00 0.00E+00 0.00E+00 0.00E+00 0.00E+00

MWAVEX= 1 0 0 0 0 0 0

NWAVEX= 3 0 0 0 0 0 0

I decided to make this modification even though it requires a new input datum in the *.OPT file, which will render

old *.OPT files inoperative. The advantage of the new version of PANDA2 is that the user can explore various general buckling modal imperfection shapes, that is, shapes with various selected $(m,n) = (MUSER,NUSER)$ pairs. There are two good reasons for the user to be able to do this:

1. One can optimize the imperfect shell in the old way, that is, letting PANDA2 determine what it "thinks" is the most critical general buckling modal imperfection shape, (m,n,s) . Then, for the design of the imperfect shell thus optimized, the user can run a series of fixed design analyses, each with use of a different $(MUSER, NUSER)$ pair in order to determine if the optimized design is truly safe. This process is especially important if the user has elected to allow PANDA2 to change the imperfection amplitude as described in Section 15.0 on p. 23 of the paper, "Difficulties in optimization of imperfect stiffened cylindrical shells", AIAA-2006-1943, 47th AIAA SDM Meeting, Newport RI, April 2006. (Also see news Item 595).
2. One can measure an imperfection in an actual shell. The user can then specify the $(MUSER,NUSER)$ pair that most closely resembles that measured imperfection shape.

NOTE: PANDA2 will optimize with the specified $(MUSER, NUSER)$ choice.

12.1.3 Results from surveys of $(MUSER, NUSER)$ for the most critical margins in Table 6

Figures 8 - 15 show the results of surveys in $(MUSER, NUSER)$ space for the most critical margins listed near the top of Table 6, that is, for “LOAD CASE NO. 1, SUBCASE NO. 1”. The following comments apply:

1. As listed for Margin No. 13 in Table 6, PANDA2 finds that the critical general buckling mode of the imperfect shell has $(m, n) = (4, 6)$ (axial, circumferential) halfwaves over the 180-degree domain (Table 1). Except for Fig. 14 (general buckling margin), $NUSER = 6$ circumferential halfwaves indeed represents the “worst” imperfection (smallest margins). In Fig. 14 $NUSER = 3, 4$, and 5 yield smaller margins than for $NUSER = 6$ but none of these margins is critical and the margin for $NUSER = 6$ is not too far above the others. $MUSER = 4$ is usually not the “worst” imperfection shape. However, it is in the range of $MUSER$ for which the margins are not too sensitive to changes in $MUSER$ and $NUSER$.
2. The values of the margins for $(MUSER, NUSER) = (4, 6)$ are slightly different from those listed near the top of Table 6. This is because no “fractional” halfwaves (Section 14 and Parts 2, 3, and 7 of Table 10 in [1K] and Table 8 in this paper) are permitted in computations for which the user specifies $(MUSER, NUSER)$. In contrast, the margins listed in Table 6 are derived permitting possible “fractional” axial (**dm**) and “fractional” circumferential (**dn**) halfwaves to exist during the computation of the prebuckling bending and twisting, **Wxx**, **Wyy**, **Wxy**, of the imperfect shell. As mentioned previously (above in Section 7.0 and in [1K]), stress and buckling margins are sensitive to the prebuckled state of the imperfect shell, that is, to the values of the prebuckling bending and twisting, **Wxx**, **Wyy**, **Wxy**, of the imperfect shell as it bends under the design load. Table 8 lists fragments from *.OPM output files pertaining to the computation of the final amplitude of the general buckling modal imperfection to be used in PANDA2 computations corresponding to the optimized design listed under Case 2 in Table 4. Part 1 of Table 8 lists results of computations in which “fractional” wave numbers, **dm** and **dn**, are permitted. Part 2 of Table 8 lists the analogous results for the same design in which “fractional” wave numbers are not permitted and the user-specified $(MUSER, NUSER) = (m,n) = (4,6)$. Although in this particular case there exists a moderate effect, about 11 per cent, of “fractional” wavenumbers on the prebuckling bending and twisting, **Wxx**, **Wyy**, **Wxy** (called “**Wxx9**”, “**Wyy9**”, “**Wxy9**” in Table 8), the effect on the most critical margins is relatively small. Had the critical values of **m** and **n** been smaller there probably would have been a much more pronounced effect because **dm** and **dn** would probably have been larger percentages of **m** and **n**, respectively.
3. For all of the most critical margins in Load Case No. 1, Sub-case No. 1 none of the margins in the $(MUSER, NUSER)$ surveys is significantly negative. Figure 12 displays two instances in which there are slightly negative stress margins corresponding to $(MUSER, NUSER) = (2,5)$ and $(3,6)$. However, these margins are greater than -0.05 and therefore permitted by PANDA2 in designs it judges to be “ALMOST FEASIBLE” (Section 12 of [1K]).
4. The results in Fig. 10 are obtained from PANDA2’s SUBROUTINE **STRTHK**, which determines the stress in a single **discretized skin-stringer module** [1A] such as that shown in Fig. 4. The effect of local bending of the type

displayed in Fig. 4 is accounted for if the “Koiter switch” is turned on (“yes Koiter” in Case 5 in Table 4). In contrast, the results in Fig. 12 are obtained from PANDA2’s SUBROUTINE **STRCON**, for which local bending is neglected and for which stresses in **both** stringer parts and ring parts are computed. The curves in Figs. 10 and 12 contain data points for which the maximum effective stress occurs in different parts of the stiffened shell. All the data points in Fig. 10 correspond to the maximum effective stress occurring in the **outstanding flange of a stringer** (Margin 6a in Table 5) except the following data points, which all correspond to the maximum effective stress occurring in the **stringer web** where this web intersects the panel skin (Margin 6b in Table 5): (MUSER=1, NUSER=1,2,5-10), (MUSER=2, NUSER=1,2,8,9,10), (MUSER=3, NUSER=1,10).

Most of the data points in Fig. 12 also correspond to the maximum effective stress occurring in the **outstanding flange of a stringer** (Margin 23a in Table 5) except for the following locations of the maximum effective stress:

Stringer web root (Margin 23b in Table 5): (MUSER=1, NUSER=1,2,3,8,9,10), (MUSER=2,3,4, NUSER=1,2), (MUSER=3, NUSER=3),

Shell skin (Margins 23c,d in Table 5): (MUSER=1, NUSER=3,5,6,7), (MUSER=2, NUSER=7,8,9), (MUSER=3, NUSER=8,9,10), (MUSER=4, NUSER=10),

Outstanding ring flange (Margin 23e in Table 5): (MUSER=1, NUSER=4), (MUSER=2, NUSER=5,6), (MUSER=3, NUSER=5,6), (MUSER=4, NUSER=6,7).

12.2 STAGS phase of the computations (including some results from BIGBOSOR4 [14F])

The STAGS phase of the computations requires more labor and more computer time than does the PANDA2 phase. Table 9 lists a rather long sequence of STAGS runs, the purpose of which is to evaluate the optimum design (Case 2) obtained by PANDA2. First, several STAGS runs are executed in order to determine the general buckling load factor and mode shape for the perfect shell and also to determine the best STAGS model to be used in the nonlinear static and dynamic runs to follow. The input files, *.bin and *.inp [18 – 21], for all the STAGS models are generated automatically through use of the PANDA2 processor called “STAGSUNIT” [1I]. Input data for STAGSUNIT are listed in the directory .../panda2/case/sdm48. The STAGSUNIT input data are stored in files with the suffix, “.stg”.

In all the STAGS models the “**480**” finite element is used throughout. Over the years the writer has found that the “480” element works better for uniformly loaded **optimized** elastic **stiffened** cylindrical shells than does the “410” element because the “480” element produces fewer “spurious” buckling modes, such as that shown in Fig. 7 of [1I] and those shown in Figs. 67 and 70 of [1K], in regions where the nodal point spacing is sparse. Also, given a nodal point distribution such as that shown in Fig. 24, models constructed with the “410” element generate many more eigenvalues smaller than that corresponding to the critical general buckling mode than is the case for models constructed with the “480” element. For example, in the Case 2 model displayed in Fig. 24, the critical general buckling mode determined with the use of “410” elements corresponds to the 5001st eigenvalue in the spectrum. Figure 24 demonstrates that, in contrast to the model with “410” finite elements, in the model with “480” elements the critical general buckling mode corresponds to the 610th eigenvalue in the spectrum. The “480” element “filters out” many “spurious” local buckling modes because it tends to “approach from above”, that is, eigenvalues corresponding to given buckling modes usually decrease with increasing nodal mesh density. In contrast, the “410” element usually “approaches from below”, that is, eigenvalues usually increase with increasing nodal point density. This unfavorable property of the “410” element produces an eigenvalue spectrum in which the eigenvalues corresponding to short-wavelength local buckling have been shifted downward compared to those with relatively long-wavelength general buckling. The reverse holds for the “480” element.

For **perfect** shells that have been optimized, local buckling load factors and general buckling load factors are usually nearly the same. (See the top part of Table 10, for example) Therefore, models consisting of “410” elements will tend to have many, many local buckling modes with eigenvalues below that corresponding to general buckling because the local buckling eigenvalues are underestimated relative to the general buckling eigenvalues especially in regions where the nodal point mesh is relatively crude. This makes it difficult to extract the unique critical general buckling mode from the dense spectrum of eigenvalues. With optimized **imperfect** shells the situation is worse because optimization cycles on imperfect shells tend to force the critical general buckling load factor higher relative

to the local buckling load factors than is the case for optimized perfect shells. (See the top part of Table 7, for example, and compare it to the top part of Table 10).

There is another reason that the “480” element is preferable to the “410” element for the analysis of **optimized stiffened** shells. In the nonlinear static analysis (STAGS index, INDIC=3) of a cylindrical shell with a general buckling modal imperfection of the shape shown in Fig. 24, the STAGS model constructed with “480” elements loads up to a load factor, PA = 0.975, without any convergence difficulties. (See Fig. 25). Eigenvectors computed at that load level exhibit the expected local buckling shape, and the largest local buckling modal displacements occur in the region where the nodal point mesh is most dense. (See Figs. 26 and 27). These nonlinear local buckling modes can be used as additional initial imperfections in further nonlinear static and dynamic runs. (See Table 9 and Figs. 28 – 32). In contrast, a nonlinear static analysis with the same general buckling modal imperfection shape and amplitude and with the same nodal mesh but constructed with “410” elements instead of “480” elements, fails to converge above a load factor, PA = 0.581. Near that load level there are many, many very closely spaced eigenvalues the corresponding eigenvectors of which are “spurious”; they represent very poor approximations of local buckling in all regions **except** where the nodal point mesh is most dense. They cannot be used as additional imperfections because they are too “jagged” and there are too many of them in the immediate neighborhood of the load level PA at which nonlinear convergence fails. This behavior is a consequence of the unfavorable “approach-from-below” property of the “410” finite element.

12.2.1 Finding the buckling loads of the perfect shell and the best STAGS model

Parts 1–4 of Table 9 and Figs. 16–24 pertain to this subsection. Our first task is to find the critical general buckling mode of the optimized shell with the amplitude of the general buckling modal imperfection, $W_{imp} = 0$. This may be difficult because the critical general buckling eigenvalue may be embedded in a “thicket” of local buckling eigenvalues. This phenomenon has been described in previous papers [1K]. As seen from Margin No. 11 in the top part of Table 7, according to PANDA2 the margin for general buckling of the perfect shell, 0.890, is higher than many of the margins corresponding to more local buckling. This is a characteristic typical of optimized **imperfect stiffened** shells. The **general buckling margin** of optimized imperfect stiffened shells is forced higher during optimization cycles because prebuckling bending of the imperfect shell increases with applied load approximately hyperbolically as the applied load approaches the general buckling load of the imperfect shell [1E]. If the general buckling load of the optimized imperfect shell were close to the design load there would be so much prebuckling bending near that design load that local buckling margins for the stiffener parts and for the panel skin would become negative because these parts of the structure would become highly stressed.

Because the general buckling load of the perfect shell optimized with a general buckling modal imperfection present is usually considerably higher than many local buckling loads and therefore hard to find with refined STAGS models, it is beneficial to obtain very good estimates of the general buckling load of the perfect shell from models which do not permit much or any local buckling. These “approximate” models can all be produced automatically by the PANDA2 processor, STAGSUNIT. A model in which **both** stringers and rings are smeared in the manner of Baruch and Singer [12] has **only** general buckling modes (Fig. 16). A model in which the stringers are smeared and only the rings are modeled as shell units (two shell units for each T-shaped ring, one for the web and the other for the outstanding flange) may or may not have local buckling modes with eigenvalues lower than that corresponding to the critical general buckling load. In this particular case the smallest eigenvalue happens to correspond to general buckling (Figs. 17,18).

Figures 16–23 pertain to Part 1 of Table 9. Figures 16–18 show STAGS models of the complete (360 degrees) perfect cylindrical shell in which the there is a 120-degree sector where nodal points are denser than around the rest of the circumference. Figure 16 corresponds to a model in which both stringers and rings are smeared [12]. Figures 17 and 18 correspond to a model in which the stringers are smeared and the rings are modeled as shell units. In both models the lowest eigenvalue corresponds in this particular example to a general buckling mode with 4 axial halfwaves and 6 circumferential full waves. From Fig. 18 we see that, indeed, the critical general buckling mode has six full circumferential waves (12 circumferential halfwaves). This $(m,n) = (M,N) = (4,6)$ mode agrees with that predicted for the perfect shell by PANDA2. (See Margin No. 11 in the top part of Table 7). PANDA2 yields a margin 0.890, equivalent in this example in which the factor of safety is very close to unity to a buckling load factor of 1.890. The buckling load factors, pcr, from STAGS, pcr = 1.9189 in Fig. 16 and pcr = 1.9017 in Figs. 17 and 18,

are in good agreement with PANDA2's prediction of 1.890.

With the absence of in-plane shear loading (torque) and anisotropy, the buckling pattern displayed in Fig. 18 indicates that a STAGS model spanning as little as 30 degrees of circumference with symmetry conditions applied along the two straight edges [see Item 667 of Section 9.0] would be sufficient to capture the critical $(m,n) = (4,6)$ general buckling mode. While the critical general buckling mode and load factor (eigenvalue) would be accurately captured by such a model, the maximum stress and minimum local stringer buckling load factors and mode shapes would not because, as mentioned above, the stiffeners that run along the edges of a STAGS model generated by STAGSUNIT [11] have half the stiffness and half the loading of the stiffeners that lie in the interior of the domain of the STAGS model. (This modeling permits STAGS models of sub-domains or “patches” of the entire shell that act as if they were embedded in the entire shell and therefore experience the proper prebuckling states). Hence, in this paper in all STAGS models that subtend a small portion of the circumference of the cylindrical shell, we establish the minimum sector as that which contains at least one **full** circumferential wave of the critical general buckling mode, **not** merely one **half** circumferential wave. In this particular case that **full wave sector spans 60 degrees of the circumference**.

Figure 19 shows the lowest buckling mode and load factor, $p_{cr} = 1.4017$, obtained from a 60-degree STAGS model with uniform nodal point spacing. In this model both the stringers and the rings are modeled with shell units, two shell units for each stiffener, one for the stiffener web and the other for the stiffener outstanding flange. Figure 20a shows a STAGS model of a sub-domain containing four stringer bays (five stringers) and three ring bays (four rings). The STAGS buckling modes and load factors are in reasonably good agreement with one another. The mode shown in Fig. 19 has not really converged with respect to nodal point density whereas the similar mode shown in Fig. 20a has converged.

Several STAGS linear buckling runs with different eigenvalue shifts were required to find the **bending-torsion** buckling mode shown in Fig. 20a, which is embedded in a cluster of very closely spaced **local** buckling eigenvalues and modes. The buckling mode and eigenvalue from STAGS, $p_{cr} = 1.3826$ in Fig. 20a, agree very well with the equivalent mode and load factor predicted by PANDA2 for the perfect shell. PANDA2 Margin Numbers 2 and 4 listed near the top of Table 7 correspond to the type of buckling shown in Fig. 20a, a “bending-torsion” mode. The buckling load factors from PANDA2 corresponding to Margins 2 and 4 are 1.378 and 1.407, respectively. Note that with PANDA2 the domain included in the “bending-torsion” and “lateral-torsional” buckling modals includes an axial length equal to the ring spacing. Hence, the string, “M=2” in Margin No. 2 and “m=2” in Margin No. 4 mean “2 axial halfwaves between adjacent rings”. Figure 20a demonstrates that the critical buckling mode from the converged STAGS sub-domain model has six axial halfwaves over three ring bays, or 2 axial halfwaves per bay, in agreement with the “bending-torsion” and “lateral-torsional” buckling modes obtained by PANDA2 and listed as Margins 2 and 4 in Table 7.

Figure 21a shows the critical (lowest) general buckling load factor, $p_{cr} = 1.8968$, and mode shape for the 60-degree STAGS model with **uniform nodal point spacing**. This buckling mode corresponds to the 861st eigenvalue for the STAGS model displayed in Fig. 19. Three additional STAGS runs, each with a different initial eigenvalue “shift”, were required to extract the critical general buckling mode from a dense “thicket” of local modes. In the first STAGS run the eigenvalue “shift” was set equal to 1.9017, the best estimate of the general buckling load factor determined so far (Figs. 17,18). The general buckling load factor from STAGS, $p_{cr} = 1.8968$ in Fig. 21a, is in very good agreement with that obtained from PANDA2, $p_{cr}(\text{PANDA2}) = 1.0 + (\text{Margin 11 in Table 7}) = 1.890$. The general buckling mode shape from both STAGS and PANDA2 models has four axial halfwaves and six circumferential waves: one full circumferential wave in the 60-degree STAGS model (as shown in insert (a) of Fig. 21a) and six circumferential halfwaves in the 180-degree PANDA2 model (as listed in Margin 11 in Table 7). Notice from the expanded insert (c) that the general buckling mode displayed in Fig. 21a includes a significant component of the more local “bending-torsion” buckling mode of the type shown in Figs. 19 and 20a.

The axial densities of nodal points in the STAGS models displayed in Figs. 19 and 21a are not sufficient to capture local buckling of the panel skin and stringer web and outstanding flange. Figure 22 shows a new STAGS model in which the nodal point density is concentrated over part of the axial length. **The axial positioning of the refined region is established based on the shape of the general buckling mode** shown in Fig. 21a. The region with the highest nodal point density in both the axial and circumferential directions in the STAGS model displayed in Fig. 22 is centered at the location of a peak in the general buckling mode in the STAGS model shown in

Fig. 21a. (It could just as well have been centered at the location of a valley in the general buckling mode). In the new STAGS model of the perfect shell the critical (lowest) buckling load factor and mode shape correspond to local buckling where the mesh density is highest, as demonstrated in Fig. 22. Figure 23a shows a sub-domain containing six stringer bays and only one ring bay. A very high nodal point density is used for this model, the purpose of which is to obtain a very accurate estimate of local buckling of the perfect shell from STAGS. The critical (lowest) buckling load factor, $p_{cr}=1.0758$, (assumed to be a converged result) corresponds to local buckling with approximately 10 or 11 axial halfwaves between adjacent rings. This local buckling mode and eigenvalue, $p_{cr} = 1.0758$, agree well with the prediction from PANDA2: Margin No. 1 listed in the top part of Table 7, for which $p_{cr}(PANDA2) = 1.0 + \text{Margin } 1 = 1.0636$ and $M = 11$ axial halfwaves between rings. Although the local buckling load factor from the sub-domain STAGS model, $p_{cr}=1.0758$, displayed in Fig. 23a is about 2.5 per cent lower than that obtained for the 60-degree full-length STAGS model shown in Fig. 22, the model shown in Fig. 22 is deemed accurate enough to use for all the nonlinear STAGS analyses to be conducted for this configuration (Case 2 in Table 4).

A critical general buckling mode and load factor still must be found with use the newest STAGS model, that displayed in Fig. 22. Starting with the best estimate of the general buckling load factor determined so far, $p_{cr} = 1.8968$ (Fig. 21a) as an initial “eigenvalue shift”, five linear buckling STAGS runs with various “eigenvalue shifts” were required to extract the new critical general buckling mode and load factor. The most important results from STAGS (abridged *.out2 files from the five STAGS runs) are listed in Part 2 of Table 9 for these five STAGS runs. (One can imagine how many STAGS runs would have been required, each with a slightly different eigenvalue shift, if we did not already have a very good estimate of the general buckling eigenvalue from previous simpler models!) The final critical general buckling mode shape and load factor, $p_{cr} = 1.8931$, are shown in Fig. 24. The critical general buckling load factor from STAGS for the perfect shell agrees extremely well with that from PANDA2, $p_{cr}(PANDA2) = 1.0 + \text{Margin } 11 = 1.890$ (Margin No. 11 in the top part of Table 7). Note that the mode shape shown in Fig. 24 is “purer” general buckling than that shown in Fig. 21a, which has a significant component of a “bending-torsion” mode of the type displayed in Figs. 19 and 20a. The three central stringers appear darker in Fig. 24 than the other stringers because they have more nodal points over their webs and outstanding flanges than do the others. (See **Item 669** in Section 9.0).

The **negative** of the mode shape shown in Fig. 24 is used as an initial imperfection in the nonlinear STAGS runs to follow. A negative amplitude is chosen rather than a positive amplitude because we want an inward lobe of the general buckling mode to coincide with the location where the nodal point density in the STAGS finite element model is highest (Fig. 22). **It is emphasized here that the SIGN of the general buckling modal imperfection is significant. Optimum designs obtained with PANDA2 should be evaluated by two STAGS models in which a positive amplitude of the general buckling modal imperfection shape has been specified in one set of nonlinear static and dynamic runs and a negative amplitude has been specified in the other set of nonlinear static and dynamic runs.** (See the end of Section 13.5).

In the PANDA2 model the initial user-specified amplitude of the general buckling modal imperfection is 0.25 inch and its user-specified axial halfwavelength is equal to the length of the cylindrical shell, 75 inches (Table 1). Because the imperfect shell was optimized by PANDA2 with the “**yes change imperfection**” option (see Case 2 in Table 4 and Item 4 in Section 11.0), the amplitude of the general buckling modal imperfection in the STAGS model should be the negative of $0.25/4.0 = 0.0625$ inch. The initial user-specified amplitude, 0.25 inch, is divided by 4.0 because the axial halfwavelength of the actual critical buckling modal imperfection in Fig. 24 is one fourth of the axial halfwavelength initially specified in the PANDA2 model: 75 inches, the full axial length of the shell. (See Expression 11.1).

Note that, because of the possible existence of a “**fractional**” axial wavenumber, **dm**, in a PANDA2 model (Part 1 of Table 8), the reduced amplitude of the general buckling modal imperfection may be different in PANDA2 models optimized with the “**yes change imperfection**” option from that in STAGS models. The concept of “fractional” wave numbers is not relevant in STAGS models. In each of the cases explored here the critical general buckling mode obtained from the STAGS model has an integral number of axial halfwaves. In this **ICONSV = -1** case (Case 2 in Table 4) the general buckling modal imperfection has exactly four axial halfwaves, as shown in Fig. 24. Therefore, corresponding to the user-specified imperfection amplitude, **Wimp(user) = 0.25** in PANDA2, the imperfection amplitude to be used in the STAGS nonlinear models is plus or minus **0.25/4.0 = 0.0625 inches**, as mentioned in the previous paragraph. However, because there might exist a non-zero “**fractional**” number of axial

halfwaves, \mathbf{dm} , in the PANDA2 model, as listed in Part 1 of Table 8 for example, the imperfection amplitude used by PANDA2 is different in this particular case from that to be used in the STAGS nonlinear models. With the “yes change imperfection” option, the amplitude of the general buckling modal imperfection in the PANDA2 models is plus or minus $0.25/(\mathbf{m}+\mathbf{dm})$, in which \mathbf{dm} can be either positive, zero, or negative. From part 1 of Table 8 we see that in this particular case the amplitude of the general buckling modal imperfection in the PANDA2 model is $0.25/(\mathbf{m}+\mathbf{dm}) = 0.25/(5 - 0.41628) = 0.054541$ inches. The STAGS model of the imperfect shell is somewhat conservative relative to the PANDA2 model in this case because it has a general buckling modal imperfection with a somewhat higher amplitude, $W_{imp} = 0.0625$ inch, compared to the PANDA2 amplitude, $W_{imp} = 0.054541$ inch.

12.2.2 Results from linear buckling analyses with BIGBOSOR4 [14F]

There are PANDA2 processors, PANEL (Fig. 36, p. 539 of [1A]) and PANEL2 (Fig. 33 of [1G]), by means of which input files for BOSOR4 (or BIGBOSOR4) [14] are generated automatically. Figures 20b, 21b, and 23b pertain to this sub-section.

The **PANEL** processor generates an input file, *.ALL, for the BIGBOSOR4 [14F] **buckling analysis of the portion of the optimized stiffened cylindrical shell between rings** (multiple skin-stringer modules each module of which is similar to the one module shown in Fig. 4). The sector of the stringer-stiffened portion of the cylindrical shell shown in Figs. 20b and 23b is modeled as a segment of a toroidal shell ([26], also see Fig. 192, p. 221 of [8]) with a large radius R to the center of meridional curvature. (R is close to 286 inches in this case). Figures 23b and 20b display **local** and **bending-torsion** buckling modes, respectively, predicted by BIGBOSOR4. BIGBOSOR4 computes buckling load factors (eigenvalues) over a user-specified range of circumferential wave numbers, N , as listed in the table inserted on the right-hand side of Fig. 23b. In the BIGBOSOR4 model generated by PANEL there are no rings. The rings are replaced by anti-symmetry (simple support) boundary conditions, that is, two adjacent rings are replaced by two nodal lines in the trigonometric circumferential variation of buckling modal displacements. These two nodal lines lie parallel to the plane of the paper. The spacing between them is equal to the ring spacing, of course. In Figs. 23b and 20b \mathbf{m} , the number of axial halfwaves between rings, is listed in the title: $\mathbf{m} = 11$ in Fig. 23b and $\mathbf{m} = 2$ in Fig. 20b. $N = 100 \times \mathbf{m}$ is the number of **full** waves around the entire circumference of the huge toroidal shell. $N = 100$ corresponds a circumferential **halfwavelength** equal to the ring spacing, which is 9.375 inches in Case 2 (Table 4). (NOTE: the ring spacing and the circumferential halfwavelength of a buckling mode in this “huge torus” model are measured **normal** to the plane of the paper. The average horizontal radius, $R(ave)$, from the axis of revolution of the huge torus to the halfway point along the meridional arc of the multi-module model displayed in Figs. 23b and 20b can be computed as follows: $2 \times \pi \times R(ave) = 2 \times 100 \times 9.375$ inches. Therefore, $R(ave) = 298.4$ inches.) The critical **local** buckling mode (Fig. 23b) has $N = 1100$ circumferential full waves around the circumference of the huge toroidal shell. Hence, there are $\mathbf{m} = 11$ halfwaves between rings. The critical **bending-torsion** buckling mode (Fig. 20b) has 200 circumferential full waves around the circumference of the huge toroidal shell. Therefore $\mathbf{m} = 2$ halfwaves between rings. The buckling load factors (eigenvalues), $Eig(local) = 1.0862$ (Fig. 23b) and $Eig(bending-torsion) = 1.289$ (Fig. 20b), agree well with the PANDA2 margins listed in Table 7: Margin No. 1 (Sub-case 1) = 0.0636 (corresponding load factor = 1.0636) and Margin No. 2 (Sub-case 2) = 0.291 (corresponding load factor = 1.291), respectively. The small inserts in Figs. 20b and 23b show buckling modes that correspond to **edge buckling**. These modes have eigenvalues that are lower than that corresponding to buckling over the entire toroidal sector. However, they are not of interest in the comparison of predictions from BIGBOSOR4 with those from PANDA2 and STAGS because edge buckling of the types displayed in the small inserts in Figs. 20b and 23b is not permitted in the PANDA2 and STAGS models.

The **PANEL2** processor generates a BIGBOSOR4 input file, *.ALL, for the **buckling analysis of the entire optimized stiffened shell**. In this model the stringers are smeared out in the manner of Baruch and Singer [12] and the rings are modeled as branched shell structures. The shell is simply supported along the two curved ends. Figure 21b shows the critical **general** buckling mode predicted by BIGBOSOR4. The mode shape, $(\mathbf{m}, \mathbf{n}) = (M, N) = (4, 6)$, agrees with that predicted by PANDA2, as seen from Margin No. 11 in the top part of Table 7. Margin No. 11 = 0.890, which corresponds to a load factor 1.890. This load factor agrees very well with the load factor from BIGBOSOR4: $Eig(general) = 1.8767$, listed in both the title and in the small table inserted in Fig. 21b.

12.2.3 Results from the nonlinear static and dynamic STAGS runs

Results from the static and dynamic nonlinear STAGS runs are abbreviated in Parts 5 – 13 of Table 9. Parts 5 – 9 of Table 9 and Figs. 25-29 pertain to **nonlinear static** STAGS runs. Parts 10 – 13 of Table 9 and Figs. 30-32 pertain to **nonlinear dynamic STAGS** runs.

Part 5 of Table 9 lists the *.bin file (in which “*” = “test2”). Part 6 lists the small part of the *.out2 file that contains the list of converged load steps and load factors, PA and the six nonlinear buckling eigenvalues “requested” in the *.bin file listed in Part 5. Convergence failed for load factor $PA > 0.974853$, probably because of nearby bifurcation points on the nonlinear equilibrium path. Note that “**Riks path reversal**” is noted for Load Steps 15 and 16 in Part 6 of Table 9. This STAGS phenomenon, described in Fig. 17 of [23], frequently occurs in the neighborhood of points for which STAGS has difficulty converging to a nonlinear equilibrium solution. “Riks path reversal” means “load path reversal”. Had the nonlinear STAGS run been continued the shell would probably have unloaded completely. Another example of “Riks path reversal” appears in Fig. 93.

Figure 25 shows the distribution of effective stress at Load Step 16, for which $PA = 0.974853$. There is only a single buckling modal imperfection shape in the STAGS model, as listed near the top of Part 5 in Table 9. The maximum effective stress occurs in the outstanding flange of the stringer that runs along the center of the 60-degree model. (The three stringers nearest the center of the 60-degree model have more nodal points over their cross sections than the rest of the stringers). The maximum effective stress at $PA = 0.974853$, $s_{bar}(max) = 61.62$ ksi, is in good agreement with the maximum effective stress at the design load ($PA = 1.0$) in the PANDA2 model of the imperfect shell. Margins 3 and 6 in Table 6 demonstrate that for the optimized design of the PANDA2 model the effective stress margins are all critical, some of them more so than others. Since the allowable stress is 60 ksi (Table 1), the actual effective stress at the design load is within 4 per cent of 60 ksi in the PANDA2 model. In fact, in Table 6 the “worst” stress margin, -0.0384 for Margin No. 6 in Load case 1, Sub-case 2 (at the axial location of a typical ring) corresponds to an effective stress equal to $60/(1.0-0.0384) = 62.4$ ksi at $PA = 1.0$ (the design load), slightly in excess of the maximum value, 61.62 ksi predicted by STAGS at a slightly lower load level, $PA = 0.974853$, the final load level at which converged results were obtained in this first nonlinear static STAGS run.

Figures 26 and 27 show the **nonlinear buckling modes** and buckling load factors, $p_{cr}=1.0037$ and $p_{cr} = 1.0084$, respectively, determined from the STAGS model at Load Step No. 16, that is, at $PA = 0.974853$. The first mode (Fig. 26) appears to be a combination of local buckling of the panel skin and “bending-torsion” buckling of the stringer cross sections. (See inserts (a) and (c) in Fig. 26). The second mode (Fig. 27) is pure local buckling of the panel skin with some participation of the stringer webs and outstanding flanges. It is emphasized that these nonlinear buckling modes and loads properly account for the prebuckling bending of the shell with the general buckling modal imperfection of amplitude -0.0625 inch shown (greatly exaggerated) in Fig. 24. The nonlinear buckling loads from STAGS agree very well with those predicted by PANDA2 for the imperfect shell. (See Margin No. 1 in all load cases and sub-cases in Table 6 and Margin No. 2 in Load Case 1, Sub-case 2 in Table 6). Therefore, the PANDA2 model of stress redistribution due to prebuckling bending of a globally imperfect shell (see Item 1 in Section 7.0) seems to be accurate enough to produce optimum designs that are not unconservative nor overly conservative.

Part 7 of Table 9 lists results from STAGS for the same model except that **two new imperfection shapes have been added to the negative of the general buckling mode**: that shown in Fig. 26 and that shown in Fig. 27, each with an amplitude, $W_{imp(imperf.2)} = W_{imp(imperf.3)} = 0.0005$ inch. The purpose of these extremely small initial imperfections is to “trigger” nonlinear behavior in the neighborhoods of what were bifurcation points on or very near the nonlinear equilibrium path in the previous nonlinear static STAGS run, thereby permitting STAGS to find nonlinear static solutions for higher load factors than that obtained with only the general buckling modal imperfection with amplitude -0.0625, that is, for higher load factors than $PA= 0.974853$ (Fig. 25).

Figure 28 shows the distribution of effective stress at the highest load factor (Load Step 18 in Part 7 of Table 9) for which converged results were obtained. A comparison of this figure with Fig. 25 reveals that

1. The maximum effective stress, $s_{bar}(max) = 71.82$ ksi, is considerably higher than that for the model with only the general buckling modal imperfection present (Fig. 25, in which $s_{bar}(max)=61.62$ ksi).
2. Evidence of local deformation of the panel skin is much more pronounced in Fig. 28 than in Fig. 25.

3. There is some sidesway of the stringers in the five central stringers in Fig. 28 that is not evident in Fig. 25.

These three characteristics result from the addition of the two new nonlinear buckling modal imperfections, which grow in amplitude as the applied load approaches the design load.

The maximum effective stress predicted by STAGS and displayed in Fig. 28, $s_{\text{bar}}(\text{max}) = 71.82 \text{ ksi}$ at load factor 0.996 (very close to the design load, $\text{PA} = 1.0$), significantly exceeds the maximum stress predicted by PANDA2 at the design load (close to 60 ksi) because the Case 2 optimum design was obtained with the “no Koiter” option, that is, local deformations of panel skin and stringer web and flange of the type shown in Fig. 4 are not accounted for in Case 2. According to STAGS the optimum design is “ALMOST FEASIBLE” at load factor $\text{PA} = 0.974853$ (Fig. 25) but “NOT FEASIBLE” at a load factor, $\text{PA} = 0.996238$. To avoid this kind of difficulty, one should obtain optimum designs with use of the “yes Koiter” option, as recommended in the column in Table 4 headed “Case 5”.

Part 8 of Table 9 lists results from a continuation of the previous (2nd) nonlinear static STAGS run. In this 3rd nonlinear static STAGS run convergence was obtained for Load Steps 19 - 48. Figure 29 shows the distribution of effective stress at the maximum load factor, $\text{PA} = 1.02487$, attained during the run. The maximum effective stress, $s_{\text{bar}}(\text{max}) = 78.37 \text{ ksi}$, is considerably higher than that from the previous run (Fig. 28, in which $s_{\text{bar}}(\text{max})=71.82 \text{ ksi}$), but the overall pattern remains the same.

Part 9 of Table 9 lists results from a continuation of the previous run. While STAGS obtained converged results for Load Steps 49 – 70, no useful new information was gained. Repeated “**Riks path reversals**” occur. Therefore, in the three nonlinear dynamic STAGS runs to be described next computations always restart at Load Step 48, not at Load Step 70.

Part 10 of Table 9 lists the ***.bin** file for the first **nonlinear dynamic** run. The most significant input data are in bold face. The best strategy seems to be to initiate the first nonlinear dynamic run at a load level from one to three per cent higher than the highest static load level successfully attained in a previous nonlinear static run [23]. The load factor, PA , is to be maintained at $\text{CA1} = 1.05$ in the first nonlinear dynamic STAGS run. The ***.bin** file for the last two nonlinear dynamic runs is the same as that listed in Part 10 except the value of CA1 is first changed from 1.05 to 1.04 for the second nonlinear dynamic run and then from 1.04 to 1.035 for the third nonlinear dynamic run. **The purpose of the three very similar nonlinear dynamic runs is to obtain an accurate value for the load factor at which elastic collapse occurs.**

Part 11 of Table 9 lists the results from the last dynamic time step in the first nonlinear dynamic run (load factor held constant at $\text{PA} = 1.05$). The large values of kinetic energy indicate dynamic collapse of the shell. The collapse mode (not displayed here) is very like that shown in Fig. 30. Part 12 of Table 9 lists the same for the second nonlinear dynamic run (load factor, PA , is maintained at a slightly lower load level, $\text{PA} = \text{CA1} = 1.04$). Figure 30 shows the deformation at the last time step processed and stored by STAGS, Step 310. The shell collapses in the first ring bay. Part 13 of Table 9 lists the same for the third dynamic run (load factor, PA , is maintained at $\text{PA} = \text{CA1} = 1.035$). In this case the shell does not collapse but reaches the stable equilibrium state displayed in Fig. 31. The deformed shape in Fig. 31 is similar to that shown in Fig. 29, which corresponds to a slightly lower load factor, $\text{PA} = 1.02487$. Collapse occurs between $\text{PA} = 1.035$ (Fig. 31) and 1.04 (Fig. 30). The mode of collapse exhibited in this case is similar to that observed in all the cases in Table 4 for which nonlinear static and dynamic analyses were attempted except Case 7: collapse at one ring bay or at both of the ring bays nearest the ends of the cylindrical shell. In Case 7 collapse occurs simultaneously at the two end ring bays and at an interior ring bay. The collapse modes differ when elastic-plastic material behavior is included in the STAGS model, as described in Section 14.0.

Figure 32 shows the sidesway in the first ring bay of two of the central stringers as functions of time for the three nonlinear dynamic runs (Runs 6, 7, 8 in Parts 11, 12, 13 of Table 9). Collapse (very large sidesway) occurs with the load factor PA maintained at 1.05 (Run 6) and at 1.04. (Run 7) See the collapse mode in Fig. 30. The stringer sidesway in the first bay remains small when the load factor is maintained at a slightly lower level, $\text{PA} = 1.035$, in Run 8 (Fig. 31).

It is emphasized here that in all the models described so far the material is assumed to remain elastic. Hence, the

collapse load in Case 2, which for elastic material is in the range $1.035 < PA(\text{collapse}) < 1.040$, would, if plastic flow were included in the STAGS model, doubtless be above $PA = 0.974853$, for which the maximum effective stress, $s_{\text{bar}}(\text{max}) = 61.62 \text{ ksi}$ (Fig. 25) is just slightly above the maximum allowable stress of 60 ksi and perhaps below $PA = 1.02487$, for which the maximum effective stress, $s_{\text{bar}}(\text{max}) = 78.37 \text{ ksi}$ (Fig. 29) significantly exceeds the maximum allowable stress of 60 ksi. (However, see Section 14.0 for what actually happens!)

Another important point: We do not actually know what the maximum elastic collapse load factor PA is corresponding to collapse in a ring bay remote from the ends of the cylindrical shell. Probably it is not far above $PA = 1.04$ in this particular case because there is a significant amount of stringer sidesway at a load factor, $PA = 1.035$, evident in the three central stringers within the “patch” with the dense nodal point spacing shown in Fig. 31. (See Section 14.0).

13.0 SELECTED DETAILS FROM SOME OF THE OTHER CASES LISTED IN TABLE 4

Figures 33 – 80 and Tables 10 - 12 pertain to this section. Table 10 and Figs. 33 – 41 pertain to the perfect shell (Case 1). Figures 42 – 65 pertain to Case 4. Figures 66 – 71 and Tables 11 and 12 pertain to Case 5. Figures 72 – 74 pertain to Case 6. Figures 75 – 80 pertain to Case 7. The results in this section are all for models with **elastic** material.

13.1 Some results from Case 1, the perfect shell

Table 10 lists the margins corresponding to the optimized design of the perfect shell (Case 1 in Table 4).

Figures 33, 34, and 35 are analogous to Figs. 23b, 20b, and 21b, respectively. In this case the ring spacing is 6.25 inches rather than the 9.375 inches for Case 2, to which Figs. 23b, 20b, and 21b apply. R, the large radius to the center of meridional curvature of the huge torus, is close to 190 inches in this case. R(ave), the average horizontal radius from the axis of revolution of the huge torus to the midpoint along the meridional arc of the multi-module model displayed in Fig. 33 is calculated from $2 \times \pi \times R(\text{ave}) = 2 \times 100 \times 6.25$ inches; hence $R(\text{ave}) = 198.9$ inches. The critical **local** buckling mode (Fig. 33) has $N = 900$ circumferential full waves around the circumference of the huge toroidal shell. Therefore $\mathbf{m} = 9$ halfwaves between rings. The critical **inter-ring** buckling mode (Fig. 34) has 100 circumferential full waves around the circumference of the huge toroidal shell. Therefore $\mathbf{m} = 1$ halfwave between rings. The buckling load factors (eigenvalues) from BIGBOSOR4, $\text{Eig}(\text{local}) = 1.032$ (Fig. 33) and $\text{Eig}(\text{inter-ring}) = 1.380$ (Fig. 34), agree well with the PANDA2 margins listed in Table 10: Margin No. 1 = 0.0099 (corresponding load factor = 1.0099) and Margin No. 5 = 0.353 (corresponding load factor = 1.353), respectively.

In the PANDA2 model of inter-ring buckling (Margin No. 5 in Table 10) the stringers are smeared and the rings are modeled as flexible shell branches. This is a big difference in modeling between the PANDA2 model and the BIGBOSOR4 “torus” model. That is one of the reasons why there is such a large discrepancy in the critical number of circumferential waves: $\mathbf{n} = 5$ halfwaves over 180 degrees of the cylindrical shell in the PANDA2 model and $\mathbf{n} \gg 5$ halfwaves over 180 degrees in the meridional coordinate direction in the “huge torus” BIGBOSOR4 model. (The meridional direction in Figs. 33 and 34 is the direction in the plane of the paper along the arc of the shell skin in the multi-module torus model). The other reason for the discrepancy in predicted critical mode shape is that in both the PANDA2 and in the BIGBOSOR4 models the eigenvalues for modes similar to that displayed in Fig. 34 are very closely spaced. PANDA2 first computes eigenvalues (buckling load factors) over a range of circumferential wave numbers, \mathbf{n} . After PANDA2 has found a minimum buckling load with respect to \mathbf{n} it computes a knockdown factor to compensate for the inherent unconservativeness of smearing the stringers. This knockdown factor depends on \mathbf{n} , decreasing with increasing \mathbf{n} . With closely spaced eigenvalues this strategy may lead to an incorrect buckling mode shape although it is not expected to lead to a significantly overestimated buckling load factor. As with Figs. 20b and 23b, the **edge buckling modes** displayed in the small inserts in Figs. 33 and 34 are **not of interest** in comparisons of predictions from BIGBOSOR4 with those from PANDA2 and STAGS because the PANDA2 and STAGS models do not permit edge buckling of these types.

Figure 35, analogous to Fig. 21b, shows the critical **general** buckling mode predicted by BIGBOSOR4 for Case 1.

The mode shape, $(m,n) = (M,N) = (1,4)$, agrees with that predicted by PANDA2, as seen from Margin No. 11 in the top part of Table 10. Margin No. 11 equals -0.0228, which corresponds to a load factor 0.9772. This load factor is somewhat lower than the critical load factor from BIGBOSOR4, $Eig(general) = 1.0552$, in Fig. 35. PANDA2's prediction is conservative because its knockdown factors for smearing stringers, for smearing rings, and for compensating for transverse shear deformation (t.s.d) effects are conservative. (ICONSV=1 in Case 1). BIGBOSOR4 has no knockdown factors for transverse shear deformation effects or for smearing stringers.

At the top of Fig. 35 the following phrase occurs: "**PANDA2 gets 1.07 before knockdowns and 0.9772 after knockdowns**". Similar phrases occur in other figures in this paper. "PANDA2 gets 1.07" means "PANDA2 computes a buckling load factor of 1.07"; "**before knockdowns**" means "**before applying the knockdown factors for smearing stringers, for smearing rings, and for the effect of t.s.d.**" (The "knockdowns" referred to in this context have nothing to do with imperfection sensitivity). Information about PANDA2's buckling load factors before and after "knockdowns" is included in the figures in order to demonstrate that usually PANDA2's buckling load factors after application of the "knockdowns" are conservative compared to the buckling load factors obtained by BIGBOSOR4 and by STAGS, at least in the cases explored in this paper for which ICONSV = 1. In fact, in the cases explored in this paper for which ICONSV = 1, the predictions from PANDA2 **before** application of the three "knockdowns" for smearing stringers, for smearing rings, and for t.s.d are generally very close to the linear buckling predictions from BIGBOSOR4 and from STAGS. (With ICONSV= 0 and ICONSV= -1 the "knockdowns" for smearing stringers and for smearing rings are milder than those computed when ICONSV = 1. The knockdown for transverse shear deformation effects (t.s.d). [1A] does not depend on ICONSV).

Note that the table inserted into Fig. 35 exhibits two minima, one at $n=4$ circumferential waves and the other at $n=7$. Figure 36 shows the more complex **general** buckling mode, $(m,n) = (M,N) = (4,7)$ obtained from the same BIGBOSOR4 model. The corresponding eigenvalue from BIGBOSOR4, $Eig(general) = 1.0803$ is fairly close to that corresponding to the much simpler critical $(m,n) = (M,N) = (1,4)$ mode, for which $Eig(general)=1.0552$ (Fig. 35). PANDA2 also predicts this more complex $(m,n) = (4,7)$ mode. Its buckling load factor "before knockdowns" agrees with that from BIGBOSOR4. (PANDA2 does not obtain "knockdowns" corresponding to this $(m,n)=(4,7)$ buckling mode because that is not the **critical** general buckling mode).

Figures 37 – 40 display buckling modes predicted by STAGS from models generated via STAGSUNIT [11]. The modes shown in Figs. 37 and 38 are predicted from models in which **both stringers and rings are smeared** [12]. The modes shown in Figs. 39 and 40 are predicted from models in which the **stringers are smeared and the rings are modeled as shell units**. Note that **the order of the modes changes** when the modeling of the rings changes. Also, the eigenvalue corresponding to the $(m,n) = (M,N) = (1,4)$ mode is higher for the STAGS model with precisely modeled rings (Fig. 40) than it is for the STAGS model in which the rings are smeared (Fig. 37). The reason for what seems to be an anomaly is unknown. Intuition tells us that the model with the precisely modeled rings should yield the lower buckling load factor, given the mode shape. The eigenvalues from PANDA2 before "knockdowns", from BIGBOSOR4, and from STAGS agree well with one another.

Figure 41 shows a STAGS model for local buckling of the Case 1 configuration. The local buckling mode and eigenvalue agree well with that from BIGBOSOR4 shown in Fig. 33 and with that from PANDA2 listed as Margin No. 1 in Table 10.

13.2 Some results from Case 4

Figures 1a,b,c, 2, and 42 – 65 pertain to this sub-section.

Figures 42 – 46 show plots generated from the "design sensitivity" branch of PANDA2 (analysis indicator, ITYPE = 4). With ITYPE = 4 the user chooses a load set and sub-case for which to perform design sensitivity. During a PANDA2 run with ITYPE=4 all decision variables are held fixed except a user-selected decision variable, which varies over a user-specified range. In Figs. 42 – 46 the user-selected decision variables are B(STR), B(RNG), H(STR), H(RNG), and T(1)(SKN), respectively. (See Table 2 for definitions of the decision variables). The values of B(STR), B(RNG), H(STR), H(RNG), and T(1)(SKN) [called T(SKN) in Fig. 46] corresponding to the optimized design are listed under Case 4 in Table 4 and at the top of Figs. 42-46. In Figs. 42-46 all the margins exceed -0.05 at the values of the decision variables that correspond to the optimum design. (PANDA2 accepts designs as "ALMOST

“FEASIBLE” provided that all margins exceed -0.05 . PANDA2 accepts designs as “FEASIBLE” provided that all margins exceed -0.01 .) Notice that at the optimum several of the margins cluster near zero, which is to be expected. Of course, it is not necessary for ALL the margins to be near zero at the optimum design. Figures 42-46 all correspond to margins computed for Load set 1, Sub-case 1. Analogous figures could have been produced for Load set 1, Sub-case 2 and for Load set 2, Sub-cases 1 and 2.

Figures 47 – 65 show STAGS results corresponding to the optimum design listed under Case 4 in Table 4. Figure 47 displays the local buckling mode for a 60-degree model analogous to that displayed in Fig. 22 for Case 2. Figure 48 shows the local buckling mode for a sub-domain model analogous to that displayed in Fig. 23a for Case 2. For Case 4, PANDA2 predicts local buckling of the perfect shell at a load factor, $\text{pcr}(\text{PANDA2})=1.074$, which is in good agreement with the STAGS prediction, $\text{pcr}=1.0876$, listed in Fig. 48. While the STAGS local buckling load factor listed in Fig. 47, $\text{pcr}=1.1255$, has not fully converged to the value given in Fig. 48, $\text{pcr}=1.0876$, the model shown in Fig. 47 is deemed accurate enough to proceed with nonlinear static and dynamic STAGS runs.

Figure 49, analogous to Fig. 24 for Case 2, shows the critical general buckling mode for Case 4. Notice that this mode contains a significant component of stringer sidesway along its entire 75-inch axial length and a significant component of very local deformation of the outstanding stringer flanges in the region between Rings 6 and 7 where the finite element mesh is most dense. (See the expanded insert in Fig. 49). As mentioned previously in connection with the discussion of Case 2 in Section 12, the negative of the mode shape displayed in Fig. 49 is used as an imperfection shape in the nonlinear STAGS runs. Its amplitude is -0.0625 inch.

Figure 50 shows the distribution of outer fiber effective stress at a load factor, $\text{PA} = 0.98$, the highest load factor attained in the **nonlinear static** STAGS analysis of the imperfect shell. **The maximum effective stress, 63.53 ksi, occurs in one of the outstanding stringer flanges in the region where the finite element mesh is most dense.** PANDA2 predicts a maximum effective stress equal to **62.42 ksi** at the same location for this case. Figure 51 shows the distribution of effective stress in the panel **skin** at $\text{PA} = 0.98$ according to STAGS. The maximum value, 47.21 ksi, is about 10 percent less than the maximum value predicted by PANDA2 in the panel **skin** at a slightly higher load, the design load for which $\text{PA} = 1.0$. PANDA2’s prediction of the maximum effective stress in the panel skin at $\text{PA} = 1.0$ is 52.43 ksi.

With the use of a single imperfection shape, that shown in Fig. 49, STAGS was unable to obtain a converged nonlinear static equilibrium state for load factor $\text{PA} > 0.98$. To obtain a converged equilibrium state at the design load, $\text{PA} = 1.0$, from the STAGS model it was decided in this case to perform a **nonlinear dynamic** analysis. (See Section 14.2 and the figures associated with Section 14.2 for STAGS predictions from a different choice in strategy: the use of additional imperfection shapes). Several nonlinear dynamic STAGS runs were executed, all with the load factor PA held constant at $\text{PA} = 1.0$, about 2 per cent higher than the highest nonlinear static PA for which converged results were obtained. Figure 52 shows the dynamic response for $0 < \text{time} < .012$ seconds in one of the finite elements in the dense region. This **panel skin finite element**, no. 1234, lies midway between Stringers 12 and 13 (counting from the bottom edge of the expanded view of the model displayed in Fig. 49). It is the 12th finite element counting from the left-hand edge of the dense region and the 2nd finite element counting from the bottom edge of the dense region. The increase in maximum effective stress at this location in the panel skin from 47.21 ksi at $\text{PA} = 0.98$ (Fig. 51) to a maximum peak of about 67 ksi at $\text{PA} = 1.0$ and time = 0.0013 seconds (Fig. 52) is caused mostly by additional local bending stress generated from local buckling of the panel skin in a manner similar to that predicted by PANDA2 and displayed in Fig. 4.

Figure 53a shows the stress distribution at $\text{PA} = 1.0$ at the 920th time step, for which time = 0.0875 seconds. The maximum effective stress, $\text{sbar}(\text{max})=70.38$ ksi, occurs in one of the outstanding stringer flanges. Figure 53b shows the distribution of effective stress in the panel skin at the same instant. The maximum effective stress in the panel skin is $\text{sbar}(\text{max}) = 60.61$ ksi. At time step no. 920 the dynamic response has died away enough to permit resumption of a sequence of nonlinear **static** analyses starting at load factor $\text{PA} = 1.0$.

Compare Fig. 53a with Fig. 50 and Fig. 53b with Fig. 51. Notice that the maximum effective stress, $\text{sbar}(\text{max})=70.38$ ksi, listed in Fig. 53a for load factor $\text{PA} = 1.0$ (the design load, $\text{Nx} = -3000$ lb/in) significantly exceeds the maximum allowable effective stress, $\text{sbar}(\text{allowable}) = 60$ ksi (Table 1). At the design load, $\text{PA} = 1.0$, STAGS predicts the Case 4 optimized design is “NOT FEASIBLE”. However, PANDA2 predicts the same design is “FEASIBLE”. PANDA2’s prediction is unconservative because the Case 4 optimum design was obtained with use

of the “no Koiter” option: local skin buckling and stringer bending of the type shown in Fig. 4 has been ignored. This is why in Table 4 the recommended PANDA2 model for optimization has the “yes Koiter” option. The user should allow PANDA2 to enter the local postbuckling branch [1C] even though, because of increased maximum stress for a given configuration, the resulting optimized design might be heavier than that obtained with use of the “no Koiter” option. When the user chooses “yes koiter” he/she must also set the factor of safety for local buckling equal to a small value, such as 0.1, so that the local buckling margins will not constrain the design. In Figs. 53a and 53b local bending stresses are much more evident than they are in Figs. 50 and 51. During the nonlinear dynamic STAGS run local bending of the type displayed in Figs. 4 and 48 develops.

Figures 54 and 55 display the responses as functions of time of effective stress at the centroid of a **panel skin** finite element, Element No. 1456, in the dense region (Fig. 54) and of the normal displacement \mathbf{w} in the first ring bay, where collapse of the shell occurs (Fig. 55). The arrays of vertically oriented data points at time = 0 and time = 0.0875 correspond to nonlinear static STAGS runs. Collapse occurs at $1.06687 < PA < 1.08$ in the first ring bay, as shown in Fig. 56, which is analogous to Fig. 30 for Case 2.

Figures 57 – 60 show the outer fiber effective stress versus applied load factor PA in finite elements at various locations in the region where the nodal mesh is the most dense. Figures 57 and 58 show stress in the outstanding flanges of Stringer No. 12 and Stringer No. 14, respectively. Figures 59 and 60 show stress in the panel skin midway between Stringers 14 and 15 and midway between Stringers 12 and 13, respectively. The data points that lie along horizontal lines at load factors, $PA = 1.0$ and 1.08 , correspond to nonlinear dynamic STAGS runs. From Fig. 57 it is seen that the maximum effective stress in the outstanding flange of Stringer No. 12 exceeds the allowable stress, 60 ksi, at $PA = 0.98$. This effective stress is higher than the maximum allowable stress because there is significant local deformation of the outstanding flanges of the stringers in the general buckling mode, as can be seen from the expanded insert in Fig. 49. This local deformation pattern is amplified by the applied load. This local deformation pattern is not present in the PANDA2 model because in that model the general buckling modal imperfection is “pure”; it has no local bending components. The abrupt jumps in effective stress between $PA = 0.98$ and $PA = 1.0$ are caused by local buckling, as explained in the discussion concerning Figs. 52 and 53a,b. **The high maximum effective stresses at load factor $PA = 1.0$ indicate the need to optimize with the “Koiter branch” [1C] of PANDA2 turned ON in order to avoid the fabrication of an unconservative design.** As described previously in Item 3 of Section 11.0, the “Koiter branch” of PANDA2 computes the stress margins accounting for local bending of the panel skin between stiffeners and local bending of the stringer web and outstanding flange. This local bending is neglected in PANDA2 during the Case 4 optimization, for which the “no Koiter” option holds (Table 4).

Figures 1a,b,c, Fig. 2 and Figs. 61 – 65 pertain to a “compound” STAGS model of the type described in [1K]. (See **Item 643** in Section 9.0). A 45-degree sector has all stiffeners modeled as shell units (two shell units per stiffener). The remaining 315 degrees of circumference has smeared stringers and rings composed of two shell units each, one for the web and the other for the outstanding flange. (See Item 643 in [1L] for details about how to construct a “compound” model).

Figures 1a,b,c show the critical general buckling mode. For a complete perfect cylindrical shell (360 degrees) most eigenvalues appear in pairs. In one member of the pair the buckling mode has a certain circumferential orientation. The other member of the pair has the same mode with a different circumferential orientation. Figures 1b and 1c demonstrate.

Figure 2 shows the outer fiber effective stress distribution for the cylindrical shell with two buckling modal imperfections: the general buckling mode shown in Fig. 1a with amplitude 0.0625 inch and the local “bending-torsional” mode shown in Fig. 61 with amplitude -0.0005 inch. The “bending-torsional” mode displayed in Fig. 61 was obtained from a **nonlinear** static STAGS run at load factor, $PA = 1.0$ (the design load). The eigenvalue, $pcr = 1.1386$ from the nonlinear bifurcation buckling analysis, agrees reasonably well with the PANDA2 prediction of the same mode for Case 4. (load factor corresponding to Margin 3 in Table 5, $pcr(PANDA2) = 1.0433$). PANDA2’s prediction is conservative because Case 4 was run with $ICONSV = 1$, an option for which PANDA2 predicts more overall prebuckling bending of the imperfect shell than it does with use of the less conservative options, $ICONSV = 0$ and $ICONSV = -1$. With more overall prebuckling bending there is more stress redistribution between panel skin and stiffener segments. Consequently, local buckling load factors such as that corresponding to Margin 3 in Table 5 are reduced somewhat.

Note that in the left-most expanded insert in Fig. 2 the stringer nearest the top of the insert has much less effective stress than its neighbor. This is because stiffeners that run along the edges of a sub-domain (“patch”) in a STAGS model have half the stiffness and half the loading of stiffeners in the interior of the sub-domain.

Figure 62 shows the distribution of outer fiber effective stress at a load factor, PA = 1.078, just before collapse of the shell. The maximum effective stress, $s_{bar}(max) = 91.72$ ksi, greatly exceeds the maximum allowable stress, $s_{bar}(allowable) = 60$ ksi.

Figure 63 shows the collapsed state at PA = 1.089. Both Figs. 62 and 63 were generated from data obtained from **nonlinear dynamic** STAGS runs. Note that the predicted collapse load and mode from the “compound” STAGS model agree very well with those from the 60-degree model displayed in Fig. 56, for which the collapse load factor, PA equals 1.080. This agreement of predictions from the 360-degree compound model and from the 60-degree sector model justifies the use of sector models of the imperfect cylindrical shells treated in this paper.

Figure 64 shows the normal displacement w versus time in the first ring bay (where collapse eventually occurs) according to the two nonlinear dynamic STAGS runs at PA = 1.078 and 1.089. Figure 65 shows the maximum effective stress from both nonlinear static and nonlinear dynamic STAGS runs. Results from the nonlinear dynamic phase of the analysis appear as the horizontally oriented data at PA = 1.078 and at PA = 1.089.

Note that the compound model displayed in Figs. 2 and 61 – 63 cannot capture local buckling and bending such as shown in Figs. 47 and 53a,b. The finite element mesh is not dense enough. As is reported in [1K], attempts to run 360-degree compound STAGS models with variations in nodal point density in both the axial and circumferential directions analogous to that displayed in Fig. 47, for example, failed.

13.3 Some results from Case 5

Tables 11 and 12 and Figures 66 – 71 pertain to this sub-section.

Case 5 is the same as Case 4 except that the “Koiter branch” of PANDA2 is “switched on” during optimization (“yes Koiter” in Table 4). Table 11 demonstrates what happens when the design listed under Case 4 (“no Koiter” = Part 1 of Table 11) is analyzed with the “yes Koiter” condition (Part 2 of Table 11), that is, when PANDA2 accounts for local bending/buckling of the panel skin between stiffeners and local bending of the stringer web and outstanding flange. Notice in **Load Case No. 2, Sub-case No. 1** that one of the effective stress margins becomes significantly negative when “no Koiter” (Part 1 of Table 11) is changed to “yes Koiter” (Part 2 of Table 11) for the same design (Case 4 design). The optimum design in Case 4 is NOT FEASIBLE if one accounts for the local bending/buckling behavior, a typical example of which is shown in Fig. 4 (greatly exaggerated). We have already seen this local bending/buckling behavior in the STAGS model described in previous sub-sections (Case 2: Figs. 28, 29 and Case 4: Figs. 53a,b).

The **first effective stress margin** (Margin No. 3 in both Parts 1 and 2 of Table 11), computed in SUBROUTINE STRTHK, is significantly affected by the change from “no Koiter” to “yes Koiter”:

Part 1, “no Koiter”: Mar. 3= 1.13E-01 eff.stress:matl=1,SKN,Dseg=2,node=6,layer=1,z=0.0174; MID.;FS=1.
Part 2, “yes Koiter” Mar. 3= -3.57E-01 eff.stress:matl=1,SKN,Dseg=1,node=1,layer=1,z=0.0174; MID.;FS=1.

With “no Koiter” the maximum effective stress is in the panel skin at the root of the stringer web ($Dseg=2$, $node=6$). With “yes Koiter” the maximum effective stress is in the panel skin midway between stringers ($Dseg=1$, $node=1$). (See Fig. 4 for a picture of the discretized skin-stringer module. “ $Dseg=1$ ” and “ $Dseg=2$ ” are Segments 1 and 2 of the skin-stringer module that form the left part of the panel skin in Fig. 4. Segment 2 forms the base under the stringer web where nodal points are concentrated. In Segments 1 and 2 nodal points are numbered from left to right. Node 6 in Segment 2 coincides with node 1 of the stringer web. The stringer web is Segment 3; the outstanding flange is Segment 4; the rightmost part of the panel skin is Segment 5.)

The **second stress margin**, Margin No. 6 in Part 1 of Table 11 and Margin No. 9 in Part 2 of Table 11, is changed but little. This second stress margin, computed in SUBROUTINE STRCON, does not directly account for local

bending/buckling of the panel skin and stringer web and outstanding flange. Also, in the “yes Koiter” analysis local buckling deformation of the rings, if any exists, is neglected.

The margins, “buckling margin **stringer Iseg.3**”, “buckling margin **stringer Iseg.4**”, and “buckling **stringer Isegs.3+4 together**”, are reduced somewhat when local bending/buckling is included (“yes Koiter”, Part 2 of Table 11) because more of the axial load is shifted from the locally bent/buckled panel skin to the web and outstanding flange of the stringer than is the case with the “no Koiter” option (Part 1 of Table 11). (Iseg.3 and Iseg.4 signify the web and outstanding flange, respectively, of the stringer). Hence, these three margins are higher in Part 1 of Table 11 (Margins 7,8,9) than in Part 2 of Table 11 (Margins 10,11,12).

The **general buckling margin** (Margin 13 in Part 1 of Table 11 and Margin 22 in Part 2 of Table 11) is reduced in Part 2 compared to Part 1 because the locally bent/buckled skin-stringer module in the “yes Koiter” strategy has less average axial, circumferential, and in-plane shear stiffness than it does in the “no Koiter” strategy. This interaction between local and general buckling, relatively mild in this particular case, was first studied by van der Neut [24]. Notice that the critical general buckling mode in Part 1 of Table 11 has the mode shape $(m,n) = (4,6)$ (axial, circumferential) halfwaves, whereas the critical general buckling mode in Part 2 of Table 11 has $(m,n) = (3,5)$ halfwaves.

The stringer segment buckling margins labeled “NOPO” in Part 2 of Table 11, that is,

- 16 **7.07E-01** buckling margin stringer Iseg.3 . Local halfwaves=13 .NOPO;FS=1.
- 17 **6.31E-02** buckling margin stringer Iseg.4 . Local halfwaves=13 .NOPO;FS=1.
- 18 **1.07E-01** buckling stringer Isegs.3+4 together.M=13 ;C=0. ;NOPO;FS=1.4

are computed from a different model from those labeled “MID”, that is,

- 10 **9.23E-01** buckling margin stringer Iseg.3 . Local halfwaves=13 .MID.;FS=1.
- 11 **8.05E-01** buckling margin stringer Iseg.4 . Local halfwaves=13 .MID.;FS=1.
- 12 **3.94E-01** buckling stringer Isegs.3+4 together.M=13 ;C=0. ;MID.;FS=1.4

“NOPO” in Margins 16-18 means “no local postbuckling”. However, there are other differences in modeling from that corresponding to the “MID” margins, 10-12. In particular, a strategy index, IQUICK, is set equal to unity rather than zero in the computation of the “NOPO” margins. This change in IQUICK from zero (Margins 10-12) to unity (Margins 16-18) causes the “worst” (most destabilizing) sign of the general buckling modal imperfection amplitude to be used in the calculation of the “NOPO” margins. That is why Margins 16-18 are significantly lower than Margins 10-12. (Compare especially Margin 17 with Margin 11).

Table 12 lists the **average stiffness in the various parts of the structure** derived from the “no Koiter” option (Part 1 of Table 12) and from the “yes Koiter” option (Part 2 of Table 12) for the Case 4 geometry. Notice the decrease in stiffnesses when local buckling/bending of the panel skin and stringer parts is accounted for (“yes Koiter” option) relative to those computed when local deformations of the type displayed in Fig. 4 are neglected (“no Koiter” option). Especially significant are the decrease in effective average axial stiffness of the panel skin and the decrease in the “(1,2)” stiffness, C(1,2), of the panel skin, which is similar to a decrease in the effective Poisson ratio of the locally buckled skin.

In Case 5 the stiffened cylindrical shell is optimized with the “Koiter branch” turned on (“yes Koiter”). The optimum design is somewhat heavier than that in Case 4 (“no Koiter”). The **general buckling** mode shape and load factor per for the perfect shell modeled for STAGS are displayed in Fig. 66. Nodal points are concentrated in ring bays 3 and 4. The load factor (eigenvalue), per equals 2.0155, compared with PANDA2’s prediction of 2.04 “before knockdowns” and 1.870 “after knockdowns”. PANDA2’s “after knockdowns” prediction is conservative because Case 5 is developed with ICONSV=1, for which conservative knockdown factors are used to compensate for the inherent unconservativeness of smearing stringers and rings. (See **Item 676** of Section 9.0).

Figure 67 shows the distribution of outer fiber effective stress in the shell with an initial general buckling modal imperfection with shape displayed in Fig. 66 and with amplitude, Wimp = -0.0625 inch. The shell is loaded in axial compression, Nx = -3000 lb/in, which is the design load, PA = 1.0. In comparing Fig. 67 (Case 5) with Fig. 53a

(Case 4), we see that the maximum effective stress at the design load, $PA = 1.0$, is acceptable in Case 5 [$s_{\text{bar}}(\text{max}) = 57.27 \text{ ksi}$ in Fig. 67] but is not acceptable in Case 4 [$s_{\text{bar}}(\text{max}) = 70.38 \text{ ksi}$ in Fig. 53a].

It is therefore recommended that, in general, optimum designs be obtained with the “Koiter branch” turned on (“yes Koiter”). Of course, as long as one plans to evaluate the optimum designs obtained by PANDA2 through use of a nonlinear general-purpose finite element program such as STAGS, one is free to choose the most unconservative option, $\text{ICONSV} = -1$, and/or turn off the “Koiter branch” in the PANDA2 optimization runs (Case 2). After evaluation of the PANDA2 optimum designs thus generated one can use one’s judgment in deciding which of the PANDA2 optimum designs actually to fabricate. If one does **not** plan to use a general-purpose finite element program such as STAGS to verify the optimum design developed by PANDA2, then it is best always to use the “yes Koiter” option with a factor of safety for local buckling equal to 0.1 or some other value enough smaller than unity that the local buckling margins do not constrain the evolution of the design during optimization cycles.

Figure 68 shows the lowest bifurcation buckling mode and load factor, $pcr=1.1446$, that occurs on the **nonlinear equilibrium path** for the Case 5 shell with only the general buckling modal imperfection with amplitude, $W_{\text{imp}} = -0.0625 \text{ inch}$. The mode shown in Fig. 68 is accepted as an additional imperfection shape with amplitude, $W_{\text{imp}}(2) = -0.001 \text{ inch}$, in the **nonlinear static** STAGS runs that lead to Figs. 69 – 71.

Figure 69 displays the maximum **sidesway** of two of the central stringers (Stringers 14 and 15 counting from the bottom edge of the model in Fig. 68) as a function of load factor PA in the ring bay no. 3 (counting from the left end of the STAGS model in Fig. 68). Figure 70 shows how the central stringers bend and twist (**“bending-torsional” buckling**) in ring bays 3 and 4 and near the right-hand end of the STAGS model at the highest load factor attained in Case 5, $PA = 1.13344$. Eventually the shell collapses near the right-hand end of the STAGS model, as shown in Fig. 71. During collapse the applied loading decreases and the stringer sidesway in ring bay no. 3, plotted in Fig. 69 and displayed in Fig. 70, becomes smaller and smaller as the stringer sidesway near the right-hand end of the shell (ring bay no. 8 in Fig. 68) becomes larger and larger (not plotted here except as Fig. 71). In Case 5 nonlinear dynamic STAGS runs were not needed to obtain the elastic collapse load, $PA = 1.13344$.

13.4 Some results from Case 6

Figures 72 – 74 pertain to this sub-section.

In the past it has been common to account for imperfections by designing a **perfect** shell to survive higher design loads than would actually ever occur. For example, if one decides ahead of time that the **effect of initial imperfections is to halve the theoretical load-carrying capability** of a perfect shell, then one would **double the specified applied loads** and obtain an optimum design of a **perfect** shell for this harsher environment. In order to avoid an over-designed shell, one would have also to double the maximum allowable stress (or use some other factor greater than unity for the stress allowable). If the behavior is assumed to be linear, one can obtain the same or a similar optimum design through use of the actual specified applied loads and through application of a factor of safety of 2.0 for buckling and perhaps some other (probably lower) factor of safety for stress.

The Case 6 optimum design listed in Table 4 was obtained by doubling the applied load ($N_x = -6000 \text{ lb/in}$), doubling the maximum allowable effective stress [$s_{\text{bar}}(\text{allowable}) = 120 \text{ ksi}$], assuming the shell to be perfect ($W_{\text{imp}} = 0$), and setting all factors of safety equal to unity or 0.999. The optimum design thus generated was checked via a PANDA2 run in which the shell is perfect, the actual load, $N_x = -3000 \text{ lb/in}$, the actual allowable effective stress, $s_{\text{bar}}(\text{allowable}) = 60 \text{ ksi}$, all buckling factors of safety are set to 2.0, and the factor of safety for stress is set to 1.0. The margins from this model are essentially the same as those from the input used to generate the optimum design in Case 6.

The Case 6 optimum design and optimized weight should be compared to those in Case 4, since in both Case 6 and Case 4 the two options, “no Koiter” and $\text{ICONSV}=1$, are the same. (The third option, “yes change imperfection”, is irrelevant in Case 6, since $W_{\text{imp}} = 0$ in Case 6). Note that this relatively simple method of accounting for initial imperfections leads to a significantly heavier optimum design in this particular case: **46.83 lb in Case 6 compared to 40.94 lb in Case 4**.

The question still remains, will the optimum design in Case 6 be feasible if it is analyzed under the same conditions as Case 4: application of the actual load, $N_x = -3000$ lb/in, use of the actual allowable effective stress, $s_{bar}(\text{allowable}) = 60$ ksi, an initial “one per cent” imperfection, $W_{imp} = +$ and -0.25 inch, the three options, “no Koiter”, “yes change imperfection”, and $\text{ICONSV} = 1$, and all factors of safety set to unity or 0.999? The answer is yes. The margins from a PANDA2 analysis of the Case 6 optimum design under the Case 4 conditions are all positive, with only the stress margin being critical. Several of the margins that are critical in Case 4 are significantly positive in Case 6. Hence, it is clear that, given the same conditions as those specified in Case 4, the Case 6 design is not optimum. It is too heavy.

Analysis of the Case 6 optimum design with STAGS reveals a difficulty that occasionally arises with STAGS models generated via STAGSUNIT. The special boundary conditions along the two curved edges that permit the accurate representation of sub-domains (especially the constraint that the normal displacement w be **constant** along the circumferences at the two curved edges rather than being zero there), do not prevent axisymmetric buckling and axisymmetric nonlinear deformation in the neighborhoods of these edges in which the normal displacement w at the curved edges is the maximum displacement anywhere in the shell. The processor, STAGSUNIT, was improved as described in **Item 672** in Section 9.0. While this improvement makes this peculiar axisymmetric mode of collapse less likely, it does not prevent it entirely, as is demonstrated in Figs. 72 and 73.

Figures 72 and 73 show the states of the deformed Case 6 design at the beginning and at the end, respectively, of a **nonlinear dynamic** STAGS run in which the applied load factor is held constant at $PA = 1.0$ (the design load, which in this case is $N_x = -6000$ lb/in). The collapse mode is initially axisymmetric, as displayed in Fig. 72. As time passes in the nonlinear dynamic STAGS run the collapse mode develops short-circumferential-wave non-axisymmetrical edge wrinkling caused by non-axisymmetric collapse of the rings at the two ends (especially the left-hand end, as demonstrated in Fig. 73).

Figure 74 exhibits the results of several nonlinear dynamic STAGS runs, the purpose of which is to obtain an accurate value for the elastic load-bearing capability of the STAGSUNIT model of the Case 6 design. Collapse in the mode shown in Fig. 73 occurs for $0.965 < PA < 0.970$, about 3.5 per cent below the design load, $PA = 1.0$.

The PANDA2 models cannot predict the mode of failure displayed in Figs. 72 and 73. An actual shell probably would not fail in this mode because there would exist along the two curved edges stronger rings and/or locally thickened shell skin and stringer cross sections. **The inclusion of such details is beyond the scope of PANDA2.** The mode of failure shown in Figs. 72 and 73 could have been prevented by imposition of a boundary condition such as normal displacement $w = 0$ in the STAGSUNIT processor. However, a constraint such as this would have given rise to concentrations of local prebuckling circumferential compression and axial bending caused by the Poisson effect. This type of local edge behavior is not included in PANDA2 models with multiple rings. (Note, however, that local bending **is** included in the PANDA2 model in the neighborhoods of **interior** rings, as described previously in this paper and in [1E]). Local edge behavior would prevent the generation of useful sub-domain models such as those shown in Figs. 20a and 23a. There would be early local edge buckling, rendering the STAGS models thus generated unsuitable for evaluating optimum designs obtained by PANDA2.

13.5 Some results from Case 7

Figures 75 – 80 pertain to this sub-section.

There are several “classical” methods of including the effect of initial imperfections in axially compressed cylindrical shells:

1. Use Koiter’s asymptotic method [10, 11].
2. Design the shell to a harsher environment and assume that it is perfect (Case 6 in Table 4).
3. Apply “knockdown” factors obtained from tests, the literature, etc. to buckling loads of the perfect shell [9].
4. Measure imperfections in a fabricated shell or a class of similar fabricated shells and perform nonlinear collapse analyses of each shell including its measured imperfection shape [6, 7].
5. Find the critical general buckling mode of a perfect shell and use it as an **unchanging** initial imperfection in subsequent nonlinear static and dynamic analyses of that shell [1I].

Case 7 in Table 4 is based on the “classical” method number 5. As mentioned above, this method often leads to overly conservative (heavy) designs, especially for uniformly axially compressed stiffened cylindrical shells, because the critical general buckling modal imperfection shape of the optimized shell usually has many axial halfwaves and might therefore easily be detected in an actual fabricated shell. Such an imperfect shell would then be repaired or discarded. Despite this weakness in the design method used in Case 7, some results from that case are described next.

As has been described here and in previous papers of this series [1I, 1K], the search for general buckling modes is often made difficult by the presence of “dirty” general buckling modes, such as that displayed in Fig. 75. Figure 75 was generated from a linear buckling STAGS run in which the index, ILIN [20C], is set to ILIN=0 in every shell unit. With ILIN = 1 the much “cleaner” general buckling mode shown in Fig. 76 is obtained from STAGS. This mode is suitable for use as an initial imperfection shape. Replacing ILIN = 0 with ILIN = 1 for each shell unit **only in the linear bifurcation buckling STAGS model** causes many of the short-wavelength buckling modes to be “filtered out” of the eigenvalue spectrum, thereby making it less likely that some local buckling mode will have an eigenvalue that is extremely close to that corresponding to general buckling. It is apparently this extreme closeness of local and general buckling load factors that gives rise to modes such as that shown in Fig. 75. Notice that with ILIN=0 the lowest general buckling mode shape corresponds to eigenvalue no 1829 (Fig. 75). In contrast, with ILIN=1 the lowest general buckling mode corresponds to eigenvalue no. 427 (Fig. 76).

Figure 77 shows the distribution of outer fiber effective stress at the design load, PA = 1.0, with the amplitude of the general buckling modal imperfection shape shown in Fig. 76 **negative** and equal to Wimp = -0.25 inch. **In the nonlinear static STAGS run leading to Fig. 77, the index ILIN, which is equal to 1 for the prediction of the linear general buckling modal imperfection shape displayed in Fig. 76, is reset to ILIN = 0 in every shell unit.** The maximum effective stress, sbar(max) = 58.30 ksi, is slightly below the maximum allowable value, sbar(allowable) = 60 ksi (Table 1), and agrees very well with the prediction from PANDA2.

Figure 78 displays the mode of elastic collapse of the shell with Wimp = -0.25 inches. Collapse occurs at the load factor, PA = 1.22, by sidesway (“bending-torsional” buckling) of the stringers simultaneously at the five locations corresponding to the maximum inward normal deflection of the imperfect shell.

Figures 79 and 80 are generated from the same STAGS model as that shown in Fig. 77 except that the general buckling modal imperfection shape shown in Fig. 76 has a **positive amplitude**, Wimp = +0.25 inch. Figure 79 shows the distribution of outer fiber effective stress (compare with Fig. 77). The stringer that runs along the bottom edge of the expanded insert has much lower effective stresses than its neighbor because stiffeners located at edges of a STAGS model have half the stiffness and half the loading of those that are located in the interior of the domain. Figure 80 shows the mode of collapse. Collapse is initiated by sidesway (“bending-torsional” buckling) of the central stringers near the two curved ends of the STAGS model. Elastic collapse occurs at the load factor, PA = 1.15, somewhat lower than that for the shell with the negative imperfection amplitude (Fig. 78).

NOTE: Case 7 is the only case in which results are displayed here for both positive and negative imperfection amplitudes. However, STAGS runs were made for **both positive and negative imperfection amplitudes** in all the other relevant cases for which the sign of the imperfection affects the behavior. In all the other cases the worst imperfection is the one in which the initial imperfection has an inward lobe (valley) centered on the region where the finite element mesh is the most dense. **The sign of the general buckling modal imperfection matters** in every model that contains a local “patch” in which the nodal point mesh is more dense than in the rest of the STAGS model. This is because local buckling can only be captured reasonably accurately within the “patch” and the local bending and buckling behavior of course depend on the sign of the general buckling modal imperfection, that is, whether in the loaded, imperfect shell the panel skin is compressed more than the outstanding flanges of the stringers or whether the reverse holds in the “patch” where the nodal point mesh is the most dense.

14.0 THE EFFECTS OF ELASTIC-PLASTIC MATERIAL BEHAVIOR IN STAGS MODELS

Figures 81 – 95 pertain to this section. The elastic and elastic-plastic stress-strain curves used in this paper appear in Fig. 81. The elastic-plastic stress-strain curve used in the generation of the results presented in this section resembles a combination of the stress-strain curves for tension and compression of a 7075-T6 aluminum alloy plate specimen [27]. **Cases 2, 4, 5, and 7 were re-run with elastic-plastic effects included in the STAGS models.** The optimum designs are the same as those listed in Table 4, since PANDA2 cannot handle the effect of plasticity. The STAGSUNIT processor of PANDA2 was modified as described in Item 684 of [1L] so that STAGS models including elastic-plastic material behavior can be generated automatically from the PANDA2 data base.

14.1 STAGS elastic-plastic results from Case 2

Figures 82 – 87 pertain to this sub-section. The Case 2 optimum design is evaluated with plasticity included in the STAGS models by means of a sequence of STAGS runs analogous to that used for the elastic model:

1. First a general buckling modal imperfection shape is generated via a sequence of linear buckling runs (INDIC=1) with slightly different eigenvalue “shifts”, starting with an eigenvalue shift of 1.893075, which is the general buckling load factor determined from the elastic model (Fig. 24). After several linear buckling STAGS runs a new, slightly different, buckling load factor, $p_{cr}=1.898937$, is determined. (Even though the new linear general buckling load factor differs only in the fourth significant figure from the old, three STAGS runs with slightly different eigenvalue “shifts” were required to capture the general buckling mode!) The general buckling mode shape is essentially the same as that displayed in Fig. 24. It corresponds to the 607th eigenvalue. (With the elastic model the general buckling mode corresponds to the 610th eigenvalue). Plasticity plays no role in the determination of linear buckling load factors; the slight difference in results from those obtained for the elastic STAGS model is caused by certain modifications in the STAGS program having to do with material properties and shell wall fabrication generated via what in STAGS jargon is called “GCP” [20].
2. A nonlinear static STAGS run is executed with a single buckling modal imperfection, the one analogous to that shown in Fig. 24 with amplitude, $W_{imp} = -0.0625$ inches. At the maximum STAGS load factor reached in this nonlinear static run, $PA = 0.98$ in this case, several buckling load factors and mode shapes are determined analogous to those displayed in Figs. 26 and 27. In this case the first buckling load factor determined at Load Step 18 is $p_{cr} = 1.0074$, and the corresponding nonlinear buckling mode shape resembles that shown in Fig. 26. The second buckling load factor is $p_{cr} = 1.0111$, and the corresponding nonlinear buckling mode shape resembles that shown in Fig. 27.
3. A second nonlinear static STAGS run is executed (starting from zero load) with three buckling modal imperfections: the general buckling mode with amplitude $W_{imp1} = -0.0625$ inches, the first nonlinear buckling mode with amplitude, $W_{imp2} = +0.0005$ inches, and the second nonlinear buckling mode with amplitude, $W_{imp3} = +0.0005$ inches. Figure 82 shows the deformed state of the imperfect shell at the highest load level reached in the nonlinear static run, STAGS load factor $PA = 1.019$. (The two nonlinear buckling modes determined in Item 2 are shown as expanded inserts, c and d, in Fig. 82). In comparing Fig. 82 with Fig. 29 for the elastic model, we see that in the elastic-plastic model there is much more stringer sidesway at approximately the same load level than exists in the elastic model.
4. One or more nonlinear dynamic STAGS models are next executed in order to determine the collapse load factor and the mode of collapse. Figure 83 displays the dynamic behavior when the load level is held constant at $PA = 1.03$. The structure is stable at $PA = 1.03$. Figure 83 is analogous to the curves labeled “Run 8” in Fig. 32. Figure 84 shows the stringer sidesway as a function of load factor PA . Collapse does not occur at $PA = 1.03$, but it is imminent. Figures 85 – 87 are analogous to Figs. 82 – 84, with the STAGS load factor, $PA = 1.04$ rather than 1.03. Collapse occurs in the mode shown in Fig. 85. Compare Fig. 85 with Fig. 30 for the elastic model. Note that the mode of collapse is different: **in the elastic-plastic model collapse occurs in the region where the nodal point density is highest.** In contrast, in the elastic model collapse occurs near the left end of the STAGS model. Figure 86 is analogous to Fig. 32, “Run 7”. Figure 87 shows the stringer sidesway as a function of load factor PA .

Note that the inclusion of plasticity does not affect the load level at which collapse occurs in this particular case: PA(collapse) = 1.04 in both the elastic and the elastic-plastic STAGS models. However, the presence of plastic flow does affect the mode of collapse.

14.2 STAGS elastic-plastic results from Case 4

Figures 88 - 92 pertain to this section. The same sequence of STAGS runs is executed as for that described in Sub-section 14.1.

Figure 88 is analogous to Fig. 82, except that Parts (a) and (b) of Fig. 88 display the outer fiber effective stress rather than the deformation shown in Parts (a) and (b) of Fig. 82. The linear buckling load factor corresponding to general instability, pcr equals 2.035752 (785th eigenvalue). Compare with pcr equals 2.0288 (790th eigenvalue) in the elastic model (Fig. 49). The two nonlinear local buckling modes shown in the expanded inserts (c) and (d) in Fig. 88, are associated with load factors, pcr = 1.0251 (c) and pcr = 1.0885 (d). These nonlinear local buckling load factors are in reasonably good agreement with those from PANDA2 for the imperfect shell: pcr = 0.982 (local buckling in Load set 2, Sub-case 1) and pcr = 1.01 (bending-torsion buckling in Load set 1, Sub-case 2). The nonlinear buckling mode shapes from STAGS also agree with those predicted by PANDA2. The PANDA2 predictions are somewhat conservative because the conservative option, ICONSV = 1 is used in the Case 4 PANDA2 model. With ICONSV = 1 there is more prebuckling bending of the shell with a general buckling modal imperfection than exists for the identical design with the ICONSV = 0 or ICONSV = -1 models. With more prebuckling bending there is more stress redistribution and hence smaller local buckling margins. See Fig. 99 and the discussion in Section 9.0 under **Item 676**.

In this case the elastic model is treated differently from the elastic-plastic model: There is only a **single** buckling modal imperfection in the elastic model: that shown in Fig. 49. The **local bending** behavior evident in Figs. 53a and 53b develops “automatically” during a nonlinear **dynamic** elastic STAGS run without the presence of one or more tiny initial imperfection “trigger(s)”; local bending does not grow during the initial nonlinear **static** elastic STAGS run. In contrast, in the elastic-plastic model, the local bending modes, introduced via the two nonlinear buckling modal imperfections displayed as expanded inserts (c) and (d) in Fig. 88, grow during the second nonlinear static STAGS run (Item 3 in Sub-section 14.1). This difference in modeling has implications for the STAGS user. The transition from global deformation to a mixture of global and local deformation may be achieved without the introduction of local imperfection “triggers” (buckling modal imperfections with very small user-specified amplitudes) by means of one or more nonlinear dynamic STAGS runs at load levels slightly above that for which the last converged static equilibrium state is determined. Alternatively, the user may prefer to use multiple nonlinear static STAGS runs with the introduction of local imperfection “triggers” to permit loading to higher values of load factor PA than is possible with only a general buckling modal imperfection shape.

Figure 89, which corresponds to the state of the shell displayed in Figs. 88a,b, shows the distribution of outer fiber effective axial plastic strain at the highest load level reached in the second nonlinear static STAGS run, PA = 1.05847.

Figures 90 – 92 show the elastic-plastic collapse mode. Compare Fig. 90 with Fig. 56 for the elastic model. In both the elastic-plastic and in the elastic STAGS models collapse is predicted to occur near the left-hand end of the shell (1st ring bay). Collapse occurs via sidesway of several of the central stringers. Figure 91 is analogous to Fig. 86 and Fig. 92 is analogous to Fig. 87. Collapse occurs at a load level, $1.055 < PA < 1.06$. In the elastic STAGS model collapse occurs at PA = 1.08.

14.3 STAGS elastic-plastic results from Case 5

Figures 93 and 94 pertain to this sub-section. The same sequence of STAGS runs is executed as for those described in Sub-sections 14.1 and 14.2. In this case the general buckling modal imperfection shape, which is essentially the same as that shown in Fig. 66, corresponds to a STAGS linear buckling load factor, pcr = 2.021307 (559th eigenvalue). In the elastic model the STAGS linear buckling load factor for Case 5 is pcr = 2.0155 (564th eigenvalue,

Fig. 66). The nonlinear buckling mode resembles that shown in Fig. 68 for the elastic model except that there is no buckling modal deformation near the right-hand end of the shell. The nonlinear buckling load factor is $p_{cr} = 1.1773$ compared to $p_{cr} = 1.1446$ for the elastic model. As written in the caption for Fig. 68, PANDA2 predicts 1.131 (Load set 1, Sub-case 1) for local bending-torsion stringer buckling of the imperfect shell as loaded by the design load, $PA = 1.0$.

Figure 93 is analogous to Fig. 69 for the elastic model. In Fig. 69 the load deflection curve for sidesway of two of the stringers in Ring bay 3 for increasing PA is the same as that for decreasing PA . There is no “Riks path reversal”, however, because the stringer sidesway near the right-hand end of the shell continues to increase as that in Ring bay 3 decreases, leading eventually to elastic collapse as displayed in Figs. 70 and 71. In Fig. 93 there is “modified Riks path reversal”: The load deflection curve for increasing PA differs from that for decreasing PA because some of the material in several of the stringers experiences irreversible plastic flow. The upper expanded insert in Fig. 93 displays the deformed state of some of the central stringers in ring bays 3 and 4 (Figs. 66 and 68) at the load step (Step 20) that corresponds to the stringer sidesway of largest amplitude. The lower expanded insert shows the residual stringer deformation and distribution of **axial plastic strain** remaining after the shell has unloaded completely and load direction reversal has begun. (PA equals a small negative number, $PA = -0.103$). Deformation of the stringers is greatly exaggerated in this and in the other figures in this paper.

Figure 94 is analogous to Figs. 87 and 92. Elastic-plastic collapse occurs by means of stringer sidesway in ring bays 3 and 4 where the nodal mesh density is highest. The collapse load factor is $PA = 1.09$. The expanded insert on the left-hand side of Fig. 94 shows the deformed state at the largest sidesway amplitude reached in the nonlinear static run. (The same insert is used as the upper insert in Fig. 93). The expanded insert on the right-hand side of Fig. 94 displays the deformed state at the end of the nonlinear dynamic STAGS run. In the elastic-plastic STAGS model collapse occurs in the stringers in ring bays 3 and 4 at $PA = 1.09$. In contrast, in the elastic STAGS model collapse occurs in the stringers near the right-hand end of the shell at a load factor, $PA = 1.13344$, as shown in Fig. 71.

14.4 STAGS elastic-plastic results from Case 7

Figure 95 pertains to this sub-section. The same sequence of STAGS runs is executed as for those described in Sub-sections 14.1, 14.2, and 14.3. In this case the general buckling modal imperfection shape, which is essentially the same as that shown in Fig. 76, corresponds to a STAGS linear buckling load factor, $p_{cr} = 3.798233$ (423rd eigenvalue). In the elastic model the STAGS linear buckling load factor for Case 7 is $p_{cr} = 3.7904$ (427th eigenvalue, Fig. 76). At the highest load factor reached in the first nonlinear static STAGS run, $PA = 1.08708$, the lowest two **nonlinear** buckling load factors are $p_{cr} = 1.1108$, which corresponds to stringer sidesway (bending-torsion buckling) in the region of densest nodal point mesh and $p_{cr} = 1.1409$, which corresponds to local buckling in the region of densest nodal point mesh. PANDA2 predicts $p_{cr}(\text{PANDA2}) = 0.990$ for bending-torsion buckling (Load set 1, Sub-case 2) of the imperfect shell and $p_{cr}(\text{PANDA2}) = 0.987$ for local buckling (Load set 2, Sub-case 1) of the imperfect shell. The nonlinear buckling mode shapes from STAGS (not shown in this paper) agree with those predicted by PANDA2. The PANDA2 predictions of nonlinear stringer sidesway (bending-torsion) buckling and nonlinear local buckling are somewhat conservative because the conservative option, $\text{ICONSV} = 1$ is used in the Case 7 PANDA2 model. With $\text{ICONSV} = 1$ there is more prebuckling bending of the shell with a general buckling modal imperfection than exists for the identical design with the $\text{ICONSV} = 0$ or $\text{ICONSV} = -1$ models. With more prebuckling bending there is more stress redistribution and hence smaller bending-torsion and local buckling margins. See Fig. 99 and the discussion in Section 9.0 under **Item 676**.

Figure 95 is analogous to Fig. 94. Three imperfection shapes were used for the imperfect shell, Wimp1 = general buckling mode (amplitude = -0.25 inch), Wimp2 = nonlinear bending-torsion stringer buckling mode (amplitude = +0.005 inch), and Wimp3 = nonlinear local buckling mode (amplitude = +0.005 inch). Elastic-plastic collapse occurs by means of stringer sidesway in ring bay 3 where the nodal mesh density is highest (Fig. 76). The collapse load factor is $PA = 1.13$. The expanded insert on the left-hand side of Fig. 95 shows the deformed state at the largest sidesway amplitude reached in the nonlinear static run. The expanded insert on the right-hand side of Fig. 95 displays the deformed state at the end of the nonlinear dynamic STAGS run. In the elastic-plastic STAGS model collapse occurs in the stringers in ring bay 3 at $PA = 1.13$. In the elastic STAGS model collapse occurs at the same location at a load factor, $PA = 1.22$, as shown in Fig. 78.

For the same configuration, Case 7, with a **positive** general buckling modal imperfection with amplitude, $W_{imp} = +0.25$ inch and with no other imperfection shapes, the elastic-plastic collapse load factor from STAGS is $PA = 1.08$. The mode of collapse is the same as that displayed in Fig. 80. The collapse load factor for the elastic STAGS model of Case 7 with a positive imperfection amplitude, $W_{imp} = +0.25$ inch, is $PA = 1.15$.

15.0 IMPERFECTION SENSITIVITY STUDY CORRESPONDING TO THE DESIGN IN CASE 5

Figures 96 – 98 pertain to this section. The results presented in this section were obtained for the configuration listed under Case 5 with the “yes Koiter” option and with both the “yes change imperfection” option (Fig. 97) and the “no change imperfection” option (Fig. 98). Figure 96 displays design margins as functions of the axial load N_x for a user-specified **initial** general buckling modal imperfection amplitude, $W_{imp} = 0.5$ inch. These curves were obtained with use of the “yes change imperfection” option. Additional figures analogous to Fig. 96 and not presented here to save space were also obtained with the “yes change imperfection” option and with $W_{imp} = 0.0, 0.25, 0.75$, and 1.0 inch. With the “no change imperfection” option figures analogous to Fig. 96 were obtained with $W_{imp} = 0.0625, 0.125$, and 0.25 inch. (It was not necessary to repeat the “yes change imperfection” option for $W_{imp} = 0.0$, of course).

The curves in Fig. 97 were generated by reading the value of axial load N_x that corresponds to zero margin for each of several types of buckling and stress margins, as listed at the top of Fig. 97 for each imperfection amplitude: $W_{imp} = 0.0, 0.25, 0.5, 0.75$ and 1.0 inch. For example, the small diamond located on the ordinate with zero value (corresponding abscissa value, $N_x = -2125$ lb/in) and corresponding to the margin called “8.1.1 eff.stress:matl=1,allnode;-MID.” in Fig. 96 is plotted in Fig. 97 at the abscissa value 0.5 corresponding to the margin labeled “‘yes change imperfection’ Effective stress from SUBROUTINE STRCON...”. The same procedure was used to generate Fig. 98.

In Fig. 96 many of the margins decrease very steeply as the general buckling margin (Margin no 21 listed at the top of Fig. 96) approaches zero from the right. This behavior results from the approximately hyperbolic amplification of the general buckling modal imperfection [1E], amplification that should be infinite when the general buckling margin reaches zero. In PANDA2 numerical difficulties are avoided by setting a maximum amount by which buckling modal imperfections can be amplified by the applied load. The points to the left of the point of “singularity” (general buckling margin equals zero) lie on curves that are less steep because the amount by which the general buckling modal imperfection is amplified remains constant in that region and equal to the maximum value permitted in the PANDA2 coding to avoid numerical difficulties. This artifice does not affect optimization because the maximum allowable amplification of the general buckling modal imperfection is set high enough that most of the buckling and stress margins are deeply in the unfeasible region for general buckling modal amplification of the maximum amount. Design iterations produce configurations that are, except on very rare occasions, far from that region.

The curves in Figs. 97 and 98 might be called **“knockdown” curves**. They exhibit the typical “convex-from-below” shapes presented in the literature on imperfection sensitivity [5,8,10,11]. For Case 5 the critical general buckling mode has four axial halfwaves. Therefore, with the “yes change imperfection” option the initial user-specified amplitude of the general buckling modal imperfection shape is reduced by a factor approximately equal to four, according to Expression 11.1. [However, remember the “fractional” axial halfwaves (Table 8)! Expression 11.1 yields $1/(m+dm)$, not simply $1/m$, where m is the number of axial halfwaves in the critical general buckling mode and dm is the “fractional” axial wavenumber.] **The “knockdown” curves for several margins are similar for the “yes change imperfection” option to those for the “no change imperfection” option if the scale on the abscissa in the “knockdown” curves for the “yes change imperfection” is divided by the factor by which the amplitude of the general buckling modal imperfection is reduced in the “yes change imperfection” option.**

Also included in Figs. 97 and 98 is the “imperfection sensitivity” curve from Koiter’s special theory [28] (not an asymptotic theory). This curve, presented in Fig. 262 on p. 297 of [8], applies to monocoque isotropic cylindrical shells under uniform axial compression. The “Koiter” curve in [8] is normalized. The imperfection amplitude is divided by the thickness of the monocoque cylindrical shell, and the ordinate values are divided by the general

buckling load of the perfect shell.

For the ring and stringer stiffened cylindrical shell we can derive an “effective” thickness from the equation,

$$t(\text{effective})^2 = 12 \times C_{44}(\text{neutral surface})/C_{11} \quad (15.1)$$

in which $t(\text{effective})$ is the effective thickness, $C_{44}(\text{neutral surface})$ is the axial bending stiffness relative to the neutral surface for axial bending, and C_{11} is the axial membrane stiffness. For the Case 5 design $C_{44}(\text{neutral surface}) = 36054.0$ in-lb and $C_{11} = 705580.0$ lb/in., leading to $t(\text{effective}) = 0.783$ inches.

The “knockdown” curves in Fig. 98 from PANDA2 are clustered around the “Koiter” curve. The “knockdown” curves in Fig. 97 from PANDA2 display much less imperfection sensitivity than does the “Koiter” curve because the amplitudes of the **initial user-specified** imperfections are reduced by the ratio, Expression 11.1, before the PANDA2 computations of buckling load factors and stresses are carried out. (In Case 5 the value of Expression 11.1 is approximately 1/4, or more precisely, $1/(m+dm)$, in which m is the number of axial halfwaves in the critical general buckling mode and dm is the number of “**fractional**” axial halfwaves in the critical general buckling mode).

16.0 SUMMARY, CONCLUSIONS, SUGGESTIONS FOR FURTHER WORK

16.1 Summary

1. PANDA2 and STAGS are briefly described (Sections 3.0 and 4.0).
2. The question, “Why should one use STAGS to verify PANDA2 designs?” is answered (Section 5.0).
3. A description of how to use STAGS to verify PANDA2 designs is given (Section 6.0 and Table 9).
4. The two major effects of an initial global imperfection on the behavior of stiffened cylindrical shells are described (Section 7.0).
5. A list of how this paper differs from [1K] and a list of the most important improvements to PANDA2 during the past year are provided (Sections 8.0 and 9.0).
6. A typical PANDA2 runstream used to generate a “global” optimum design is given (Section 10.0).
7. The seven optimum designs obtained by PANDA2 under various conditions are listed and discussed (Section 11.0).
8. The PANDA2 runstream used to produce the optimum designs listed in Table 4 is given (Section 12.1.1).
9. The results from an (m,n) survey of general buckling modal imperfection shapes is provided for Case 2 (Sections 12.1.2 and 12.1.3).
10. STAGS and BIGBOSOR4 models and predictions for a typical case (Case 2) are discussed and compared with those from PANDA2 (Section 12.2).
11. Selected details from several cases in Table 4 other than Case 2 are given (Section 13.0).
12. The effect of plasticity is included in four of the STAGS models: Case 2, Case 4, Case 5, and Case 7. (Section 14.0)
13. A study of imperfection sensitivity is conducted for the Case 5 design with use of the: 1. “yes change imperfection” option and with use of the 2. “no change imperfection” option (Section 15.0).

14. A plot is given of several margins vs the “conservativeness” index, ICONSV for the Case 4 configuration (Fig. 99).

16.2 Conclusions

1. The agreement between PANDA2, BIGBOSOR4, and STAGS predictions is reasonable.
2. Optimum designs obtained from a PANDA2 model with a fixed imperfection amplitude are too heavy.
3. In almost every case it is necessary to execute both nonlinear static and nonlinear dynamic STAGS runs in order to obtain the elastic collapse load factor.
4. Elastic collapse usually occurs in one or both of the end bays of the imperfect cylindrical shells, not in an interior ring bay.
5. It is probably best to obtain optimum designs with PANDA2 run in the “yes Koiter” mode, that is, allowing PANDA2 to enter its analysis branch in which local bending of the panel skin and stringer parts is accounted for [1C].
6. The (m,n) survey demonstrates that with Case 2 the “worst” general buckling modal imperfection shape is indeed that computed by PANDA2, that is, the general buckling mode for which $(m,n) = (m,n)\text{critical}$ with axial and circumferential wave numbers, m and n , being computed by PANDA2 rather than being specified in advance by the PANDA2 user.
7. Imperfect shells that are optimized as if they were perfect but subjected to an increased axial load, $N_x(\text{applied load}) = N_x(\text{design load}) / (\text{typical knockdown factor})$, will probably be too heavy.
8. Including the effect of elastic-plastic material behavior in the STAGS models “compresses” the predicted collapse load factors for the various models listed in Table 4. That is, the lowest collapse load (least conservative model, Case 2) is not affected while the highest collapse load (most conservative model, Case 7) is reduced by the most amount. Whereas collapse of the elastic models most often occurs in one of the end bays of the shell, collapse of the elastic-plastic models most often occurs in the interior region where the nodal mesh density is the greatest. With **negative** general buckling modal imperfections the collapse load factors from STAGS for the **elastic** models of Case 2, Case 4, Case 5, and Case 7 are $PA = 1.04, 1.08, 1.13$, and 1.22 , respectively. The collapse load factors from STAGS for the **elastic-plastic** models of Case 2, Case 4, Case 5, and Case 7 are $PA = 1.04, 1.06, 1.09$, and 1.13 , respectively. For Case 7 with the **positive** general buckling modal imperfection, the STAGS **elastic** model yields $PA = 1.15$ and the STAGS **elastic-plastic** model yields $PA = 1.08$.
9. The “knockdown” curves for several margins are similar for the “yes change imperfection” option to those for the “no change imperfection” option if the scale on the abscissa in the “knockdown” curves for the “yes change imperfection” is divided by the factor by which the amplitude of the general buckling modal imperfection is reduced in the “yes change imperfection” option.
10. Buckling and stress margins of a given design decrease monotonically as the “conservativeness” index, ICONSV, is increased from -1 to 0 to $+1$. The monotonic decrease in margins is caused by the monotonic increase in prebuckling bending of the shell with a given general buckling modal imperfection shape and amplitude and loaded by the given design load.

16.3 Suggestions for further work

1. Perhaps PANDA2 should be changed so that the user can provide two input data: 1. the minimum detectable error in axial slope of a generator of the cylindrical shell, and 2. the minimum detectable error in circumferential slope. Then PANDA2 would compute the amplitude of the general buckling modal imperfection as the maximum value

such that neither the minimum detectable error in axial slope nor the minimum detectable error in circumferential slope would be exceeded during optimization cycles.

2. We do not know what a typical “minimum detectable error” in axial slope or in circumferential slope is in actual shells fabricated in various ways. Perhaps actual shells could be measured to gather data.

3. It would be a good idea to generate a program in which STAGS is used within the optimization loop rather than being used only after an optimum design has been determined by PANDA2. Perhaps several different STAGS models could be incorporated into such a program with use of different sub-domains (“patches”), all of which experience the same prebuckled state. Different STAGS models would be used for local, “semi-local”, and general buckling.

4. STAGSUNIT could be expanded to handle more general cases via the STAGS “GCP” input scheme [20C].

5. STAGSUNIT could be expanded to permit more general “compound” models (Figs. 1, 2, 61-63 and [1K]) than it can now handle.

17.0 DEDICATION

This paper is dedicated to the memory of our close friend and colleague for many, many years, Frank Brogan, co-author of STAGS.



FRANCIS A. BROGAN, 1925 - 2006

Francis Allen Brogan, 81, died at Stanford Hospital on August 16. Mr. Brogan, known as Frank to his friends, was a long-time resident of Palo Alto, California until moving to Menlo Park, California seven years ago.

He was born May 3, 1925 in Omaha, Nebraska, the second of three children of Maurice Perley and Marjorie Frances (Rutter) Brogan. His father, a consulting engineer, was also a Nebraska native. His paternal grandfather, Francis Albert Brogan, was a prominent Omaha attorney. His maternal grandfather, Thomas Nixon Rutter, managed an investment brokerage in Omaha.

Frank attended Carleton College in Northfield, Minnesota, as did his younger sister, Maude, graduating Phi Beta Kappa in 1949 with degrees in mathematics and music. After college, he became an officer in the U.S. Navy, studying Chinese at the Naval Postgraduate School in Monterey, and serving for eight years as a translator, stationed in the Pacific and in Washington D. C. He then came to Berkeley to earn a graduate degree in mathematics, where he became a member of the Berkeley Chamber Singers.

After completing his coursework in 1961, he worked for many years at the Palo Alto Research Laboratory of the Lockheed Missiles & Space Company, creating software that is used in the U.S. space program. After his retirement in 1986 and for the remainder of his life he consulted on a continuing basis both here and abroad in his specialties: computerized numerical analysis, data base management, and finite element development, mostly in connection with the STAGS computer program.

Mr. Brogan enjoyed hiking in the Sierras, continued to participate in musical groups as a performer, and was an avid concert-attendee. He had wide-ranging interests and remained active until his death.

The Structural Analysis of General Shells (STAGS) code has been under continuous development for almost forty years. STAGS enjoys a solid reputation for solving problems involving aerospace structures that experience the types of nonlinear static and dynamic response most challenging to model accurately. It has played a pivotal role in our space program, including the analysis of the Challenger solid rocket booster accident, the characterization of the Super Lightweight Space Shuttle Tank, and many, many smaller structures of importance to NASA. In no small part, STAGS owes this reputation to Frank Brogan, who from the inception of STAGS worked with its architects, first Bo Almroth and after Bo's death Charles Rankin. Frank was the person who could translate advanced concepts into efficiently organized computer instructions. His ability to see through a problem to its core is legendary, with the result that almost every challenge, no matter how complex, was met with success usually in a matter of days, not months. STAGS would never have existed without Frank. It was Frank who many years ago single-handedly organized data structures that hold their own today. This is remarkable given the fact that much of his work was with punch cards long before the "interactive" era of terminals and personal computers. He was, as far as we know, the first to organize solution algorithm computer instructions based purely on functionality, long before C++ constructs existed, coded in what some today would deride as "primitive FORTRAN." None of this would have been possible if Frank had not, from the very beginning, grasped the essentials of the physics involved. Frank indeed bridged the disciplines of mathematics, mechanics, physics, and music. This combination made Frank the essential resource from STAGS' humble beginnings as a research finite-difference code through its transformation into an advanced finite element engine capable of tackling the nonlinear response of structures undergoing unstable collapse and progressive failure through the use of reliable models with hundreds of thousands of degrees of freedom.

18.0 ACKNOWLEDGMENTS

The author is most grateful for the help of Dr. Charles Rankin, a friend and colleague who was always available to advise about the proper input data for STAGS models and to interpret STAGS output. The author also appreciates the help of Dr. Frank Weiler, a friend and colleague at Lockheed Martin in Palo Alto, California. Dr. Weiler frequently helped the author whenever any problems arose in connection with updating and executing STAGS on various computers at the Lockheed Martin Advanced Technology Center and whenever any problems arose in connection with transferring files via email. On one occasion Dr. Weiler came to Lockheed Martin on a holiday in order to reboot a computer the author needed to use. The author is also grateful for the help of Ms. Liz Ling, another colleague at the Lockheed Martin Advanced Technology center, who was often called upon to transfer files via email. Dr. Norm Strampach, a third colleague at the Lockheed Martin Advanced Technology Center, helped the author learn how to manipulate figures and add them to the electronic document. Ms. Miriam Palm, a friend of Frank Brogan from his music world, wrote the part of the dedication to Frank Brogan that is not about STAGS; Charles Rankin wrote the part about Frank's contribution to the development of STAGS. Thanks also to the Lockheed Martin Advanced Technology Center for permitting the retired author to have an office.

19.0 REFERENCES

- [1] Bushnell, D., et al, (A) "PANDA2 - Program for minimum weight design of stiffened, composite, locally buckled panels", Computers and Structures, Vol. 25 (1987) pp. 469-605. See also: (B) "Theoretical basis of the PANDA computer program for preliminary design of stiffened panels under combined in-plane loads", Computers and Structures, v. 27, No. 4, pp 541-563, 1987; (C) "Optimization of composite, stiffened, imperfect panels under combined loads for service in the postbuckling regime", Computer Methods in Applied Mechanics and Engineering,

Vol. 103, pp 43-114, 1993; (D) "Recent enhancements to PANDA2" 37th AIAA Structures, Dynamics, and Materials (SDM) Conference, April 1996; (E) "Approximate method for the optimum design of ring and stringer stiffened cylindrical panels and shells with local, inter-ring, and general buckling modal imperfections", Computers and Structures, Vol. 59, No. 3, 489-527, 1996, with W. D. Bushnell; (F) "Optimum design via PANDA2 of composite sandwich panels with honeycomb or foam cores", AIAA Paper 97-1142, AIAA 38th SDM Conference, April 1997; (G) "Additional buckling solutions in PANDA2", AIAA 40th SDM Conference, p 302-345, April 1999, with H. Jiang and N. F. Knight, Jr.; (H) "Minimum-weight design of a stiffened panel via PANDA2 and evaluation of the optimized panel via STAGS", Computers and Structures, Vol. 50, 569-602 (1994); (I) "Optimization of perfect and imperfect ring and stringer stiffened cylindrical shells with PANDA2 and evaluation of the optimum designs with STAGS", AIAA Paper 2002-1408, pp 1562-1613, Proceedings of the 43rd AIAA SDM Meeting, April, 2002, with C. Rankin; (J) "Optimum design of stiffened panels with substiffeners, AIAA Paper 2005-1932, AIAA 46th SDM Conference, April 2005, with C. Rankin; (K) "Difficulties in optimization of imperfect stiffened cylindrical shells, AIAA Paper 2006-1943, AIAA 47th SDM Conference, April 2006, with C. Rankin; (L).../panda2/doc/panda2.news, a continually updated file distributed with PANDA2 that contains a log of all significant modifications to PANDA2 from 1987 on.

[2] (A) Dickson, J.N., Biggers, S.B., and Wang, J.T.S., "Preliminary design procedure for composite panels with open-section stiffeners loaded in the post-buckling range," in: Advances in Composite Materials, A. R. Bunsell, et al, editors, Pergamon Press Ltd., Oxford, England, 1980, pp 812-825. Also see: (B) Dickson, J.N. and Biggers, S.B., "POSTOP: Postbuckled open-stiffened optimum panels, theory and capability", NASA Langley Research Center, Hampton, Va., NASA Contractor Report from NASA Contract NAS1 -15949, May 1982.

[3] (A) Butler, R. and Williams, F. W., "Optimum design features of VICONOPT, an exact buckling program for prismatic assemblies of anisotropic plates," AIAA Paper 90-1068-CP, Proceedings 31st AIAA/ASME Structures, Structural Dynamics, and Materials (SDM) Meeting, pp 1289-1299, 1990. Also see: (B) Williams, F. W., Kennedy, D., Anderson, M.S., "Analysis features of VICONOPT, an exact buckling and vibration program for prismatic assemblies of anisotropic plates,", AIAA Paper 90-0970-CP, Proceedings 31st AIAA/ASME Structures, Structural Dynamics, and Materials Meeting, pp 920-929, 1990.

[4] (A) Anderson, M.S. and Stroud, W.J., "General panel sizing computer code and its application to composite structural panels," AIAA Journal, 17, (1979) pp. 892-897. Also see: (B) Stroud, W.J. and Anderson, M.S., "PASCO: Structural panel analysis and sizing code, capability and analytical foundations," NASA TM-80181, NASA Langley Research Center, Hampton, Va., 1981; (C) Stroud, W.J., Greene, W.H., and Anderson, M.S., "Buckling loads of stiffened panels subjected to combined longitudinal compression and shear: Results obtained with PASCO, EAL, and STAGS computer programs," NASA TP 2215, Nasa Langley Research Center, Hampton, Va., January 1984.

[5] Brush, D. O. and Almroth, B. O., *Buckling of Bars, Plates, and Shells*, McGraw-Hill, New York, 1975

[6] Jones, Robert M., *Buckling of Bars, Plates, and Shells*, Bull Ridge Publishing, Blacksburg, VA, 2006

[7] Singer, J., Arbocz, J., and Weller, T., *Buckling Experiments – Experimental Methods in Buckling of Thin-Walled Structures*, John Wiley & Sons Inc., 2002

[8] Bushnell, D., *Computerized Buckling Analysis of Shells*, published by Nijhoff, The Netherlands, 1985, reprinted by Kluwer Academic Publishers, 1989

[9] Weingarten, V. I., Seide, P., and Peterson, J. P., *Buckling of Thin-Walled Circular Cylinders*, NASA Special Publication SP-8007, September 1965, Revised August 1968

[10] Koiter, W. T., *Over de Stabiliteit van het elastisch evenwicht*, thesis, Technical Institute – Delft, H. J. Paris, Amsterdam, 1945; English translations: *On the Stability of Elastic Equilibrium*, NASA TT-F-10833, March 1967 and AFFDL-TR-70-25, February 1970

[11] Hutchinson, J. W. and Amazigo, J. C., "Imperfection sensitivity of eccentrically stiffened cylindrical shells", AIAA J., Vol. 5, No. 3, pp. 392-401, 1967

- [12] Baruch, M. and Singer, J., "Effect of eccentricity of stiffeners on the general instability of stiffened cylindrical shells under hydrostatic pressure", *Journal of Mechanical Engineering Science*, 5, (1) (1963) pp.23-27.
- [13] Bushnell, D., "PANDA – interactive program for minimum weight design of stiffened cylindrical panels and shells", *Computers & Structures*, Vol. 16, No. 1-4, pp. 167 – 185, 1983
- [14] (A) Bushnell, D., "BOSOR4: Program for stress, buckling, and vibration of complex shells of revolution," *Structural Mechanics Software Series - Vol. 1*, (N. Perrone and W. Pilkey, editors), University Press of Virginia, Charlottesville, 1977, pp. 11-131. See also: (B) *Computers and Structures*, Vol. 4, (1974) pp. 399-435; (C) *AIAA J*, Vol. 9, No. 10, (1971) pp. 2004-2013; (D) *Structural Analysis Systems*, Vol. 2, A. Niku-Lari, editor, Pergamon Press Oxford, 1986, pp. 25-54; (E) *Computers and Structures*, 18, (3), (1984) pp. 471-536. For a fairly recent version of BOSOR4, called BIGBOSOR4, see the following: (F) "Automated optimum design of shells of revolution with application to ring-stiffened cylindrical shells with wavy walls", *AIAA Paper 2000-1663*, 41st AIAA SDM Conference, April, 2000 and a Lockheed Martin report with the same title, LMMS P525674, November 1999.
- [15] Koiter, W. T., "Het Schuifplooiveld by Grote Overschrijdingen van de Knikspanning", National Luchtvaart Laboratorium, The Netherlands, Report X295, November 1946 (in Dutch).
- [16] Vanderplaats, G. N., "ADS--a FORTRAN program for automated design synthesis, Version 2.01", *Engineering Design Optimization*, Inc, Santa Barbara, CA, January, 1987
- [17] Vanderplaats, G. N. and Sugimoto, H., "A general-purpose optimization program for engineering design", *Computers and Structures*, Vol. 24, pp 13-21, 1986
- [18] Almroth, B. O. and Brogan, F. A., "The STAGS computer code", *NASA CR-2950*, NASA Langley Research Center, Hampton, VA, 1978.
- [19] STAGS Brochure (2002) available online by request: crankin@rhombuscgicom (pdf format).
- [20] (A) Rankin, C.C., Stehlin, P., and Brogan, F.A., "Enhancements to the STAGS computer code", *NASA CR-4000*, NASA Langley Research center, Hampton, VA, 1986. See also: (B) Rankin, C.C., "Application of Linear Finite Elements to Finite Strain Using Corotation." *AIAA Paper AIAA-2006-1751*, 47th AIAA Structures, Structural Dynamics and Materials Conference, May 2006; (C) Rankin, C.C., Brogan, F.A., Loden, W.A., Cabiness, H.D., "STAGS User Manual – Version 5.0," Rhombus Consultants Group, Inc., Palo Alto, CA, Revised January 2005 (on-line). Previously Report No. LMSC P032594, Lockheed Martin Missiles and Space Company, Palo Alto, CA, June 1998; (D) Rankin, C.C., "The use of shell elements for the analysis of large strain response, *AIAA Paper 2007-2384*, 48th AIAA Structures, Structural Dynamics and Materials Conference, Hawaii, April 2007.
- [21] Riks, E., Rankin C. C., Brogan F. A., "On the solution of mode jumping phenomena in thin walled shell structures", First ASCE/ASM/SES Mechanics Conference, Charlottesville, VA, June 6-9, 1993, in: *Computer Methods in Applied Mechanics and Engineering*, Vol. 136, 1996.
- [22] Bushnell, D. and Bushnell, W.D., "Optimum design of composite stiffened panels under combined loading", *Computers and Structures*, Vol. 55, pp 819-856 (1995).
- [23] Bushnell, D., Rankin, C.C., and Riks, E., "Optimization of stiffened panels in which mode jumping is accounted for", *AIAA Paper 97-1141*, Proc. 38th AIAA SDM Conference, pp 2123-2162, April 1997.
- [24] van der Neut, A., "The interaction of local buckling and column failure of thin-walled compression members", Proc. of the Twelfth International Congress of Applied Mechanics, edited by Hetenyi, M. and Vincenti, W.G., Springer, Berlin, pp. 389-399, 1969.
- [25] (A) Sanders, J.L., Jr., "Nonlinear theories for thin shells", *Quarterly of Applied Mathematics*, Vol. 21, pp 21-36, 1963. Also see: (B) "An improved first-approximation theory for thin shells", *NASA TR R-24*, Langley Research Center, 1959.

[26] Bushnell, D., "Stress, buckling and vibration of prismatic shells", AIAA J. Vol. 9, No. 10, pp. 2004-2013, 1974

[27] Anonymous, **Metallic Materials and Elements for Aerospace Vehicle Structures**, Vol. 1, MIL-HDBK-5G, November, 1994. (See p. 3-368 for stress-strain curves for aluminum alloy 7075-T5 plate).

[28] Koiter, W.T., "The effect of axisymmetric imperfections on the buckling of cylindrical shells under axial compression", Kononkl. Ned. Akad. Wetenschap, Proc., B66, pp 265-279 (1963)

Table 1 Geometry, material properties, and loading of the stiffened cylindrical shell. (PANDA2 names for dimensions such as H(STR), B(STR), etc., are defined in Table 2).

Geometry (cylindrical shell):

Length = 75 inches
 Radius = 25 inches
 External T-shaped major stringers
 Internal T-shaped major rings

Material properties (aluminum):

Young's modulus = 10 msi
 Poisson ratio = 0.3
 Maximum allowable effective (von Mises) stress = sbar(allowable) = 60 ksi; Stress constraints are active.
 The material remains **elastic** in all the models explored in this paper. The effect of elastic-plastic material behavior is also determined for four of the STAGS models. (See the stress-strain curve is given in Fig. 81.)

Loading used for all cases except one:

-3000.0 \$ Axial Resultant (lb/in), Nx(1) Load Set A (The axial resultant Nx = -6000 lb/in in Case 6)
 -0.1 \$ Hoop Resultant (lb/in), Ny(1) Load Set A
 0.0 \$ In-plane shear (lb/in), Nxy(1) Load Set A
 -0.004 \$ Uniform pressure, (psi), p(1) Load Set A
 Zero loading in Load Set B

Boundary conditions:

Simple support, but free to expand radially in the prebuckling phase.

Imperfection:

General buckling modal imperfection amplitude, Wimp = +0.25 inch and -0.25 inch.

Imperfect shells have two load cases:

Load Set 1: Wimp= +0.25 inch
 Load Set 2: Wimp= -0.25 inch

User-specified axial halfwavelength of the initial general buckling modal imperfection equals 75 inches.

In several of the cases PANDA2 is permitted to change the imperfection amplitude, Wimp, as described in the text.

NOTE:

In PANDA2 the complete cylindrical shell is modeled as a panel that spans 180 degrees. In the absence of in-plane shear loading (torque, Nxy) and anisotropy the behavior of the 180-degree panel simply supported along its two straight edges is identical to that of a complete cylindrical shell. The optimum weights listed in Table 4 are the weights of half (180 degrees) of the cylindrical shells.

Margins corresponding to inequality constraints (see next table for definitions of variables, V(i), i = 1,13):

1. $-V(3)^1 + 20.V(6)^1 - 1$. (stringer web height, H(STR), is less than 20 x stringer web thickness, T(2)(STR))
1. $-V(4)^1 + 20.V(7)^1 - 1$. (stringer flange width, W(STR), is less than 20 x stringer flange thickness, T(3)(STR))
1. $-V(10)^1 + 20.V(12)^1 - 1$. (ring web height, H(RNG), is less than 20 x ring web thickness, T(4)(RNG))
1. $-V(11)^1 + 20.V(13)^1 - 1$. (ring flange width, W(RNG), is less than 20 x ring flange thickness, T(5)(RNG))
1. $+V(8)^1 - V(11)^1 - 1$. (ring flange width, V(11) = W(RNG), is less than ring spacing, V(8) = B(RNG))
1. $-V(1)^1 + 5.V(8)^1 - 1$. (stringer spacing, V(1) = B(STR), is less than 5 x ring spacing, V(8) = B(RNG))

Linking constraint:

There is one linking constraint: the stringer base width, B2(STR), must equal 0.1 x (stringer spacing B(STR)). In this paper the stringer base has the same thickness and properties as the skin between stringers; there are no faying flanges in any of the cases explored here.

Table 2 Definitions of variables used in the PANDA2 examples

Variable Number	Variable Name	Definition	Structural Part
1	B(STR)	stiffener spacing, b: STR	stringer
2	B2(STR)	width of stringer base, b2 (must be > 0)	stringer
3	H(STR)	height of stiffener (type H for sketch), h	stringer
4	W(STR)	width of outstanding flange of stiffener, w	stringer
5	T(1)(SKN)	thickness for layer index no.(1): SKN seg=1	panel skin
6	T(2)(STR)	thickness for layer index no.(2): STR seg=3	stringer web
7	T(3)(STR)	thickness for layer index no.(3): STR seg=4	stringer flange
8	B(RNG)	stiffener spacing, b: RNG	ring
9	B2(RNG)	width of ring base, b2 (zero is allowed)	ring
10	H(RNG)	height of stiffener (type H for sketch), h	ring
11	W(RNG)	width of outstanding flange of stiffener, w	ring
12	T(4)(RNG)	thickness for layer index no.(4):RNG seg=3	ring web
13	T(5)(RNG)	thickness for layer index no.(5):RNG seg=4	ring flange

Table 3 A typical runstream for finding a "global" optimum design with PANDA2

Command	Meaning of the command	Input file(s)	Output file(s)
panda2log	activate PANDA2 command set	.	.
begin	user provides starting design	test2.BEG	test2.OPB
setup	PANDA2 sets up matrix templates	none	many files
decide	user chooses decision variables	test2.DEC	test2.OPD
mainsetup	user chooses loading, strategy	test2.OPT	none
.	.	.	.
superopt	PANDA2 finds "global" optimum	test2.OPT	test2.OPM, -.OPP
chooseplot	user chooses what to plot	test2.CPL	test2.OPL
diplot	user obtains plot hard copies	.	test2.5.ps, etc.
.	.	.	.
superopt	PANDA2 finds "global" optimum	test2.OPT	test2.OPM, -.OPP
chooseplot	user chooses what to plot	test2.CPL	test2.OPL
diplot	user obtains plot hard copies	.	test2.5.ps, etc.
.	.	.	.
superopt	PANDA2 finds "global optimum	test2.OPT	test2.OPM, -.OPP
chooseplot	user chooses what to plot	test2.CPL	test2.OPL
diplot	user obtains plot hard copies	.	test2.5.ps, etc.
.	.	.	.
superopt	PANDA2 finds "global optimum"	test2.OPT	test2.OPM, -.OPP
chooseplot	user chooses what to plot	test2.CPL	test2.OPL
diplot	user obtains plot hard copies	.	test2.5.ps

Table 4 Optimum designs from PANDA2 suitable for analysis by STAGS (dimensions in inches)

.	Case 1 Perfect, no Koiter, ICONSV=1	Case 2 Imperfect, no Koiter, yes change imperfection amplitude, ICONSV=-1	Case 3 Imperfect, no Koiter, yes change imperfection amplitude, ICONSV=0	Case 4 Imperfect, no Koiter, yes change imperfection amplitude, ICONSV=1	Case 5 Imperfect, yes Koiter, yes change imperfection amplitude, ICONSV=1	Case 6 As if perfect, no Koiter, $N_x=6000$, $s_{bar}=120$ ksi ICONSV=1	Case 7 Imperfect, no Koiter, no change in imperfection amplitude, ICONSV=1
Variable Name	Optimum Design	Optimum Design	Optimum Design	Optimum Design	Optimum Design	Optimum Design	Optimum Design
B(STR)	0.75519	0.93500	0.93500	0.98170	0.93500	0.93500	1.5708
B2(STR)	0.075519	0.093500	0.093500	0.0981710	0.093500	0.093500	0.15708
H(STR)	0.39795	0.57079	0.58395	0.63651	0.55261	0.55330	0.92254
W(STR)	0.35593	0.38639	0.36056	0.39946	0.29593	0.36761	0.64833
T(1)(SKN)	0.030240	0.033988	0.033795	0.034878	0.039964	0.044110	0.048160
T(2)(STR)	0.019897	0.028540	0.029197	0.031826	0.027631	0.033536	0.046127
T(3)(STR)	0.022209	0.026779	0.029411	0.022835	0.032576	0.024673	0.033702
B(RNG)	6.25	9.3750	8.3333	8.3333	9.3750	8.3333	15.000
B2(RNG)	0.0	0.0	0.0	0.0	0.0	0.0	0.0
H(RNG)	0.52160	0.79425	0.75877	0.79978	0.77659	0.92137	0.86341
W(RNG)	0.17891	0.10000	0.12313	0.24075	0.31922	0.35255	1.0804
T(4)(RNG)	0.026080	0.039713	0.037939	0.040078	0.038830	0.046069	0.043170
T(5)(RNG)	0.021847	0.097842	0.086763	0.029339	0.037873	0.017627	0.054020
WEIGHT	31.81 lb	39.40 lb	40.12 lb	40.94 lb	41.89 lb	46.83 lb	56.28 lb
Critical margins from PANDA2, Table 5	1, 6a,b, 23a,b, 26, 44, 55, 56, 57, see Table 6.	1, 3, 6a,c,e, 10, 23a, 26, 47, 55, 56, 57,	1, 3, 6a,c,e, 10, 23a, 26, 47, 55, 56, 57	1, 3, 6a,d, 10, 11, 23a, 44, 25, 26, 44, 47, 55, 56, 57	1, 3, 6a,c,e, 10, 11, 23a, 25, 26, 44, 47, 55, 56, 57	1, 3, 6a,c,e, 10, 11, 23e, 25, 26, 44, 47, 55, 56, 57, 58	1, 3, 6a,c,e, 10, 11, 23e, 25, 26, 44, 47, 55, 56, 57, 58
Almost critical margins from STAGS and mode of elastic collapse	1, 6a, 44, Collapse was not computed	1, 6a, 47, Stringer sidesway and first bay collapse at PA=1.04	1, 6a, 47, Stringer sidesway and first bay collapse at PA= 1.05	1, 6a, 47, Stringer sidesway and first bay collapse at PA=1.08	1, 6a, 47, Stringer sidesway and first bay collapse at PA=1.13	1, 6a, 11, 44, 47, Axisym- metric edge collapse at PA=0.970; rv(edge)=0 on 2 curved edges.	1, 6a, 11, 47, Stringer sidesway, first,middle and last bay collapse at PA= 1.22(-) PA= 1.15(+)
Tables & Figures pertaining to the case	Table 10, Figs. 3, 33-41	Figs. 8-32		Figs. 1a-c, 2, 4-7, 42-65	Table11, Figs. 66-71	Figs. 72-74	Figs. 75-80
Comments	This shell is not practical because no one can fabricate a perfect structure.	With this option you MUST check the results via a general-purpose code such as STAGS.	With this option you are strongly URGED to check result with use of a general-purpose program.	This option may lead to shells with local skin & stringer bending & therefore possibly excessive stresses.	This is the best option if you do not plan to check PANDA2 designs. Even so, you SHOULD check them.	This widely used option generates a heavy shell. PANDA2 cannot predict axisymmetric collapse.	This option is too conservative, in my opinion. The imperfection can probably be detected easily.

Table 5 List of all possible PANDA2 margins for a T-ring and T-stringer stiffened cylindrical shell fabricated of one isotropic material. The margin numbers listed in Table 4 correspond to those listed in Column 1 below.

MARGIN NO.	MARGIN DEFINITION
1	Local buckling from discrete model-1.,M=10 axial halfwaves;FS=0.999
2	Local buckling from PANDA model, M=10 axial halfwaves;FS=0.999
3	Long-axial-wave bending-torsion buckling; M=2 ;FS=0.999
4	Bending-torsion buckling; M=2; FS=1.0
5	Local buckling from Koiter theory,M=10 axial halfwaves;FS=0.999
6a	eff.stress:matl=1,STR,Dseg=4,node=11,layer=1,z=-0.0134;MID.;FS=1.
6b	eff.stress:matl=1,STR,Dseg=3,node=1,layer=1,z=0.0143;MID.;FS=1.
6c	eff.stress:matl=1,SKN,Dseg=2,node=6,layer=1,z=0.0241;MID.;FS=1.
6d	eff.stress:matl=1,SKN,Dseg=1,node=1,layer=1,z=0.02;MID.;FS=1.
6e	eff.stress:matl=1,STR,Dseg=5,node=11,layer=1,z=0.017;RNGS;FS=1.
7	stringer popoff margin:(allowable/actual)-1, web 1 MID.;FS=1.
8	stringer popoff margin:(allowable/actual)-1, web 2 MID.;FS=1.
9	Hi-axial-wave post-post-buckling of module - 1; M=20 ;FS=1.
10	(m=2 lateral-torsional buckling load factor)/(FS)-1;FS=0.999
11	Inter-ring buckling, discrete model, n=33 circ.halfwaves;FS=0.999
12	Ring sidesway buckling, discrete model, n=4 circ.halfwaves;FS=1.0
13	Ring web buckling, discrete model, n=? circ.halfwaves;FS=1.0
14	Ring flange buckling,discrete model,n=54 circ.halfwaves;FS=1.0
15	Hi-n Inter-ring buckling,discrete model,n=? circ.halfwaves;FS=1.0
16	Hi-n Ring sidesway, discrete model,n=? circ.halfwaves;FS=1.0
17	Hi-n Ring web buckling,discrete model,n=27 circ.halfwaves;FS=1.0
18	Hi-n Ring flange buckling,discrete model,n=67 circ.halfwaves;FS=1.0
19	Lo-n Inter-ring buckling,discrete model,n=? circ.halfwaves;FS=1.0
20	Lo-n Ring sidesway, discrete model, n=7 circ.halfwaves;FS=1.0
21	Lo-n Ring web buckling, discrete model,n=? circ.halfwaves;FS=1.0
22	Lo-n Ring flange buckling,discrete model,n=? circ.halfwaves;FS=1.0
23a	eff.stress:matl=1,STR,Iseg=4,allnode,layer=1,z=0.0134;-MID.;FS=1.
23b	eff.stress:matl=1,STR,Iseg=3,at:ROOT,layer=1,z=0.;;-MID.;FS=1.
23c	eff.stress:matl=1,SKN,Iseg=2,at:n=6,layer=1,z=0.0241;-MID.;FS=1.
23d	eff.stress:matl=1,SKN,Iseg=1,at:n=1,layer=1,z=-0.017;-MID.;FS=1.
23e	eff.stress:matl=1,RNG,Iseg=4,allnode,layer=1,z=0.0978;-MID.;FS=1.
24	buckling margin stringer Iseg.3 . Local halfwaves=17 .MID.;FS=1.
25	buckling margin stringer Iseg.4 . Local halfwaves=16 .MID.;FS=1.
26	buckling stringer Isegs.3+4 together.M=13 ;C=0. ;MID.;FS=1.4
27	buckling stringer Iseg 4 as beam on foundation. M=380;MID.;FS=1.2
28	buckling(SANDERS);simple-support local buckling; (0.95*altsol);FS=1.
29	buckling(SANDERS);simple-support inter-ring; (1.00*altsol);FS=0.999
30	buckling(SANDERS);simple-support smear string;M=1;N=8;slope=25.;FS=0.999
31	buckling(SANDERS);simple-support smear rings; M=126;N=1;slope=0.02;FS=1.
32	buckling margin ring Iseg.3 . Local halfwaves=111.MID.;FS=1.
33	buckling margin ring Iseg.4 . Local halfwaves=10 .MID.;FS=1.
34	buckling ring Isegs.3+4 together.M=5 ;C=0. ;MID.;FS=1.4
35	buckling ring Iseg 4 as beam on foundation. M=349;MID.;FS=1.2
36	buckling margin stringer Iseg.3 . Local halfwaves=17 .NOPO;FS=1.
37	buckling margin stringer Iseg.4 . Local halfwaves=16 .NOPO;FS=1.
38	buckling stringer Isegs.3+4 together.M=16 ;C=0. ;NOPO;FS=1.4
39	buckling stringer Iseg 4 as beam on foundation. M=380;NOPO;FS=1.2
40	buckling margin ring Iseg.3 . Local halfwaves=111.NOPO;FS=1.
41	buckling margin ring Iseg.4.Local halfwaves=10.NOPO;FS=1.

42	buckling ring Isegs.3+4 together.M=5 ;C=0.;NOPO;FS=1.4
43	buckling ring Iseg 4 as beam on foundation. M=349;NOPO;FS=1.2
44	buckling(SANDERS);simple-support general buck;M=4;N=6;slope=0.;FS=0.999
45	buckling load factor simple-support general buck;(0.85*altsol)
46	buckling(SANDERS);rolling with smeared stringers; M=1;N=24;slope=0.;FS=0.999
46b	buckling(SANDERS);rolling with smeared rings; M=119;N=1;slope=0.;FS=0.999
47	buckling(SANDERS);rolling only of stringers;M=20;N=0;slope=0.;FS=1.4
48	buckling(SANDERS);hiwave rolling of stringers;M=148;N=0;slope=0.;FS=1.2
49	buckling(SANDERS);hiwave rolling of rings; M=0,N=121;slope=0.;FS=1.2
50	buckling(SANDERS);rolling only axisym.rings;M=0;N=0;slope=0.;FS=1.4
51	buckling(SANDERS); STRINGERS: web buckling;M=17;N=1;slope=0.01;FS=1.
52	buckling(SANDERS); RINGS: web buckling;M=101;N=1;slope=0.3285;FS=1.
53	(Max.allowable ave.axial strain)/(ave.axial strain) -1; FS=1.
54	0.3333 *(Stringer spacing, b)/(Stringer base width, b2)-1;FS=1.
55	1. -V(3)^1 +20.V(6)^1 -1. (inequality constraint)
56	1. -V(4)^1 +20.V(7)^1 -1. (inequality constraint)
57	1. -V(10)^1 +20.V(12)^1 -1. (inequality constraint)
58	1. -V(11)^1 +20.V(13)^1 -1. (inequality constraint)
59	1. +V(8)^1 -V(11)^1 -1. (inequality constraint)
60	1. -V(1)^1 +5.V(8)^1 -1. (inequality constraint)

“SANDERS” means that Sanders’ shell equations [25] are used in the computations. “M” or “m” is the number of axial halfwaves; “N” or “n” is the number of circumferential halfwaves except in Margins 23 where “n” means nodal point number in a module; “slope” is the slope of the buckling nodal lines; “FS” is the factor of safety; “STR” = stringer; “SKN” = panel skin; “RNG” = ring; “Dseg” = segment number in the discretized skin-stringer single module model (Fig. 4): Dseg=1 = panel skin in left-hand part of Fig. 4; Dseg=2 = base under the stringer where the stringer web root intersects the panel skin; Dseg=3 = stringer web; Dseg=4 = outstanding stringer flange; Dseg=5 = panel skin in right-hand part of Fig. 4. “z” is the thickness coordinate in a shell or stiffener segment wall; “MID” means “midway between rings” (same as Sub-case 1); “RNGS” means “at ring stations” (same as Sub-case 2); “Iseg” means skin-stringer or skin-ring single module segment number (PANDA-type model, not discretized module): Iseg=1 = panel skin; Iseg=2 = base under the stiffener (either stringer or ring); Iseg=3 = stiffener web; Iseg=4 = stiffener outstanding flange. “ROOT” means “at web root” (where a stiffener web intersects the panel skin); “allnode” means “at all nodal points in the panel skin”; “C=0” means “slope of buckling nodal lines=0”; “NOPO” means “neglecting local postbuckling effects”. “V(i)” is the ith variable. See Table 2 for definitions of the variables, V(i), i = 1 to 13.

Table 6 Margins from PANDA2 for the Case 2 design with an initial general buckling modal imperfection with initial amplitude, Wimp(initial) = (+ and -) 0.25 inch and a reduced amplitude, Wimp(reduced)=0.25/(m+dm)=0.054541 inch (see Part 1 of Table 8). Margins less than 0.3 are in bold face.

POSITIVE Wimp

ITERATION NO., LOAD SET NO., SUBCASE NO. = 0 1 1 **MIDWAY BETWEEN RINGS**

BUCKLING LOAD FACTORS FOR LOCAL BUCKLING FROM KOITER v. BOSOR4 THEORY:

Local buckling load factor from KOITER theory = 1.1123E+00

Local buckling load factor from BOSOR4 theory = 1.0140E+00

MARGINS FOR CURRENT DESIGN: LOAD CASE NO. 1, SUBCASE NO. 1

mar. margin

no. value definition

- 1 **1.50E-02 Local buckling from discrete model-1.,M=10 axial halfwaves;FS=0.99**
 - 2 **7.95E-02 Long-axial-wave bending-torsion buckling; M=2 ;FS=0.999**
 - 3 **3.58E-02 eff.stress:matl=1,STR,Dseg=4,node=11,layer=1,z=-0.0134; MID.;FS=1.**
 - 4 **1.14E-01 (m=2 lateral-torsional buckling load factor)/(FS)-1;FS=0.999**
 - 5 3.91E-01 Inter-ring buckling, discrete model, n=41 circ.halfwaves;FS=0.999
 - 6 **2.85E-02 eff.stress:matl=1,STR,Iseg=4,allnode,layer=1,z=0.0134;-MID.;FS=1.**
 - 7 7.44E-01 buckling margin stringer Iseg.3 . Local halfwaves=16 .MID.;FS=1.
 - 8 5.65E-01 buckling margin stringer Iseg.4 . Local halfwaves=16 .MID.;FS=1.
 - 9 **1.97E-01 buckling stringer Isegs.3+4 together.M=15 ;C=0. ;MID.;FS=1.4**
 - 10 3.64E+00 buckling stringer Iseg 4 as beam on foundation. M=412;MID.;FS=1.2
 - 11 1.13E+01 buckling margin ring Iseg.3 . Local halfwaves=116.MID.;FS=1.
 - 12 3.24E+01 buckling ring Iseg 4 as beam on foundation. M=228;MID.;FS=1.2
 - 13 5.62E-01 buck.(SAND);simp-support general buck;M=4;N=6;slope=0.;FS=0.999
 - 14 1.64E+01 buck.(SAND);rolling with smear rings; M=100;N=1;slope=0.;FS=0.999
 - 15 **2.22E-01 buck.(SAND);rolling only of stringers;M=16;N=0;slope=0.;FS=1.4**
 - 16 6.70E-01 buck.(SAND);hiwave roll. of stringers;M=144;N=0;slope=0.;FS=1.2
 - 17 1.28E+01 buck.(SAND);rolling only axisym.rings;M=0;N=0;slope=0.;FS=1.4
 - 18 5.68E-01 buck.(SAND); STRINGERS: web buckling;M=16;N=1;slope=0.01;FS=1.
 - 19 1.26E+01 buck.(SAND); RINGS: web buckling;M=99;N=1;slope=0.3285;FS=1.
 - 20 2.06E+02 (Max.allowable ave.axial strain)/(ave.axial strain) -1; FS=1.
 - 21 2.33E+00 0.3333 *(Stringer spacing, b)/(Stringer base width, b2)-1;FS=1.
 - 22 **0.00E+00 1.-V(3)^1+20.V(6)^1-1**
 - 23 **1.49E-01 1.-V(4)^1+20.V(7)^1-1**
 - 24 **-5.96E-08 1.-V(10)^1+20.V(12)^1-1**
 - 25 1.86E+00 1.-V(11)^1+20.V(13)^1-1
 - 26 9.89E-01 1.+V(8)^1-V(11)^1-1
-

POSITIVE Wimp

ITERATION NO., LOAD SET NO., SUBCASE NO. = 0 1 2 **AT RINGS**

BUCKLING LOAD FACTORS FOR LOCAL BUCKLING FROM KOITER v. BOSOR4 THEORY:

Local buckling load factor from KOITER theory = 1.1455E+00

Local buckling load factor from BOSOR4 theory = 1.0220E+00

MARGINS FOR CURRENT DESIGN: LOAD CASE NO. 1, SUBCASE NO. 2

mar. margin

no. value definition

- 1 **2.31E-02 Local buckling from discrete model-1.,M=10 axial halfwaves;FS=0.99**
- 2 **2.70E-02 Long-axial-wave bending-torsion buckling; M=2 ;FS=1.**
- 3 **-1.85E-02 eff.stress:matl=1,STR,Dseg=4,node=11,layer=1,z=-0.0134; RNGS;FS=1.**
- 4 **7.45E-02 (m=2 lateral-torsional buckling load factor)/(FS)-1;FS=0.999**
- 5 8.15E-01 Inter-ring buckling, discrete model, n=34 circ.halfwaves;FS=0.999

6 -3.84E-02 eff.stress:matl=1,STR,Iseg=4,allnode,layer=1,z=-0.0134;-RNGS;FS=1.
 7 7.12E-01 buckling margin stringer Iseg.3 . Local halfwaves=16 .RNGS;FS=1.
 8 4.85E-01 buckling margin stringer Iseg.4 . Local halfwaves=16 .RNGS;FS=1.
9 1.60E-01 buckling stringer Isegs.3+4 together.M=15 ;C=0. ;RNGS;FS=1.4
 10 3.40E+00 buckling stringer Iseg 4 as beam on foundation. M=412;RNGS;FS=1.2
 11 1.17E+01 buckling margin ring Iseg.3 . Local halfwaves=116.RNGS;FS=1.
 12 3.29E+01 buckling ring Iseg 4 as beam on foundation. M=228;RNGS;FS=1.2
 13 1.63E+01 buck.(SAND);rolling with smear rings; M=100;N=1;slope=0.;FS=0.999
14 1.71E-01 buck.(SAND);rolling only of stringers;M=16;N=0;slope=0.;FS=1.4
 15 6.02E-01 buck.(SAND);hiwave roll. of stringers;M=144;N=0;slope=0.;FS=1.2
 16 1.30E+01 buck.(SAND);rolling only axisym.rings;M=0;N=0;slope=0.;FS=1.4
 17 5.43E-01 buck.(SAND); STRINGERS: web buckling;M=16;N=1;slope=0.01;FS=1.
 18 1.32E+01 buck.(SAND); RINGS: web buckling;M=99;N=1;slope=0.335;FS=1.
 19 2.08E+02 (Max.allowable ave.axial strain)/(ave.axial strain) -1; FS=1.

NEGATIVE Wimp

ITERATION NO., LOAD SET NO., SUBCASE NO. = 0 2 1 MIDWAY BETWEEN RINGS
 BUCKLING LOAD FACTORS FOR LOCAL BUCKLING FROM KOITER v. BOSOR4 THEORY:

Local buckling load factor from KOITER theory = 9.6089E-01

Local buckling load factor from BOSOR4 theory = 9.8060E-01

MARGINS FOR CURRENT DESIGN: LOAD CASE NO. 2, SUBCASE NO. 1

mar. margin

no. value definition

1 -1.84E-02 Local buckling from discrete model-1.,M=11 axial halfwaves;FS=0.99
 2 7.36E-01 Long-axial-wave bending-torsion buckling; M=2 ;FS=0.999
3 9.65E-02 eff.stress:matl=1,SKN,Dseg=2,node=6,layer=1,z=0.017; MID.;FS=1.
 4 7.55E-01 (m=2 lateral-torsional buckling load factor)/(FS)-1;FS=0.999
 5 8.16E-01 Inter-ring buckling, discrete model, n=32 circ.halfwaves;FS=0.999
6 2.85E-02 eff.stress:matl=1,STR,Iseg=4,allnode,layer=1,z=0.0134;-MID.;FS=1.
 7 9.57E-01 buckling margin stringer Iseg.3 . Local halfwaves=16 .MID.;FS=1.
 8 1.53E+00 buckling margin stringer Iseg.4 . Local halfwaves=16 .MID.;FS=1.
 9 5.21E-01 buckling stringer Isegs.3+4 together.M=15 ;C=0. ;MID.;FS=1.4
 10 6.49E+00 buckling stringer Iseg 4 as beam on foundation. M=412;MID.;FS=1.2
 11 1.13E+01 buckling margin ring Iseg.3 . Local halfwaves=116.MID.;FS=1.
 12 3.24E+01 buckling ring Iseg 4 as beam on foundation. M=228;MID.;FS=1.2
 13 5.62E-01 buck.(SAND);simp-support general buck;M=4;N=6;slope=0.;FS=0.999
 14 1.71E+01 buck.(SAND);rolling with smear rings; M=103;N=1;slope=0.;FS=0.999
 15 7.55E-01 buck.(SAND);rolling only of stringers;M=16;N=0;slope=0.;FS=1.4
 16 1.37E+00 buck.(SAND);hiwave roll. of stringers;M=144;N=0;slope=0.;FS=1.2
 17 1.28E+01 buck.(SAND);rolling only axisym.rings;M=0;N=0;slope=0.;FS=1.4
 18 7.44E-01 buck.(SAND); STRINGERS: web buckling;M=16;N=1;slope=0.01;FS=1.
 19 1.26E+01 buck.(SAND); RINGS: web buckling;M=99;N=1;slope=0.3285;FS=1.
 20 2.06E+02 (Max.allowable ave.axial strain)/(ave.axial strain) -1; FS=1.

NEGATIVE Wimp

ITERATION NO., LOAD SET NO., SUBCASE NO. = 0 2 2 AT RINGS

BUCKLING LOAD FACTORS FOR LOCAL BUCKLING FROM KOITER v. BOSOR4 THEORY:

Local buckling load factor from KOITER theory = 9.8706E-01

Local buckling load factor from BOSOR4 theory = 9.8925E-01

MARGINS FOR CURRENT DESIGN: LOAD CASE NO. 2, SUBCASE NO. 2

mar. margin

no. value definition

1 -9.76E-03 Local buckling from discrete model-1.,M=11 axial halfwaves;FS=0.99

2 6.03E-01 Long-axial-wave bending-torsion buckling; M=2 ;FS=1.
 3 **1.32E-01 eff.stress:matl=1,STR,Dseg=5,node=11,layer=1,z=0.017; RNGS;FS=1.**
 4 6.57E-01 (m=2 lateral-torsional buckling load factor)/(FS)-1;FS=0.999
 5 3.90E-01 Inter-ring buckling, discrete model, n=40 circ.halfwaves;FS=0.999
 6 **-3.84E-02 eff.stress:matl=1,STR,Iseg=4,allnode,layer=1,z=-0.0134; RNGS;FS=1.**
 7 9.17E-01 buckling margin stringer Iseg.3 . Local halfwaves=16 .RNGS;FS=1.
 8 1.33E+00 buckling margin stringer Iseg.4 . Local halfwaves=16 .RNGS;FS=1.
 9 4.62E-01 buckling stringer Isegs.3+4 together.M=15 ;C=0. ;RNGS;FS=1.4
 10 5.89E+00 buckling stringer Iseg 4 as beam on foundation. M=412;RNGS;FS=1.2
 11 1.17E+01 buckling margin ring Iseg.3 . Local halfwaves=116.RNGS;FS=1.
 12 3.29E+01 buckling ring Iseg 4 as beam on foundation. M=228;RNGS;FS=1.2
 13 1.70E+01 buck.(SAND);rolling with smear rings; M=103;N=1;slope=0.;FS=0.999
 14 6.52E-01 buck.(SAND);rolling only of stringers;M=16;N=0;slope=0.;FS=1.4
 15 1.24E+00 buck.(SAND);hiwave roll. of stringers;M=144;N=0;slope=0.;FS=1.2
 16 1.30E+01 buck.(SAND);rolling only axisym.rings;M=0;N=0;slope=0.;FS=1.4
 17 7.13E-01 buck.(SAND); STRINGERS: web buckling;M=16;N=1;slope=0.01;FS=1.
 18 1.32E+01 buck.(SAND); RINGS: web buckling;M=99;N=1;slope=0.335;FS=1.
 19 2.08E+02 (Max.allowable ave.axial strain)/(ave.axial strain) -1; FS=1.
 **** ALL 2 LOAD SETS PROCESSED ****

SUMMARY OF INFORMATION FROM OPTIMIZATION ANALYSIS

var. no.	dec. var.	escape var.	link. var.	linked to	linking constant	lower bound	current value	upper bound	definition
1	N	N	N	0	0.00	0.00	9.3500E-01	0.00	B(STR) (*)
2	N	N	N	0	0.00	0.00	9.3500E-02	0.00	B2(STR)
3	Y	N	N	0	0.00	1.00E-01	5.7079E-01	5.00	H(STR)
4	Y	N	N	0	0.00	1.00E-01	3.8639E-01	5.00	W(STR)
5	Y	Y	N	0	0.00	1.00E-02	3.3988E-02	1.00	T(1)(SKN)
6	Y	Y	N	0	0.00	1.00E-02	2.8540E-02	1.00	T(2)(STR)
7	Y	Y	N	0	0.00	1.00E-02	2.6779E-02	1.00	T(3)(STR)
8	N	N	N	0	0.00	0.00	9.3750E+00	0.00	B(RNG) (*)
9	N	N	N	0	0.00	0.00	0.0000E+00	0.00	B2(RNG)
10	Y	N	N	0	0.00	1.00E-01	7.9425E-01	5.00	H(RNG)
11	Y	N	N	0	0.00	1.00E-01	1.0000E-01	5.00	W(RNG)
12	Y	Y	N	0	0.00	1.00E-02	3.9713E-02	1.00	T(4)(RNG)
13	Y	Y	N	0	0.00	1.00E-02	9.7842E-02	1.00	T(5)(RNG)

(*) B(STR) and B(RNG) are not decision variables for STAGS-compatible models. During **initial** optimization both B(STR) and B(RNG) **are** decision variables. Then the lower bound of B(STR)=0.935 inch in all cases except for Case 1 (perfect shell), for which it is B(STR) = 0.500 inch. The lower bound of B(RNG) = 2.0 inches. The upper bounds of B(STR) and B(RNG) are 30.0 and 25.0 inches, respectively.

CURRENT VALUE OF THE OBJECTIVE FUNCTION:

var. no.	str/ seg. rng	layer no.	current value	definition
0	0	3.940E+01		Weight of the entire panel (180 deg. of cyl. shell)
TOTAL WEIGHT OF SKIN=				2.0021E+01
TOTAL WEIGHT OF SUBSTIFFENERS=				0.0000E+00
TOTAL WEIGHT OF STRINGERS=				1.6782E+01
TOTAL WEIGHT OF RINGS=				2.5966E+00
SPECIFIC WEIGHT (WEIGHT/AREA) OF STIFFENED PANEL=				6.6885E-03
***** END OF test2.OPM FILE *****				

Table 7 Margins from PANDA2 for the Case 2 design with the general buckling imperfection amplitude Wimp set equal to zero. (Margins less than 0.3 are in bold face).

ITERATION NO., LOAD SET NO., SUBCASE NO. = 0 1 2 MIDWAY BETWEEN RINGS		
BUCKLING LOAD FACTORS FOR LOCAL BUCKLING FROM KOITER v. BOSOR4 THEORY:		
Local buckling load factor from KOITER theory = 1.0616E+00		
Local buckling load factor from BOSOR4 theory = 1.0625E+00		
MARGINS FOR CURRENT DESIGN: LOAD CASE NO. 1, SUBCASE NO. 1		
mar. margin		
no.	value	definition
1	6.36E-02 Local buckling from discrete model-1.,M=11 axial halfwaves;FS=0.99	
2	3.78E-01 Long-axial-wave bending-torsion buckling; M=2 ;FS=0.999	
3	2.45E-01 eff.stress:matl=1,STR,Dseg=3,node=1,layer=1,z=0.0143; MID.;FS=1.	
4	4.07E-01 (m=2 lateral-torsional buckling load factor)/(FS)-1;FS=0.999	
5	9.05E-01 Inter-ring buckling, discrete model, n=26 circ.halfwaves;FS=0.999	
6	2.45E-01 eff.stress:matl=1,STR,Iseg=3,at:ROOT,layer=1,z=0.:-MID.;FS=1.	
7	8.55E-01 buckling margin stringer Iseg.3 . Local halfwaves=16 .MID.;FS=1.	
8	9.34E-01 buckling margin stringer Iseg.4 . Local halfwaves=16 .MID.;FS=1.	
9	3.40E-01 buckling stringer Isegs.3+4 together.M=15 ;C=0. ;MID.;FS=1.4	
10	4.73E+00 buckling stringer Iseg 4 as beam on foundation. M=412;MID.;FS=1.2	
11	8.90E-01 buck.(SAND);simp-support general buck;M=4;N=6;slope=0.;FS=0.999	
12	1.76E+01 buck.(SAND);rolling with smear rings; M=103;N=1;slope=0.;FS=0.999	
13	4.92E-01 buck.(SAND);rolling only of stringers;M=16,N=0;slope=0.;FS=1.4	
14	1.04E+00 buck.(SAND);hiwave roll. of stringers;M=144;N=0;slope=0.;FS=1.2	
15	8.49E-01 buck.(SAND); STRINGERS: web buckling;M=16;N=1;slope=0.;FS=1.	
16	2.06E+02 (Max.allowable ave.axial strain)/(ave.axial strain) -1; FS=1.	
17	2.33E+00 0.3333 *(Stringer spacing, b)/(Stringer base width, b2)-1;FS=1.	
18	1.00E-05 1.-V(3)^1+20.V(6)^1-1	
19	1.49E-01 1.-V(4)^1+20.V(7)^1-1	
20	1.00E-05 1.-V(10)^1+20.V(12)^1-1	
21	1.86E+00 1.-V(11)^1+20.V(13)^1-1	
22	9.89E-01 1.+V(8)^1-V(11)^1-1	

ITERATION NO., LOAD SET NO., SUBCASE NO. = 0 1 2 **AT RINGS**

BUCKLING LOAD FACTORS FOR LOCAL BUCKLING FROM KOITER v. BOSOR4 THEORY:

Local buckling load factor from KOITER theory = 1.0928E+00

Local buckling load factor from BOSOR4 theory = 1.0719E+00

MARGINS FOR CURRENT DESIGN: **LOAD CASE NO. 1, SUBCASE NO. 2**

mar. margin

no. value

definition

1	7.29E-02 Local buckling from discrete model-1.,M=11 axial halfwaves;FS=0.99
2	2.91E-01 Long-axial-wave bending-torsion buckling; M=2 ;FS=1.
3	2.05E-01 eff.stress:matl=1,STR,Dseg=4,node=11,layer=1,z=-0.0134; RNGS;FS=1.
4	3.41E-01 (m=2 lateral-torsional buckling load factor)/(FS)-1;FS=0.999
5	9.05E-01 Inter-ring buckling, discrete model, n=26 circ.halfwaves;FS=0.999
6	1.83E-01 eff.stress:matl=1,STR,Iseg=4,allnode,layer=1,z=-0.0134;-RNGS;FS=1.
7	8.19E-01 buckling margin stringer Iseg.3 . Local halfwaves=16 .RNGS;FS=1.
8	8.13E-01 buckling margin stringer Iseg.4 . Local halfwaves=16 .RNGS;FS=1.
9	2.94E-01 buckling stringer Isegs.3+4 together.M=15 ;C=0. ;RNGS;FS=1.4
10	4.37E+00 buckling stringer Iseg 4 as beam on foundation. M=412;RNGS;FS=1.2
11	1.75E+01 buck.(SAND);rolling with smear rings; M=103;N=1;slope=0.;FS=0.999
12	4.16E-01 buck.(SAND);rolling only of stringers;M=16,N=0;slope=0.;FS=1.4
13	9.36E-01 buck.(SAND);hiwave roll. of stringers;M=144;N=0;slope=0.;FS=1.2
14	7.66E-01 buck.(SAND); STRINGERS: web buckling;M=16;N=1;slope=0.;FS=1.
15	2.08E+02 (Max.allowable ave.axial strain)/(ave.axial strain) -1; FS=1.

Table 8 PANDA2 results for Case 2 in Table 4 pertaining to amplitude reduction of the general buckling modal imperfection and prebuckling bending and twisting, Wxx, Wyy, Wxy, of the imperfect cylindrical shell including and not including “fractional” wave numbers. Margins less than 0.3 are in bold face.

PART 1: Fractional wave numbers ARE permitted:

*** NOTE: The number of circ. halfwaves in the general buckling mode of the PERFECT panel is less than or equal to that for the IMPERFECT panel. Therefore, the IMPERFECT panel mode is used for computation of deformations Wxx, Wyy, Wxy in SUBROUTINE CURIMP.

General buckling mode for the PERFECT panel (PANDA theory):

(m= 5, dm= -4.80E-01, n= 6, dn= 1.45E-01, slope= 0.00E+00, ICD91= 1)

General buckling mode for the IMPERFECT panel (PANDA theory):

(m= 5, dm= -4.16E-01, n= 6, dn= 2.01E-01, slope= 0.00E+00 ICD9= 1)

(0.1 radian)/(shell wall rotation), AMPTST = 1.6126E+00

General imperfection amplitude is modified because the critical buckling mode has a shorter axial halfwavelength than that specified by the user: AXLINP= 7.5000E+01
 Critical buckling mode axial halfwavelength, AXLTST= 1.6362E+01
 Imperfection amplitude is reduced by factor, AMPMD9= 2.1816E-01

QUANTITIES USED FOR OVERALL BENDING OF IMPERFECT PANEL

(used for generation of WXX9,WYY9,WXY9), IMOD= 0:

Amplitude of overall ovalization, WG1=	0.0000E+00
Amplitude of general buckling modal imperf. AMWIMP=	5.4541E-02
Effective load factor for general buckling, EIGEFF=	1.7046E+00
Number of axial halfwaves in general mode, m= 5	
Fractional axial halfwaves in general mode, dm= -4.1628E-01	
Number of circumferential halfwaves in general mode, n= 6	
Fractional circumferential halfwaves in general mode, dn= 2.0102E-01	
Slope of nodal lines in general buckling mode, slope=	0.0000E+00
Additional amplitude factor, FACIM3=	1.0000E+00
Original imperfection is increased by 1/(EIGEFF-1)=	1.4192E+00
Amplitude of prebuckling bending due to loading, WAMP=WIMP/(EIGEFF-1)=	-7.7403E-02 in which

WIMP = Amplitude of initial buckling modal imperfection=5.4541E-02 ↵ used for results in Table 6

***** NOTE ***** NOTE ***** NOTE *****

Prebuckling bending and twist from general imperfection growth:

Wxx9,Wyy9,Wxy9,ICD9= -2.8535E-03 -4.7621E-03 -3.6863E-03 1

BUCKLING LOAD FACTORS FOR LOCAL BUCKLING FROM KOITER v. BOSOR4 THEORY:

Local buckling load factor from KOITER theory = 1.1123E+00

Local buckling load factor from BOSOR4 theory = 1.0140E+00

MARGINS FOR CURRENT DESIGN: LOAD CASE NO. 1, SUBCASE NO. 1 (BETWEEN RINGS)

mar. margin

no. value definition

1 1.50E-02 Local buckling from discrete model-1.,M=10 axial halfwaves;FS=0.99

2 7.95E-02 Long-axial-wave bending-torsion buckling; M=2 ;FS=0.999

3 3.58E-02 eff.stress:matl=1,STR,Dseg=4,node=11,layer=1,z=-0.0134; MID.;FS=1.

4 **1.14E-01 (m=2 lateral-torsional buckling load factor)/(FS)-1;FS=0.999**
 5 3.91E-01 Inter-ring bucklng, discrete model, n=41 circ.halfwaves;FS=0.999
 6 **2.85E-02 eff.stress:matl=1,STR,Iseg=4,allnode,layer=1,z=0.0134;-MID.,FS=1.**
 7 7.44E-01 buckling margin stringer Iseg.3 . Local halfwaves=16 .MID.;FS=1.
 8 5.65E-01 buckling margin stringer Iseg.4 . Local halfwaves=16 .MID.;FS=1.
 9 **1.97E-01 buckling stringer Isegs.3+4 together.M=15 ;C=0. ;MID.;FS=1.4**
 10 3.64E+00 buckling strigner Iseg 4 as beam on foundation. M=412;MID.;FS=1.2
 11 1.13E+01 buckling margin ring Iseg.3 . Local halfwaves=116.MID.;FS=1.
 12 3.24E+01 buckling ring Iseg 4 as beam on foundation. M=228;MID.;FS=1.2
 13 5.62E-01 buck.(SAND);simp-support general buck;M=4;N=6;slope=0.;FS=0.999
 14 1.64E+01 buck.(SAND);rolling with smear rings; M=100;N=1;slope=0.;FS=0.999
 15 **2.22E-01 buck.(SAND);rolling only of stringers;M=16;N=0;slope=0.;FS=1.4**
 16 6.70E-01 buck.(SAND);hiwave roll. of stringers;M=144;N=0;slope=0.;FS=1.2
 17 1.28E+01 buck.(SAND);rolling only axisym.rings;M=0;N=0;slope=0.;FS=1.4
 18 5.68E-01 buck.(SAND); STRINGERS: web buckling;M=16;N=1;slope=0.01;FS=1.
 19 1.26E+01 buck.(SAND); RINGS: web buckling;M=99;N=1;slope=0.3285;FS=1.
 20 2.06E+02 (Max.allowable ave.axial strain)/(ave.axial strain) -1; FS=1.
 21 2.33E+00 0.3333 *(Stringer spacing, b)/(Stringer base width, b2)-1;FS=1.
 22 **0.00E+00 1.-V(3)^1+20.V(6)^1-1**
 23 **1.49E-01 1.-V(4)^1+20.V(7)^1-1**
 24 **-5.96E-08 1.-V(10)^1+20.V(12)^1-1**
 25 1.86E+00 1.-V(11)^1+20.V(13)^1-1
 26 9.89E-01 1.+V(8)^1-V(11)^1-1

PART 2: Fractional wave numbers ARE NOT permitted:

General buckling mode for the PERFECT panel (PANDA theory):
 (m= 4, dm= 0.00E+00, n= 6, dn= 0.00E+00, slope= 0.00E+00, ICD91= 1)

General buckling mode for the IMPERFECT panel (PANDA theory):
 (m= 4, dm= 0.00E+00, n= 6, dn= 0.00E+00, slope= 0.00E+00 ICD9= 1)

(0.1 radian)/(shell wall rotation), AMPTST = 1.6667E+00

General imperfection amplitude is modified because the critical buckling mode has a shorter axial halfwavelength than that specified by the user: AXLINP= 7.5000E+01
 Critical buckling mode axial halfwavelength,AXLTST= 1.8750E+01
 Imperfection amplitude is reduced by factor,AMPMD9= 2.5000E-01

QUANTITIES USED FOR OVERALL BENDING OF IMPERFECT PANEL

(used for generation of WXX9,WYY9,WXY9), IMOD= 0:

Amplitude of overall ovalization, WG1=	0.0000E+00
Amplitude of general buckling modal imperf.,AMWIMP=	6.2500E-02
Effective load factor for general buckling, EIGEFF=	1.6848E+00
Number of axial halfwaves in general mode, m= 4	
Fractional axial halfwaves in general mode, dm= 0.0000E+00	
Number of circumferential halfwaves in general mode, n= 6	
Fractional circumferential halfwaves in general mode, dn= 0.0000E+00	
Slope of nodal lines in general bucklng mode,slope=	0.0000E+00
Additional amplitude factor, FACIM3=	1.0000E+00
Original imperfection is increased by 1/(EIGEFF-1)=	1.4603E+00
Amplitude of prebuckling bending due to loading, WAMP=WIMP/(EIGEFF-1)=	-9.1269E-02 in which

WIMP = Amplitude of initial buckling modal imperfection=6.2500E-02 ↵ used in STAGS models

***** NOTE ***** NOTE ***** NOTE *****

Prebuckling bending and twist from general imperfection growth:

Wxx9,Wyy9,Wxy9,ICD9= -2.5623E-03 -5.2571E-03 -3.6701E-03 1

BUCKLING LOAD FACTORS FOR LOCAL BUCKLING FROM KOITER v. BOSOR4 THEORY:

Local buckling load factor from KOITER theory = 1.0955E+00

Local buckling load factor from BOSOR4 theory = 1.0078E+00

MARGINS FOR CURRENT DESIGN: LOAD CASE NO. 1, SUBCASE NO. 1 (BETWEEN RINGS)

mar. margin

no. value definition

- 1 8.77E-03 Local buckling from discrete model-1.,M=10 axial halfwaves;FS=0.99**
- 2 8.67E-02 Long-axial-wave bending-torsion buckling; M=2 ;FS=0.999**
- 3 5.87E-02 eff.stress:matl=1,STR,Dseg=4,node=11,layer=1,z=-0.0134; MID.;FS=1.**
- 4 1.22E-01 (m=2 lateral-torsional buckling load factor)/(FS)-1;FS=0.999**
- 5 3.46E-01 Inter-ring buckling, discrete model, n=41 circ.halfwaves;FS=0.999
- 6 4.95E-02 eff.stress:matl=1,RNG,Iseg=4,allnode,layer=1,z=0.0978;-MID.;FS=1,**
- 7 7.58E-01 buckling margin stringer Iseg.3 . Local halfwaves=16 .MID.;FS=1.
- 8 5.99E-01 buckling margin stringer Iseg.4 . Local halfwaves=16 .MID.;FS=1.
- 9 2.12E-01 buckling stringer Iseg.3+4 together.M=15 ;C=0. ;MID.;FS=1.4**
- 10 3.74E+00 buckling stringer Iseg 4 as beam on foundation. M=412;MID.;FS=1.2
- 11 8.65E+00 buckling margin ring Iseg.3 . Local halfwaves=107.MID.;FS=1.
- 12 2.78E+01 buckling ring Iseg 4 as beam on foundation. M=228;MID.;FS=1.2
- 13 5.27E-01 buck.(SAND);simp-support general buck;M=4;N=6;slope=0.;FS=0.999
- 14 1.66E+01 buck.(SAND);rolling with smear rings; M=103;N=1;slope=0.;FS=0.999
- 15 2.47E-01 buck.(SAND);rolling only of stringers;M=16;N=0;slope=0.;FS=1.4**
- 16 7.04E-01 buck.(SAND);hiwave roll. of stringers;M=144;N=0;slope=0.;FS=1.2
- 17 1.05E+01 buck.(SAND);rolling only axisym.rings;M=0;N=0;slope=0.;FS=1.4
- 18 5.96E-01 buck.(SAND); STRINGERS: web buckling;M=16;N=1;slope=0.01;FS=1.
- 19 9.64E+00 buck.(SAND); RINGS: web buckling;M=99;N=1;slope=0.2848;FS=1.
- 20 2.06E+02 (Max.allowable ave.axial strain)/(ave.axial strain) -1; FS=1.
- 21 2.33E+00 0.3333 *(Stringer spacing, b)/(Stringer base width, b2)-1;FS=1.
- 22 1.00E-05 1.-V(3)^1+20.V(6)^1-1**
- 23 1.49E-01 1.-V(4)^1+20.V(7)^1-1**
- 24 1.00E-05 1.-V(10)^1+20.V(12)^1-1**
- 25 1.86E+00 1.-V(11)^1+20.V(13)^1-1
- 26 9.89E-01 1.+V(8)^1-V(11)^1-1

Table 9 Sequence of STAGS runs to obtain the best STAGS model, to obtain the critical general buckling modal imperfection shape, and to obtain nonlinear static and dynamic response and elastic collapse of an imperfect shell previously optimized by PANDA2. This table corresponds to Case 2 in Table 4. The same strategy applies to most of the cases in Table 4.

PART 1: First determine the best STAGS model:

Run 1, 360 degrees: All the stiffeners are smeared, ILIN = 0 (**Fig. 16**)

Run 2, 360 degrees: The stringers are smeared and the rings are modeled as shell units, ILIN=0 (**Figs. 17,18**)

Run 3, 60 degrees: All the stiffeners are modeled as shell units. The nodal point spacing is uniform. (**Fig. 19**)

Run 4, Subdomain model with 4 stringer bays and 3 ring bays (**Fig. 20a**)

Runs 5, 6, 7, Same model as Run 3. Attempts to find the critical general buckling mode and load factor. (**Fig. 21a**)

Run 8, 60 degrees with a high-nodal-point-density “patch” to capture local buckling (**Fig. 22**)

Run 9, Subdomain model with 6 stringer bays and 1 ring bay with dense mesh for accurate local buckling (**Fig. 23a**)

PART 2: Now that we have the “best” STAGS model, start the numbering of STAGS runs from Run 1 again, and find the critical general buckling mode. This general buckling mode shape will be used as an imperfection in nonlinear static and dynamic runs to be executed later.

The following 5 runs (called Run 1 – Run 5) are based on the 60-degree, full 75-inch length model in which all stiffeners are shell units and the nodal point spacing is nonuniform. The STAGS model is shown in **Fig. 22**. Various eigenvalue "shifts" are used during this somewhat tedious search for the critical general buckling mode, which is to be used as an initial imperfection in the nonlinear STAGS runs.

Run 1, linear buckling analysis (INDIC=1)

Eigenvalue shift = 1.8968, 616 roots skipped. (The eigenvalue shift, 1.8968, is obtained from a previous similar model (**Fig. 21a**) with uniform nodal point spacing). The following (edited) list consists of selected STAGS output from the *.out2 file, with some additional information (columns headed “Root” and “Comment”).

Maximum number of iterations.

Convergence has been obtained for eigenvalues 1 through 1.

Convergence criterion has not been satisfied for eigenvalues 2 through 8.

No.	Eigenvalue	Load system A	Load system B	@dof	Root	Comment
1	1.893834	1.893834	0.000000	62585	612	
2	1.895507	1.895507	0.000000	227501	613	
3	1.895810	1.895810	0.000000	62603	614	
4	1.896212	1.896212	0.000000	183969	615	
5	1.896565	1.896565	0.000000	100793	----	not converged
6	1.896667	1.896667	0.000000	71201	616	
7	1.897358	1.897358	0.000000	94981	617	
8	1.897376	1.897376	0.000000	63517	618	

Run 2, linear buckling analysis (INDIC=1)

shift=1.90, 618 roots skipped

Convergence has been obtained for eigenvalues 1 through 8.

No.	Eigenvalue	Load system A	Load system B	@dof	Root
1	1.895810	1.895810	0.000000	62075	614
2	1.896212	1.896212	0.000000	183969	615
3	1.896667	1.896667	0.000000	71201	616
4	1.897358	1.897358	0.000000	94981	617
5	1.897376	1.897376	0.000000	63517	618
6	1.900049	1.900049	0.000000	79273	619
7	1.900987	1.900987	0.000000	223021	620
8	1.904193	1.904193	0.000000	168237	621

Run 3, linear buckling analysis (INDIC=1)

shift=1.91, 630 roots skipped

Convergence has been obtained for eigenvalues 1 through 8.

No.	Eigenvalue	Load system A	Load system B	@dof	Root	Comment
1	1.907943	1.907943	0.000000	173449	626	general buckling, m=5
2	1.908666	1.908666	0.000000	199677	627	
3	1.909261	1.909261	0.000000	231434	628	
4	1.909594	1.909594	0.000000	215385	629	
5	1.909723	1.909723	0.000000	84509	630	
6	1.911136	1.911136	0.000000	170661	631	
7	1.911490	1.911490	0.000000	221413	632	
8	1.912301	1.912301	0.000000	220621	633	

Run 4, linear buckling analysis (INDIC=1)

shift=1.906, 622 roots skipped

Convergence has been obtained for eigenvalues 1 through 8.

No.	Eigenvalue	Load system A	Load system B	@dof	Root	Comment
1	1.904193	1.904193	0.000000	168237	621	"dirty" general buckling
2	1.904860	1.904860	0.000000	199677	622	
3	1.906620	1.906620	0.000000	138253	623	
4	1.906628	1.906628	0.000000	62897	624	
5	1.907084	1.907084	0.000000	79369	625	
6	1.907943	1.907943	0.000000	173449	626	
7	1.908666	1.908666	0.000000	199677	627	
8	1.909262	1.909262	0.000000	231434	628	general buckling,m=5 (not the most critical mode)

Run 5, linear buckling analysis (INDIC=1)

shift=1.890, 606 roots skipped

Maximum number of iterations.

Convergence has been obtained for eigenvalues 1 through 2.

Convergence criterion has not been satisfied for eigenvalues 3 through 8.

No.	Eigenvalue	Load system A	Load system B	@dof	Root	Comment
1	1.886592	1.886592	0.000000	229507	604	not converged
2	1.886870	1.886870	0.000000	59469	605	
3	1.889596	1.889596	0.000000	116021	606	
4	1.890916	1.890916	0.000000	144445	607	
5	1.890947	1.890947	0.000000	144445	----	
6	1.892042	1.892042	0.000000	20415	608	
7	1.892399	1.892399	0.000000	210533	609	
8	1.893075	1.893075	0.000000	29889	610	general buckling, m=4 (the critical buckling mode, Fig. 24)

PART 3: Next, we wish to "reset" the run number to Run 1 again. We now know EXACTLY what the eigenvalue "shift" should be to capture **only** the most critical general buckling mode. Do the following: Set shift in test2.bin file to 1.893075, copy test2.bin to temp.bin, copy test2.inp to temp.inp, erase all test2 files, copy temp.bin to test2.bin, copy temp.inp to test2.inp, and run STAGS in the linear buckling mode one more time to obtain just one eigenvalue, the eigenvalue closest to the shift = 1.893075.)

The test2.bin file for linear buckling:

```
test2 stags input for stiffened cyl.(stagsunit=shell units)
1, $ INDIC=1 is bifur.buckling; INDIC=3 is nonlinear BEGIN B-1
1, $ IPOST=1 means save displacements every IPOSTth step
0, $ ILIST =0 means normal batch-oriented output
0, $ ICOR =0 means projection in; 1 means not in.
1, $ IMPTHE=index for imperfection theory.
0, $ ICHIST=index for crack archive option
0, $ IFLU =0 means no fluid interaction.
-1 $ ISOLVR=0 means original solver; -1 new solver.END B-1 rec
```

1.000E+00, \$ STLD(1) = starting load factor, System A. BEGIN C-1 rec.
 0.000E+00, \$ STEP(1) = load factor increment, System A
 1.000E+00, \$ FACM(1) = maximum load factor, System A
 0.000E+00, \$ STLD(2) = starting load factor, System B
 0.000E+00, \$ STEP(2) = load factor increment, System B
 0.000E+00, \$ FACM(2) = maximum load factor, System B
 0 \$ ITEMP =0 means no thermal loads. END C-1 rec.
 10000, \$ NSEC= number of CPU seconds before run termination
 0., \$ DELEV is eigenvalue error tolerance (0=.00001)
 0 \$ IPRINT=0 means print modes, iteration data, END D-2 rec.
 1, \$ NEIGS= number of eigenvalues sought. BEGIN D-3 rec.
1.893075, \$ SHIFT=initial eigenvalue shift
 0.000E+00, \$ EIGA =lower bound of eigenvalue range
 0.000E+00 \$ EIGB =upper bound of eigenvalue range. END D-3 rec.

PART 4: The new Run 1, linear buckling analysis (INDIC=1).

(Starting the STAGS run sequence over now that we know EXACTLY what eigenvalue "shift" to use to get only the lowest general buckling mode).

Results from the new Run 1:

Convergence has been obtained for eigenvalues 1 through 1.

No.	Eigenvalue	Load system A	Load system B	@dof	Root	Comment
1	1.893075	1.893075	0.000000	29889	610	general buckling

(Use **acread** to check that this mode is indeed the general buckling mode displayed in Fig. 24).

PART 5: Run 2, nonlinear static equilibrium analysis (INDIC=3) of imperfect shell with the following imperfection in the test2.inp file:

C Begin B-4, B-5 input data, if any...

-0.0625 0 1 1 \$ WIMPFA, ISTEP, IMODE, IRUN (imperf.1) B-5

The test2.bin file is given by:

optimized imperfect shell, nonlinear theory (INDIC=3)
3, \$ INDIC=1 is bifur.buckling; INDIC=3 is nonlinear BEGIN B-1
 1, \$ IPOST=1 means save displacements every IPOSTth step
 0, \$ ILIST =0 means normal batch-oriented output
 0, \$ ICOR =0 means projection in; 1 means not in.
 1, \$ IMPTHE=index for imperfection theory.
 0, \$ IOPTIM=0 means bandwith optimization will be performed
 0, \$ IFLU =0 means no fluid interaction.
 -1 \$ ISOLVR= 0 means original solver; -1 new solver.END B-1 rec
5.000E-02, \$ STLD(1) = starting load factor, System A. BEGIN C-1 rec.
5.000E-02, \$ STEP(1) = load factor increment, System A
1.000E+00, \$ FACM(1) = maximum load factor, System A
 0.000E+00, \$ STLD(2) = starting load factor, System B
 0.000E+00, \$ STEP(2) = load factor increment, System B
 0.000E+00, \$ FACM(2) = maximum load factor, System B
 0 \$ ITEMP =0 means no thermal loads. END C-1 rec.
 0, \$ ISTART=restart from ISTARTth load step. BEGIN D-1 rec.
 20000,\$ NSEC= number of CPU seconds before run termination
 10,\$ NCUT = number of times step size may be cut
 -20, \$ NEWT = number of refactorings allowed
 -1,\$ NSTRAT=-1 means path length used as independent parameter
 0.0001,\$ DELX=convergence tolerance
 0. \$ WUND = 0 means initial relaxation factor =1.END D-1 rec.
 0, **6**, 0 \$ NPATH=0: Riks method, NEIGS=no.of eigs, NSOL=0: contin. ET-1

PART 6: Results from Run 2 (1 Wimp, static, nonlinear equilibrium, INDIC=3, from test2.out2):

List of load steps and load factors

STEP	PA	PB	COMMENT
0	0.500000E-01	0.000000E+00	
1	0.500000E-01	0.000000E+00	
2	0.100000E+00	0.000000E+00	
3	0.137483E+00	0.000000E+00	
4	0.193674E+00	0.000000E+00	
5	0.277865E+00	0.000000E+00	
6	0.403850E+00	0.000000E+00	
7	0.591702E+00	0.000000E+00	
8	0.867935E+00	0.000000E+00	
9	0.934206E+00	0.000000E+00	
10	0.967124E+00	0.000000E+00	
11	0.975400E+00	0.000000E+00	
12	0.977844E+00	0.000000E+00	
13	0.978832E+00	0.000000E+00	
14	0.978891E+00	0.000000E+00	maximum load
15	0.978171E+00	0.000000E+00	Riks path reversal
16	0.974853E+00	0.000000E+00	Riks path reversal [23]

(Figure 25 shows the stress distribution corresponding to Load Step 16: Load Factor, PA=0.974853)

Convergence has been obtained for eigenvalues 1 through 6.

No.	Eigenvalue	Load system A	Load system B	@dof	Comment
1	2.964273E-02	1.003750E+00	0.000000E+00	141277	Wimp(2) to be used in next run, Fig. 26
2	3.445293E-02	1.008439E+00	0.000000E+00	26991	Wimp(3) to be used in next run, Fig. 27
3	4.161188E-02	1.015418E+00	0.000000E+00	26019	
4	4.358378E-02	1.017340E+00	0.000000E+00	35217	
5	7.165507E-02	1.044706E+00	0.000000E+00	141277	
6	8.760331E-02	1.060253E+00	0.000000E+00	19701	

PART 7: Run 3, nonlinear static equilibrium analysis (INDIC=3) of imperfect shell with the following three imperfections in the test2.inp file:

C Begin B-4, B-5 input data, if any...

```
-0.0625 0 1 1 $ WIMPFA, ISTEP, IMODE, IRUN (imperf.1) B-5
0.0005 16 1 2 $ WIMPFA, ISTEP, IMODE, IRUN (imperf.2) B-5
0.0005 16 2 2 $ WIMPFA, ISTEP, IMODE, IRUN (imperf.3) B-5
```

The test2.bin file is the same as that listed above for Run 2. We start the loading from zero because we have two new imperfections, Wimp(2) = imperf.2 and Wimp(3) = imperf.3).

Results from Run 3 (3 Wimps, static, nonlinear equilibrium, INDIC=3, from test2.out2):

List of load steps and load factors

STEP	PA	PB	COMMENT
0	0.500000E-01	0.000000E+00	Start over from zeroth step because
1	0.500000E-01	0.000000E+00	there are two new imperfection shapes,
2	0.100000E+00	0.000000E+00	Wimp(2) = imperf.2 and Wimp(3)=imperf.3.
3	0.137483E+00	0.000000E+00	
4	0.193674E+00	0.000000E+00	
5	0.277865E+00	0.000000E+00	
6	0.403848E+00	0.000000E+00	

7	0.591696E+00	0.000000E+00
8	0.867836E+00	0.000000E+00
9	0.933520E+00	0.000000E+00
10	0.952230E+00	0.000000E+00
11	0.962920E+00	0.000000E+00
12	0.968995E+00	0.000000E+00
13	0.974678E+00	0.000000E+00
14	0.979911E+00	0.000000E+00
15	0.986198E+00	0.000000E+00
16	0.989330E+00	0.000000E+00
17	0.992391E+00	0.000000E+00
18	0.996238E+00	0.000000E+00

Continue from step 18 in next run.

(Figure 28 shows the stress distribution corresponding to Load Step 18: Load Factor, PA=0.996238)

PART 8: Run 4, nonlinear static equilibrium analysis (INDIC=3) of imperfect shell with the following imperfections in the test2.inp file. (continuation of nonlinear static Run 3, starting from Step 18):

C Begin B-4, B-5 input data, if any...

```
-0.0625 0 1 1 $ WIMPFA, ISTEP, IMODE, IRUN (imperf.1) B-5
0.0005 16 1 2 $ WIMPFA, ISTEP, IMODE, IRUN (imperf.2) B-5
0.0005 16 2 2 $ WIMPFA, ISTEP, IMODE, IRUN (imperf.3) B-5
```

Results from Run 4 (3 Wimps, static, nonlinear equilibrium, INDIC=3, from test2.out2):

List of load steps and load factors

STEP	PA	PB	COMMENT
18	0.996238E+00	0.000000E+00	last converged step, previous run
19	0.996973E+00	0.000000E+00	
20	0.998071E+00	0.000000E+00	
21	0.100031E+01	0.000000E+00	
22	0.100317E+01	0.000000E+00	
23	0.100492E+01	0.000000E+00	
24	0.100664E+01	0.000000E+00	
25	0.100825E+01	0.000000E+00	
26	0.100941E+01	0.000000E+00	
27	0.101056E+01	0.000000E+00	
28	0.101205E+01	0.000000E+00	
29	0.101283E+01	0.000000E+00	
30	0.101436E+01	0.000000E+00	
31	0.101540E+01	0.000000E+00	
32	0.101621E+01	0.000000E+00	
33	0.101723E+01	0.000000E+00	
34	0.101818E+01	0.000000E+00	
35	0.101896E+01	0.000000E+00	
36	0.101951E+01	0.000000E+00	
37	0.102020E+01	0.000000E+00	
38	0.102097E+01	0.000000E+00	
39	0.102164E+01	0.000000E+00	
40	0.102221E+01	0.000000E+00	
41	0.102264E+01	0.000000E+00	
42	0.102288E+01	0.000000E+00	
43	0.102294E+01	0.000000E+00	
44	0.102316E+01	0.000000E+00	
45	0.102354E+01	0.000000E+00	
46	0.102356E+01	0.000000E+00	

47 0.102375E+01 0.000000E+00
 48 **0.102487E+01** 0.000000E+00 **Continue from Step 48 in the next run.**

(Figure 29 shows the stress distribution corresponding to Load Step 48: Load Factor, PA=1.02487)

PART 9: Run 5, nonlinear static equilibrium analysis (INDIC=3) of imperfect shell with the following imperfections in the test2.inp file. (continuation of static Run 4, starting from Step 48):

C Begin B-4, B-5 input data, if any...
 -0.0625 0 1 1 \$ WIMPFA, ISTEP, IMODE, IRUN (imperf.1) B-5
 0.0005 16 1 2 \$ WIMPFA, ISTEP, IMODE, IRUN (imperf.2) B-5
 0.0005 16 2 2 \$ WIMPFA, ISTEP, IMODE, IRUN (imperf.3) B-5

Results from Run 5 (3 Wimps, static, nonlinear equilibrium, INDIC=3, from test2.out2):

List of load steps and load factors

STEP	PA	PB	COMMENT
48	0.102487E+01	0.000000E+00	last converged step, previous run
49	0.102486E+01	0.000000E+00	Riks path reversal?
50	0.102423E+01	0.000000E+00	
51	0.102419E+01	0.000000E+00	
52	0.102416E+01	0.000000E+00	
53	0.102420E+01	0.000000E+00	
54	0.102303E+01	0.000000E+00	
55	0.102232E+01	0.000000E+00	
56	0.102221E+01	0.000000E+00	
57	0.102166E+01	0.000000E+00	
58	0.102142E+01	0.000000E+00	
59	0.102235E+01	0.000000E+00	Riks path reversal?
60	0.102393E+01	0.000000E+00	
61	0.102410E+01	0.000000E+00	
62	0.102425E+01	0.000000E+00	
63	0.102438E+01	0.000000E+00	
64	0.102403E+01	0.000000E+00	Riks path reversal?
65	0.102191E+01	0.000000E+00	
66	0.102171E+01	0.000000E+00	
67	0.102173E+01	0.000000E+00	
68	0.102203E+01	0.000000E+00	Riks path reversal?
69	0.102297E+01	0.000000E+00	
70	0.102333E+01	0.000000E+00	Steps 49-70 accomplish nothing. Start from Step 48 in the next run.

PART 10: Run 6, nonlinear dynamic equilibrium analysis (INDIC=6) of imperfect shell with the following imperfections in the test2.inp file, starting from Step 48 with PA = 1.05):

C Begin B-4, B-5 input data, if any...
 -0.0625 0 1 1 \$ WIMPFA, ISTEP, IMODE, IRUN (imperf.1) B-5
 0.0005 16 1 2 \$ WIMPFA, ISTEP, IMODE, IRUN (imperf.2) B-5
 0.0005 16 2 2 \$ WIMPFA, ISTEP, IMODE, IRUN (imperf.3) B-5

test2.bin file for nonlinear **dynamic** run, Run 6:

test2 first transient run
6, \$ INDIC=1 is bifur.buckling; INDIC=3 is nonlinear BEGIN B-1
5, \$ IPOST=10 means save displacements every 10th step

0, \$ ILIST =0 means normal batch-oriented output
 0, \$ ICOR =0 means projection in; 1 means not in.
 0, \$ IMPTHE=index for imperfection theory.
 0, \$ IOPTIM=0 means bandwith optimization will be performed
 0, \$ IFLU =0 means no fluid interaction. END B-1 rec
 -1 \$ ISOLVR= 0 means original solver; -1 new solver.END B-1 rec
1.02487, \$ STLD(1) = starting load factor, System A. BEGIN C-1 rec.
 0.000E+00, \$ STEP(1) = load factor increment, System A
1.02487, \$ FACM(1) = maximum load factor, System A
 0.000E+00, \$ STLD(2) = starting load factor, System B
 0.000E+00, \$ STEP(2) = load factor increment, System B
 0.000E+00, \$ FACM(2) = maximum load factor, System B
 0 \$ ITEMPL =0 means no thermal loads. END C-1 rec.
48, \$ ISTART=restart from ISTARTth load step. BEGIN D-1 rec.
50000, \$ NSEC= number of CPU seconds before run termination
 10,\$ NCUT = number of times step size may be cut
 -1, \$ NEWT = number of refactorings allowed
 -1,\$ NSTRAT=-1 means path length used as independent parameter
0.0002,\$ DELX=convergence tolerance
 0. \$ WUND = 0 means initial relaxation factor =1.END D-1 rec.
 0.,\$ TMIN = 0. means starting time is zero. BEGIN E-1 rec.
 1.000E-01, \$ TMAX = final time for transient analysis.
1.000E-04, \$ DT = time increment for transient analysis.
 0., \$ SUP = maximum expected displacement (irrelevant)
1.500E-01, \$ ALPHA=damping factor for mass matrix=DAMPNG*2*PI*CPS
2.000E-04, \$ BETA =damping factor for stiffness matrix=DAMPNG/2*PI*CPS
 0.000E+00, \$ GAMMA=damping factor for velocity-dependent forces
 0.000E+00 \$ THOLD can be used to suppress time step changes. END E-1
 0, \$ IMPL = 0 means implicit time integration. BEGIN E-2 rec.
 4, \$ METHOD=4 means use Parks formula for time integration
 1, \$ IERRF =1 means use variable (automatic) time step
 0, \$ IVELO =0 means number of modal initial velocities
 0, \$ IFORCE=0 means no user-written FORCET
 1, \$ IPA = 1 means linear variation (constant) applied load
 0 \$ IPB = 0 means load system B is not included. END E-2
1.05, \$ CA1 = transient load parameter(case (a), p3-21) BEGIN E-3
 0.000E+00, \$ CA2 = transient load parameter(case (a), p3-21)
 0.000E+00, \$ CA3 = transient load parameter(case (a), p3-21)
 1.000E+03, \$ CA4 = transient load parameter(case (a), p3-21)
 1.000E+03, \$ CA5 = transient load parameter(case (a), p3-21)
 0.000E+00 \$ CA6 = transient load parameter(case (a), p3-21) END E-3

PART 11: Results from Run 6 (3 Wimps, dynamic, nonlinear equilibrium, **INDIC=6, PA=1.05**, from test2.out2):

step 170, time= 6.75625E-03, dt= 3.12500E-06 (Time step 170 is the last time step recorded in the *.rst file).
 iter err pred_err. dof max_resid. dof max_displ. strain enrg. kinetic enrg.
 1 3.0017E-03 4.5996E-04 115901 3.6865E+02 118478 -7.0419E-03 2.1862E+04 3.7681E+03 **←large kinetic**
 2 1.5223E-03 5.6695E-04 118483 -1.7042E+02 118478 -8.1662E-03 2.1860E+04 3.7577E+03 **energy indicates**
 3 1.1334E-03 5.6249E-04 115901 1.0269E+02 118503 -3.1553E-03 2.1860E+04 3.7594E+03 **dynamic collapse.**
 4 7.6570E-04 5.7280E-04 129113 8.6554E+01 118503 2.7840E-03 2.1860E+04 3.7556E+03
 5 4.8905E-04 5.7622E-04 129113 -5.2864E+01 118503 -1.8121E-03 2.1860E+04 3.7568E+03
 6 1.8945E-04 5.7474E-04 160579 1.3702E+01 118503 7.3575E-04 2.1860E+04 3.7563E+03
 displacement, load step 170, Pa= 1.05, time= 6.75625E-03 saved on file: test2.rst
 (Dynamic response is shown in Fig. 32, Run 6).

PART 12: Run 7, nonlinear dynamic equilibrium analysis (INDIC=6) of imperfect shell with the following imperfections in the test2.inp file, starting from Step 48 with PA = 1.04):

C Begin B-4, B-5 input data, if any...

```
-0.0625 0 1 1 $ WIMPFA, ISTEP, IMODE, IRUN (imperf.1) B-5  
0.0005 16 1 2 $ WIMPFA, ISTEP, IMODE, IRUN (imperf.2) B-5  
0.0005 16 2 2 $ WIMPFA, ISTEP, IMODE, IRUN (imperf.3) B-5
```

Results from Run 7 (3 Wimps, dynamic, nonlinear equilibrium, **INDIC=6, PA=1.04**, from test2.out2):

step 310, time= 2.37500E-02, dt= 6.25000E-06 (Time step 310 is the last time step recorded in the *.rst file).
iter err pred_err. dof max_resid. dof max_displ. strain enrg. kinetic enrg.
1 6.8758E-04 2.8366E-04 160722 -4.5947E+01 160652 2.4646E-03 1.8253E+04 8.4796E+02 **←large kinetic**
2 2.8032E-04 3.0650E-04 144878 2.9390E+01 160640 6.1036E-04 1.8253E+04 8.4794E+02 **energy indicates**
3 2.3806E-04 3.1289E-04 144878 -3.7065E+01 144881 -3.1475E-04 1.8253E+04 8.4784E+02 **dynamic collapse.**
4 2.4477E-04 3.1314E-04 144878 3.3148E+01 144881 3.7793E-04 1.8253E+04 8.4786E+02
5 1.6842E-04 3.1275E-04 144878 -1.8217E+01 144881 -3.2973E-04 1.8253E+04 8.4783E+02
Maximum program execution time = 50000 seconds, exceeded. Execution terminates.
displacement, load step 310, Pa= 1.04, time= 2.37500E-02 saved on file: test2.rst

(Collapsed state of the shell at load step 310 is shown in **Fig. 30**; dynamic response is shown in **Fig. 32, Run 7**).

PART 13: Run 8, nonlinear dynamic equilibrium analysis (INDIC=6) of imperfect shell with the following imperfections in the test2.inp file, starting from Step 48 with PA = 1.035:

C Begin B-4, B-5 input data, if any...

```
-0.0625 0 1 1 $ WIMPFA, ISTEP, IMODE, IRUN (imperf.1) B-5  
0.0005 16 1 2 $ WIMPFA, ISTEP, IMODE, IRUN (imperf.2) B-5  
0.0005 16 2 2 $ WIMPFA, ISTEP, IMODE, IRUN (imperf.3) B-5
```

Results from Run 8 (3 Wimps, dynamic, nonlinear equilibrium, **INDIC=6, PA=1.035**, from test2.out2):

step 475, time= 4.27000E-02, dt= 1.00000E-04 (Time step 475 is the last time step recorded in the *.rst file).
iter err pred_err. dof max_resid. dof max_displ. strain enrg. kinetic enrg.
1 2.7334E-04 3.2054E-04 19993 -4.5067E-01 36886 -8.7210E-04 1.5522E+04 1.3751E-02 **←small kinetic**
2 1.7052E-04 5.5759E-04 25153 2.3764E-01 36886 -5.9032E-04 1.5522E+04 8.0974E-03 **energy indicates**
displacement, load step 475, Pa= 1.035, time= 4.27000E-02 saved on file: test2.rst **stable static state.**

(Deformed state of the shell at load step 475 is shown in **Fig. 31**; dynamic response is shown in **Fig. 32, Run 8**).

Table 10 PANDA2 margins for Case 1: the perfect shell. Margins less than 0.3 are in bold face.

ITERATION NO., LOAD SET NO., SUBCASE NO. = 0 1 1 MIDWAY BETWEEN RINGS		
BUCKLING LOAD FACTORS FOR LOCAL BUCKLING FROM KOITER v. BOSOR4 THEORY:		
Local buckling load factor from KOITER theory = 1.0122E+00		
Local buckling load factor from BOSOR4 theory = 1.0089E+00		
MARGINS FOR CURRENT DESIGN: LOAD CASE NO. 1, SUBCASE NO. 1		
mar. margin		
no. value	definition	
1 9.89E-03 Local buckling from discrete model-1.,M=9 axial halfwaves;FS=0.99		
2 6.73E-01 Long-axial-wave bending-torsion buckling; M=2 ;FS=0.999		
3 2.40E-02 eff.stress:matl=1,STR,Dseg=3,node=1,layer=1,z=0.0099; MID.;FS=1.		
4 7.26E-01 (m=2 lateral-torsional buckling load factor)/(FS)-1;FS=0.999		
5 3.53E-01 Inter-ring buckling, discrete model, n=5 circ.halfwaves;FS=0.999		
6 2.40E-02 eff.stress:matl=1,STR,Iseg=3,at:ROOT,layer=1,z=0.:-MID.;FS=1.		
7 5.13E-01 buckling margin stringer Iseg.3 . Local halfwaves=16 .MID.;FS=1.		
8 4.46E-01 buckling margin stringer Iseg.4 . Local halfwaves=15 .MID.;FS=1.		
9 2.60E-02 buckling stringer Isegs.3+4 together.M=12 ;C=0. ;MID.;FS=1.4		
10 3.42E+00 buckling stringer Iseg 4 as beam on foundation. M=484;MID.;FS=1.2		
11 -2.28E-02 buck.(SAND);simp-support general buck;M=1;N=4;slope=0.;FS=0.999		
12 1.46E+01 buck.(SAND);rolling with smear rings; M=103;N=1;slope=0.;FS=0.999		
13 3.36E-01 buck.(SAND);rolling only of stringers;M=18;N=0;slope=0.;FS=1.4		
14 3.60E-01 buck.(SAND);hiwave roll. of stringers;M=152;N=0;slope=0.;FS=1.2		
15 5.10E-01 buck.(SAND); STRINGERS: web buckling;M=16;N=1;slope=0.;FS=1.		
16 1.70E+02 (Max.allowable ave.axial strain)/(ave.axial strain) -1; FS=1.		
17 -9.95E-06 1.-V(3)^1+20.V(6)^1-1		
18 8.83E-02 1.-V(4)^1+20.V(7)^1-1		
19 0.00E+00 1.-V(10)^1+20.V(12)^1-1		
20 2.58E-01 1.-V(11)^1+20.V(13)^1-1		
21 9.71E-01 1.+V(8)^1-V(11)^1-1		
22 4.88E+00 1.-V(1)^1+5.V(8)^1-1		

ITERATION NO., LOAD SET NO., SUBCASE NO. = 0 1 2 AT RINGS

BUCKLING LOAD FACTORS FOR LOCAL BUCKLING FROM KOITER v. BOSOR4 THEORY:

Local buckling load factor from KOITER theory = 1.0262E+00

Local buckling load factor from BOSOR4 theory = 1.0134E+00

MARGINS FOR CURRENT DESIGN: **LOAD CASE NO. 1, SUBCASE NO. 2**

mar. margin

no. value definition

1 1.45E-02 Local buckling from discrete model-1.,M=9 axial halfwaves;FS=0.99

2 6.16E-01 Long-axial-wave bending-torsion buckling; M=2 ;FS=1.

3 6.67E-03 eff.stress:matl=1,STR,Dseg=4,node=11,layer=1,z=-0.0111; RNGS;FS=1.

4 6.82E-01 (m=2 lateral-torsional buckling load factor)/(FS)-1;FS=0.999

5 3.53E-01 Inter-ring buckling, discrete model, n=5 circ.halfwaves;FS=0.999

6 -2.38E-03 eff.stress:matl=1,STR,Iseg=4,allnode,layer=1,z=-0.0111;-RNGS;FS=1.

7 4.97E-01 buckling margin stringer Iseg.3 . Local halfwaves=16 .RNGS;FS=1.

8 3.99E-01 buckling margin stringer Iseg.4 . Local halfwaves=15 .RNGS;FS=1.

9 2.51E-03 buckling stringer Isegs.3+4 together.M=12 ;C=0. ;RNGS;FS=1.4

10 3.28E+00 buckling stringer Iseg 4 as beam on foundation. M=484;RNGS;FS=1.2

11 1.45E+01 buck.(SAND);rolling with smear rings; M=103;N=1;slope=0.;FS=0.999

12 2.98E-01 buck.(SAND);rolling only of stringers;M=18;N=0;slope=0.;FS=1.4

13 3.21E-01 buck.(SAND);hiwave roll. of stringers;M=152;N=0;slope=0.;FS=1.2

14 4.76E-01 buck.(SAND); STRINGERS: web buckling;M=16;N=1;slope=0.;FS=1.

15 1.70E+02 (Max.allowable ave.axial strain)/(ave.axial strain) -1; FS=1.

***** ALL 1 LOAD SETS PROCESSED *****

Table 11 Case 4 design margins from PANDA2 for Load case 2, Sub-case 1 for the imperfect shell. The margins are obtained with “no Koiter” (Part 1) and with “yes Koiter” (Part 2) for the same design. Note especially the effect on Margin No. 3, the effective stress margin for stresses in the skin-stringer module.

**Part 1 Case 4 margins obtained with the “yes Koiter” branch turned OFF (“no Koiter”)
(The effect of local deformation of the skin-stringer module shown in Fig. 4 is NOT included)**

MARGINS FOR CURRENT DESIGN: LOAD CASE NO. 2, SUBCASE NO. 1

mar. margin

no.	value	definition	←NOTE THIS
1	-1.83E-02	Local buckling from discrete model-1.,M=9 axial halfwaves;FS=0.99	
2	8.45E-01	Long-axial-wave bending-torsion buckling; M=2 ;FS=0.999	
3	1.13E-01	eff.stress:matl=1,SKN,Dseg=2,node=6,layer=1,z=0.0174; MID.;FS=1.	←NOTE THIS
4	8.59E-01 (m=2 lateral-torsional buckling load factor)/(FS)-1;FS=0.999		
5	8.86E-01	Ring sidesway buk., discrete model, n=24 circ.halfwaves;FS=0.999	
6	-2.86E-02	eff.stress:matl=1,RNG,Iseg=4,allnode,layer=1,z=0.0293; -MID.;FS=1.	
7	1.06E+00	buckling margin stringer Iseg.3 . Local halfwaves=13 .MID.;FS=1.	
8	9.02E-01	buckling margin stringer Iseg.4 . Local halfwaves=13 .MID.;FS=1.	
9	4.73E-01	buckling stringer Isegs.3+4 together.M=13 ;C=0. ;MID.;FS=1.4]	
10	6.69E+00	buckling stringer Iseg 4 as beam on foundation. M=460;MID.;FS=1.2	
11	5.38E+00	buckling margin ring Iseg.3 . Local halfwaves=107.MID.;FS=1.	
12	8.54E+00	buckling ring Iseg 4 as beam on foundation. M=453;MID.;FS=1.2	
13	1.49E-01	buck.(SAND);simp-support general buck;M=4;N=6;slope=0.;FS=0.999	
14	1.45E+01	buck.(SAND);rolling with smear rings; M=93;N=1;slope=0.;FS=0.999	
15	8.30E-01	buck.(SAND);rolling only of stringers;M=18;N=0;slope=0.;FS=1.4	
16	1.17E+00	buck.(SAND);hiwave roll. of stringers;M=153;N=0;slope=0.;FS=1.2	
17	9.71E+00	buck.(SAND);rolling only axisym.rings;M=0;N=0;slope=0.;FS=1.4	
18	7.83E-01	buck.(SAND); STRINGERS: web buckling;M=13;N=1;slope=0.01;FS=1.	
19	6.07E+00	buck.(SAND); RINGS: web buckling;M=98;N=1;slope=0.2017;FS=1.	
20	2.15E+02	(Max.allowable ave.axial strain)/(ave.axial strain) -1; FS=1.	

**Part 2 Case 4 margins obtained with the “yes Koiter” branch turned ON
(The effect of local deformation of the skin-stringer module shown in Fig. 4 IS included)**

MARGINS FOR CURRENT DESIGN: LOAD CASE NO. 2, SUBCASE NO. 1

mar. margin

no.	value	definition	←NOTE THIS
1	-1.83E-02	Local buckling from discrete model-1.,M=9 axial halfwaves;FS=0.99	
2	8.45E-01	Long-axial-wave bending-torsion buckling; M=2 ;FS=0.999	
3	-3.57E-01	eff.stress:matl=1,SKN,Dseg=1,node=1,layer=1,z=0.0174; MID.;FS=1.	←NOTE THIS
4	7.83E+03	stringer popoff margin:(allowable/actual)-1, web 1 MID.;FS=1.	
5	1.06E+05	stringer popoff margin:(allowable/actual)-1, web 2 MID.;FS=1.	
6	9.34E-01 (m=2 lateral-torsional buckling load factor)/(FS)-1;FS=0.999		
7	1.34E+00	Inter-ring buckling, discrete model, n=44 circ.halfwaves;FS=0.999	
8	9.60E-01	Lo-n Ring sidesway, discrete model, n=25 circ.halfwaves;FS=0.999	
9	-7.39E-03	eff.stress:matl=1,RNG,Iseg=4,allnode,layer=1,z=0.0293; -MID.;FS=1.	
10	9.23E-01	buckling margin stringer Iseg.3 . Local halfwaves=13 .MID.;FS=1.	
11	8.05E-01	buckling margin stringer Iseg.4 . Local halfwaves=13 .MID.;FS=1.	
12	3.94E-01	buckling stringer Isegs.3+4 together.M=13 ;C=0. ;MID.;FS=1.4	
13	6.30E+00	buckling stringer Iseg 4 as beam on foundation. M=460;MID.;FS=1.2	
14	5.72E+00	buckling margin ring Iseg.3 . Local halfwaves=107.MID.;FS=1.	
15	8.90E+00	buckling ring Iseg 4 as beam on foundation. M=453;MID.;FS=1.2	
16	7.07E-01	buckling margin stringer Iseg.3 . Local halfwaves=13 .NOPO;FS=1.	
17	6.31E-02	buckling margin stringer Iseg.4 . Local halfwaves=13 .NOPO;FS=1.	
18	1.07E-01	buckling stringer Isegs.3+4 together.M=13 ;C=0. ;NOPO;FS=1.4	

- 19 3.30E+00 buckling stringer Iseg 4 as beam on foundation. M=460;NOPO;FS=1.2
20 5.72E+00 buckling margin ring Iseg.3 . Local halfwaves=107.NOPO;FS=1.
21 8.90E+00 buckling ring Iseg 4 as beam on foundation. M=453;NOPO;FS=1.2
22 **4.50E-02** buck.(SAND);simp-support general buck;M=3;N=5;slope=0.;FS=0.999
23 1.45E+01 buck.(SAND);rolling with smear rings; M=93;N=1;slope=0.;FS=0.999
24 **7.63E-01** buck.(SAND);rolling only of stringers;M=18;N=0;slope=0.;FS=1.4
25 1.10E+00 buck.(SAND);hiwave roll. of stringers;M=153;N=0;slope=0.;FS=1.2
26 1.02E+01 buck.(SAND);rolling only axisym.rings;M=0;N=0;slope=0.;FS=1.4
27 7.49E-01 buck.(SAND); STRINGERS: web buckling;M=13;N=1;slope=0.01;FS=1.
28 6.43E+00 buck.(SAND); RINGS: web buckling;M=98;N=1;slope=0.2107;FS=1.
29 1.72E+02 (Max.allowable ave.axial strain)/(ave.axial strain) -1; FS=1.
-
-

Table 12 Case 4 stiffnesses from PANDA2 with "no Koiter" and with "yes Koiter": Load Set 2, Sub-case 1

PART 1 STIFFNESSES WITHOUT LOCAL POSTBUCKLING ANALYSIS: "NO KOITER"

*** BEGIN SUBROUTINE DEFCIJ (NOT POST-LOCALLY BUCKLED CS(I,J)) ***

Effective stiffnesses of undeformed and of locally deformed module segments:

		Undeformed	Deformed
Effective axial stiffness of panel SKIN + BASE	=	3.8327E+05	3.8327E+05
Effective hoop stiffness of panel SKIN + BASE	=	3.8327E+05	3.8327E+05
Effective (1,2) stiffness of panel SKIN + BASE	=	1.1498E+05	1.1498E+05
Effective axial stiffness of stringer WEB	=	3.4974E+05	3.4974E+05
Effective axial stiffness of stringer FLANGE	=	2.5093E+05	2.5093E+05
Effective shear stiffness of panel SKIN + BASE	=	1.3415E+05	1.3415E+05
Effective shear stiffness of stringer WEB	=	1.2241E+05	1.2241E+05
Effective shear stiffness of stringer FLANGE	=	8.7827E+04	8.7827E+04

Integrated stringer stiffnesses...

Effective axial stiffness of stringer, STIFL = 2.9927E+05

Effective first moment, Int[STIF*zdz], STIFM = 1.3003E+05

Effective second moment, Int[STIF*z**2dz], STIFMM=6.9957E+04

Constitutive law, CS(i,j), for locally deformed panel with smeared stringers and rings.....

6.8254E+05	1.1498E+05	0.0000E+00	1.3003E+05	0.0000E+00	0.0000E+00
1.1498E+05	4.3022E+05	0.0000E+00	0.0000E+00	-2.2979E+04	0.0000E+00
0.0000E+00	0.0000E+00	1.3415E+05	0.0000E+00	0.0000E+00	0.0000E+00
1.3003E+05	0.0000E+00	0.0000E+00	6.9996E+04	1.1656E+01	0.0000E+00
0.0000E+00	-2.2979E+04	0.0000E+00	1.1656E+01	1.4449E+04	0.0000E+00
0.0000E+00	0.0000E+00	0.0000E+00	0.0000E+00	0.0000E+00	2.4065E+01

Constitutive law, C(i,j), for locally deformed panel between rings with smeared stringers.....

6.8254E+05	1.1498E+05	0.0000E+00	1.3003E+05	0.0000E+00	0.0000E+00
1.1498E+05	3.8327E+05	0.0000E+00	0.0000E+00	0.0000E+00	0.0000E+00
0.0000E+00	0.0000E+00	1.3415E+05	0.0000E+00	0.0000E+00	0.0000E+00
1.3003E+05	0.0000E+00	0.0000E+00	6.9996E+04	1.1656E+01	0.0000E+00
0.0000E+00	0.0000E+00	0.0000E+00	1.1656E+01	3.8854E+01	0.0000E+00
0.0000E+00	0.0000E+00	0.0000E+00	0.0000E+00	0.0000E+00	2.1851E+01

*** END SUBROUTINE DEFCIJ (NOT POST-LOCALLY BUCKLED CS(I,J)) ***

PART 2 STIFFNESSES WITH LOCAL POSTBUCKLING ANALYSIS: "YES KOITER"

*** BEGIN SUBROUTINE DEFCIJ (YES POST-LOCALLY BUCKLED CS(I,J)) ***

Effective stiffnesses of undeformed and of locally deformed module segments:

		Undeformed	Deformed
Effective axial stiffness of panel SKIN + BASE	=	3.8327E+05	1.8550E+05
Effective hoop stiffness of panel SKIN + BASE	=	3.8327E+05	2.6202E+05
Effective (1,2) stiffness of panel SKIN + BASE	=	1.1498E+05	3.2891E+03
Effective axial stiffness of stringer WEB	=	3.4974E+05	3.2739E+05
Effective axial stiffness of stringer FLANGE	=	2.5093E+05	2.4685E+05
Effective shear stiffness of panel SKIN + BASE	=	1.3415E+05	1.2640E+05
Effective shear stiffness of stringer WEB	=	1.2241E+05	1.2241E+05
Effective shear stiffness of stringer FLANGE	=	8.7827E+04	8.7827E+04

Integrated stringer stiffnesses...

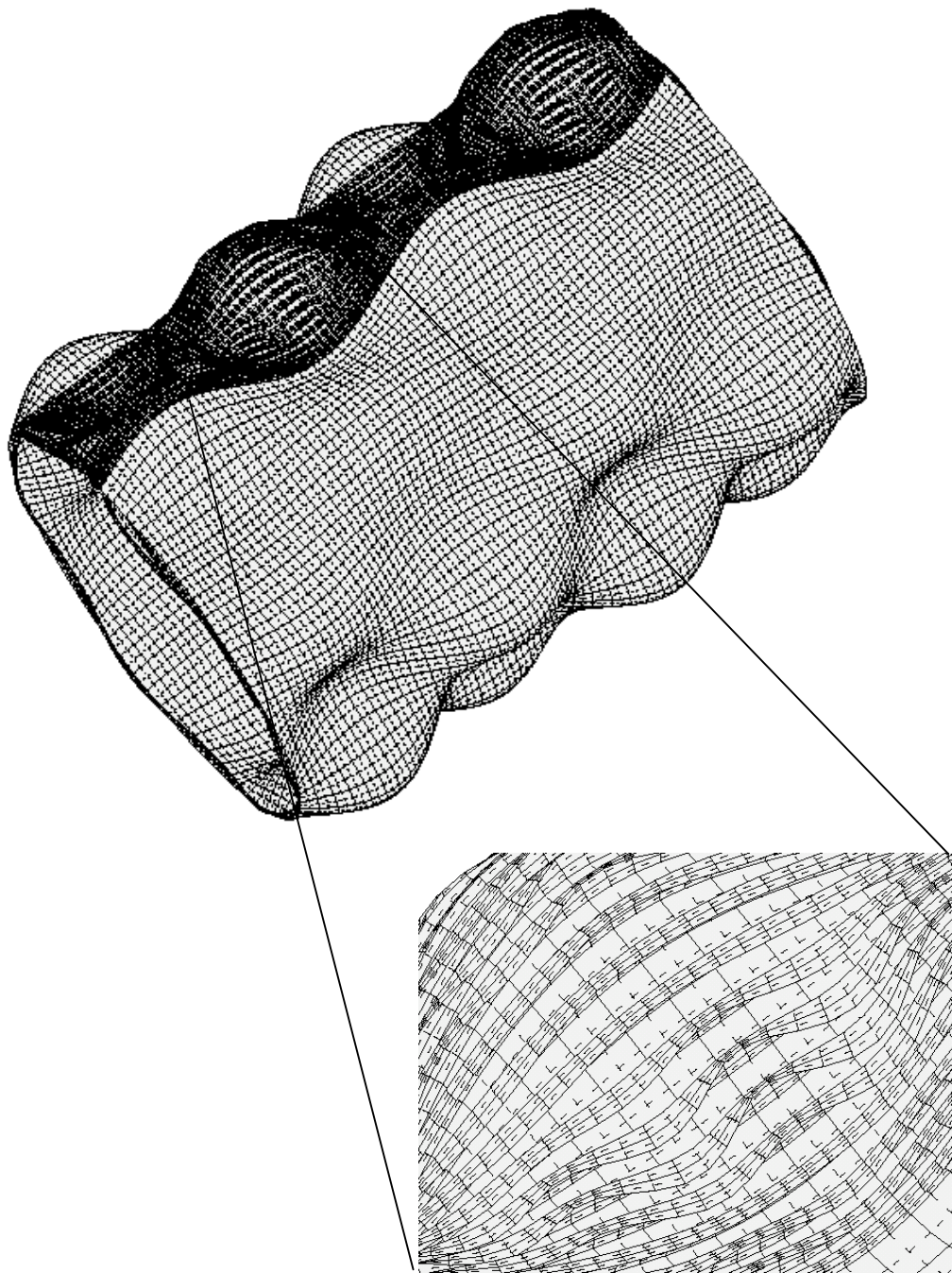
Effective axial stiffness of stringer, STIFL =2.8590E+05
Effective first moment, Int[STIF*zdz], STIFM =1.2561E+05
Effective second moment,Int[STIF*z**2dz], STIFMM=6.8156E+04

Constitutive law, CS(i,j), for locally deformed panel with smeared stringers and rings.....

4.7275E+05 3.7298E+03 0.0000E+00 1.2561E+05 0.0000E+00 0.0000E+00
3.7298E+03 3.0896E+05 0.0000E+00 0.0000E+00 -2.2979E+04 0.0000E+00
0.0000E+00 0.0000E+00 1.2640E+05 0.0000E+00 0.0000E+00 0.0000E+00
1.2561E+05 0.0000E+00 0.0000E+00 6.8195E+04 1.1656E+01 0.0000E+00
0.0000E+00 -2.2979E+04 0.0000E+00 1.1656E+01 1.4449E+04 0.0000E+00
0.0000E+00 0.0000E+00 0.0000E+00 0.0000E+00 0.0000E+00 2.4065E+01

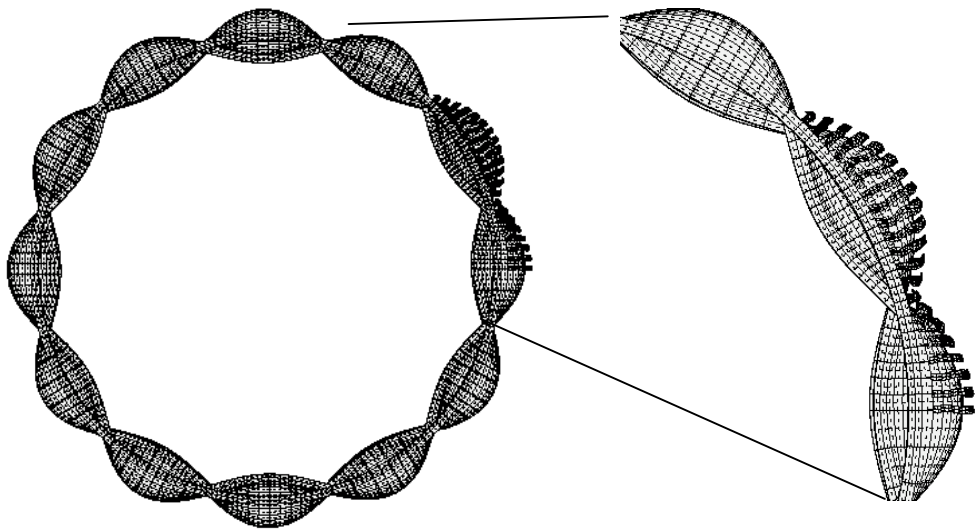
Constitutive law, C(i,j), for locally deformed panel between rings with smeared stringers.....

4.7275E+05 3.7298E+03 0.0000E+00 1.2561E+05 0.0000E+00 0.0000E+00
3.7298E+03 2.6202E+05 0.0000E+00 0.0000E+00 0.0000E+00 0.0000E+00
0.0000E+00 0.0000E+00 1.2640E+05 0.0000E+00 0.0000E+00 0.0000E+00
1.2561E+05 0.0000E+00 0.0000E+00 6.8195E+04 1.1656E+01 0.0000E+00
0.0000E+00 0.0000E+00 0.0000E+00 1.1656E+01 3.8854E+01 0.0000E+00
0.0000E+00 0.0000E+00 0.0000E+00 0.0000E+00 0.0000E+00 2.1851E+01
**** END SUBROUTINE DEFCIJ (YES POST-LOCALLY BUCKLED CS(I,J)) ****



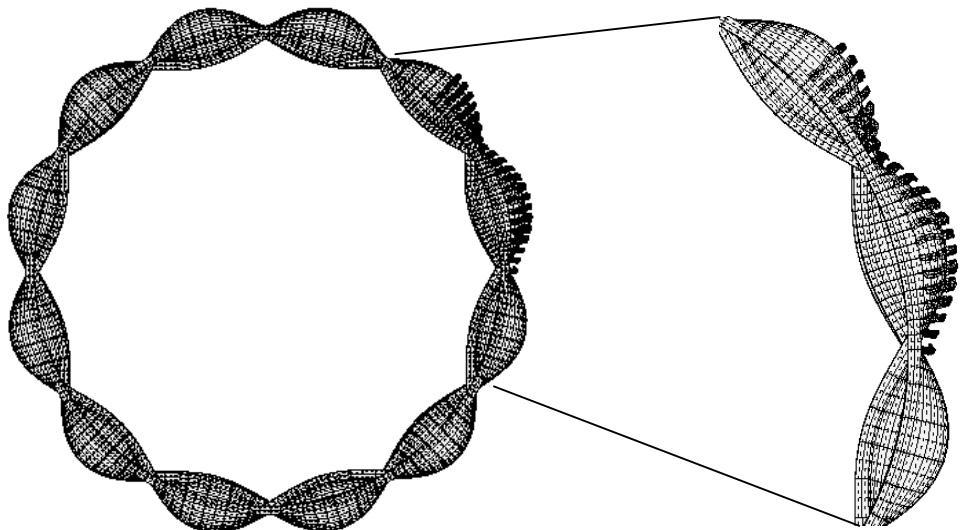
STAGS model of Case 4 in Table 4: no Koiter, yes change imperfection, ICONSV=1; compare with Fig.49. STAGS Mode 395 = lowest general buckling mode, load factor, pcr=2.0308; BIGBOSOR4 predicts 2.0008 (\mathbf{m}, \mathbf{n})=(\mathbf{m} = 4 axial halfwaves, \mathbf{n} = 6 circumferential full waves); PANDA2 predicts 2.07 (\mathbf{m}, \mathbf{n})=(4,6) before the application of three “knockdown” factors: (1) for smearing stringers, (2) for smearing rings, and (3) for transverse shear deformation (t.s.d). PANDA2 predicts 1.774 after application of these three “knockdowns”. Note from the expanded insert that the general buckling mode includes a significant component of bending-torsion buckling of the stringers. The nodal mesh density is not sufficiently refined to capture local skin/stringer bending and buckling of the type shown in Fig. 48.

FIG.1a Linear general buckling mode from a “compound” STAGS model.



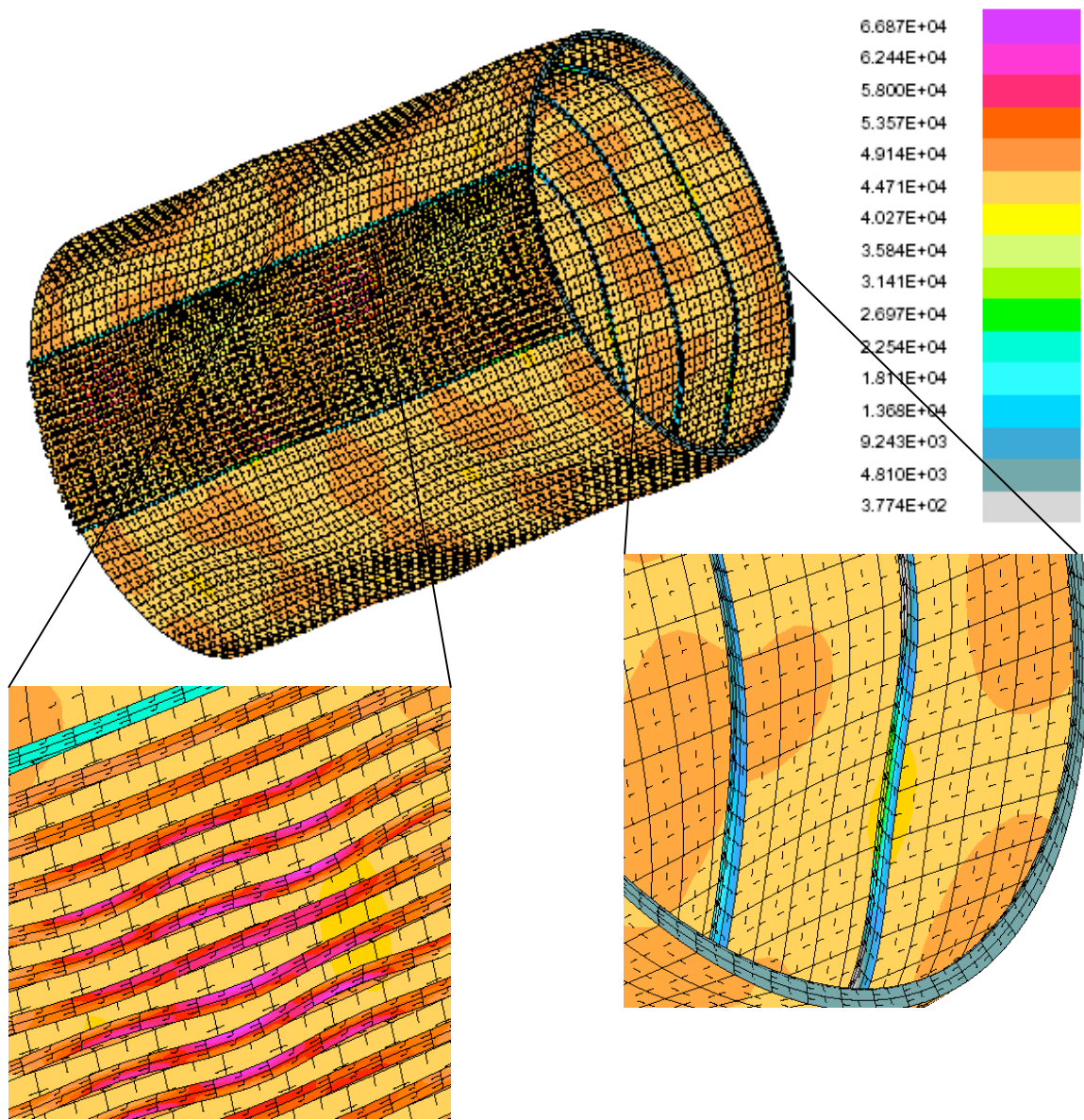
STAGS model of Case 4 in Table 4: no Koiter, yes change imperfection, ICONSV=1. STAGS Mode 395 = general buckling; load factor, pcr=2.0308; first of a pair of modes. The region in which the stringers are modeled as shell units spans 45 degrees of the circumference.

FIG. 1b End view of the same linear buckling mode as that shown in the previous figure.



STAGS model of Case 4 in Table 4: no Koiter, yes change imperfection, ICONSV=1. Compare with Fig. 1b. With a complete (360-deg) cylindrical shell the modes almost always occur in pairs. STAGS Mode 396, buckling load factor, pcr=2.0309; second of a pair of modes.

FIG. 1c End view of the next buckling mode to that shown in the previous figure.



STAGS model of Case 4 in Table 4: no Koiter, yes change imperfection, ICONSV=1; also see Figs. 61-63. Nonlinear equilibrium state from STAGS at the load factor, PA=1.00516 (very close to the design load, for which PA = 1.0). The imperfect shell has two initial buckling modal imperfection shapes: Fig. 1a with amplitude, Wimp1=+0.0625 and Fig. 61 with amplitude, Wimp2= -0.0005 inch. Prebuckling bending of the imperfect shell causes redistribution of stresses among the shell skin and the stiffener segments. Also, prebuckling bending gives rise to “flattened” regions with an “effective” circumferential radius of curvature larger than nominal that causes early general buckling. (See the right-most expanded insert for an example of a “flattened” region). The stringer at the top of the left-most insert has a stress that is very different from that of its neighbor because stiffeners that run along the edges of a “patch” in the STAGS model have half the stiffness and half the loading of the interior stiffeners.

FIG. 2 STAGS prediction of outer fiber effective stress (psi) at axial load, Nx= -3000 x 1.00516 lb/in.

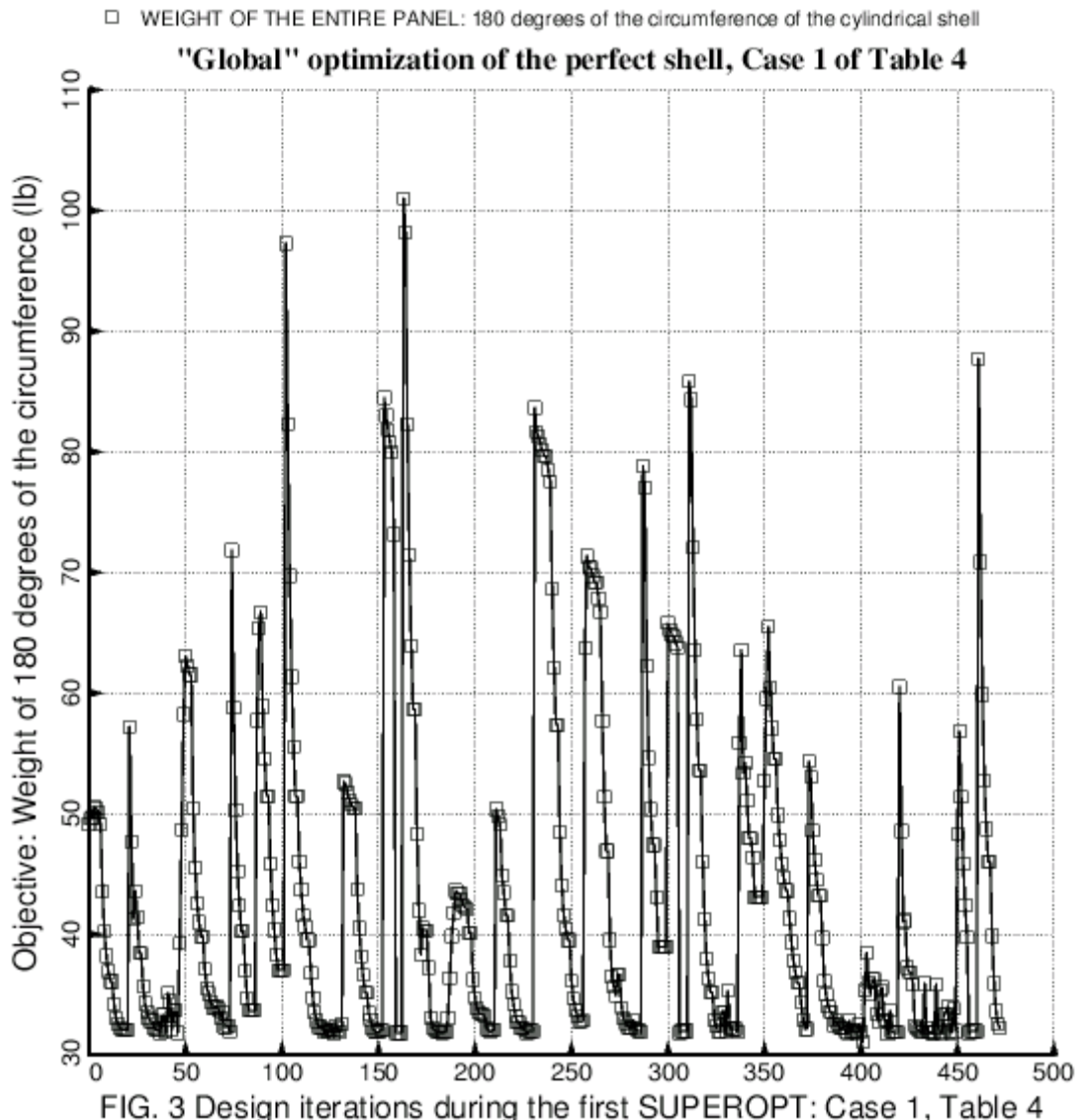


FIG. 3 PANDA2 results for Case 1 in Table 4: Design iterations during an execution of SUPEROPT, a PANDA2 processor the purpose of which is to seek a “global” optimum design. Each “spike” in the plot corresponds to a new starting design, which (as explained in [1D, 1K]) is generated randomly in a manner consistent with all linking and inequality constraints. See Table 3 for a typical PANDA2 runstream that includes several executions of SUPEROPT.

- 10.1.1 Panel module deformed by loads in step no. 10: $N_x = -1400 \text{ lb/in}$; Case 4 with "yes Koiter"
- 20.1.1 Panel module deformed by loads in step no. 20: $N_x = -2400 \text{ lb/in}$; Case 4 with "yes Koiter"
- 25.1.1 Panel module deformed by loads in step no. 25: $N_x = -2900 \text{ lb/in}$; Case 4 with "yes Koiter"
- 27.1.1 Panel module deformed by loads in step no. 27: $N_x = -3100 \text{ lb/in}$; Case 4 with "yes Koiter"

Local deformation of skin-stringer module with $\text{Wimp}(\text{local})=0.05xT(1)(\text{SKN})$

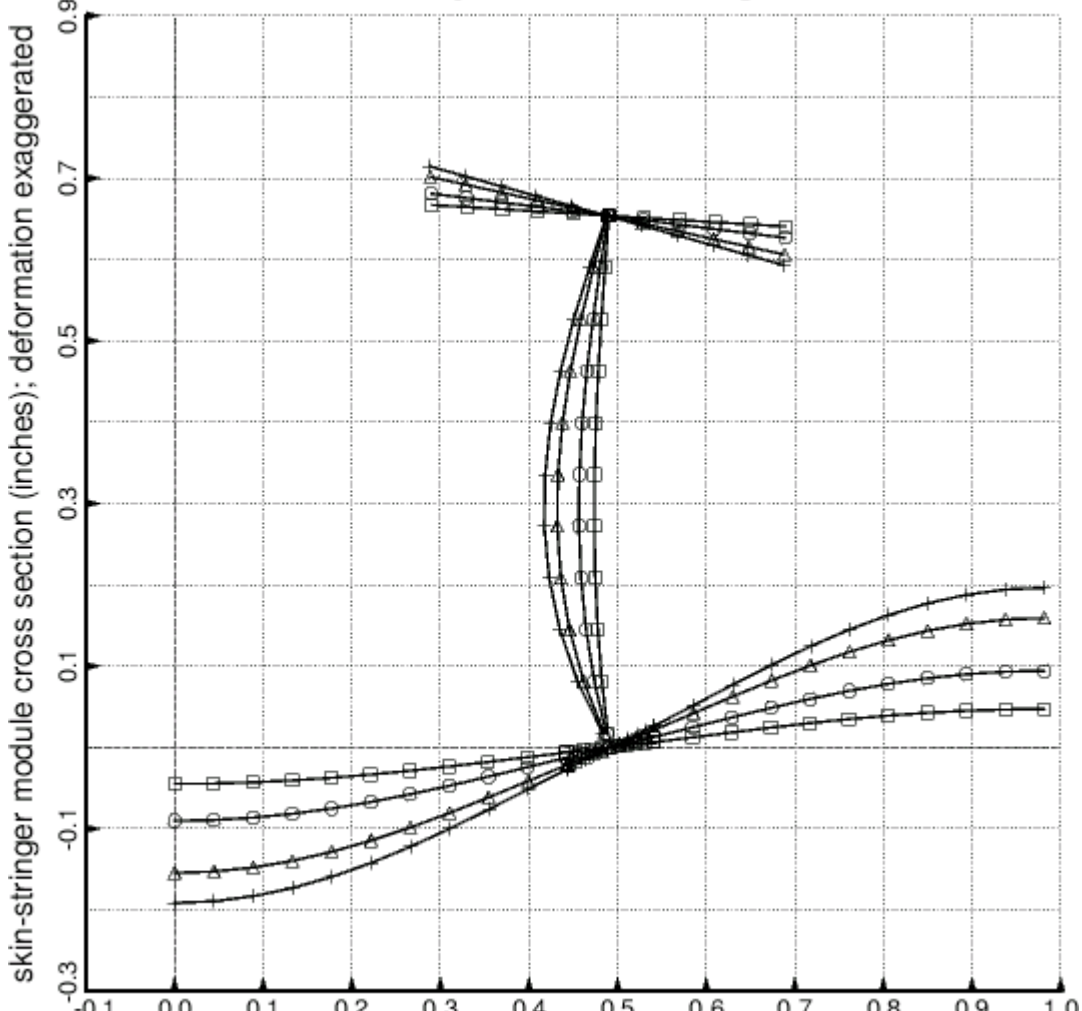


FIG. 4 Case 4 skin-stringer module cross section (inches) for 4 loads

FIG. 4 The PANDA2 discretized skin-stringer cross section corresponding to the CASE 4 optimum design. The deformed cross sections (exaggerated deformation amplitudes) are generated when the “KOITER” branch is turned on, that is, with the “yes Koiter” option (Table 4 and Item 3 in Section 11.0). Segment 1 (Dseg=1 in Margin No. 6d in Table 5) is the panel skin on the left-hand side of the figure. Segment 2 (Dseg 2 in Margin No. 6c in Table 5) is the base under the stringer where nodal points are concentrated. Segment 3 (Dseg=3 in Margin No. 6b in Table 5) is the stringer web. Segment 4 (Dseg=4 in Margin No. 6a in Table 5) is the stringer outstanding flange. Segment 5 (Dseg=5 in Margin No. 6e in Table 5) is the panel skin on the right-hand side of the figure. Nodal points are numbered from left to right in the horizontal segments and from the bottom to the top in the stringer web. Symmetry conditions are applied at the beginning of Segment 1 and at the end of Segment 5. The bending pattern shown here varies in the axial coordinate direction (normal to the plane of the paper) sinusoidally between rings with M (or m) axial halfwaves. In Case 4 $m = 9$ halfwaves between rings. See Fig. 48 for a STAGS model of local buckling of the Case 4 design.

- 2.1.1 Case4, Table 4 optimum design with "yes Koiter": panel skin norml deflection w (inches)

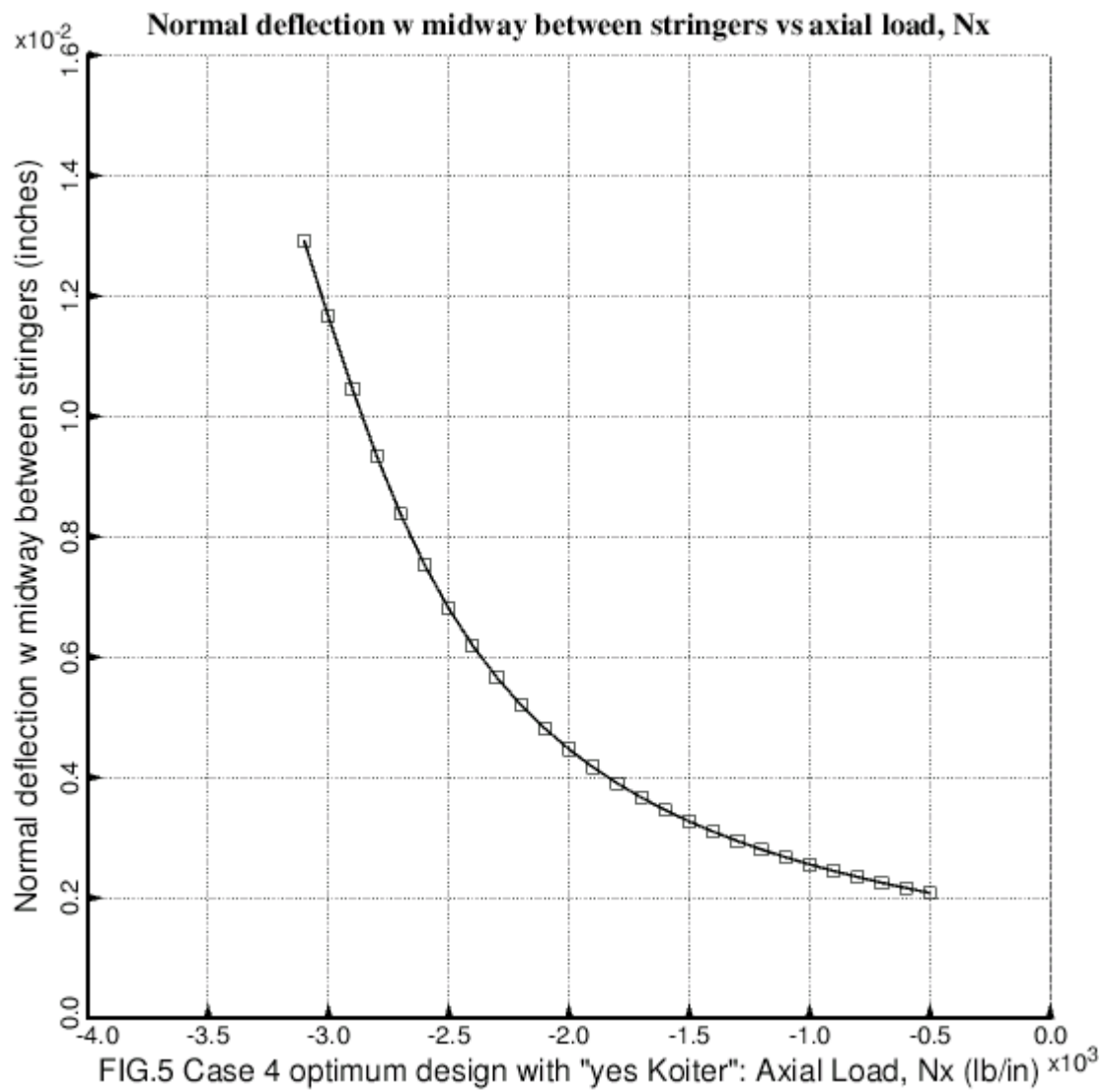


FIG. 5 PANDA2 results for Case 4 in Table 4 with “no Koiter” changed to “yes Koiter”: This figure shows how the local bending deformation displayed in the previous figure (“yes Koiter” option) grows with increasing applied axial compression, Nx. At Nx = 0.0 the initial normal displacement midway between stringers (the initial local imperfection amplitude automatically assigned by PANDA2 in the “yes change imperfection” option in this case) is five per cent of the panel skin wall thickness, or $w(\text{initial}) = 0.05 \times T(1)\text{SKN} = 0.05 \times 0.0034878 = 0.0017439$ inch. (See the Case 4 design listed in Table 4).

- 3.1.1 eff.stress: MID strthk; Load set 1, subcase 1, NO KOITER post-buckling analysis.
- 6.1.1 eff.stress: -MID strthk; Load set 1, subcase 1, NO KOITER post-buckling analysis.
- △ 28.1.1 eff.stress:-MID strocon allnode; Load set 1, subcase 1, NO KOITER post-buckling analysis.
- + 3.1.2 eff.stress: RNGS strthk; Load set 1, subcase 2, NO KOITER post-buckling analysis.
- × 7.1.2 eff.stress:-RNGS strocon allnode; Load set 1, subcase 2, NO KOITER post-buckling analysis.
- ◊ 3.2.1 eff.stress: MID strthk; Load set 2, subcase 1, NO KOITER post-buckling analysis.
- ▽ 7.2.1 eff.stress:-MID strthk; Load set 2, subcase 1, NO KOITER post-buckling analysis.
- ▣ 23.2.1 eff.stress:-MID strocon allnode; Load set 2, subcase 1, NO KOITER post-buckling analysis.
- ✳ 3.2.2 eff.stress: RNGS strthk; Load set 2, subcase 2, NO KOITER post-buckling analysis.
- ◆ 6.2.2 eff.stress:-RNGS strocon allnode; Load set 2, subcase 2, NO KOITER post-buckling analysis.
- ⊕ 3.1.1 eff.stress: MID strthk; Load set 1, subcase 1, YES KOITER post-buckling analysis.
- ⊗ 7.1.1 eff.stress:-MID strthk; Load set 1, subcase 1, YES KOITER post-buckling analysis.
- 田 3.1.2 eff.stress: RNGS strthk; Load set 1, subcase 2, YES KOITER post-buckling analysis.
- ☒ 8.1.2 eff.stress:-RNGS strocon allnode; Load set 1, subcase 2, YES KOITER post-buckling analysis.
- ☒ 3.2.1 eff.stress: MID strthk; Load set 2, subcase 1, YES KOITER post-buckling analysis.
- 9.2.1 eff.stress:-MID strocon allnode; Load set 2, subcase 1, YES KOITER post-buckling analysis.
- 31.2.1 eff.stress:-MID strocon allnode; Load set 2, subcase 1, YES KOITER post-buckling analysis.
- ▣ 3.2.2 eff.stress: RNGS strthk; Load set 2, subcase 2, YES KOITER post-buckling analysis.
- 7.2.2 eff.stress:-RNGS strocon allnode; Load set 2, subcase 2, YES KOITER post-buckling analysis.

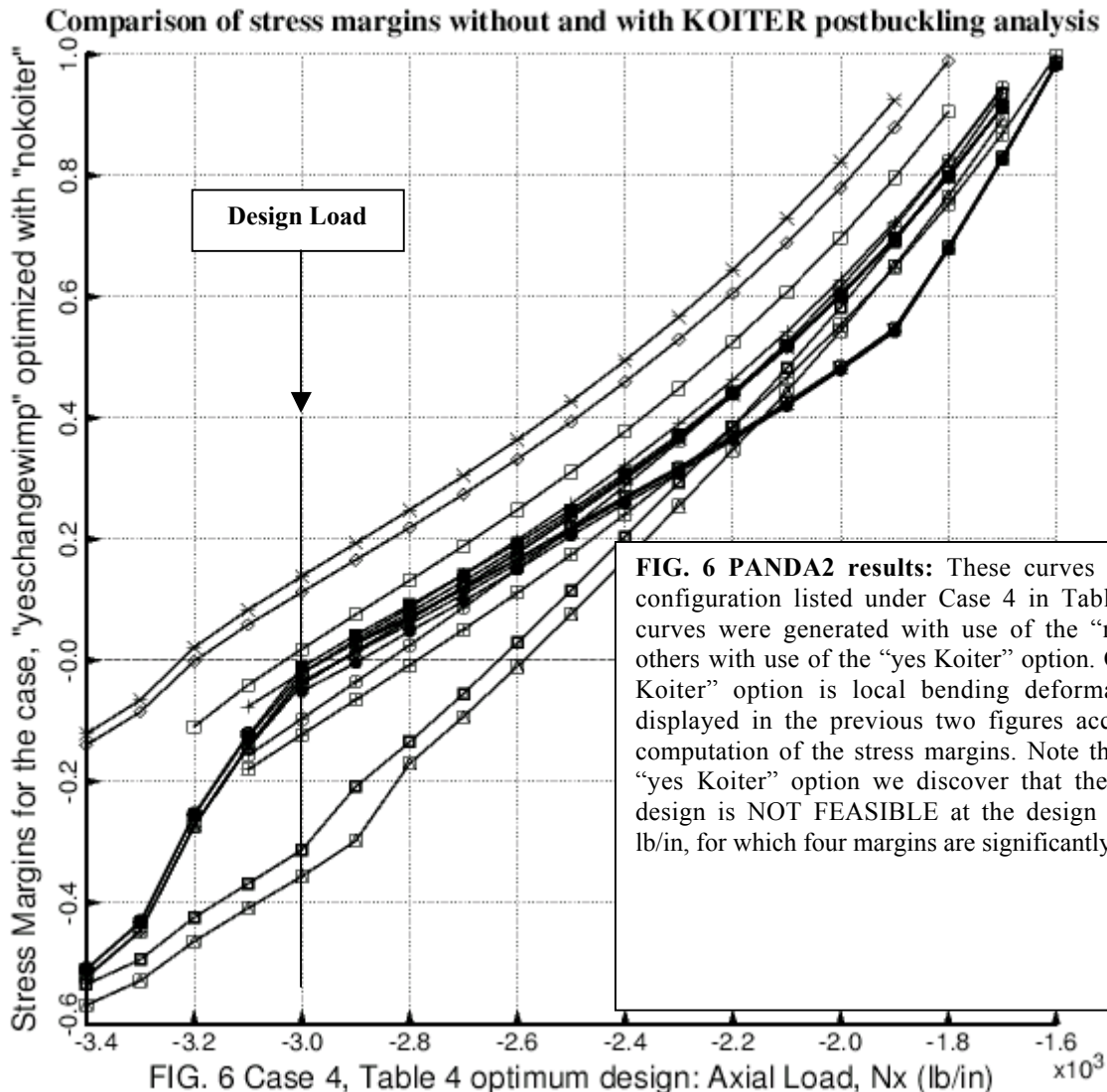
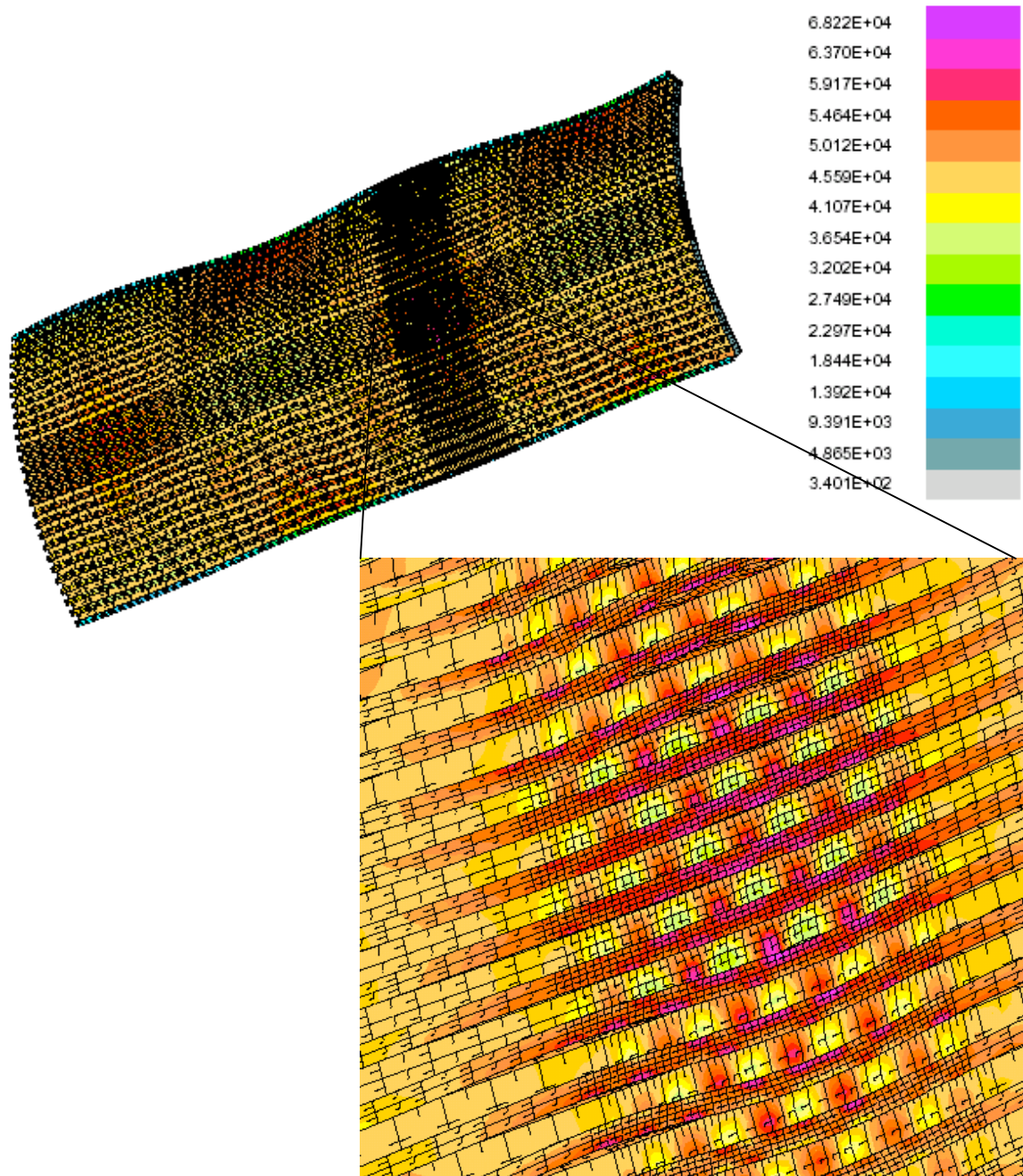


FIG. 6 PANDA2 results: These curves correspond to the configuration listed under Case 4 in Table 4. Some of the curves were generated with use of the “no Koiter” option; others with use of the “yes Koiter” option. Only with the “yes Koiter” option is local bending deformation of the type displayed in the previous two figures accounted for in the computation of the stress margins. Note that with use of the “yes Koiter” option we discover that the Case 4 optimum design is NOT FEASIBLE at the design load, $N_x = -3000$ lb/in, for which four margins are significantly negative.



STAGS model of Case 4 in Table 4: no Koiter, yes change imperfection, ICONSV=1; Compare with Fig.2. Deformed state during a nonlinear dynamic STAGS run at the design load, PA=1.0, Time = 0.00255 seconds (Fig.52). Notice local bending in the panel skin. The imperfect shell has only a general buckling modal imperfection shape (that shown in Fig. 49) with amplitude, Wimp1 = -0.0625 inches. This is a 60-degree STAGS model with symmetry conditions applied along the two straight edges. The configuration (Case4) is the same as that shown in Figs. 1 and 2. The agreement of predictions from the 360-degree compound model and the 60-degree model justifies use of the 60-degree model.

FIG. 7 STAGS prediction of outer fiber effective stress (psi) at the design load, $N_x = -3000$ lb/in

- Local buckling margin: General buckling modal imperfection shape with MUSER = 1 axial halfwave
- Local buckling margin: General buckling modal imperfection shape with MUSER = 2 axial halfwaves
- △ Local buckling margin: General buckling modal imperfection shape with MUSER = 3 axial halfwaves
- + Local buckling margin: General buckling modal imperfection shape with MUSER = 4 axial halfwaves
- × Local buckling margin: General buckling modal imperfection shape with MUSER = 5 axial halfwaves
- ◊ Local buckling margin: General buckling modal imperfection shape with MUSER = 6 axial halfwaves
- ▽ Local buckling margin: General buckling modal imperfection shape with MUSER = 7 axial halfwaves
- ◻ Local buckling margin: General buckling modal imperfection shape with MUSER = 8 axial halfwaves
- ✗ Local buckling margin: General buckling modal imperfection shape with MUSER = 9 axial halfwaves

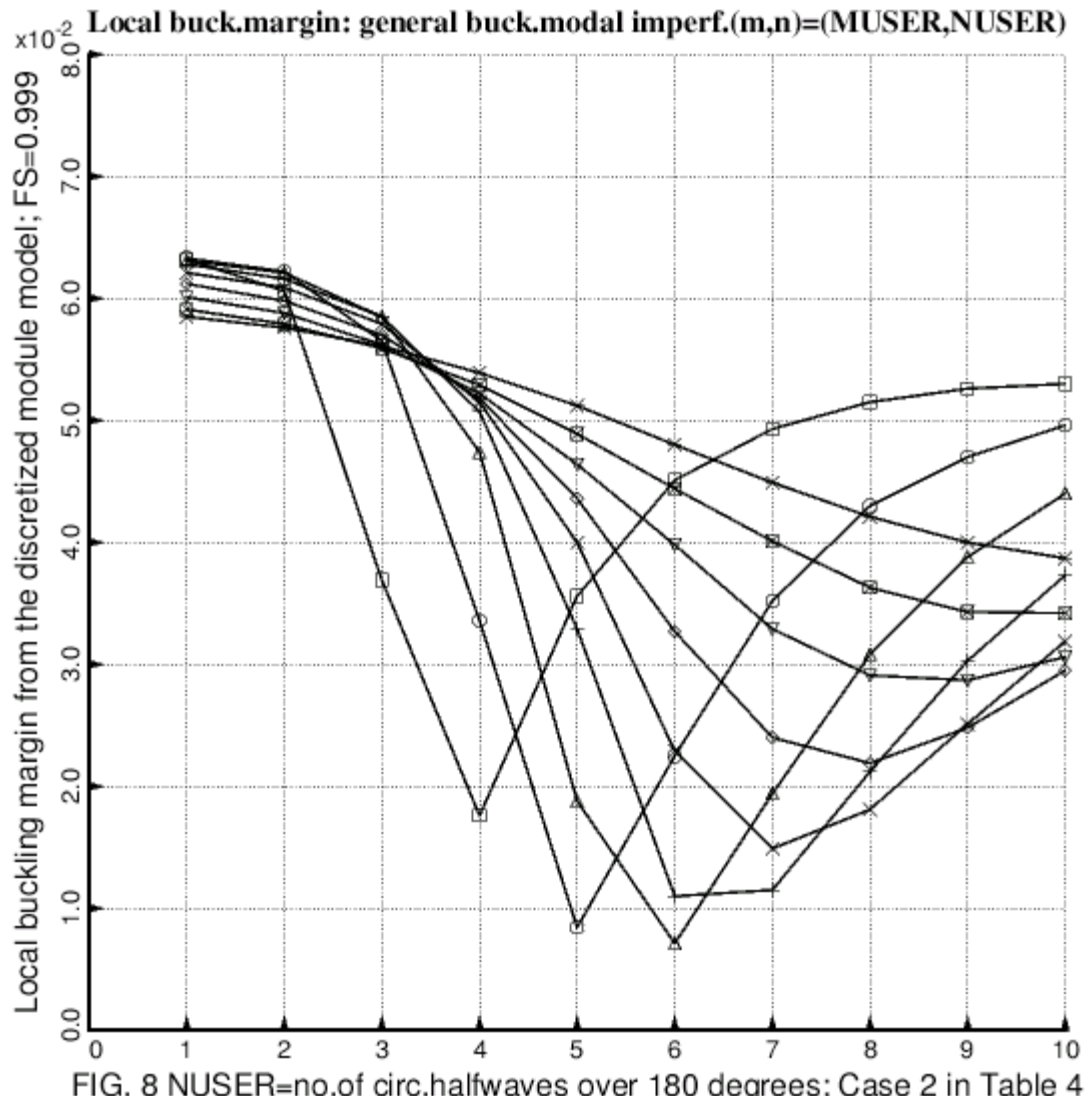


FIG. 8 NUSER=no.of circ.halfwaves over 180 degrees; Case 2 in Table 4

FIG. 8 PANDA2 results: Plotted here is the **local buckling margin** from PANDA2 (Margin No. 1 in the top part of Table 6) for the Case 2 configuration for shells with general buckling modal imperfections with mode shapes (m,n) , $m=MUSER = 1$ to 9 axial halfwaves over the 75-inch axial length of the cylindrical shell and $n=NUSER = 1$ to 10 circumferential halfwaves over 180 degrees of the circumference of the cylindrical shell. The purpose of this (m,n) survey is to determine if the **critical** general buckling mode $(m,n)_{crit} = (4,6)$ determined by PANDA2 (Margin 13 in Table 6) is the “worst” (most harmful) imperfection shape.

- Bending-torsion margin: General buckling modal imperfection shape with MUSER = 1 axial halfwave
- Bending-torsion margin: General buckling modal imperfection shape with MUSER = 2 axial halfwave
- Bending-torsion margin: General buckling modal imperfection shape with MUSER = 3 axial halfwave
- Bending-torsion margin: General buckling modal imperfection shape with MUSER = 4 axial halfwave
- Bending-torsion margin: General buckling modal imperfection shape with MUSER = 5 axial halfwave
- Bending-torsion margin: General buckling modal imperfection shape with MUSER = 6 axial halfwave
- Bending-torsion margin: General buckling modal imperfection shape with MUSER = 7 axial halfwave
- Bending-torsion margin: General buckling modal imperfection shape with MUSER = 8 axial halfwave
- Bending-torsion margin: General buckling modal imperfection shape with MUSER = 9 axial halfwave

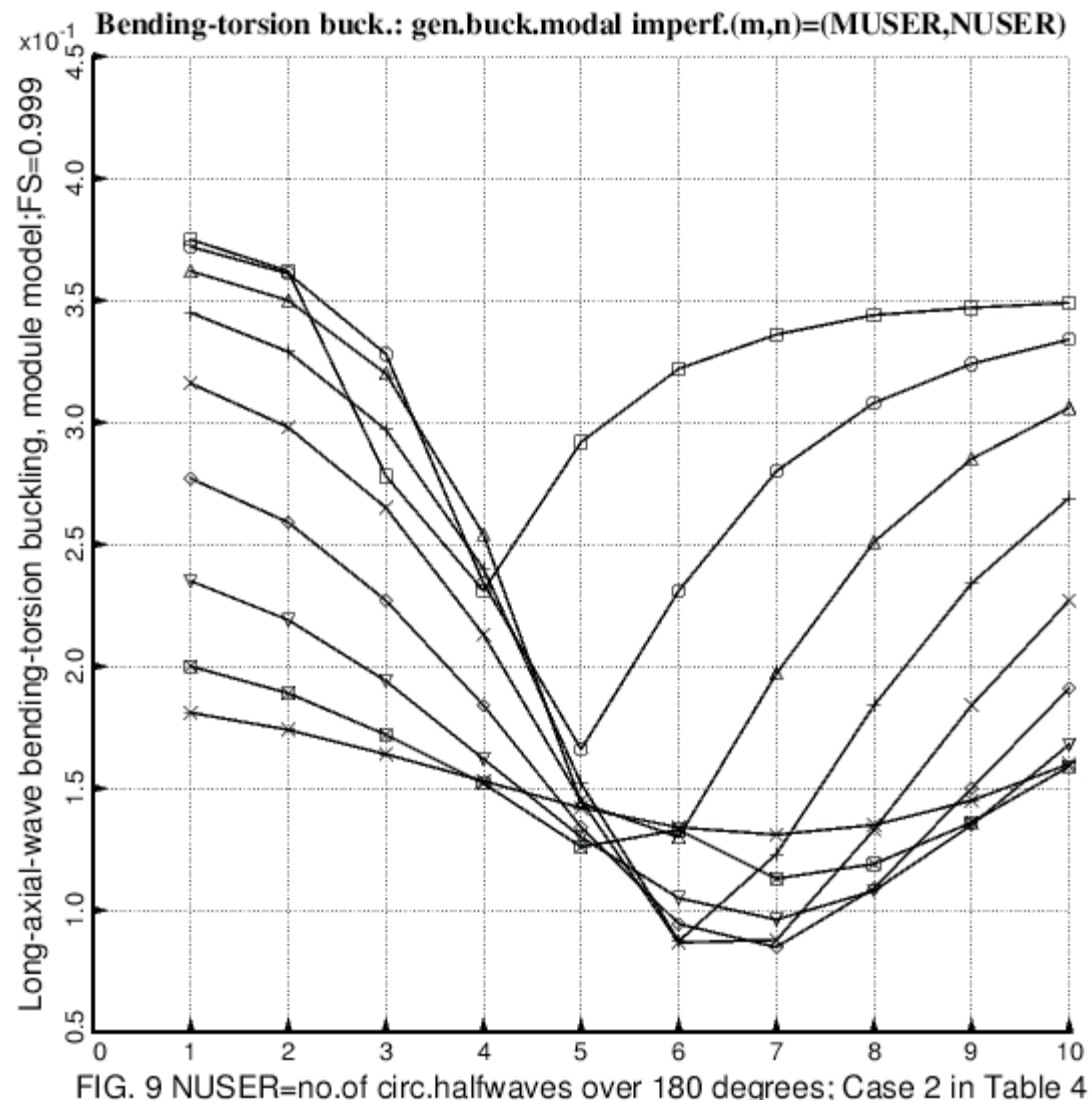


FIG. 9 PANDA2 results: Plotted here is the **bending-torsion buckling margin** from PANDA2 (Margin No. 2 in the top part of Table 6) for the Case 2 configuration for shells with general buckling modal imperfections with mode shapes (m,n) , $m=MUSER = 1$ to 9 axial halfwaves over the 75-inch axial length of the cylindrical shell and $n=NUSER = 1$ to 10 circumferential halfwaves over 180 degrees of the circumference of the cylindrical shell. The purpose of this (m,n) survey is to determine if the **critical** general buckling mode $(m,n)_{crit} = (4,6)$ determined by PANDA2 (Margin 13 in Table 6) is the “worst” (most harmful) imperfection shape.

- vonMises stress margin: General buckling modal imperfection shape with MUSER = 1 axial halfwave
- vonMises stress margin: General buckling modal imperfection shape with MUSER = 2 axial halfwave
- Δ vonMises stress margin: General buckling modal imperfection shape with MUSER = 3 axial halfwave
- $+$ vonMises stress margin: General buckling modal imperfection shape with MUSER = 4 axial halfwave
- \times vonMises stress margin: General buckling modal imperfection shape with MUSER = 5 axial halfwave
- \diamond vonMises stress margin: General buckling modal imperfection shape with MUSER = 6 axial halfwave
- \triangleright vonMises stress margin: General buckling modal imperfection shape with MUSER = 7 axial halfwave
- \blacksquare vonMises stress margin: General buckling modal imperfection shape with MUSER = 8 axial halfwave
- \times vonMises stress margin: General buckling modal imperfection shape with MUSER = 9 axial halfwave

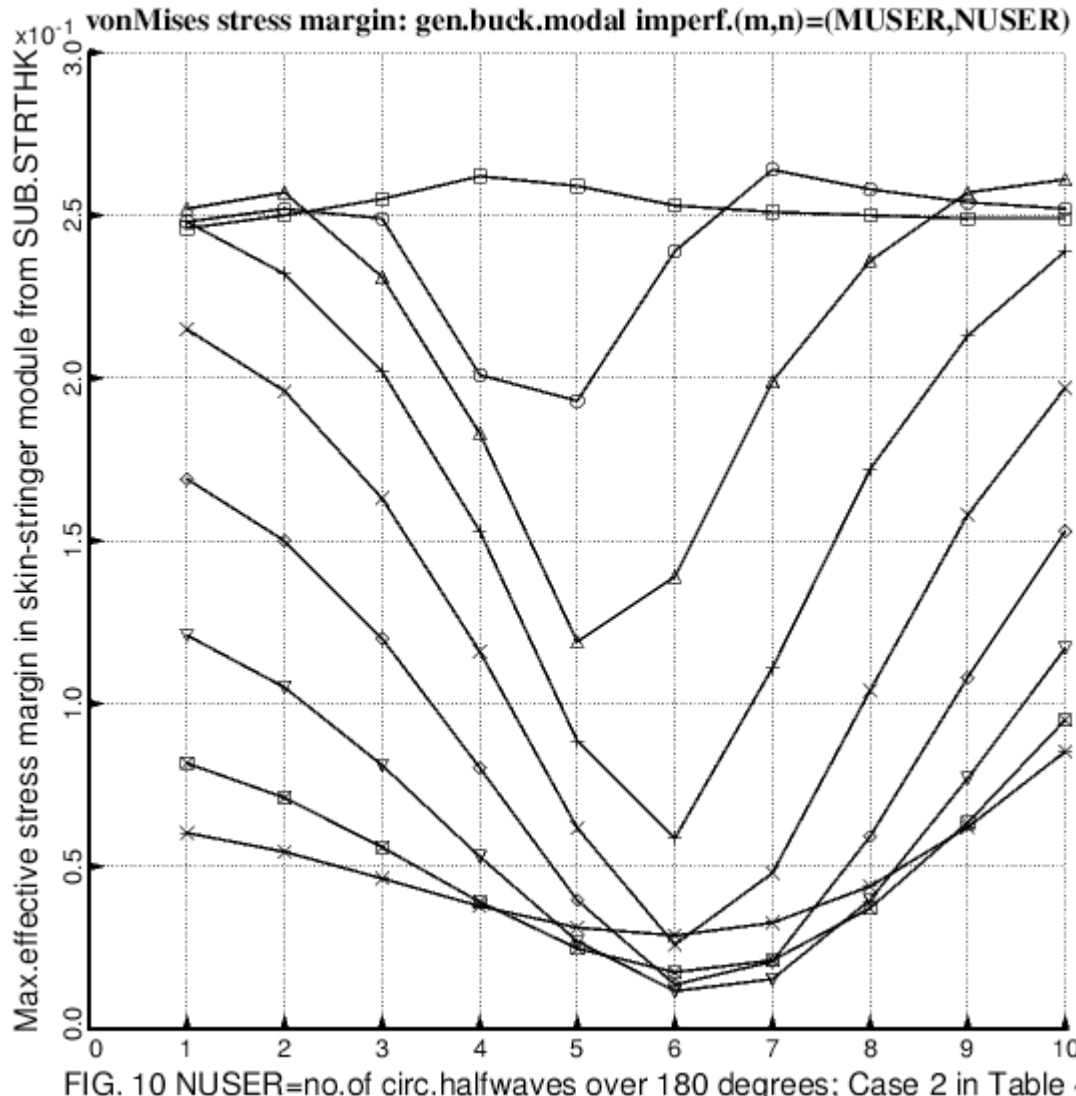


FIG. 10 NUSER=no.of circ.halfwaves over 180 degrees; Case 2 in Table 4

FIG. 10 PANDA2 results: Plotted here is the **1st effective stress margin** from PANDA2 (Margin No. 3 in the top part of Table 6) for the Case 2 configuration for shells with general buckling modal imperfections with mode shapes (m,n) , $m=MUSER = 1$ to 9 axial halfwaves over the 75-inch axial length of the cylindrical shell and $n=NUSER = 1$ to 10 circumferential halfwaves over 180 degrees of the circumference of the cylindrical shell. The purpose of this (m,n) survey is to determine if the **critical** general buckling mode $(m,n)_{crit} = (4,6)$ determined by PANDA2 (Margin 13 in Table 6) is the “worst” (most harmful) imperfection shape.

- Inter-ring buckling margin: General buck. modal imperfection shape with MUSER = 1 axial halfwave
- Inter-ring buckling margin: General buck. modal imperfection shape with MUSER = 2 axial halfwave
- △ Inter-ring buckling margin: General buck. modal imperfection shape with MUSER = 3 axial halfwave
- + Inter-ring buckling margin: General buck. modal imperfection shape with MUSER = 4 axial halfwave
- × Inter-ring buckling margin: General buck. modal imperfection shape with MUSER = 5 axial halfwave
- ◊ Inter-ring buckling margin: General buck. modal imperfection shape with MUSER = 6 axial halfwave
- ▽ Inter-ring buckling margin: General buck. modal imperfection shape with MUSER = 7 axial halfwave
- ☒ Inter-ring buckling margin: General buck. modal imperfection shape with MUSER = 8 axial halfwave
- ✕ Inter-ring buckling margin: General buck. modal imperfection shape with MUSER = 9 axial halfwave

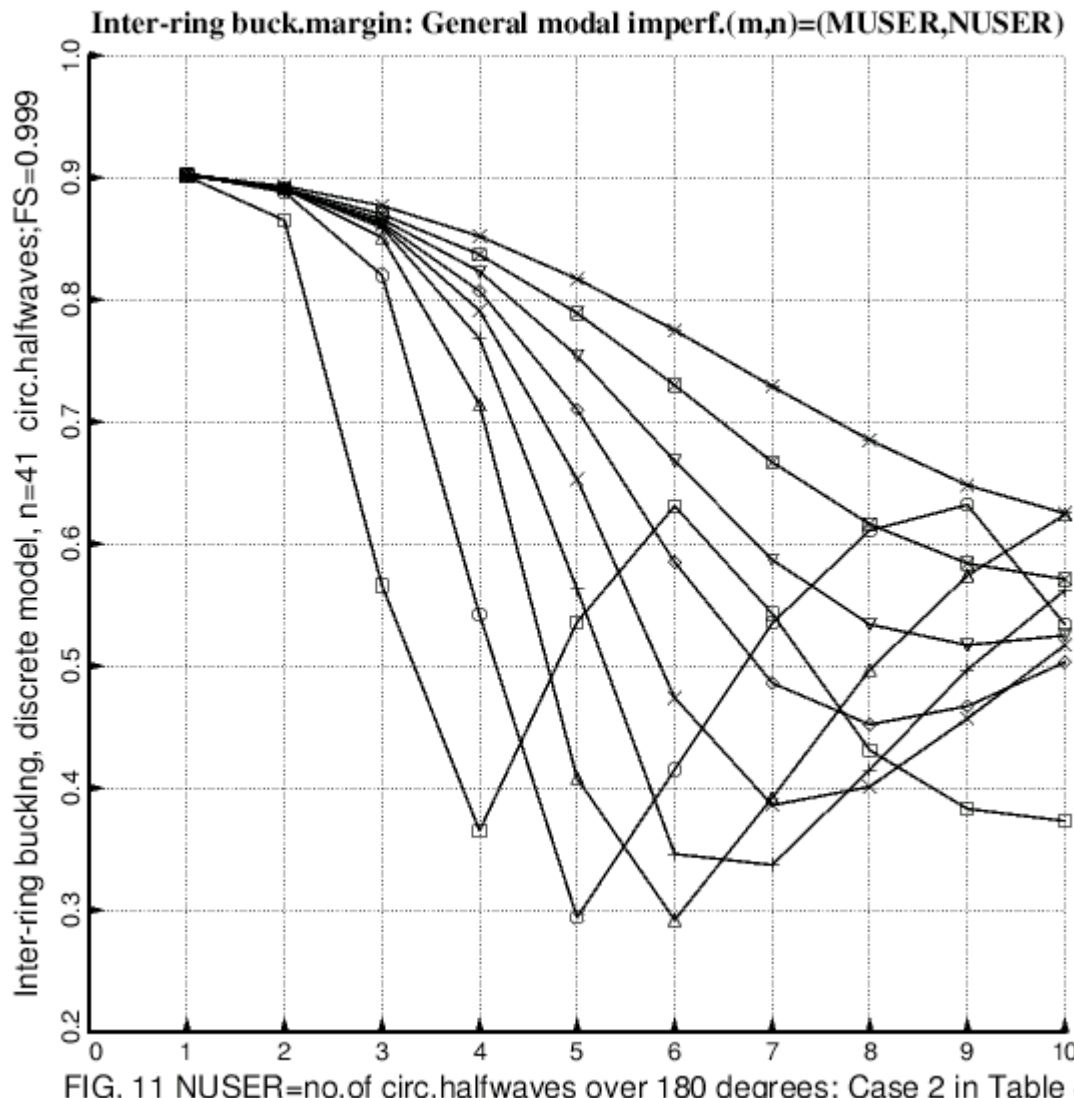


FIG. 11 NUSER=no. of circ. halfwaves over 180 degrees; Case 2 in Table 4

FIG. 11 PANDA2 results: Plotted here is the **inter-ring buckling margin** from PANDA2 (Margin No. 5 in the top part of Table 6) for the Case 2 configuration for shells with general buckling modal imperfections with mode shapes (m,n) , $m=MUSER = 1$ to 9 axial halfwaves over the 75-inch axial length of the cylindrical shell and $n=NUSER = 1$ to 10 circumferential halfwaves over 180 degrees of the circumference of the cylindrical shell. The purpose of this (m,n) survey is to determine if the **critical** general buckling mode $(m,n)_{crit} = (4,6)$ determined by PANDA2 (Margin 13 in Table 6) is the “worst” (most harmful) imperfection shape.

- \square vonMises stress margin: General buckling modal imperfection shape with MUSER = 1 axial halfwave
- \triangle vonMises stress margin: General buckling modal imperfection shape with MUSER = 2 axial halfwave
- $+$ vonMises stress margin: General buckling modal imperfection shape with MUSER = 3 axial halfwave
- \times vonMises stress margin: General buckling modal imperfection shape with MUSER = 4 axial halfwave
- \diamond vonMises stress margin: General buckling modal imperfection shape with MUSER = 5 axial halfwave
- \triangledown vonMises stress margin: General buckling modal imperfection shape with MUSER = 6 axial halfwave
- \blacksquare vonMises stress margin: General buckling modal imperfection shape with MUSER = 7 axial halfwave
- \times vonMises stress margin: General buckling modal imperfection shape with MUSER = 8 axial halfwave
- \times vonMises stress margin: General buckling modal imperfection shape with MUSER = 9 axial halfwave

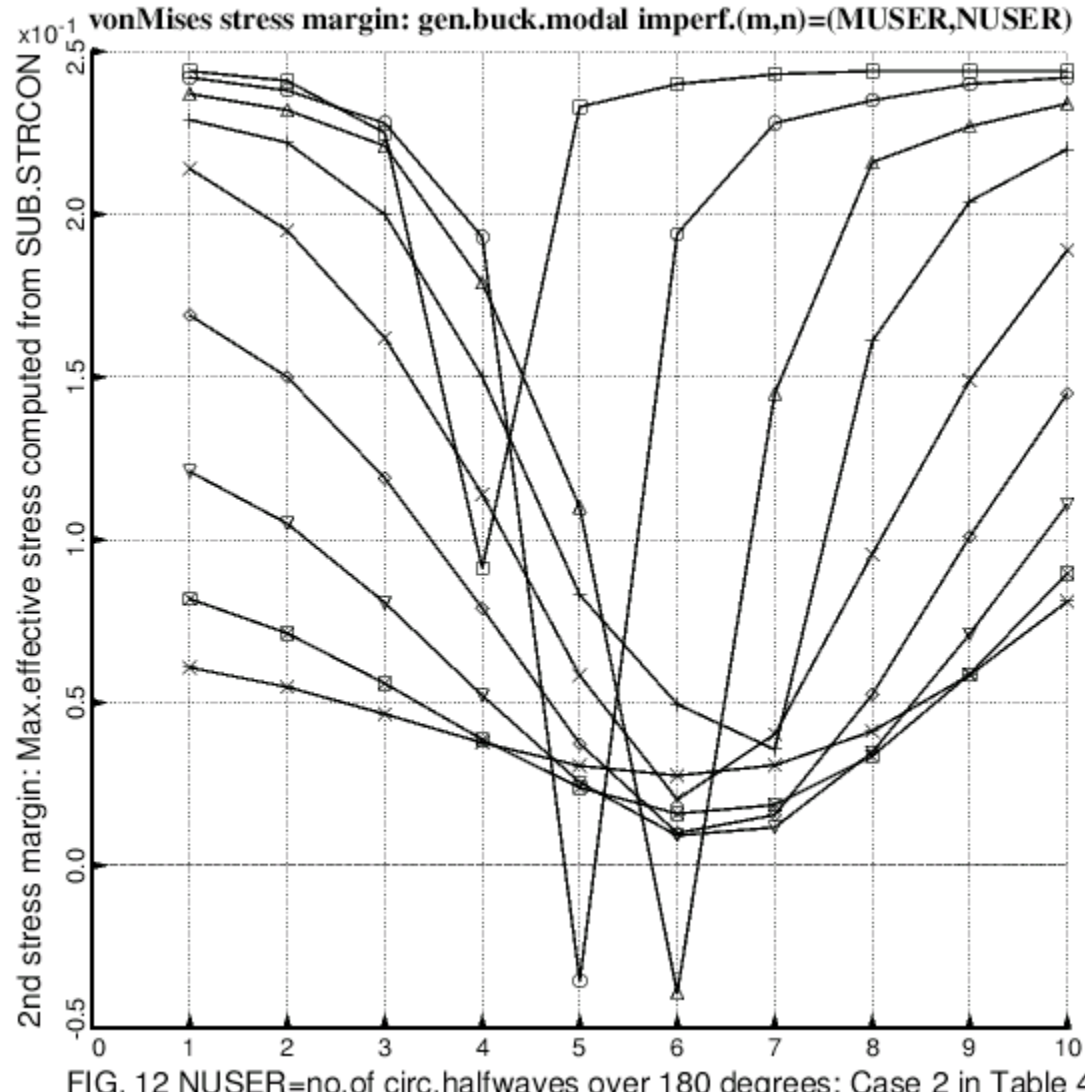


FIG. 12 NUSER=no.of circ.halfwaves over 180 degrees; Case 2 in Table 4

FIG. 12 PANDA2 results: Plotted here is the 2nd effective stress margin from PANDA2 (Margin No. 6 in the top part of Table 6) for the Case 2 configuration for shells with general buckling modal imperfections with mode shapes (m,n) , $m=MUSER = 1$ to 9 axial halfwaves over the 75-inch axial length of the cylindrical shell and $n=NUSER = 1$ to 10 circumferential halfwaves over 180 degrees of the circumference of the cylindrical shell. The purpose of this (m,n) survey is to determine if the critical general buckling mode $(m,n)_{crit} = (4,6)$ determined by PANDA2 (Margin 13 in Table 6) is the “worst” (most harmful) imperfection shape.

□ Stringer segs.3+4 margin: General buckling modal imperfection shape with MUSER = 1 axial halfwave
 □ Stringer segs.3+4 margin: General buckling modal imperfection shape with MUSER = 2 axial halfwave
 □ Stringer segs.3+4 margin: General buckling modal imperfection shape with MUSER = 3 axial halfwave
 □ Stringer segs.3+4 margin: General buckling modal imperfection shape with MUSER = 4 axial halfwave
 □ Stringer segs.3+4 margin: General buckling modal imperfection shape with MUSER = 5 axial halfwave
 □ Stringer segs.3+4 margin: General buckling modal imperfection shape with MUSER = 6 axial halfwave
 □ Stringer segs.3+4 margin: General buckling modal imperfection shape with MUSER = 7 axial halfwave
 □ Stringer segs.3+4 margin: General buckling modal imperfection shape with MUSER = 8 axial halfwave
 □ Stringer segs.3+4 margin: General buckling modal imperfection shape with MUSER = 9 axial halfwave

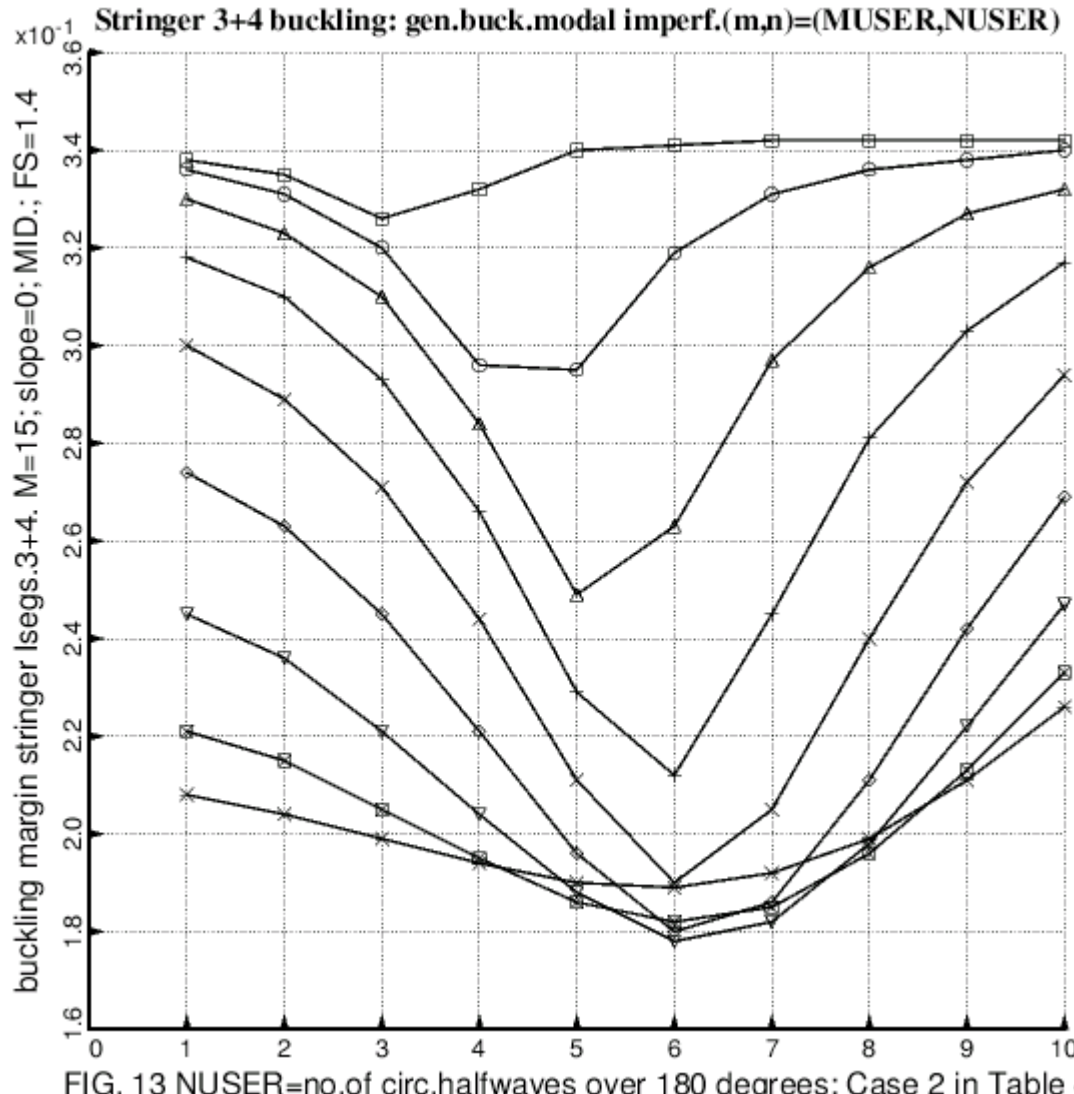


FIG. 13 NUSER=no.of circ.halfwaves over 180 degrees; Case 2 in Table 4

FIG. 13 PANDA2 results: Plotted here is the “stringer Segment 3+4” buckling margin from PANDA2 (Margin No. 9 in the top part of Table 6) for the Case 2 configuration for shells with general buckling modal imperfections with mode shapes (m,n) , $m=MUSER = 1$ to 9 axial halfwaves over the 75-inch axial length of the cylindrical shell and $n=NUSER = 1$ to 10 circumferential halfwaves over 180 degrees of the circumference of the cylindrical shell. The purpose of this (m,n) survey is to determine if the **critical** general buckling mode $(m,n)_{crit} = (4,6)$ determined by PANDA2 (Margin 13 in Table 6) is the “worst” (most harmful) imperfection shape.

- \square General buckling margin: General buckling modal imperfection shape with MUSER = 1 axial halfwave
- \circ General buckling margin: General buckling modal imperfection shape with MUSER = 2 axial halfwave
- \triangle General buckling margin: General buckling modal imperfection shape with MUSER = 3 axial halfwave
- $+$ General buckling margin: General buckling modal imperfection shape with MUSER = 4 axial halfwave
- \times General buckling margin: General buckling modal imperfection shape with MUSER = 5 axial halfwave
- \diamond General buckling margin: General buckling modal imperfection shape with MUSER = 6 axial halfwave
- \triangledown General buckling margin: General buckling modal imperfection shape with MUSER = 7 axial halfwave
- \blacksquare General buckling margin: General buckling modal imperfection shape with MUSER = 8 axial halfwave
- \times General buckling margin: General buckling modal imperfection shape with MUSER = 9 axial halfwave

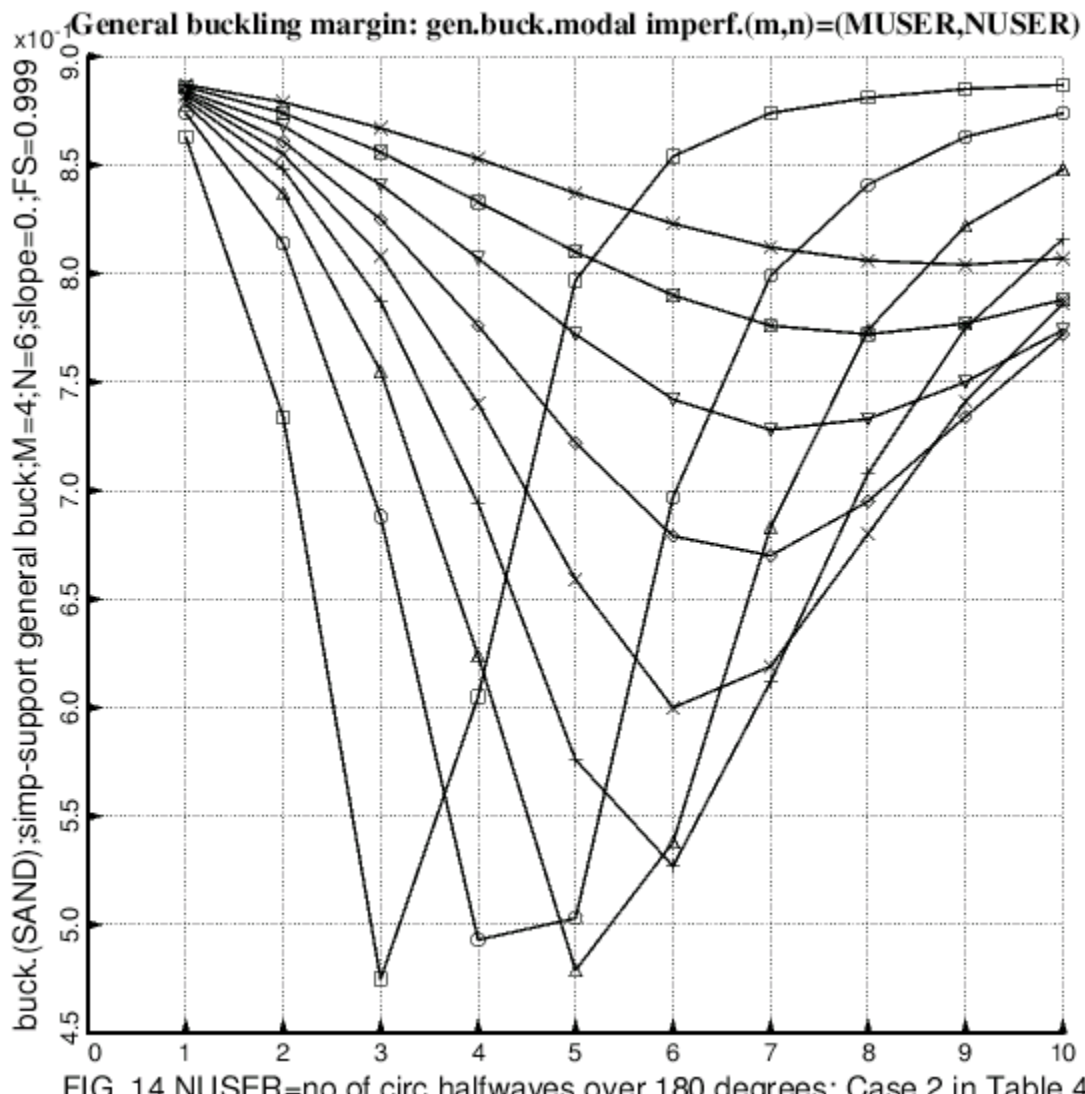


FIG. 14 NUSER=no.of circ.halfwaves over 180 degrees; Case 2 in Table 4

FIG. 14 PANDA2 results: Plotted here is the **general buckling margin** from PANDA2 (Margin No. 13 in the top part of Table 6) for the Case 2 configuration for shells with general buckling modal imperfections with mode shapes (m,n) , $m=MUSER = 1$ to 9 axial halfwaves over the 75-inch axial length of the cylindrical shell and $n=NUSER = 1$ to 10 circumferential halfwaves over 180 degrees of the circumference of the cylindrical shell. The purpose of this (m,n) survey is to determine if the **critical** general buckling mode $(m,n)_{crit} = (4,6)$ determined by PANDA2 (Margin 13 in Table 6) is the “worst” (most harmful) imperfection shape.

- stringer rolling margin: General buckling modal imperfection shape with MUSER = 1 axial halfwave
- stringer rolling margin: General buckling modal imperfection shape with MUSER = 2 axial halfwave
- △ stringer rolling margin: General buckling modal imperfection shape with MUSER = 3 axial halfwave
- + stringer rolling margin: General buckling modal imperfection shape with MUSER = 4 axial halfwave
- × stringer rolling margin: General buckling modal imperfection shape with MUSER = 5 axial halfwave
- ◊ stringer rolling margin: General buckling modal imperfection shape with MUSER = 6 axial halfwave
- ▽ stringer rolling margin: General buckling modal imperfection shape with MUSER = 7 axial halfwave
- ⊗ stringer rolling margin: General buckling modal imperfection shape with MUSER = 8 axial halfwave
- ✗ stringer rolling margin: General buckling modal imperfection shape with MUSER = 9 axial halfwave

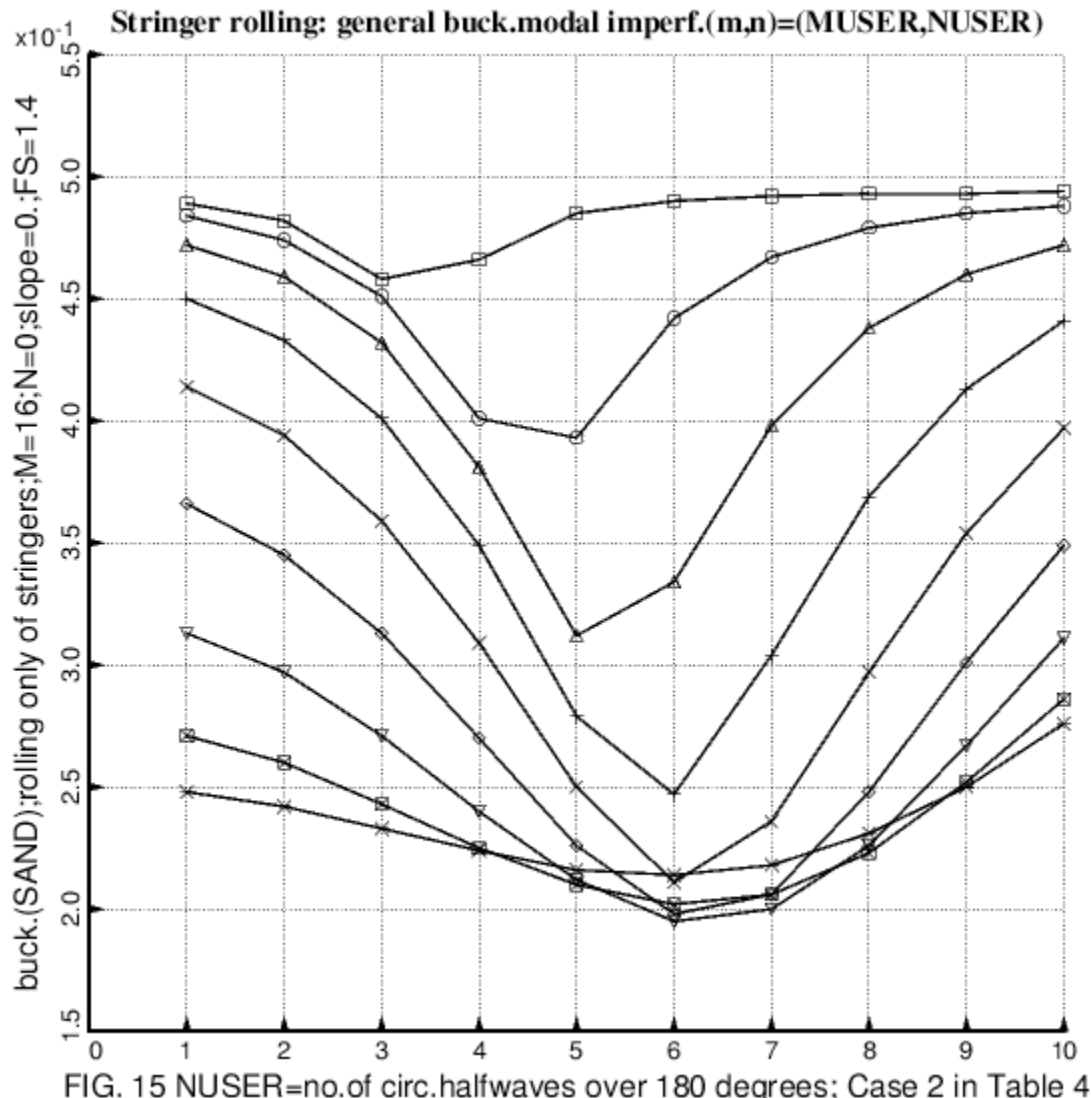
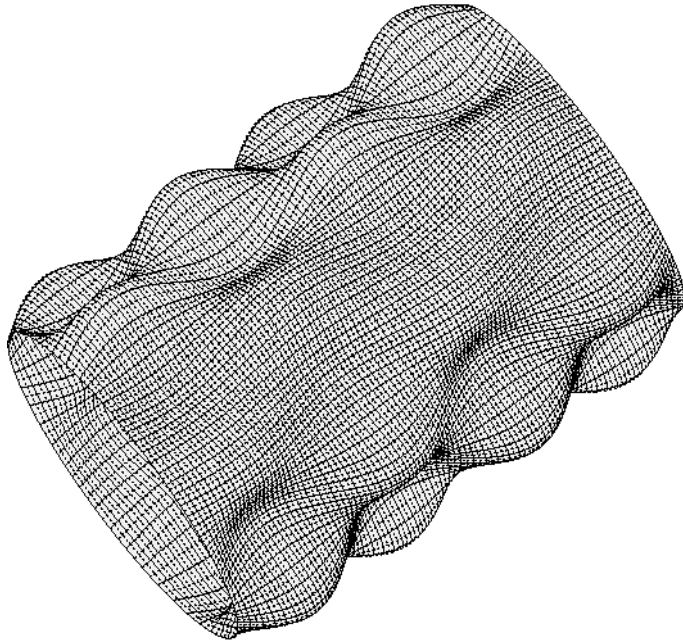


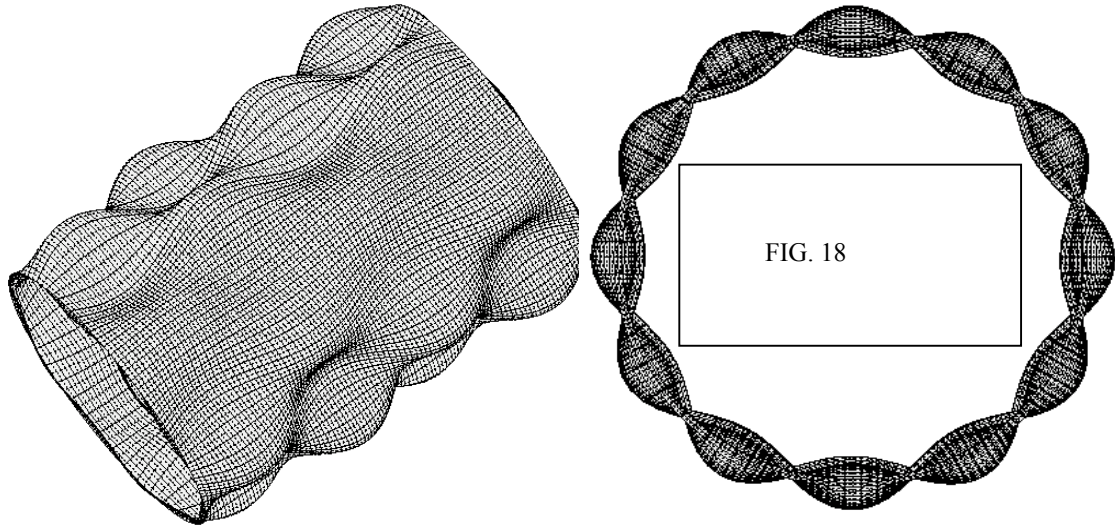
FIG. 15 NUSER=no. of circ. halfwaves over 180 degrees; Case 2 in Table 4

FIG. 15 PANDA2 results: Plotted here is the **stringer rolling margin** from PANDA2 (Margin No. 15 in the top part of Table 6) for the Case 2 configuration for shells with general buckling modal imperfections with mode shapes (m,n) , $m=MUSER = 1$ to 9 axial halfwaves over the 75-inch axial length of the cylindrical shell and $n=NUSER = 1$ to 10 circumferential halfwaves over 180 degrees of the circumference of the cylindrical shell. The purpose of this (m,n) survey is to determine if the **critical** general buckling mode $(m,n)_{crit} = (4,6)$ determined by PANDA2 (Margin 13 in Table 6) is the “worst” (most harmful) imperfection shape.



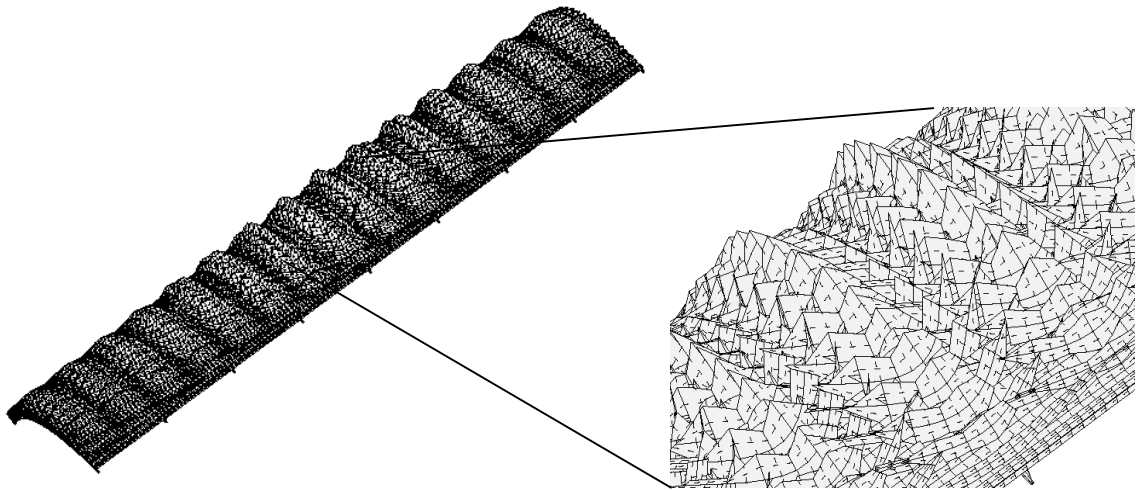
STAGS model of Case 2, Table 4: no Koiter, yes change imperfection, ICONSV = -1. Compare with Fig. 17. STAGS Mode no. 1, load factor, pcr=1.9189; PANDA2 predicts a load factor of 1.890. The linear buckling mode agrees with that from PANDA2: $(m,n)=(4 \text{ axial}, 6 \text{ circumferential})$ halfwaves over 180 degrees of the circumference of the cylindrical shell. See Part 1, Run 1 of Table 9.

FIG. 16 Linear general buckling mode from the STAGS model with all stiffeners smeared.



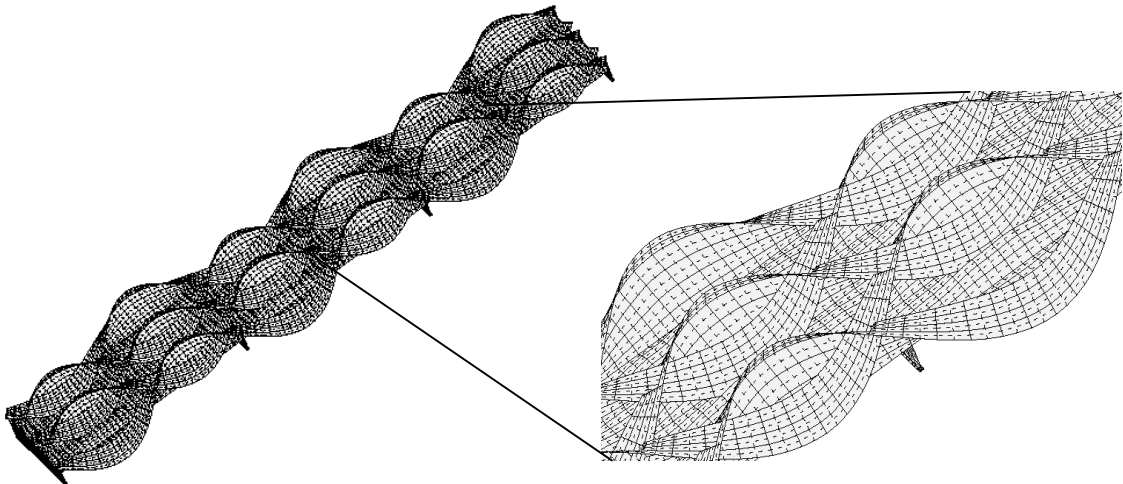
STAGS model of Case 2, Table 4: no Koiter, yes change imperfection, ICONSV = -1; Compare with Fig. 16. STAGS Mode no. 1, load factor, pcr=1.9017; PANDA2 predicts 1.890. The linear buckling mode agrees with that from PANDA2: $(m,n)=(4 \text{ axial}, 6 \text{ circumferential})$ halfwaves over 180 deg. See Part 1, Run 2 in Table 9. This STAGS model and the model in the previous figure are used to obtain good approximations of the general buckling mode shape and load factor (eigenvalue) for two reasons: 1. Determine what circumferential sector to use for more refined models (60 degrees is good in this case), and 2. Obtain a good estimate of the initial eigenvalue “shift” to use in the more refined STAGS models. A good initial value of the eigenvalue “shift” is essential in order to find the critical general buckling mode, which is hidden in a “thicket” of local buckling modes in the eigenvalue spectrum of STAGS models in which both the stringers and the rings are modeled as shell units.

FIGs. 17, 18 Linear general buckling mode from the STAGS model. Only the stringers are smeared. The rings are modeled as shell units, 2 shell units per ring: Shell unit (a) for the ring web and Shell unit (b) for the ring outstanding flange.



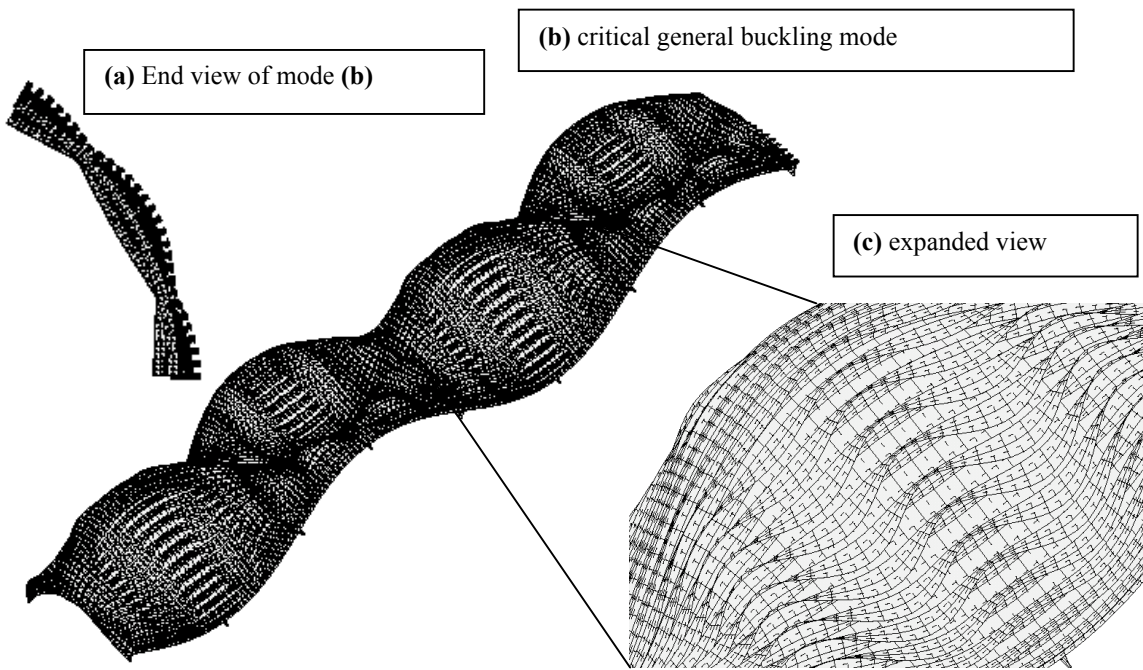
STAGS model of Case 2, Table 4: no Koiter, yes change imperfection, ICONSV = -1; Compare with Fig. 20a. STAGS Mode no. 1; load factor, pcr=1.4017; BIGBOSOR4 predicts a load factor, 1.28908. In Load set 1, PANDA2 predicts 1.378 in Subcase 1 and 1.291 in Subcase 2. This mode has a significant component of short-wavelength local buckling mixed with the longer wavelength bending-torsion buckling. See Part 1, Run 3 in Table 9

FIG. 19 Linear bending-torsion buckling mode from STAGS 60-degree model with uniform mesh. All stiffeners are modeled as shell units.



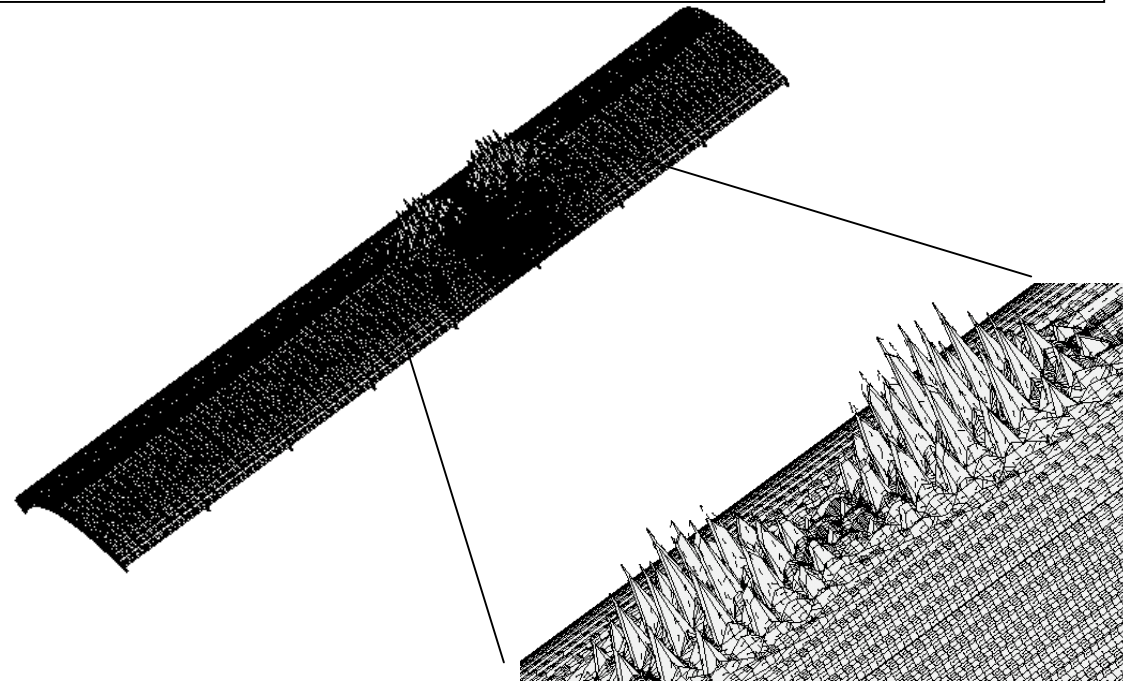
STAGS model of Case 2, Table 4: no Koiter, yes change imperfection, ICONSV = -1; Compare with Fig. 19. Mode No. ? (The lowest bending-torsion mode is hidden among many local modes). STAGS load factor, pcr=1.3826; BIGBOSOR4 predicts a load factor, 1.28908. In Load set 1, PANDA2 predicts 1.378 in Subcase 1 and 1.291 in Subcase 2. See Part 1, Run 4 in Table 9.

FIG. 20a Linear bending-torsion buckling mode from STAGS sub-domain model with uniform mesh. All stiffeners are modeled as shell units, 2 units/stiffener: Unit (a) = web and Unit (b) = outstanding flange.



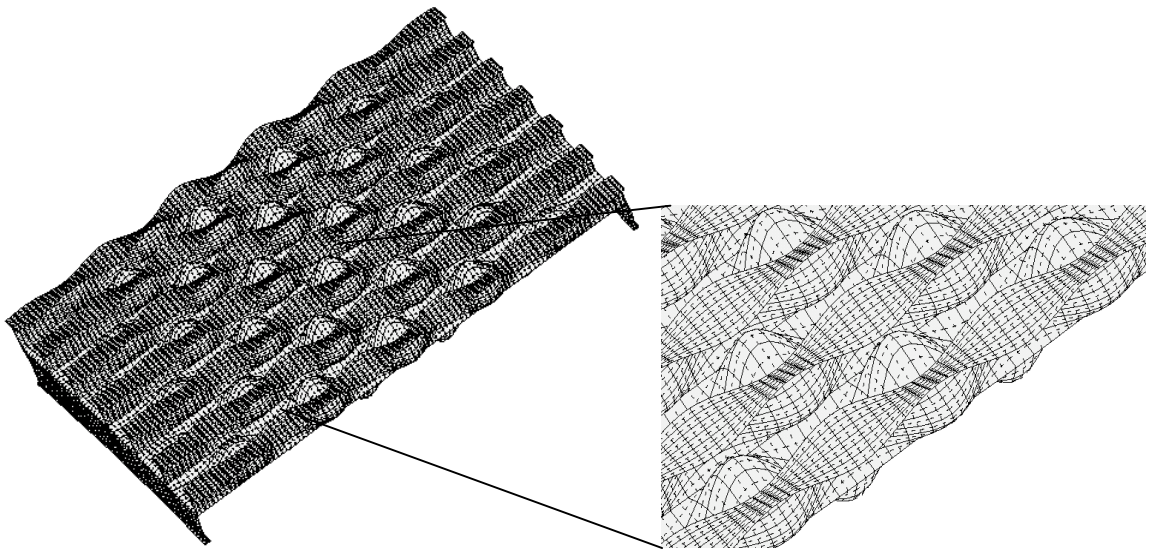
STAGS model of Case 2, Table 4: no Koiter, yes change imperfection, ICONSV = -1; Compare with Fig. 24. STAGS Mode no. 861; load factor, pcr=1.8968; PANDA2 predicts 1.890. General buckling load factor from BIGBOSOR4 = 1.8767 (\mathbf{m}, \mathbf{n})=(4,6). See Part 1, Runs 5,6,7 in Table 9.

FIG. 21a Linear general buckling mode from the STAGS 60-degree model with a uniform mesh. Note from the expanded view (c) the significant component of stringer bending-torsion buckling in the general buckling mode shape.



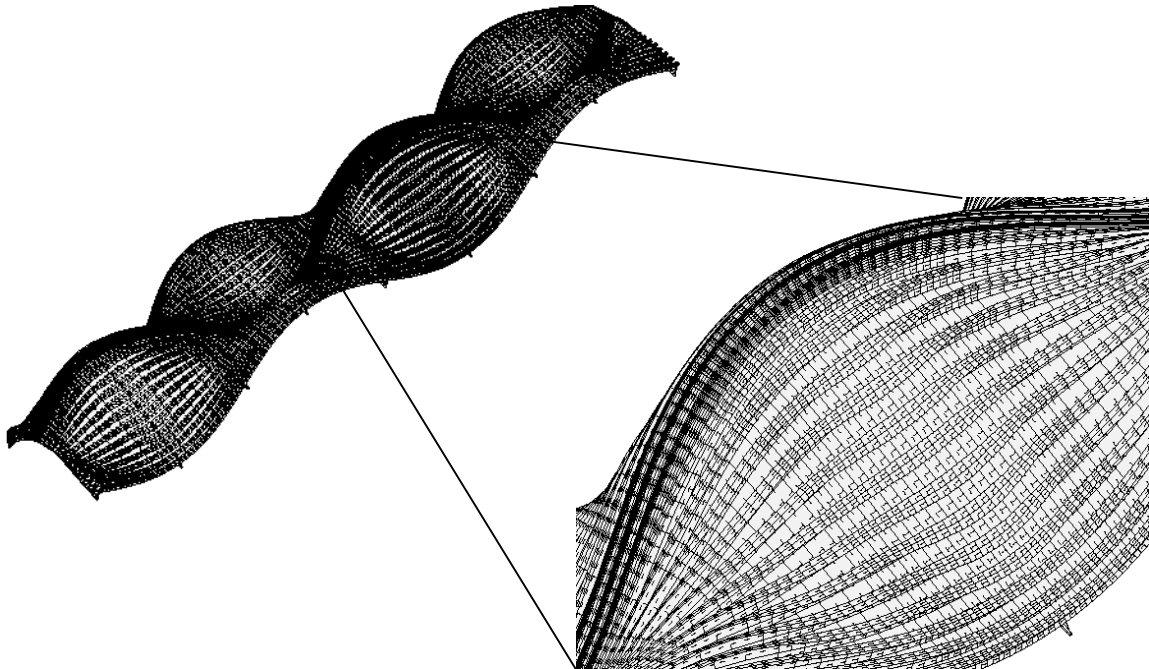
STAGS model of Case 2, Table 4: no Koiter, yes change imperfection, ICONSV = -1; Compare with Fig. 23a. STAGS Mode no. 1; load factor, pcr=1.1137. PANDA2 predicts a load factor, 1.0636, with $\mathbf{m}=11$ axial halfwaves between rings. BIGBOSOR4 predicts a load factor, 1.0862, with $\mathbf{m} = 11$ axial halfwaves between rings. See Part 1, Run 8 in Table 9.

FIG. 22 Linear local buckling mode from the STAGS 60-degree model with a non-uniform mesh.



STAGS model of Case 2, Table 4: no Koiter, yes change imperfection, ICONSV = -1. Compare with Fig. 22. STAGS Mode No. 1; load factor, pcr=1.0758. PANDA2 predicts a load factor, 1.0636, with $\mathbf{m}=11$ axial halfwaves between rings. BIGBOSOR4 predicts a load factor, 1.0862, with $\mathbf{m}=11$ axial halfwaves between rings. See Part 1, Run 9 in Table 9.

FIG. 23a Linear local buckling mode from a STAGS subdomain model with a refined mesh.



STAGS model of Case 2, Table 4: no Koiter, yes change imperfection, ICONSV = -1. See Part 4 in Table 9. STAGS Mode no. 610; load factor, pcr=1.8931. PANDA2 predicts 1.890. General buckling load factor from BIGBOSOR4 = 1.8767 (\mathbf{m}, \mathbf{n}) = (4 axial halfwaves, 6 circumferential full waves).

FIG. 24 Linear general buckling mode from the STAGS 60-degree model with a nonuniform mesh.

There is a small component of stringer bending-torsion buckling mixed with the general buckling mode. Compare with Fig. 21a.

— — Undeformed: An arc of the stiffened cylindrical shell is modeled as a huge torus [26].
 — Deformed: bending-torsion buckling; PANDA2 gets 1.291 in subcase 2; This is Case 2 in Table 4

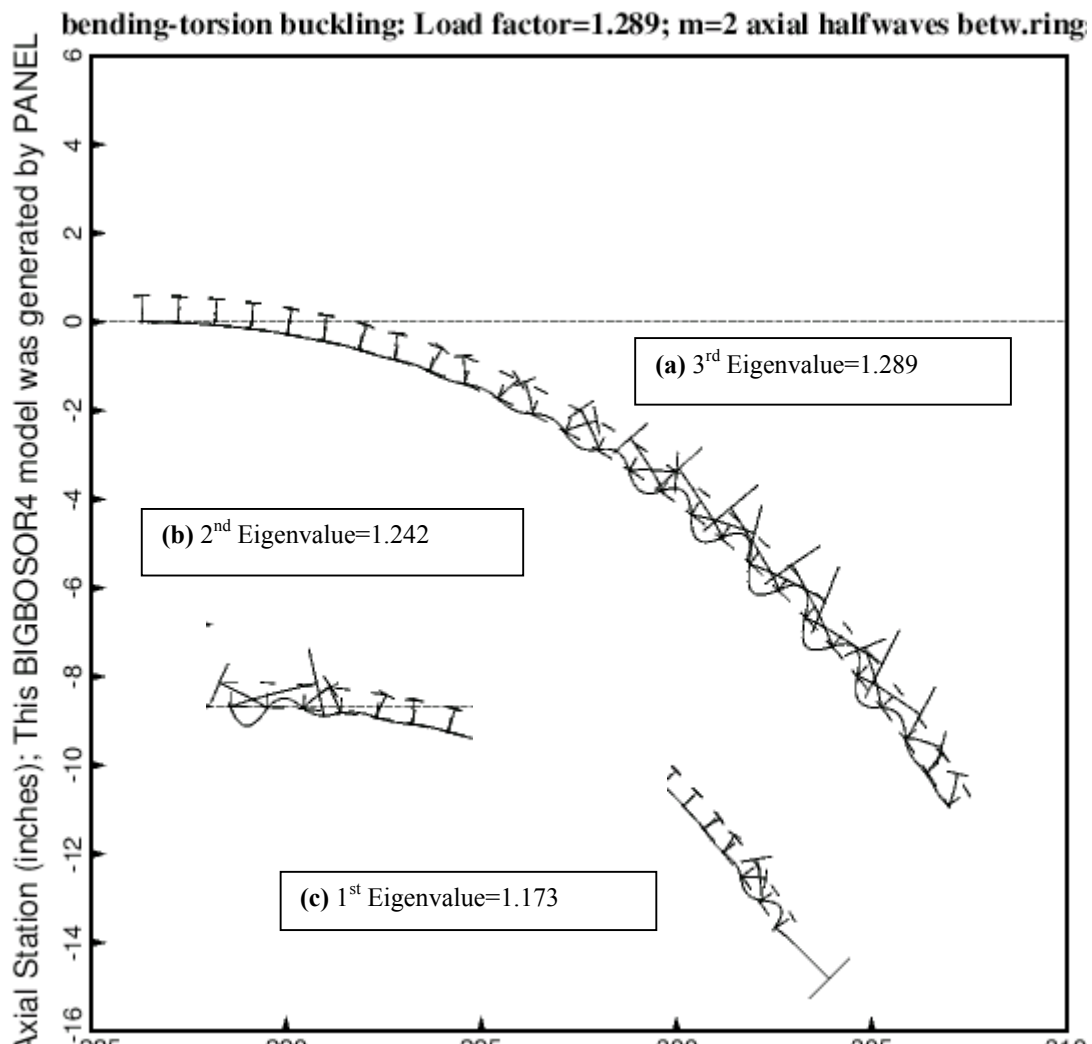


FIG. 20b BIGBOSOR4 [14] model of buckling between rings; Radius (inches)

FIG. 20b BIGBOSOR4 model of Case 2 in Table 4: Results from a BIGBOSOR4 model generated by the PANDA2 processor called PANEL. This figure shows bending-torsion buckling between rings (same buckling mode as that corresponding to PANDA2's Margin 2 in both the upper and lower parts of Table 7). This BIGBOSOR4 model is a huge toroidal segment [26] with radius to the center of meridional curvature of about 286 inches. The axial variation of the critical buckling modal displacement is trigonometric with $m = 2$ axial halfwaves between rings ($N=200$ circumferential waves around the huge torus). The axial coordinate direction for the cylindrical shell is normal to the plane of the paper in this figure. The “critical” buckling mode of interest (a) happens to correspond, in this particular case, to the 3rd eigenvalue computed for $N = 200$. The 1st and 2nd eigenvalues for $N = 200$, inserts (c) and (b), correspond to edge buckling, not permitted in the PANDA2 or STAGS models and therefore not of interest in the comparison of predictions from BIGBOSOR4 with those from PANDA2 and STAGS.

— — Undeformed; PANDA2 gets load factor=1.890 ($m,n)=(4$ axial, 6 circumferential) waves.
 — Deformed: STAGS gets load factor=1.902 (Fig.17), 1.0893(Fig.24); This is Case 2 in Table 4

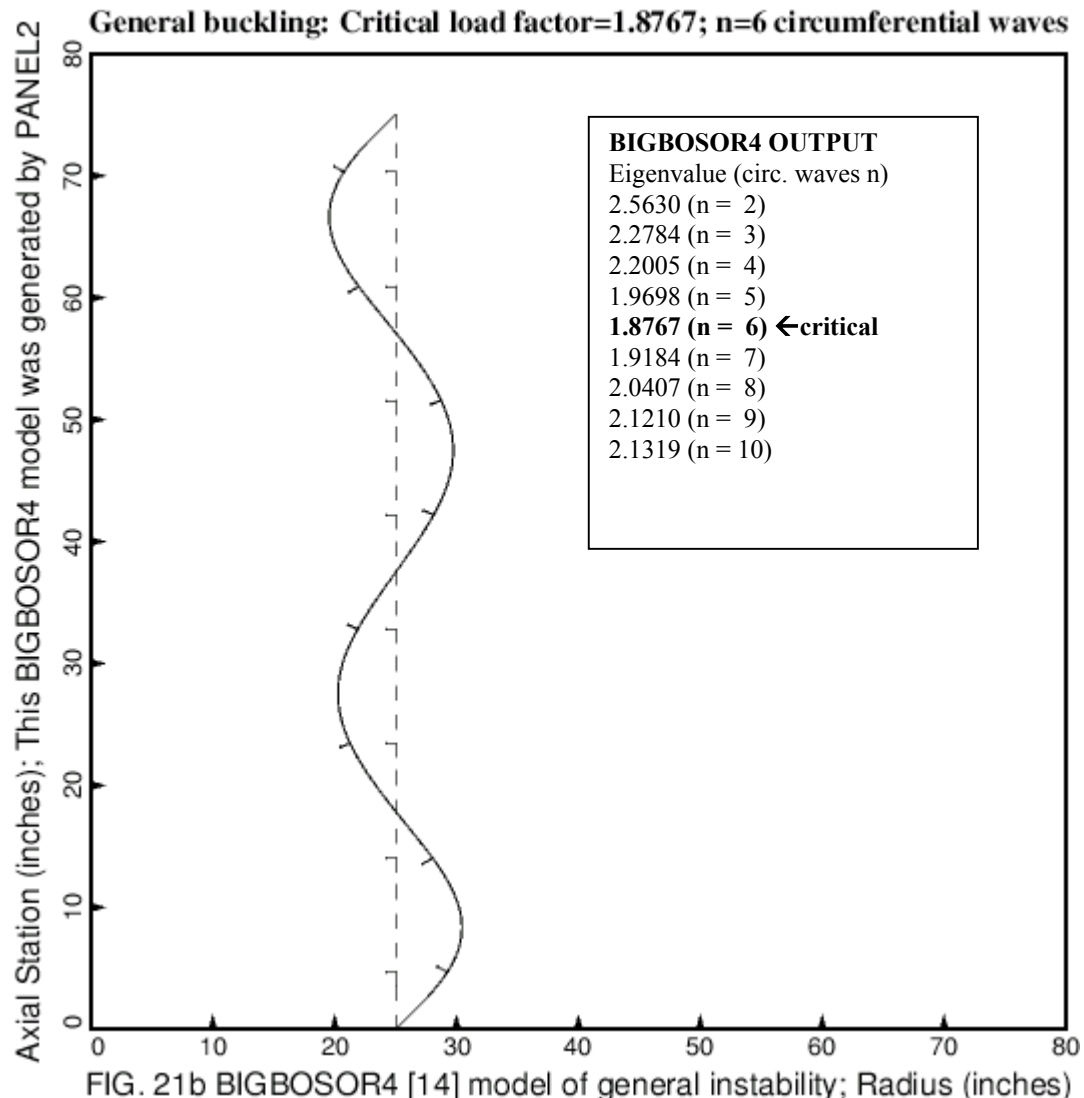


FIG. 21b BIGBOSOR4 [14] model of general instability; Radius (inches)

Fig. 21b BIGBOSOR4 model of Case 2 in Table 4: Results from a BIGBOSOR4 model generated by the PANDA2 processor called PANEL2. This figure shows the critical general buckling mode for Case 2 (same as that corresponding to PANDA2's Margin 11 in the upper part of Table 7). The outstanding flanges of the internal rings are very narrow and therefore are hardly visible in this figure. Circumferential variation of the buckling modal displacement, trigonometric with $n = 6$ full circumferential waves, is in the coordinate direction normal to the plane of the paper in this figure.

—— Undeformed: An arc of the stiffened cylindrical shell is modeled as a huge torus [26].
 —— Deformed: local buckling; PANDA2 gets 1.0636; STAGS gets 1.0758 (Fig. 23a); Case 2 in Table 4

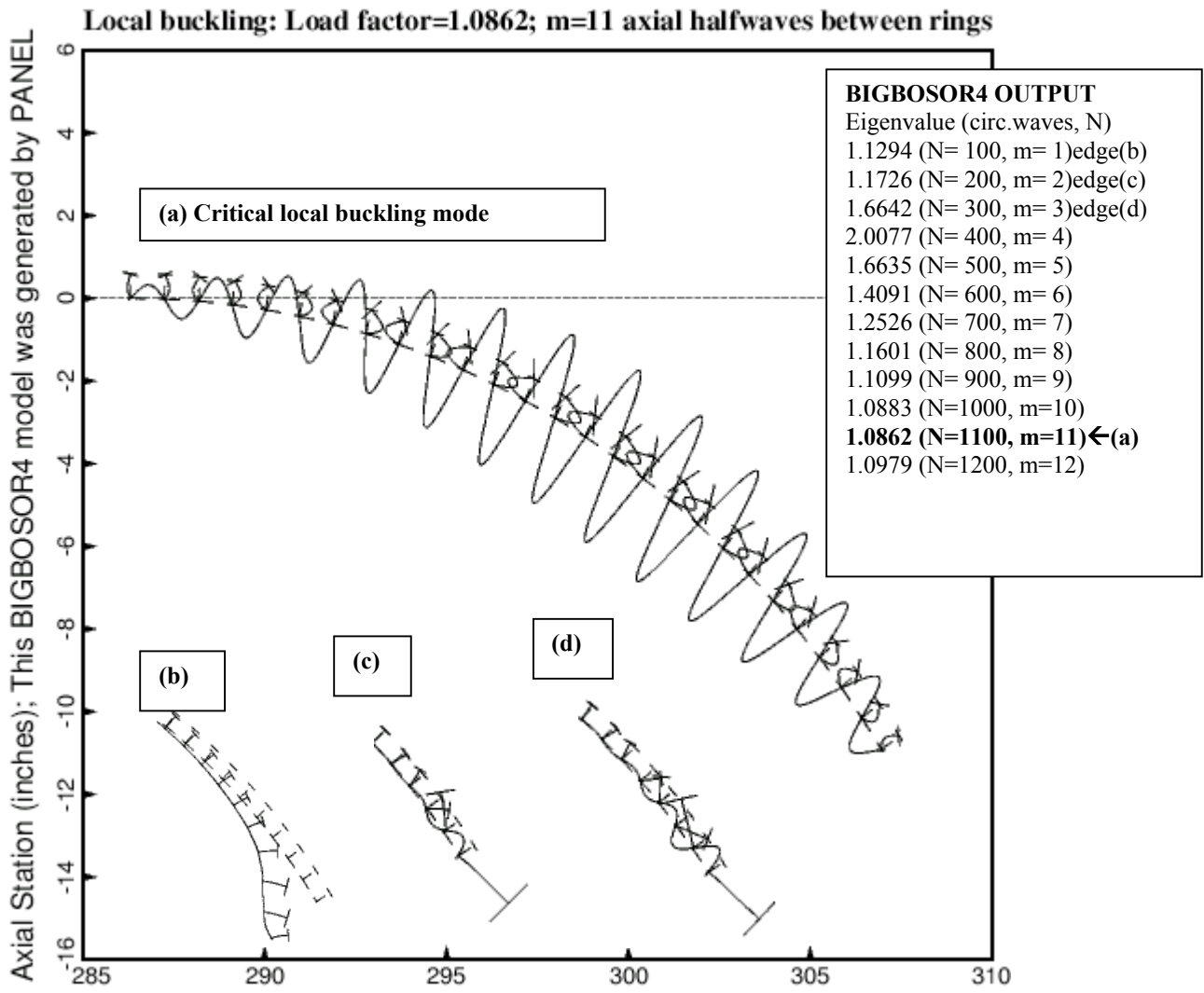
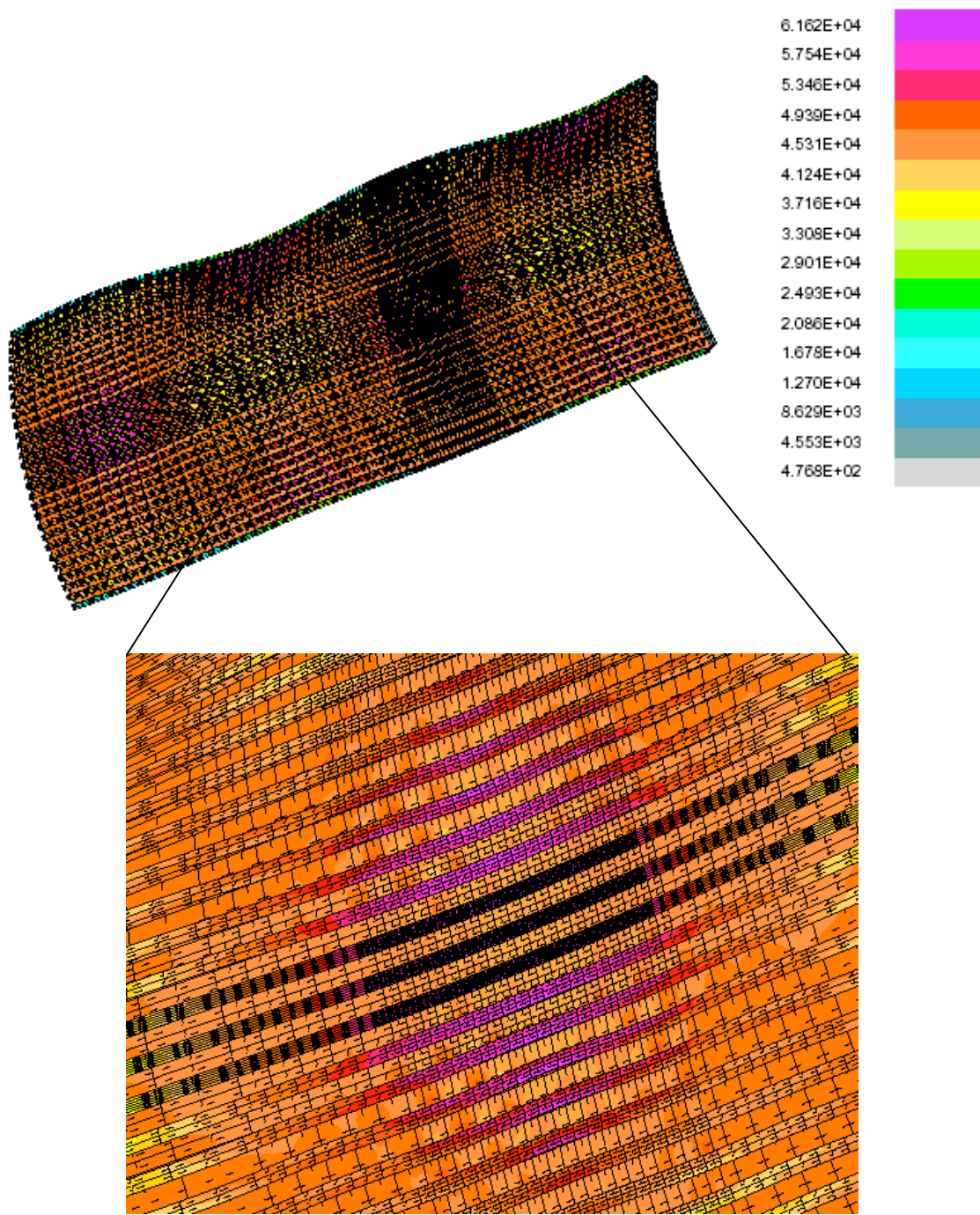


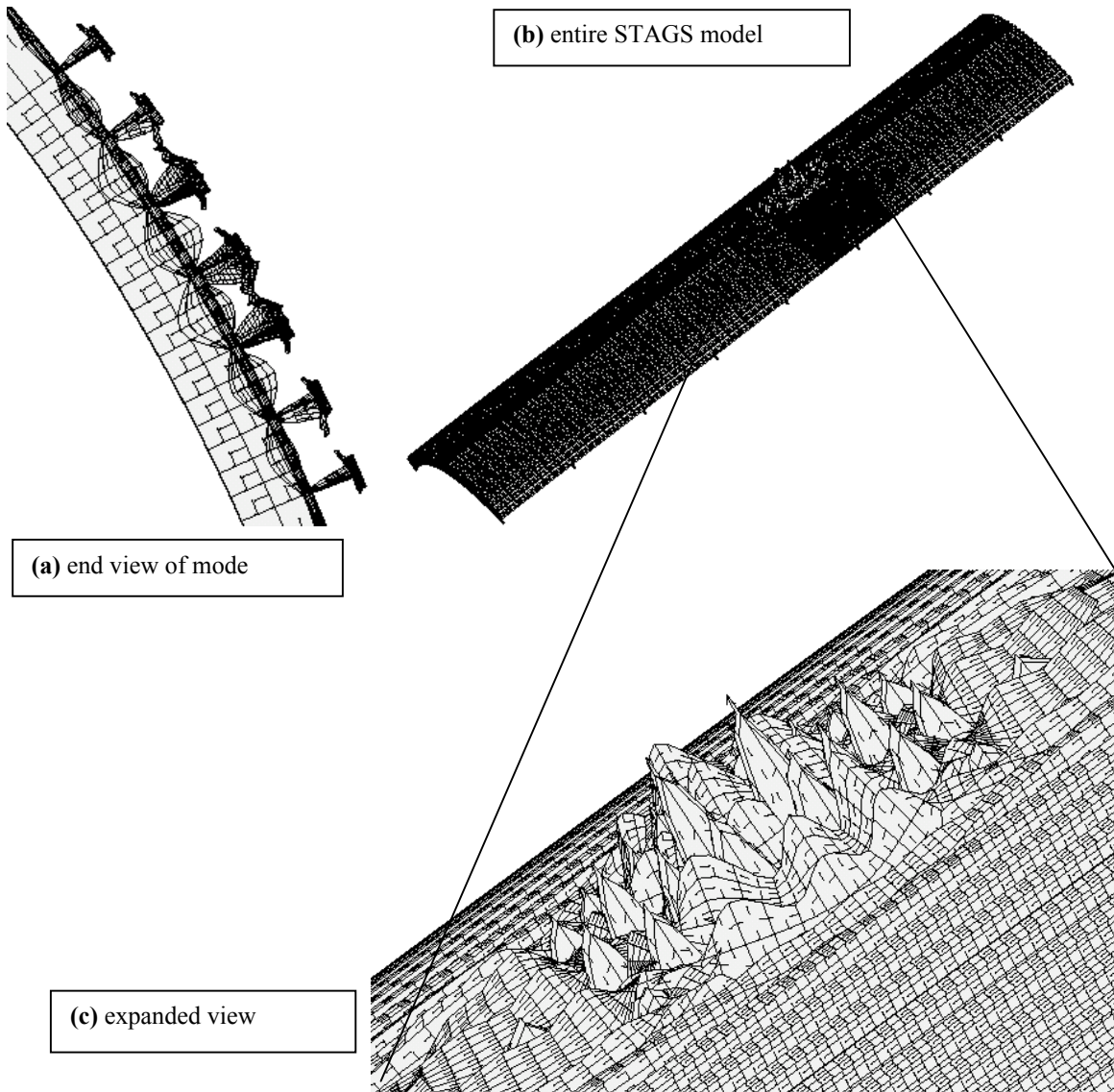
FIG. 23b BIGBOSOR4 [14] model of buckling between rings; Radius (inche

FIG. 23b BIGBOSOR4 model of Case 2 in Table 4: Results from a BIGBOSOR4 model generated by the PANDA2 processor called PANEL. This figure shows local buckling between rings (same critical buckling mode as that listed as PANDA2's Margin 1 in both the upper and lower parts of Table 7). The BIGBOSOR4 "torus" model is the same as that displayed in Fig. 20b. Only the critical number of axial halfwaves between rings, $m=11$, is different from that given in Fig. 20b. The three inserts, (b), (c), (d), near the bottom of the figure show "edge" buckling modes corresponding to $m = 1, 2$, and 3 axial halfwaves between rings. The buckling modes for all other m resemble that displayed in (a). Since edge buckling is not permitted in the PANDA2 and STAGS models, the edge buckling modes, (b), (c), (d), are not of interest and are therefore disregarded in the comparison of BIGBOSOR4 predictions with those from PANDA2 and STAGS.



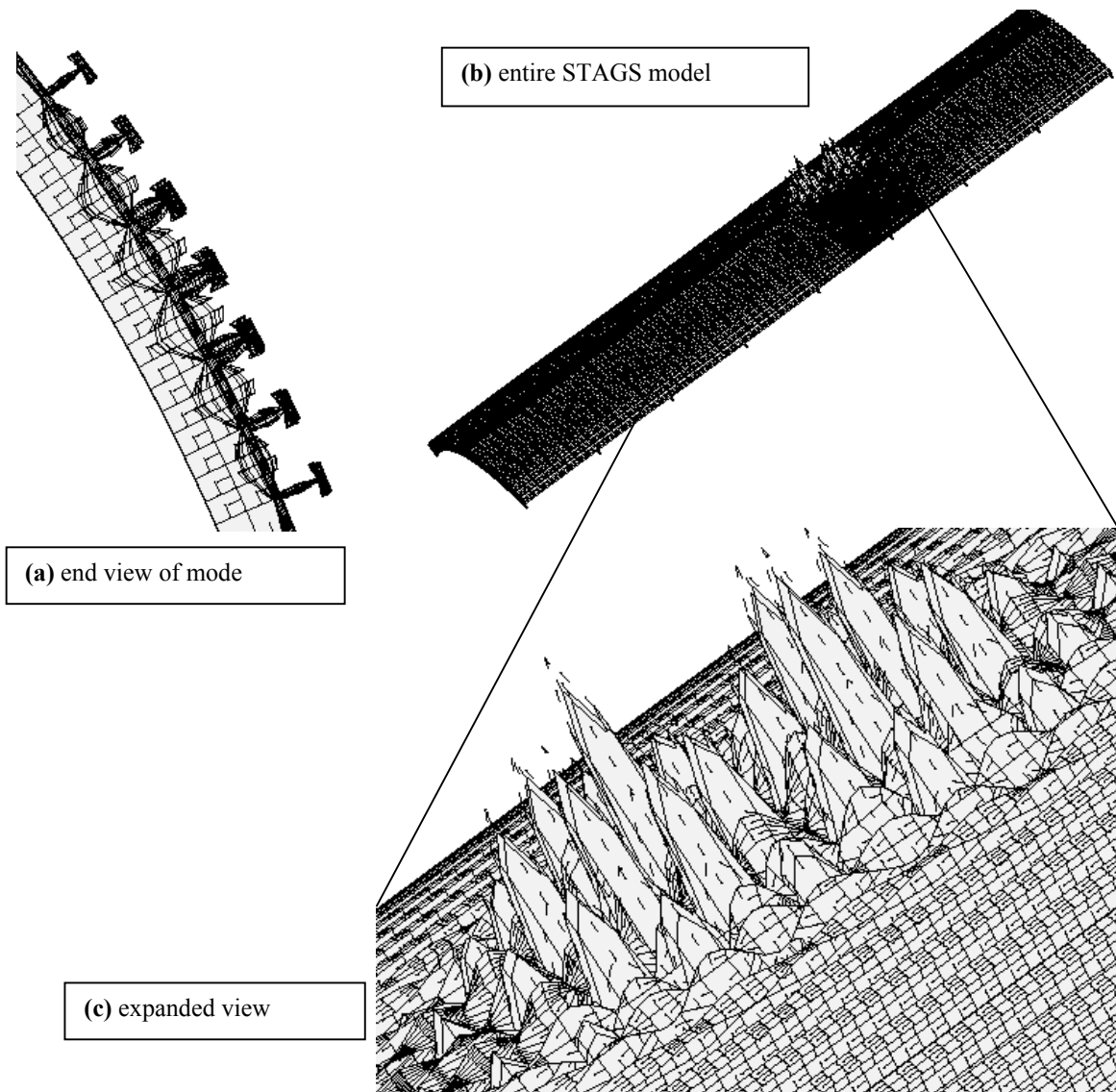
STAGS model of Case 2, Table 4: no Koiter, yes change imperfection, ICONSV = -1. See Part 6 in Table 9. This figure shows the deformed state at the highest load factor reached in the nonlinear static run, STAGS load factor, PA = 0.974853. The single imperfection shape is shown in Fig. 24. The imperfection amplitude, Wimp = -0.0625 inch.

FIG. 25 STAGS prediction of outer fiber effective stress (psi) at axial load, Nx= -3000 x 0.975 lb/in. Compare with Fig. 28.



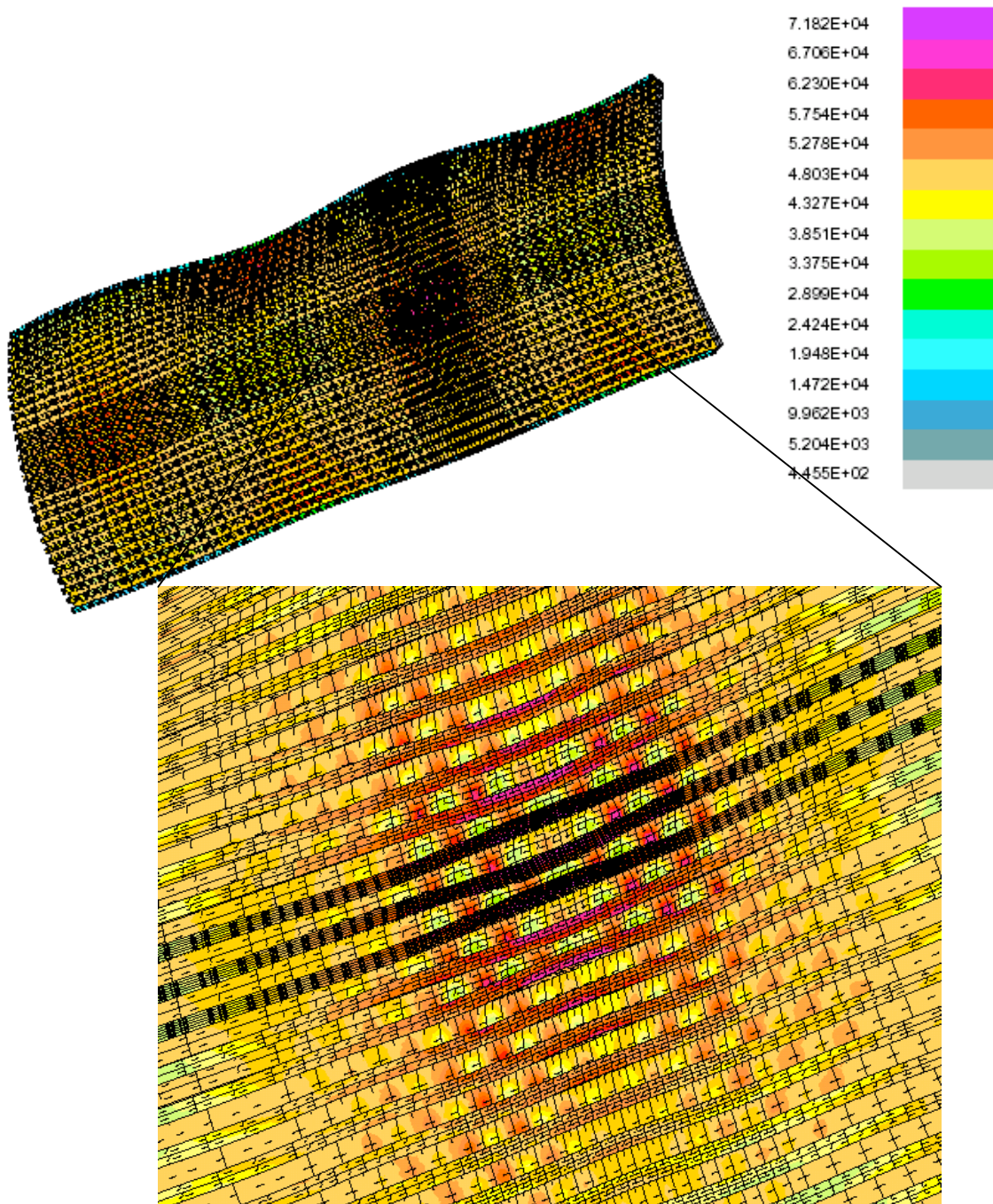
STAGS model of Case 2, Table 4: no Koiter, yes change imperfection, ICONSV = -1. See Part 6 in Table 9. STAGS nonlinear buckling Mode no. 1 = combined local/bending-torsion buckling; critical load, $\text{pcr}=1.0037$, determined at load factor, $\text{PA} = 0.974853$. For nonlinear bending-torsion buckling, PANDA2 predicts a nonlinear buckling load factor, 1.0795, for Load set 1, Subcase 1 and 1.027 for Load set 1, Subcase 2. See PANDA2's Margin 2 in Table 6. By "nonlinear buckling" is meant "bifurcation buckling from a prebuckling equilibrium state that is determined from nonlinear theory".

FIG. 26 NONLINEAR BUCKLING: local combined skin buckling and stringer bending-torsion buckling mode from the STAGS 60-degree model with a nonuniform mesh.



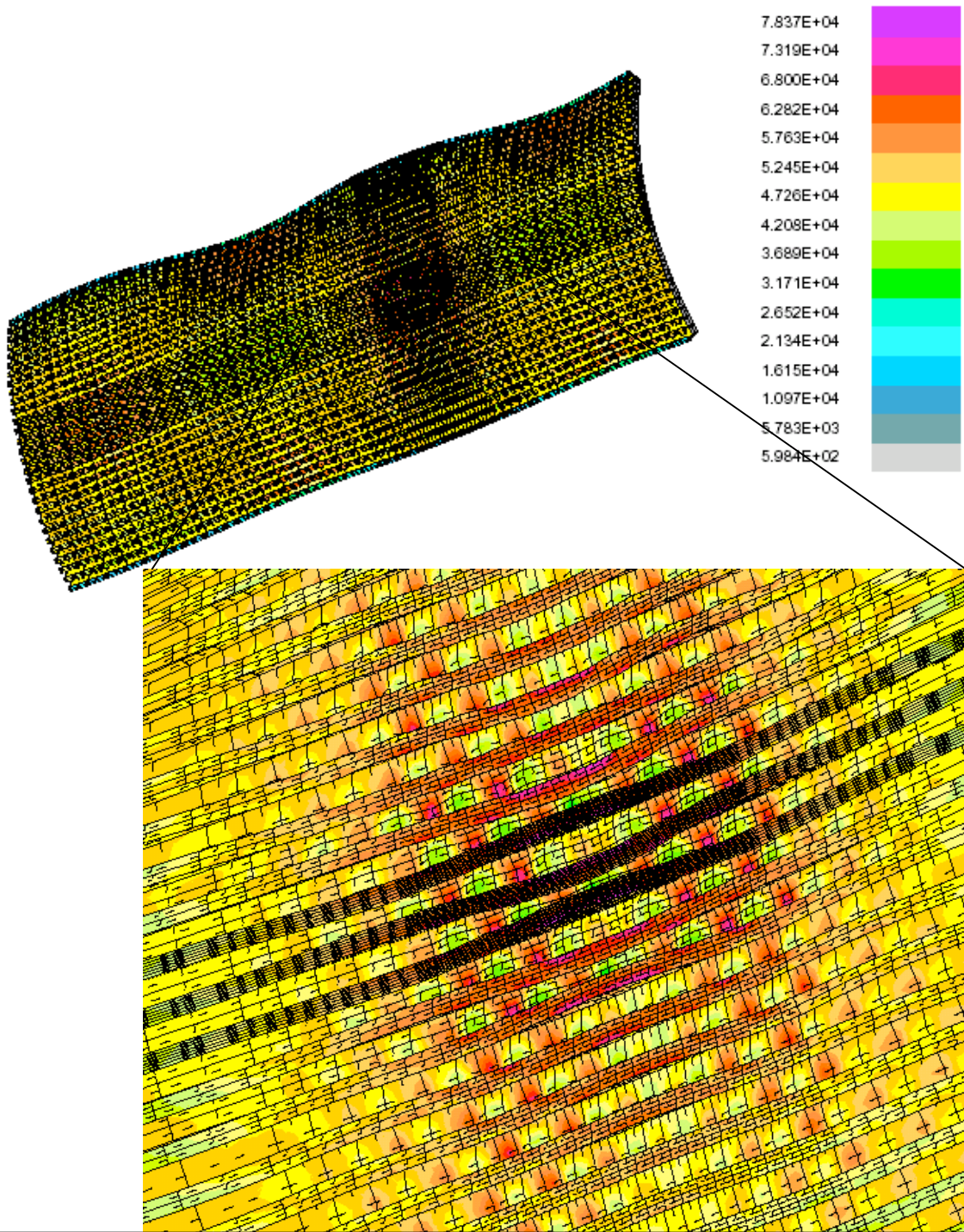
STAGS model of Case 2, Table 4: no Koiter, yes change imperfection, ICONSV = -1. See Part 6 in Table 9. STAGS nonlinear buckling Mode no. 2 = local buckling; load factor, pcr=1.0084. Nonlinear buckling mode computed at load factor, PA = 0.974853. In Load set 1 PANDA2 predicts a nonlinear buckling load factor, 1.0150, in Subcase1 and 1.0231 in Subcase 2. In Load set 2 PANDA2 predicts a nonlinear buckling load factor, 0.9816. See PANDA2's Margin 1 in Table 6.

FIG. 27 NONLINEAR BUCKLING: local mode from the STAGS 60-degree model with a nonuniform mesh.



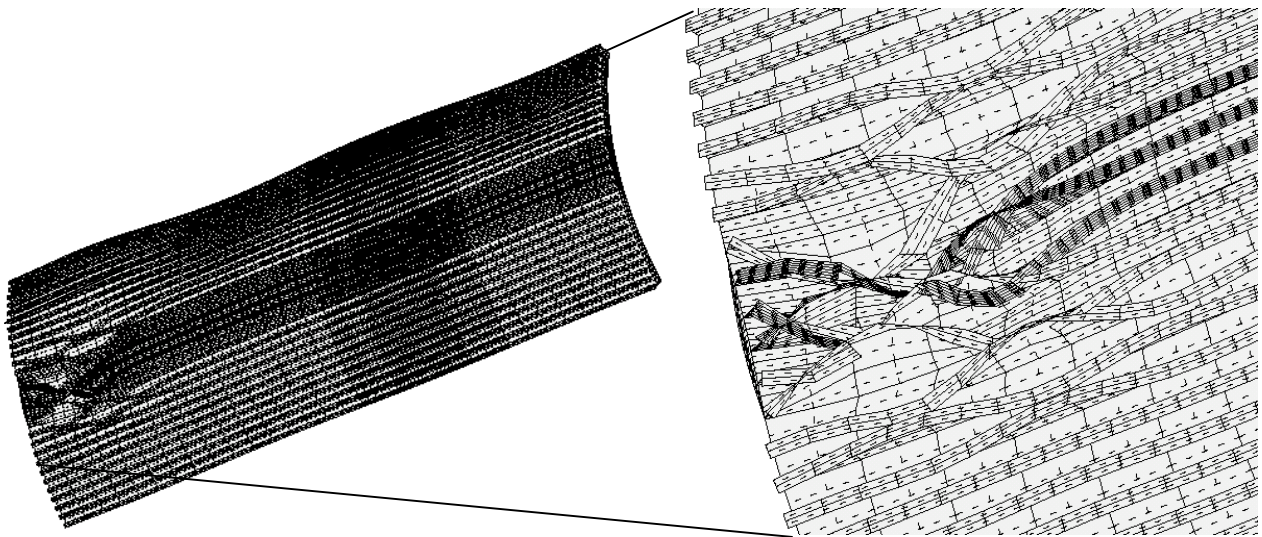
STAGS model of Case 2, Table 4: no Koiter, yes change imperfection, ICONSV = -1. See Part 7 of Table 9. The imperfect shell has 3 imperfection shapes: **1.** general buckling modal imperfection shape shown in Fig. 24 with amplitude, $W_{imp1}=-0.0625$ inch, **2.** local/bending-torsion combined shape shown in Fig. 26 with amplitude, $W_{imp2} = +0.0005$ inch, **3.** local buckling mode shape shown in Fig. 27 with amplitude, $W_{imp3} = +0.0005$ inch. This figure shows the deformed state from STAGS at the highest load factor reached in the nonlinear static run, $PA=0.996238$. Notice the local bending in the panel skin and sidesway of the central stringers in the region where the nodal mesh is dense.

FIG. 28 STAGS prediction of outer fiber effective stress (psi) for axial load, $N_x=-3000 \times 0.996238$ lb/in. Compare with Fig. 25.



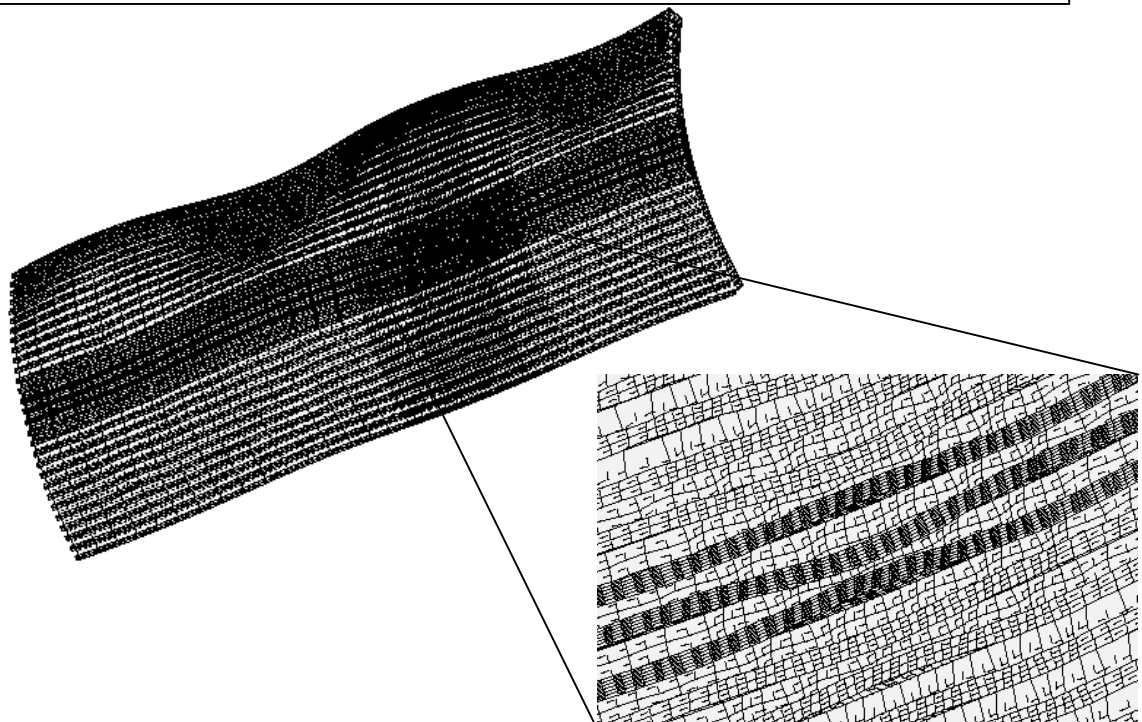
STAGS model of Case 2, Table 4: no Koiter, yes change imperfection, ICONSV=1. See Part 8 of Table 9. The configuration is the imperfect shell with same 3 imperfections as identified in the previous figure. This figure shows the deformed state predicted by STAGS at the highest load factor reached in the nonlinear static run, PA = 1.02487.

FIG. 29 STAGS prediction of outer fiber effective stress (psi) at axial load $N_x = -3000 \times 1.02487$ lb/in. Compare with previous figure. Notice sidesway of the three central stringers in the region with the highest mesh density. (The three central stringers are darker than the others because they have greater nodal point density over their cross sections). Compare with Fig. 28.



STAGS model of Case 2, Table 4: no Koiter, yes change imperfection, ICONSV = -1. See Part 12 in Table 9. STAGS load factor, PA=1.04; time of collapse=0.02375 seconds at Step 310 in the nonlinear dynamic STAGS run. The configuration is the imperfect shell with same three imperfections as those for the previous 2 figures. The STAGS load factor is held constant during the nonlinear dynamic run at PA = 1.04.

FIG. 30 Dynamic elastic collapse of the imperfect cylindrical shell from the STAGS 60-degree model with nonuniform mesh.



STAGS model of Case 2, Table 4: no Koiter, yes change imperfection, ICONSV= -1. See Part 13 in Table 9. STAGS load factor, PA=1.035; deformed state at time-0.0427 seconds at Step 475 in the nonlinear dynamic STAGS run. No collapse occurs. The same three imperfections are present as for the previous 3 figures.

FIG. 31 Stable equilibrium of the imperfect cylindrical shell at a load level, PA=1.035, just below that in the previous figure. Compare with Figs. 25, 28 and 29.

- Disp(24456,v,L) vs. time, Sidesway of Stringer 14 in first ring bay, 4 nodes from left. Run 6: PA=1.050
- Disp(27290,v,L) vs. time, Sidesway of Stringer 15 in first ring bay, 4 nodes from left. Run 6: PA=1.050
- △ Disp(24456,v,L) vs. time, Sidesway of Stringer 14 in first ring bay, 4 nodes from left. Run 7: PA=1.040
- + Disp(27290,v,L) vs. time, Sidesway of Stringer 15 in first ring bay, 4 nodes from left. Run 7: PA=1.040
- × Disp(24456,v,L) vs. time, Sidesway of Stringer 14 in first ring bay, 4 nodes from left. Run 8: PA=1.035
- ◇ Disp(27290,v,L) vs. time, Sidesway of Stringer 15 in first ring bay, 4 nodes from left. Run 8: PA=1.035

Case 2 of Table 4; Sidesway of stringers 14,15 at three load levels

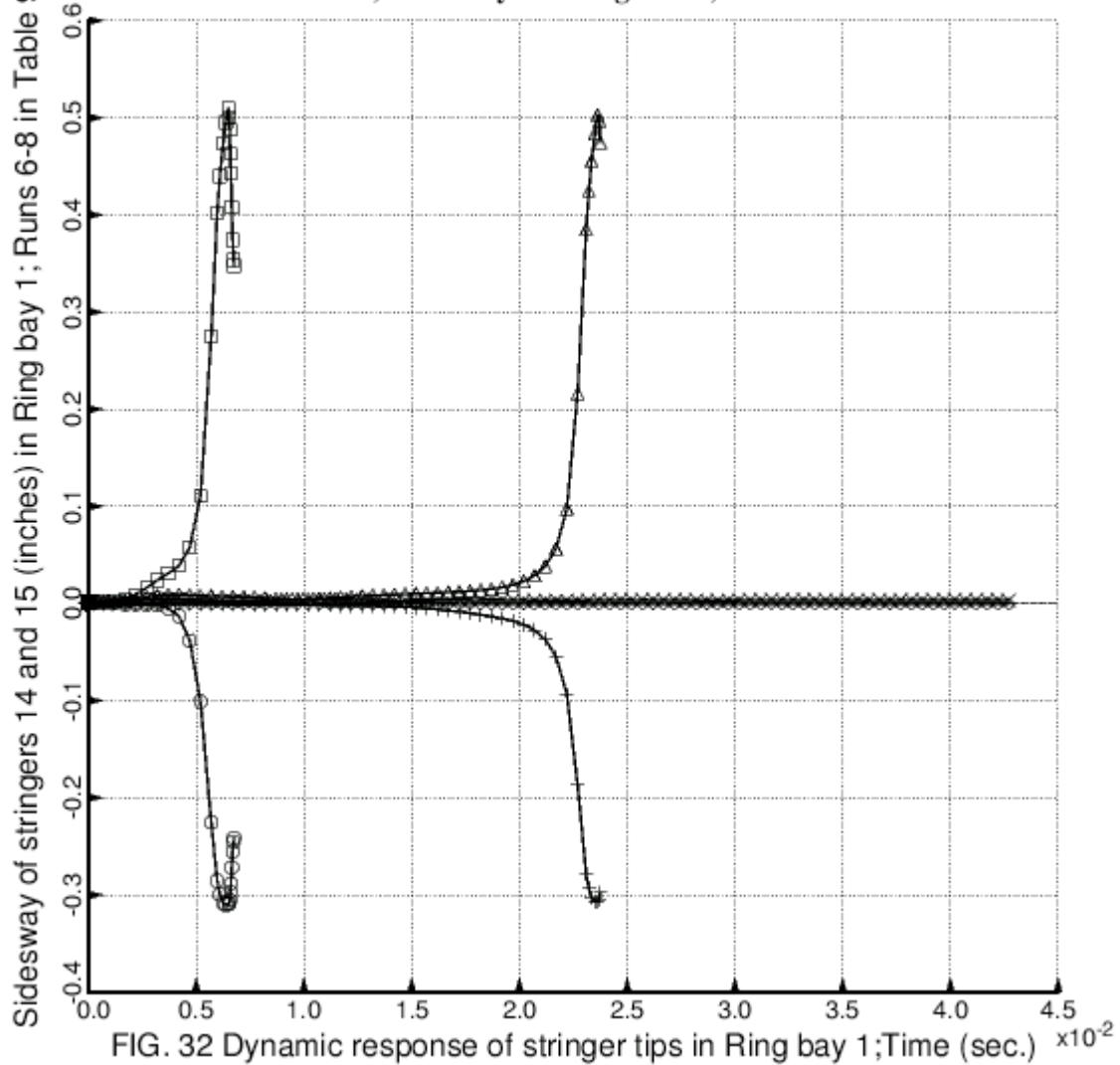


FIG. 32 STAGS model of Case 2, Table 4: Results from three STAGS nonlinear dynamic runs. For the deformed state of the shell at the end of Run 7, see Fig. 30. For the deformed state of the shell at the end of Run 8, see Fig. 31. The deformed state of the shell at the end of Run 6 is essentially the same as that shown in Fig. 30. Data corresponding to the final time step are listed in Part 11 (Run 6), Part 12 (Run 7), and Part 13 (Run 8) of Table 9.

— — Undeformed: An arc of the stiffened cylindrical shell is modeled as a huge torus [26].
 — Deformed: local buckling; PANDA2 gets 1.00989; STAGS gets 1.0245 (Fig. 41); Case 1 in Table 4

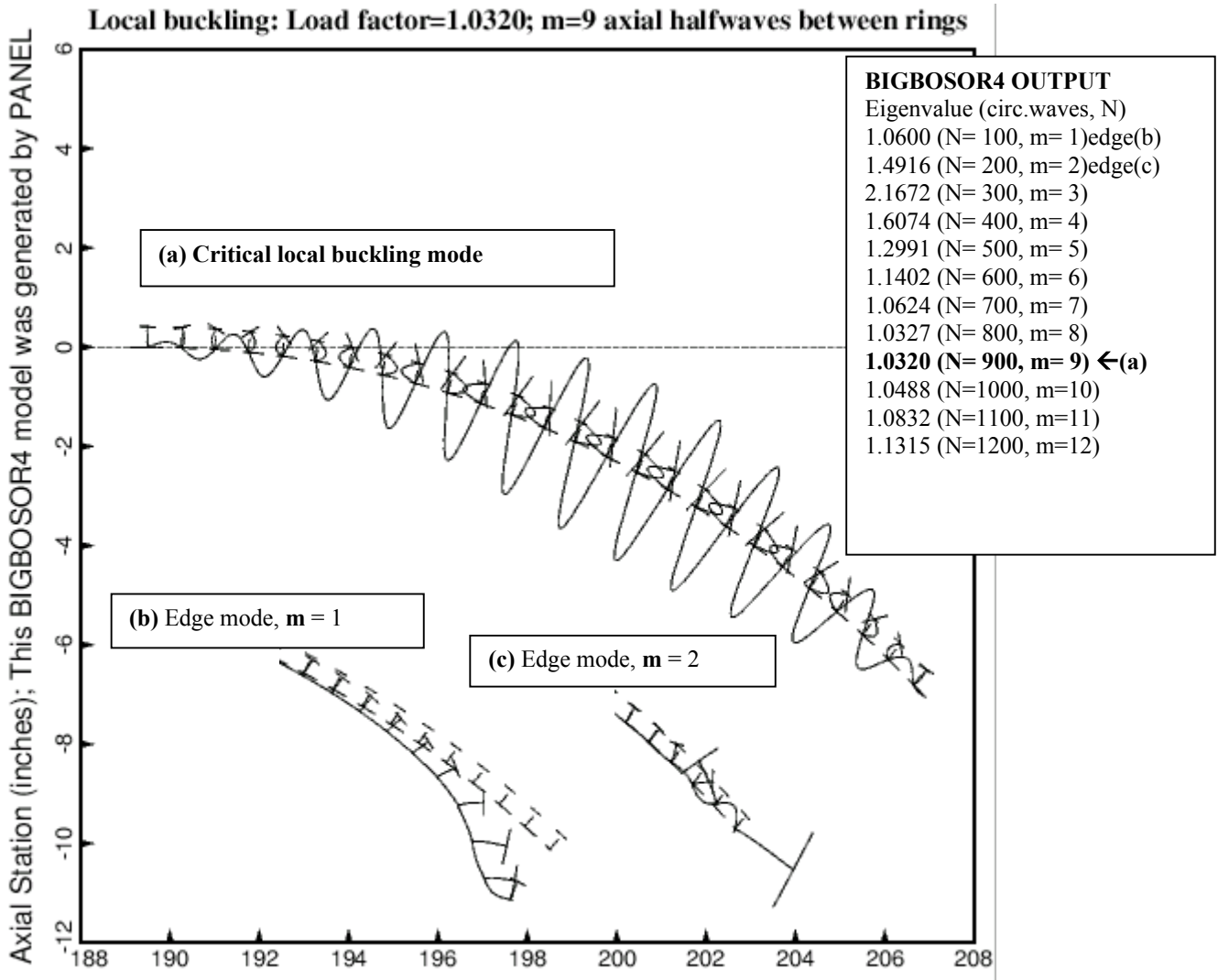


FIG. 33 BIGBOSOR4 [14] model of buckling between rings; Radius (inches)

FIG. 33 BIGBOSOR4 model of Case 1 in Table 4: Results from a BIGBOSOR4 model generated by the PANDA2 processor called PANEL. This figure is analogous to Fig. 23b. See Margin 1 in Table 10 for the PANDA2 prediction of **local buckling** of the perfect shell. The edge modes, **(b)** and **(c)**, should be disregarded in comparisons of BIGBOSOR4 predictions with those from PANDA2 and STAGS because edge modes of this type are not possible in the PANDA2 and STAGS models.

- Undeformed: An arc of the stiffened cylindrical shell is modeled as a huge torus [26].
- Deformed: Inter-ring buckling; PANDA2 gets 1.353; This is Case 1 in Table 4

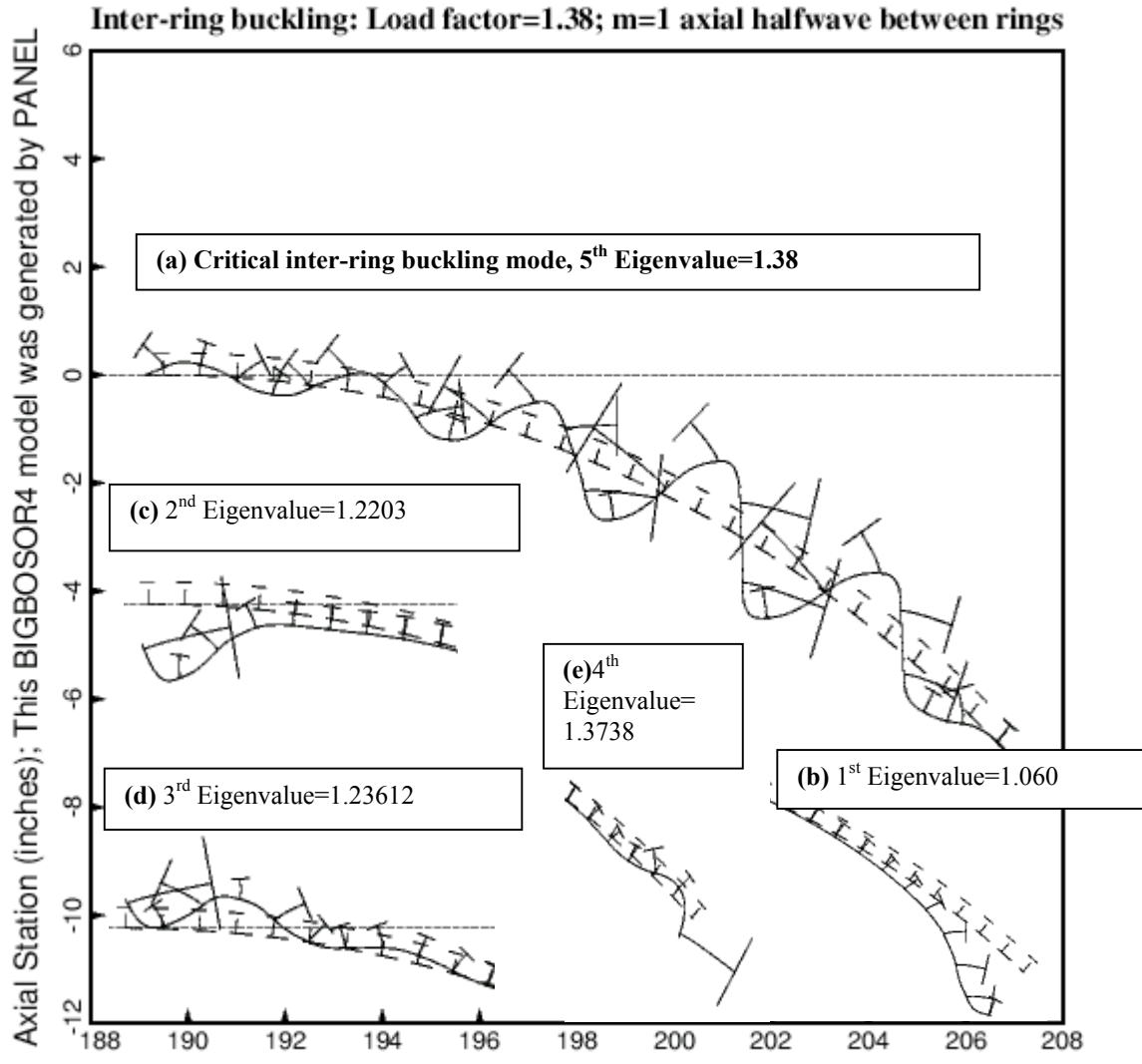


FIG. 34 BIGBOSOR4 [14] model of buckling between rings; Radius (inches)

FIG. 34 BIGBOSOR4 model of Case 1 in Table 4: Results from a BIGBOSOR4 model generated by the PANDA2 processor called PANEL. This figure is analogous to Fig. 20b. See Margin 5 in Table 10 for the PANDA2 prediction of **inter-ring buckling**. The critical buckling mode shape from BIGBOSOR4 shown here (a) does not resemble that predicted by PANDA2 for reasons given in the text in Sub-section 13.1. The four edge modes, (b) – (e), are not of interest in the comparison of BIGBOSOR4 predictions with those from PANDA2 and STAGS because PANDA2 and STAGS do not permit edge modes of this kind.

— — Undeformed; PANDA2 gets 1.07 before knockdowns and 0.9772 after knockdowns
 — Deformed: STAGS gets load factor=1.0572 (Fig.37), 1.0897(Fig.40); This is Case 1 in Table 4

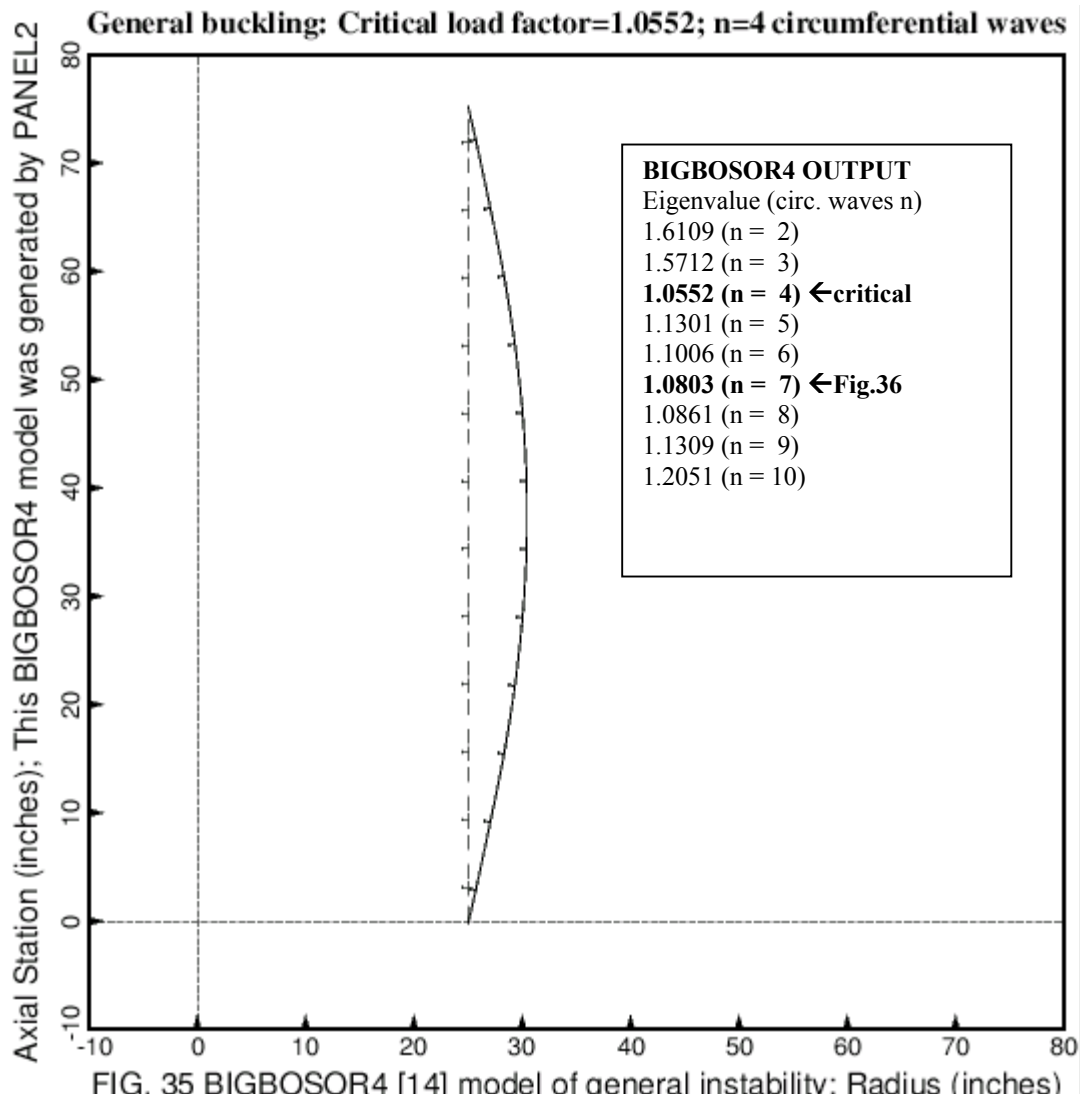


FIG. 35 BIGBOSOR4 [14] model of general instability; Radius (inches)

FIG. 35 BIGBOSOR4 model of Case 1 in Table 4: Results from a BIGBOSOR4 model generated by the PANDA2 processor called PANEL2. This figure is analogous to Fig. 21b. See Margin 11 in the top part of Table 10 for PANDA2's prediction of **general buckling** after the application of "knockdown" factors (1) for smeared stringers, (2) for smeared rings, and (3) for the effect of transverse shear deformation (t.s.d.). Notice that there are two minima with respect to number of circumferential waves **n** in the inserted list, "Eigenvalue (n)".

—— Undeformed; PANDA2 gets 1.09 corresponding to $(m,n)=(4,7)$ (axial,circ.) waves before knockdowns
 — Deformed: STAGS gets load factor=1.078 (Fig.38), 1.0748(Fig.39); This is Case 1 in Table 4

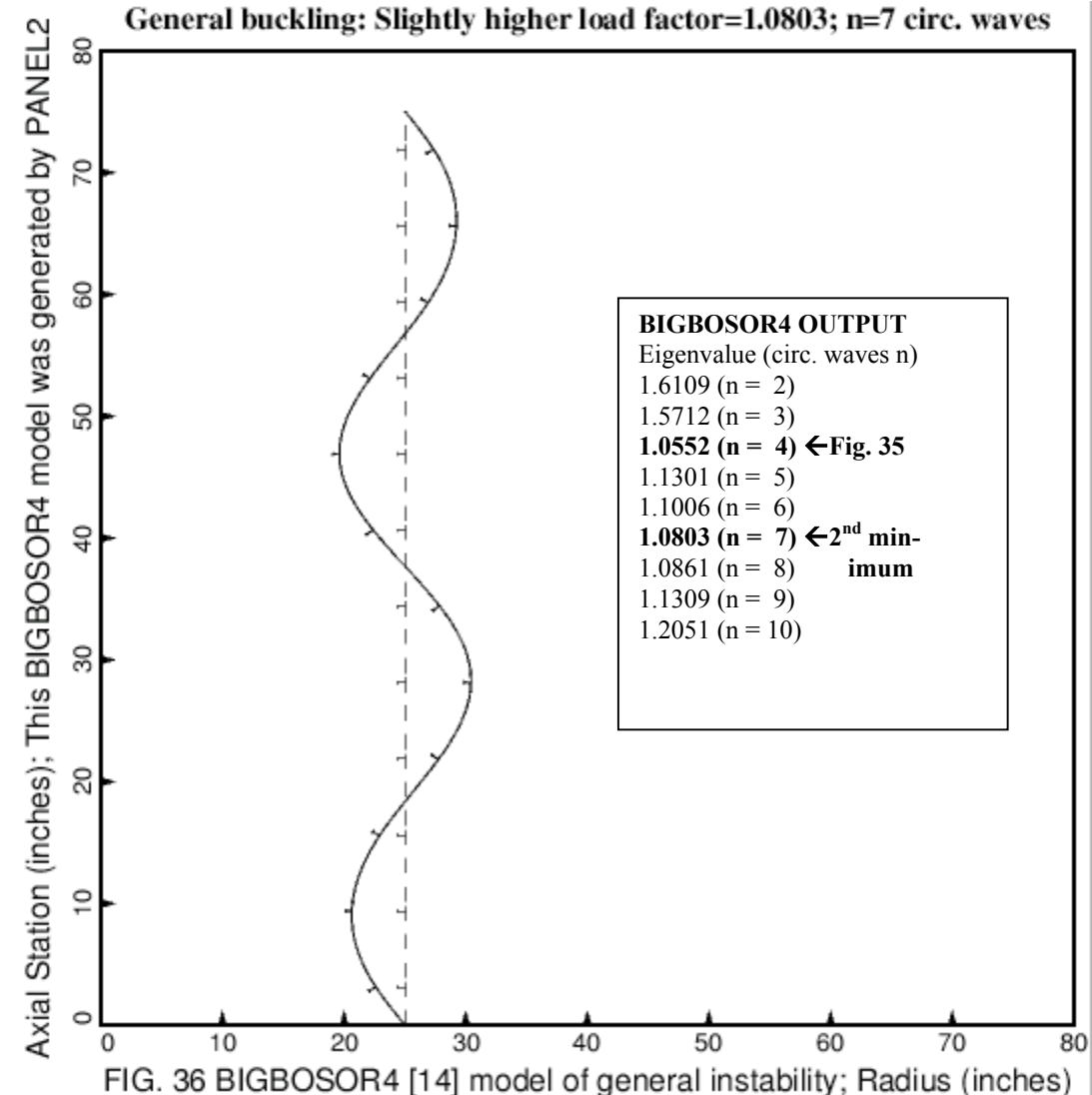
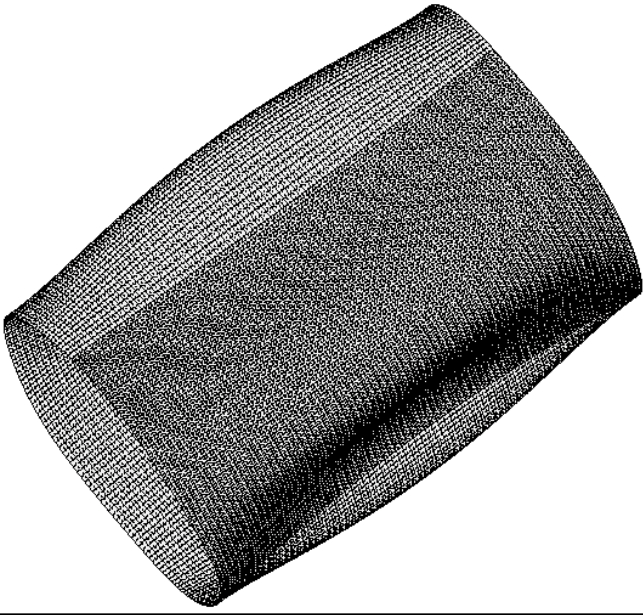


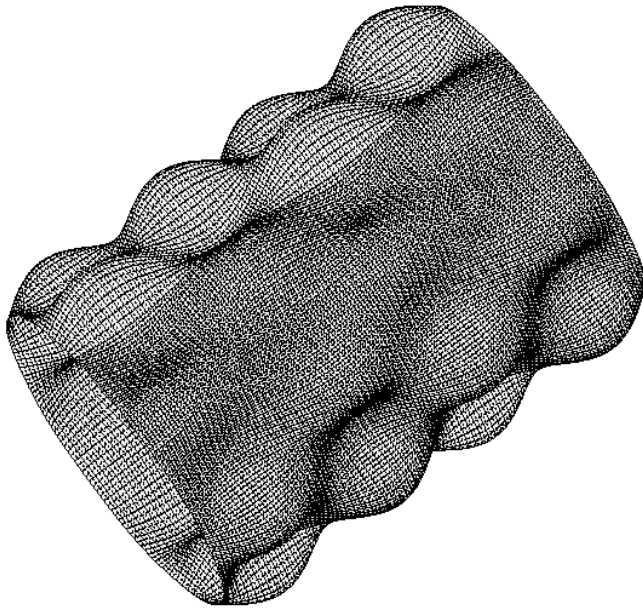
FIG. 36 BIGBOSOR4 [14] model of general instability; Radius (inches)

FIG. 36 BIGBOSOR4 model of Case 1 in Table 4: Results from a BIGBOSOR4 model generated by the PANDA2 processor called PANEL2. This figure is analogous to Fig. 21b. It represents a general buckling mode according to BIGBOSOR4 that corresponds to an eigenvalue (buckling load factor) that is slightly higher than that corresponding to the critical **general buckling** mode displayed in the previous figure. PANDA2 predicts the same, slightly-higher-than-critical buckling mode. The elaborate search conducted by PANDA2 for the critical buckling mode in (m =axial halfwave, n =circumferential halfwave, s =buckling nodal line slope) space is designed to capture multiple minimum buckling load factors as a function of (m , n , s). See ...panda2/doc/panda2.news Item Numbers 415 and 443 for details concerning this elaborate search.



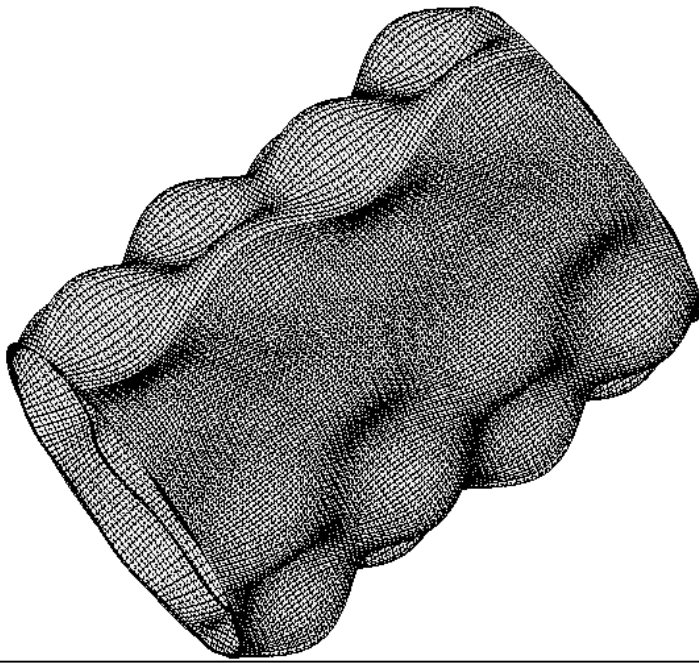
STAGS model of Case 1, Table 4: perfect shell, no Koiter, ICONSV=1. See Table 10 for PANDA2 margins. STAGS load factor, pcr=1.0572; BIGBOSOR4 predicts a load factor, 1.0552 (Fig. 35); PANDA2 predicts 1.07 before the application of knockdown factors for smearing stringers, for smearing rings, and for transverse shear deformation (t.s.d). PANDA2 obtains a load factor, 0.9772, after application of these three knockdown factors.

FIG. 37 Linear general buckling mode no. 1 from STAGS model with all stiffeners smeared. Compare with Fig. 40.



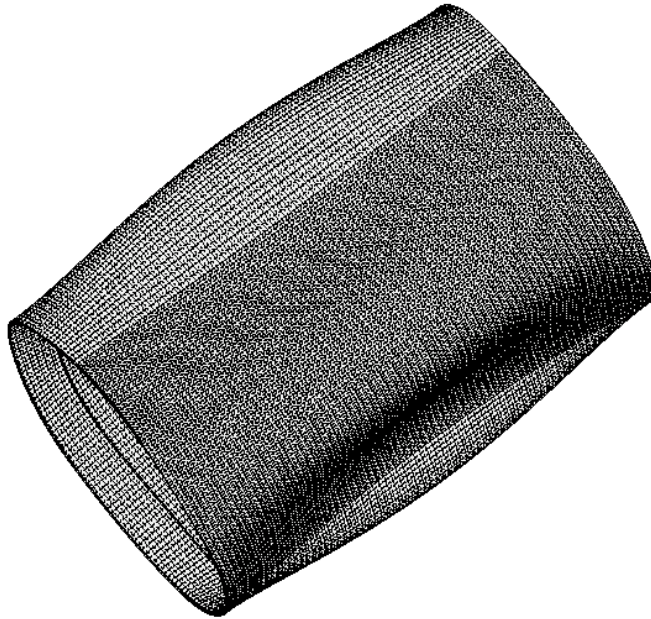
STAGS model of Case 1, Table 4: perfect shell, no Koiter, ICONSV=1. See Table 10 for PANDA2 margins. STAGS load factor, pcr=1.078; BIGBOSOR4 predicts a load factor, 1.0803 (Fig. 36); PANDA2 predicts a load factor, 1.09, before the three knockdowns listed in Fig. 37, with $(m,n)=(4 \text{ axial}, 7 \text{ circumferential})$ halfwaves over 180 degrees of circumference.

FIG. 38 Linear general buckling mode no. 3 from STAGS model with all stiffeners smeared. Compare with Fig. 39.



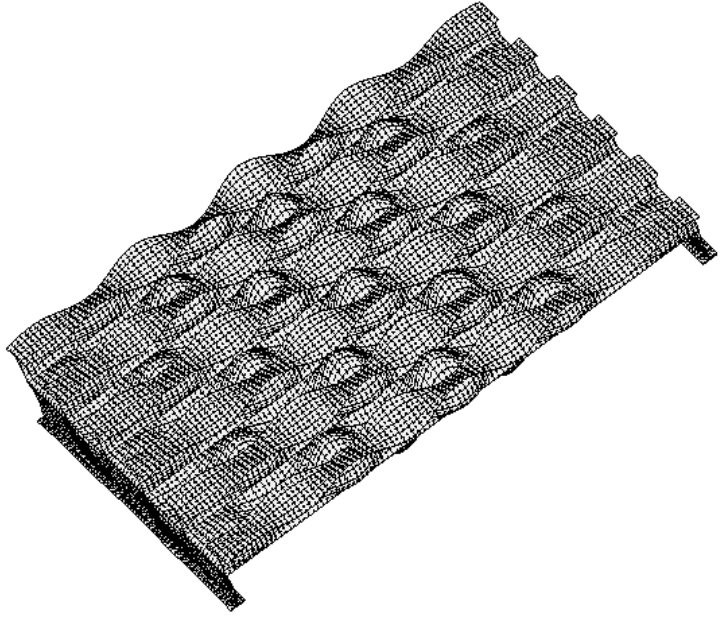
STAGS model of Case 1, Table 4: perfect shell, no Koiter, ICONSV=1. See Table 10 for PANDA2 margins. STAGS load factor, pcr=1.0748; BIGBOSOR4 predicts a load factor, 1.0803 (Fig. 36); PANDA2 predicts a load factor, 1.09, before knockdowns, with $(m,n)=(4,7)$ waves.

FIG. 39 Linear general buckling mode no. 1 from the STAGS model with only the stringers smeared. The rings are modeled as shell units. Note the reversal of the order of the two modes displayed in Figs. 39 and 40 from those shown in Figs. 37 and 38.



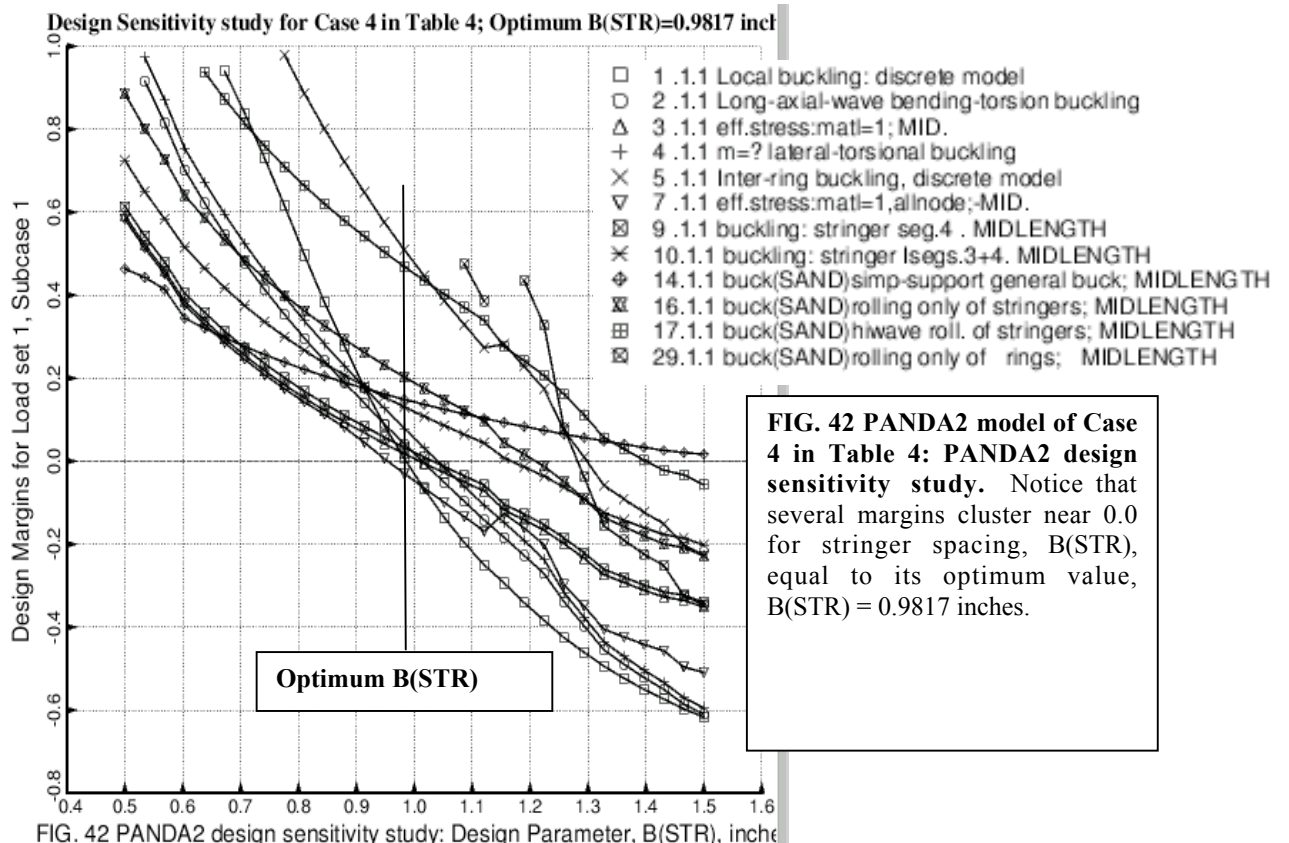
STAGS model of Case 1, Table 4: perfect shell, no Koiter, ICONSV = 1. See Table 10 for PANDA2 margins. STAGS load factor, pcr=1.0897; BIGBOSOR4 predicts a load factor, 1.0552 (Fig. 35); PANDA2 predicts a load factor, 1.07, before the three knockdowns identified in Fig. 37 and a load factor, 0.9772, after the three knockdowns.

FIG. 40 Linear general buckling mode no. 7 from the STAGS model with only the stringers smeared. The rings are modeled as shell units. Note the reversal of the order of the two modes from those shown in Figs. 37 and 38.



STAGS model of Case 1, Table 4: perfect shell, no Koiter, ICONSV = 1. See Table 10 for the PANDA2 margins. STAGS buckling load factor, pcr=1.0245; BIGBOSOR4 predicts a load factor, 1.032 (Fig. 33); PANDA2 predicts a load factor, 1.00989, with $m=9$ axial halfwaves between rings. See Margin 1 in the top part of Table 10.

FIG. 41 Linear local buckling mode from a STAGS sub-domain model with a refined mesh.



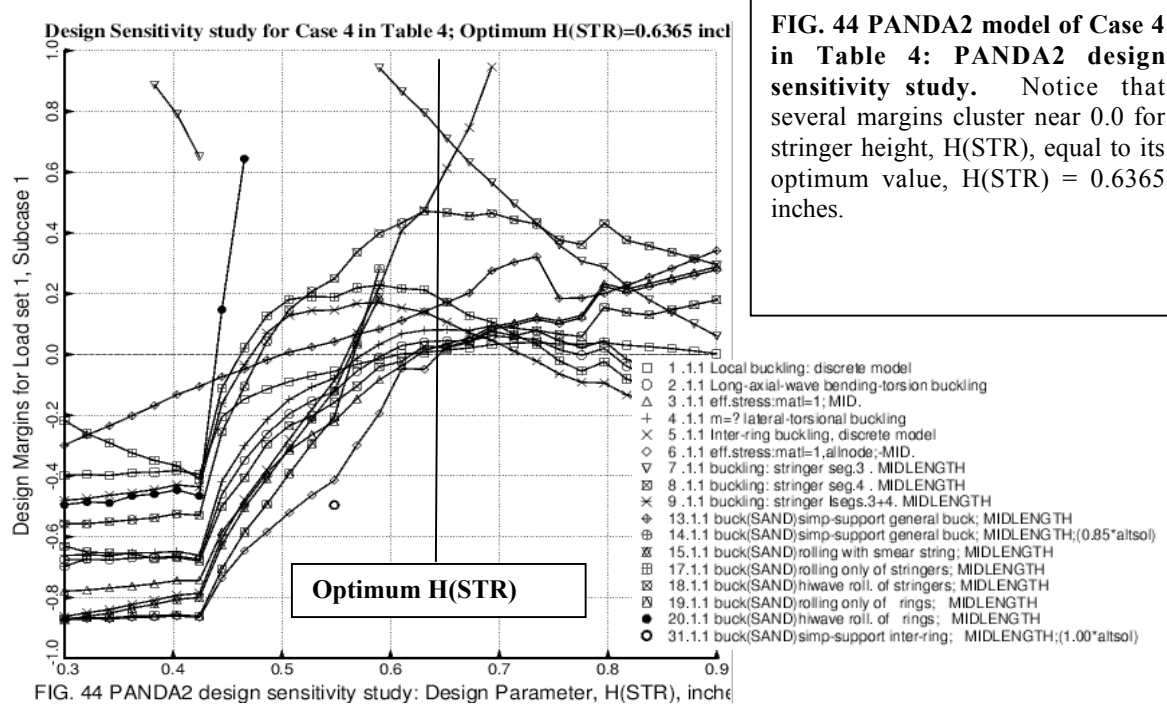
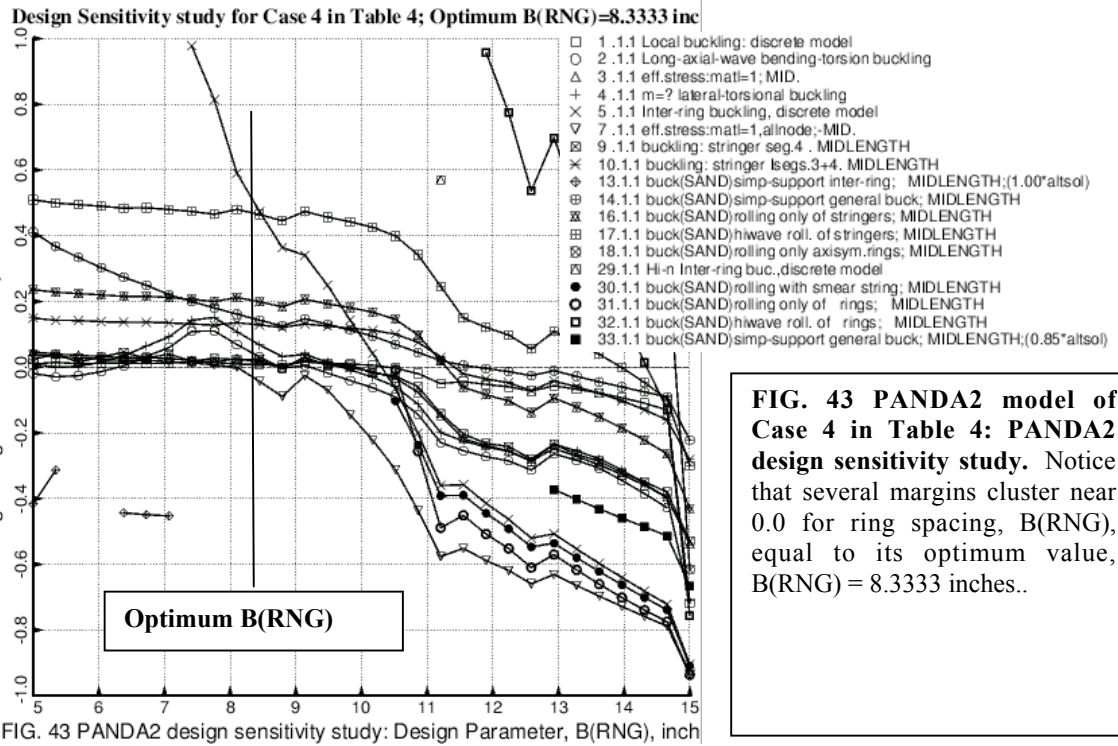


FIG. 44 PANDA2 design sensitivity study: Design Parameter, H(STR), inch

Design Sensitivity study for Case 4 in Table 4; Optimum H(RNG)=0.7998 inch

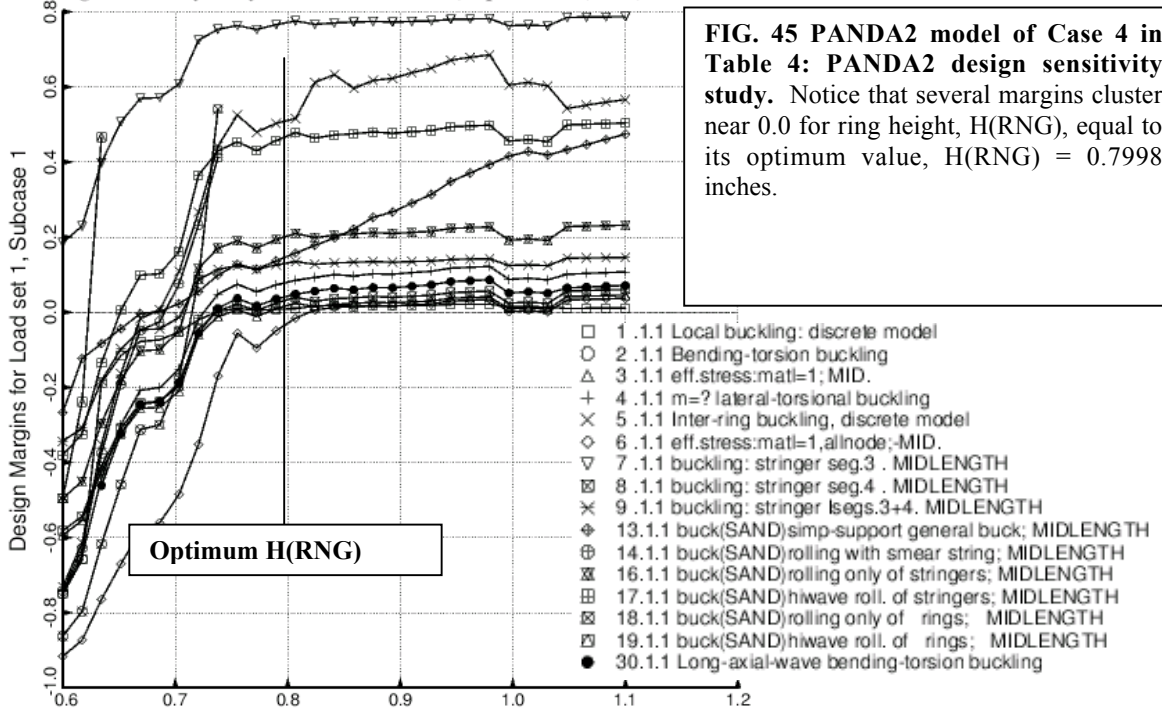


FIG. 45 PANDA2 design sensitivity study: Design Parameter, H(RNG), inch

Design Sensitivity study for Case 4 in Table 4; Optimum T(SKN)=0.03488 inch

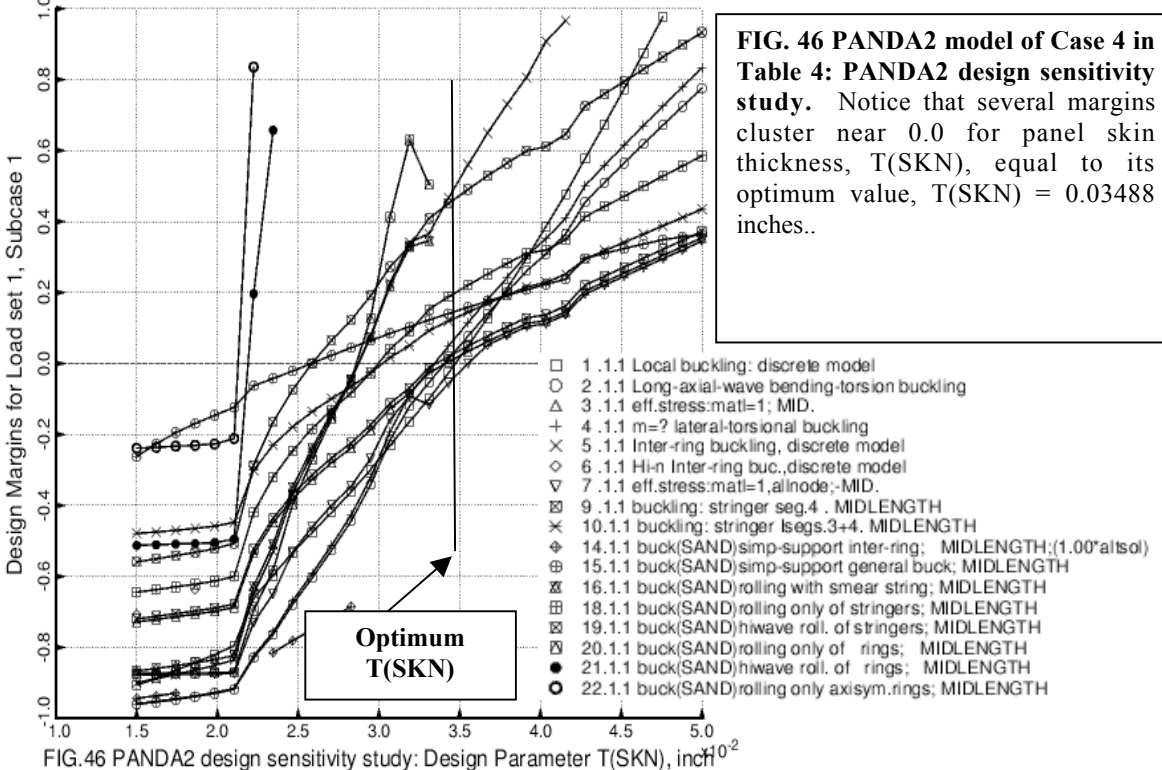
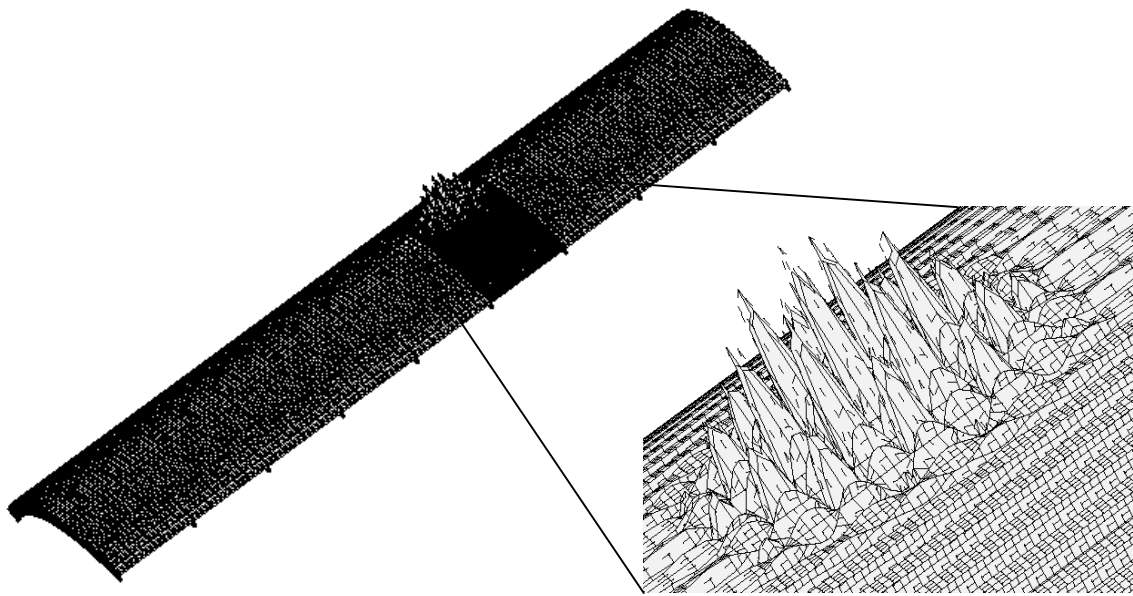


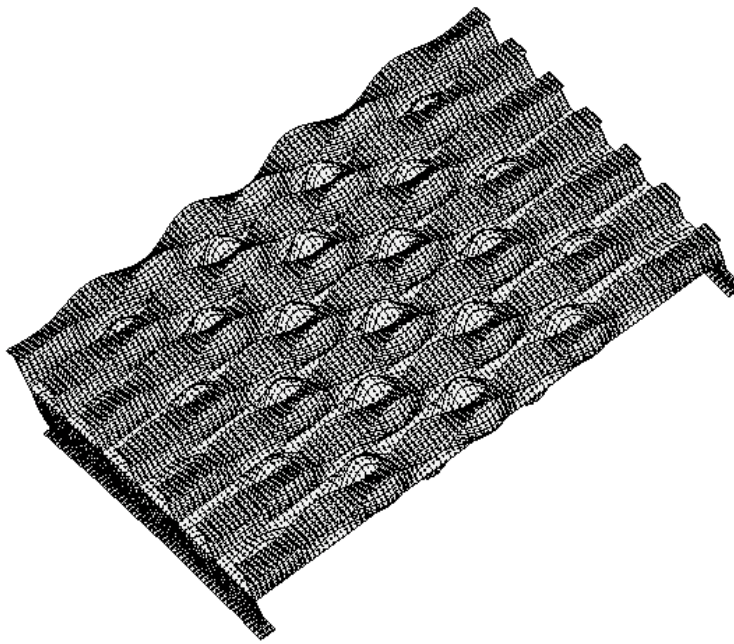
FIG. 46 PANDA2 design sensitivity study: Design Parameter T(SKN), inch^{10^2}

FIG. 45 PANDA2 model of Case 4 in Table 4: PANDA2 design sensitivity study. Notice that several margins cluster near 0.0 for ring height, H(RNG), equal to its optimum value, H(RNG) = 0.7998 inches.



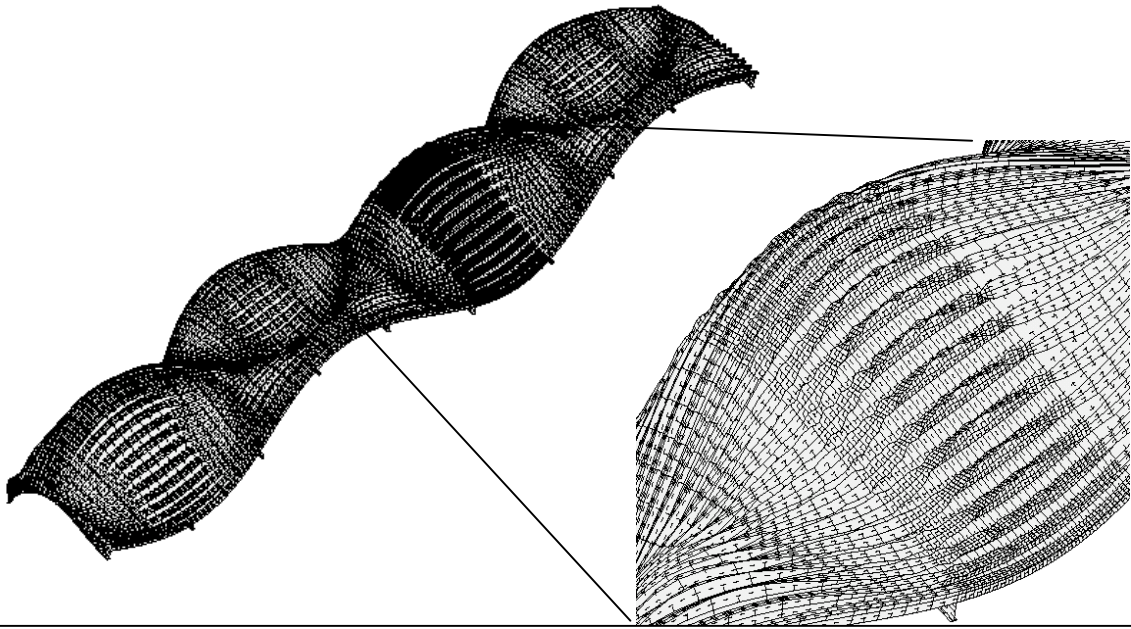
STAGS model of Case 4, Table 4: no Koiter, yes change imperfection, ICONSV = 1. STAGS Mode no. 1, load factor, pcr=1.1255; BIGBOSOR4 predicts a load factor, 1.0935, with $m=9$ axial halfwaves between rings; PANDA2 predicts a load factor, 1.074, with $m=9$ axial halfwaves between rings.

FIG. 47 Linear local buckling mode from the STAGS 60-degree model with a nonuniform mesh.



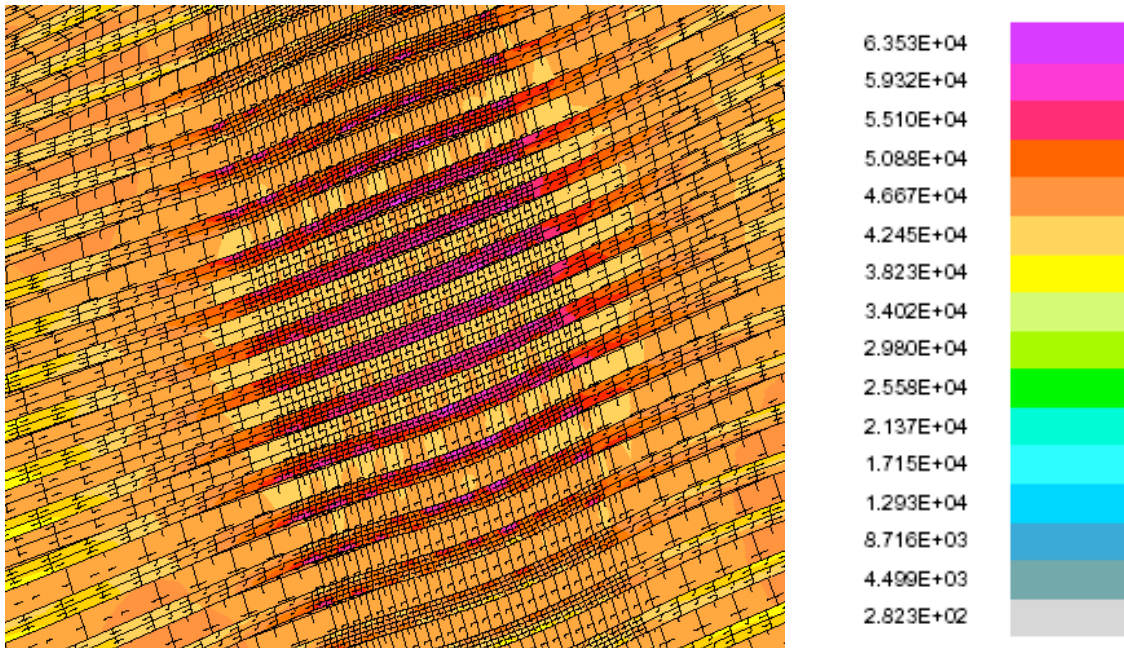
STAGS model of Case 4, Table 4: no Koiter, yes change imperfection, ICONSV = 1. STAGS Mode no. 1, load factor, pcr=1.0876; BIGBOSOR4 predicts a load factor, 1.0935, with $m=9$ axial halfwaves between rings; PANDA2 predicts a load factor, 1.074, with $m=9$ axial halfwaves between rings.

FIG. 48 Linear local buckling mode from a STAGS subdomain model with a refined mesh.



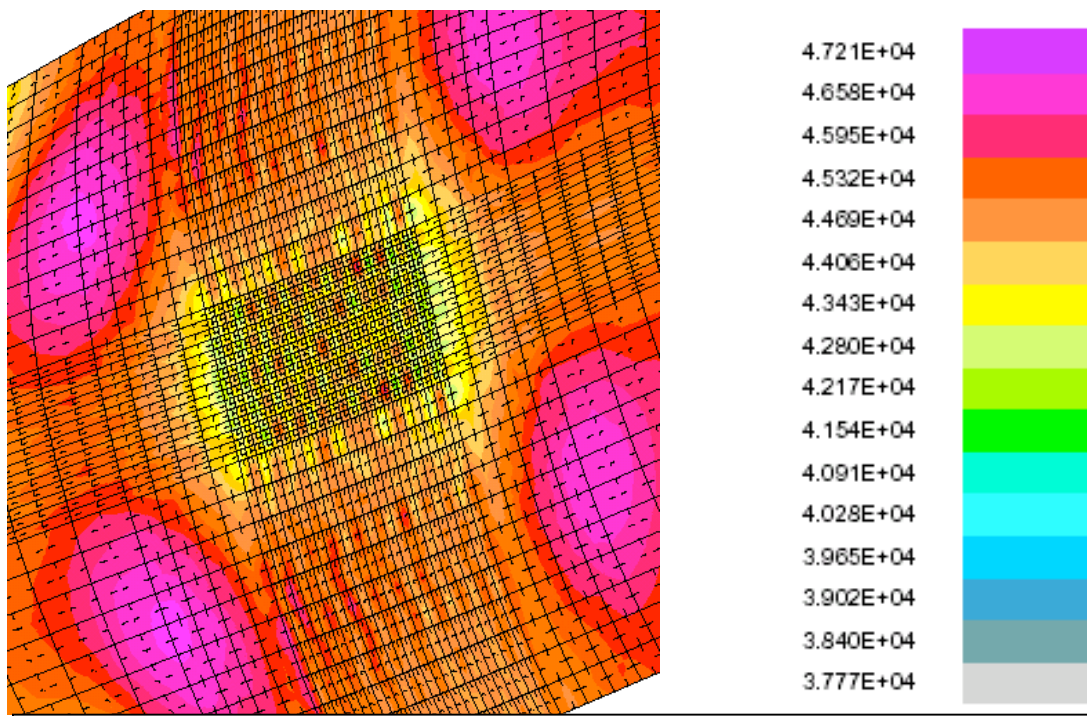
STAGS model of Case 4, Table 4: no Koiter, yes change imperfection, ICONSV = 1. Compare with Fig. 1a. STAGS Mode no. 790; load factor, pcr=2.0288; BIGBOSOR4 predicts a load factor, 2.0008 (m,n)=(4,6); PANDA2 predicts a load factor, 2.07, before application of the 3 knockdowns and a load factor, 1.774, after application of the 3 knockdowns identified in Fig. 37.

FIG. 49 Linear general buckling mode from the STAGS 60-degree model with a nonuniform mesh. Note the combined stringer sidesway plus local buckling of the outstanding stringer flanges as components of the general buckling mode.



STAGS model of Case 4, Table 4: no Koiter, yes change imperfection, ICONSV = 1. Compare with Fig. 2. The imperfection shape is shown in Fig. 49; amplitude, Wimp = -0.0625 inch. This figure shows the deformed state from the STAGS 60-degree model at the highest load factor reached in the nonlinear static run, PA = 0.98.

FIG. 50 STAGS prediction of outer fiber effective stress (psi) at axial load, $N_x = -3000 \times 0.98$ lb/in. Compare with Fig. 53a. The maximum effective stress is in the outstanding flange of one of the stringers in the region where the mesh density is greatest.



STAGS model of Case 4, Table 4: no Koiter, yes change imperfection, ICONSV = 1. Compare with Fig. 53b. The imperfection shape is shown in Fig. 49, amplitude, Wimp=-0.0625 in. This figure shows the deformed state in the panel **SKIN** (shell unit no. 1) from STAGS at the highest load factor reached in the nonlinear static run, PA=0.98.

FIG. 51 STAGS prediction of outer fiber effective stress (psi) in the panel SKIN at axial load, Nx= -3000 x 0.98 lb/in.

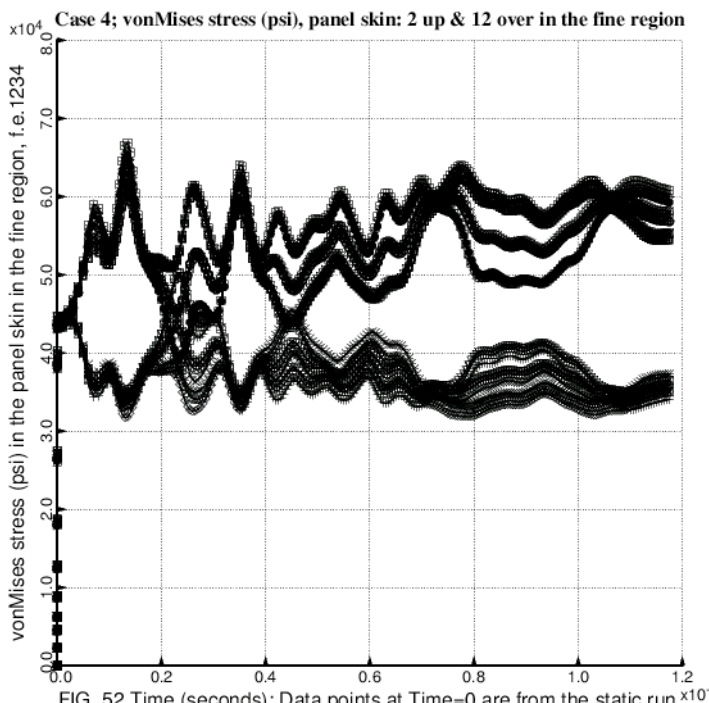
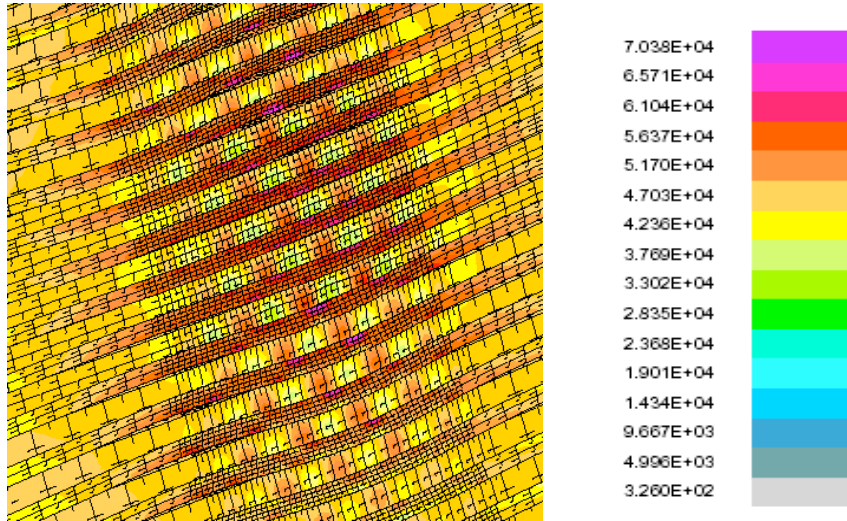


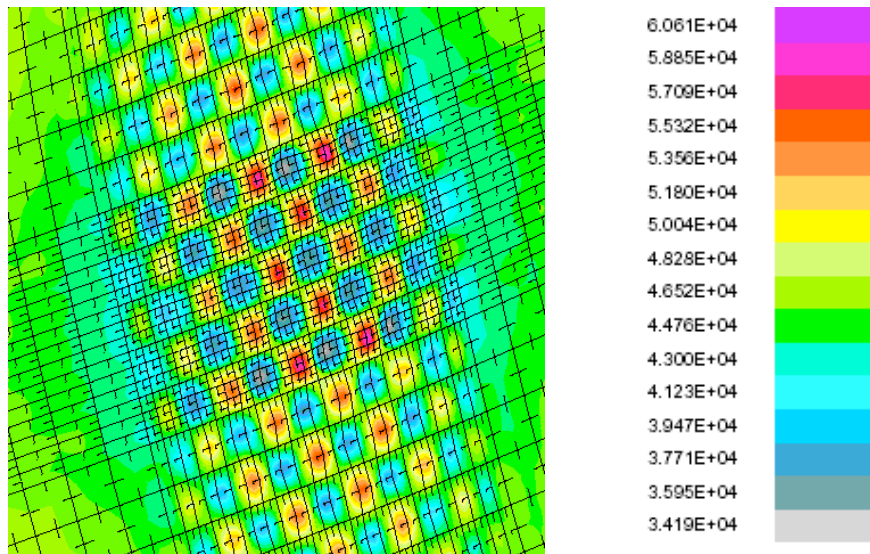
FIG. 52 Time (seconds); Data points at Time=0 are from the static run. $\times 10^{-2}$

FIG. 52 STAGS model of Case 4, Table 4: Results from a STAGS nonlinear dynamic run. The large increase in effective (vonMises) stress in the panel skin during the dynamic STAGS run in which the load factor is held constant at PA = 1.0 (the design load) is caused by local buckling of the type displayed in Figs. 4 and 48. This local buckling at PA = 1.0, occurring for an optimum design configuration derived with use of the “no Koiter” option, is the reason that in Table 4 the recommended option is to use “yes Koiter”. (See Case 5).



STAGS model of Case 4, Table 4: no Koiter, yes change imperfection, ICONSV = 1. Compare with Fig. 50. The imperfection shape is shown in Fig. 49, amplitude Wimp=-0.0625 inch. This figure shows the deformed state of the panel in the region of highest mesh density at the end of the nonlinear dynamic STAGS run, during which the load factor PA is held constant at PA=1.0. Time=0.0875 seconds. Note local bending of the panel skin and some stringer sidesway near the bottom of the figure.

FIG. 53a STAGS prediction of outer fiber effective stress (psi) in the entire panel at the axial load, Nx = -3000 x (PA=1.0) lb/in. The maximum effective stress is in the outstanding flange of one of the stringers in the region where the mesh density is greatest.



STAGS model of Case 4, Table 4: no Koiter, yes change imperfection, ICONSV = 1. Compare with Fig. 51. The single imperfection shape is shown in Fig. 49, amplitude Wimp=-0.0625 inch. This figure shows the deformed state of the panel SKIN in the region of highest mesh density at the end of the dynamic STAGS run, Time=0.0875 seconds. Note local skin bending and compare the maximum effective stress with that in Fig. 51.

FIG. 53b STAGS prediction of outer fiber effective stress (psi) in the panel SKIN at axial load, Nx = -3000 x (PA=1.0) lb/in at the end of the STAGS nonlinear dynamic run.

Finite Element 1456 is 2 elements up, 18 from the left in SKIN in fine region

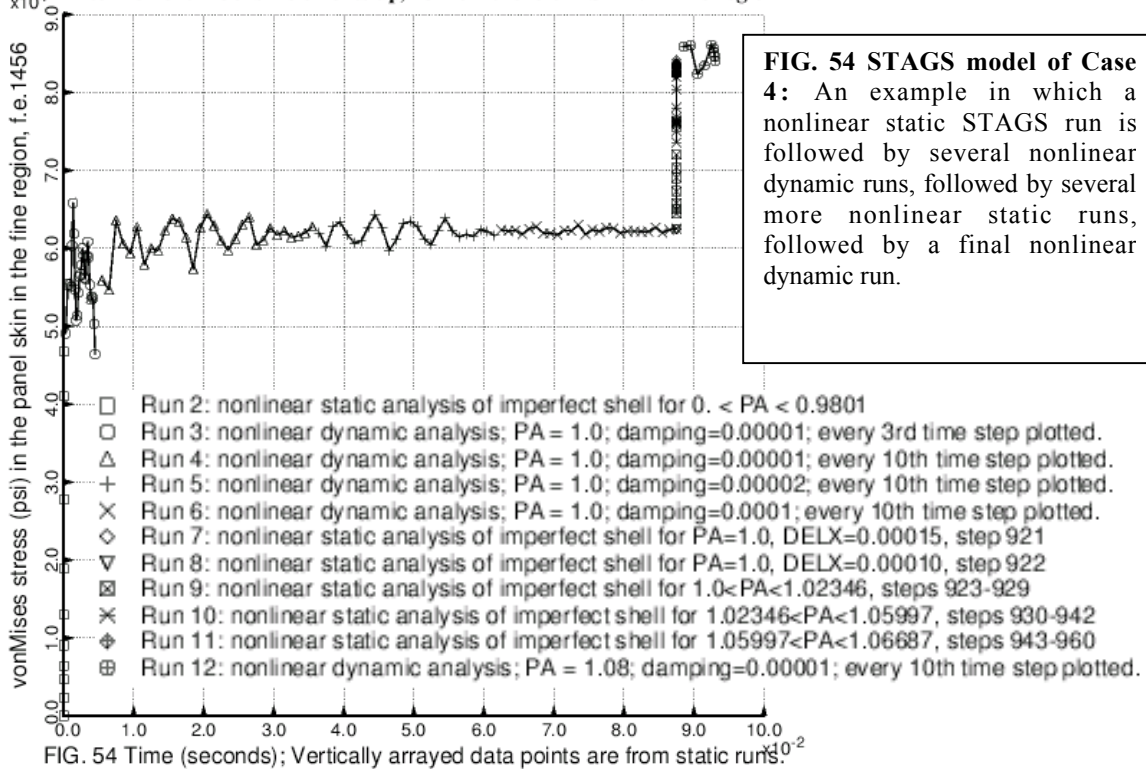


FIG. 54 STAGS model of Case 4: An example in which a nonlinear static STAGS run is followed by several nonlinear dynamic runs, followed by several more nonlinear static runs, followed by a final nonlinear dynamic run.

Normal displacement w where the shell collapses in the first ring bay

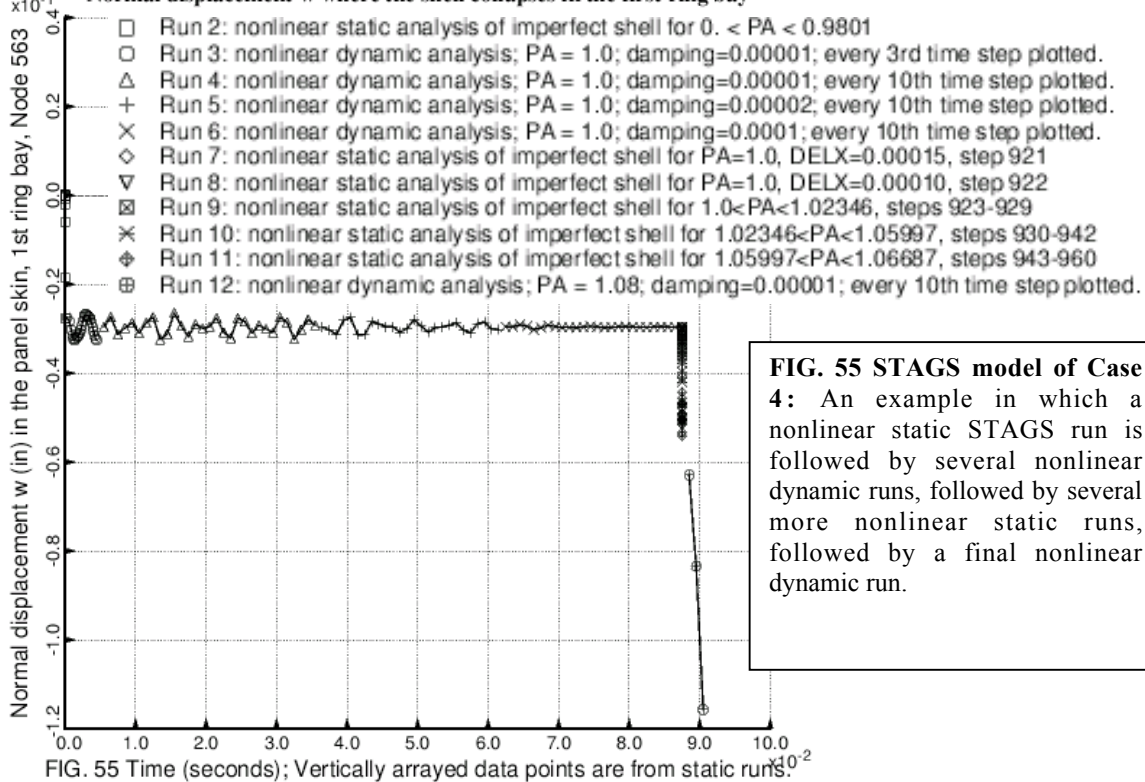
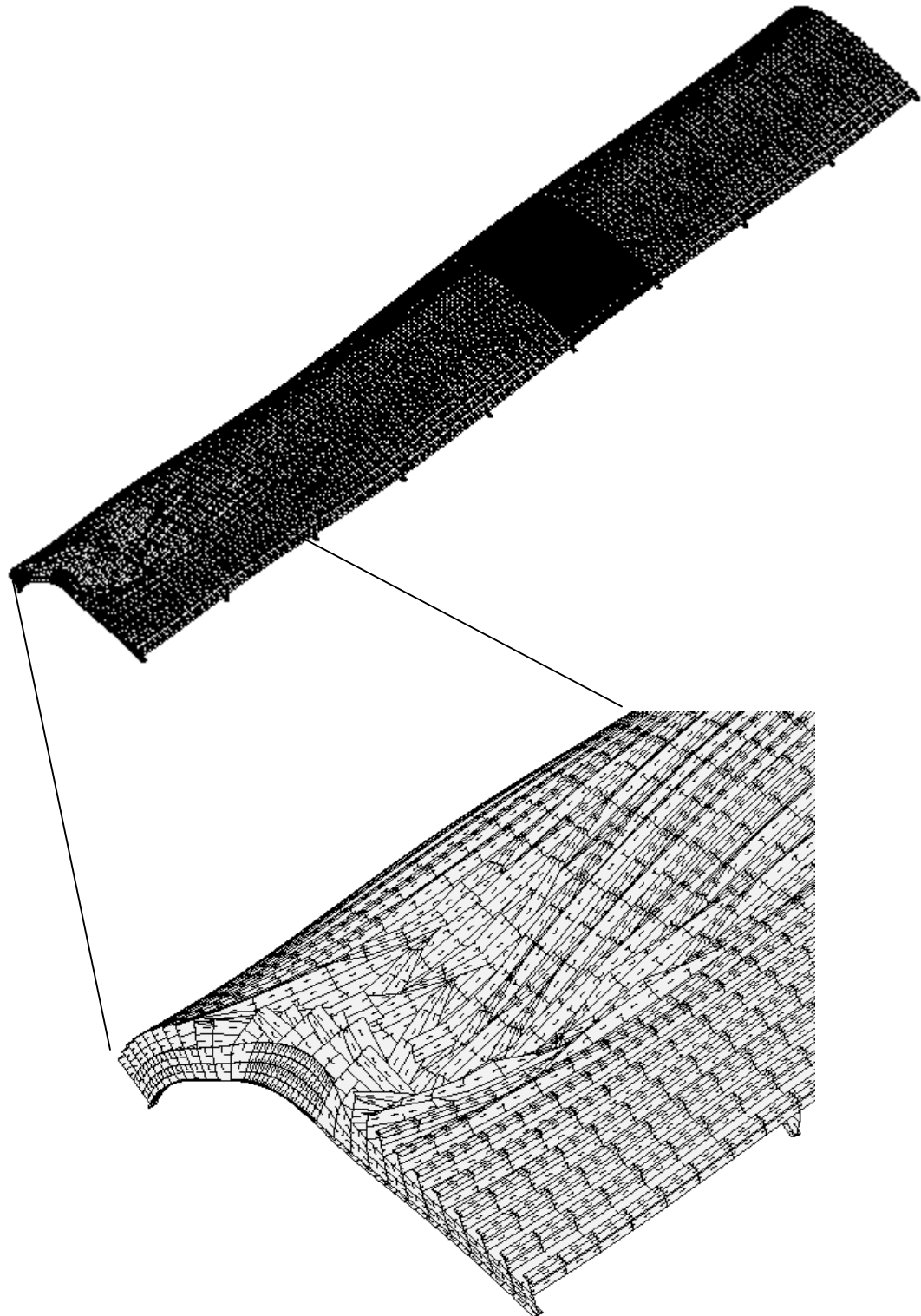


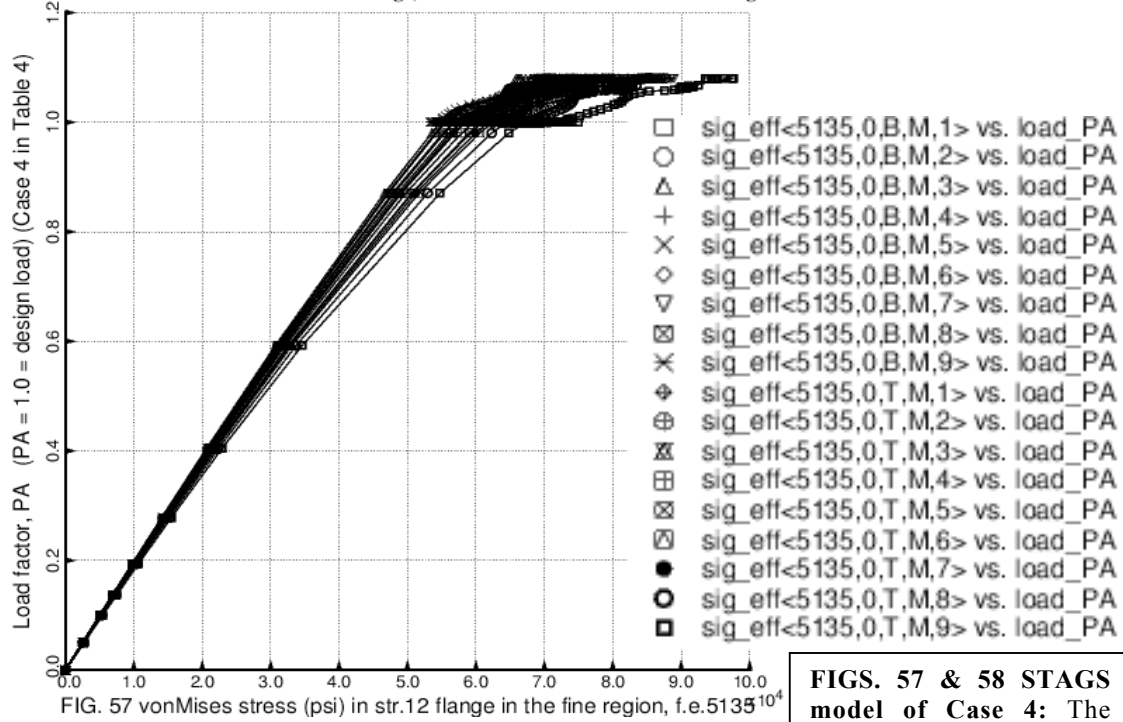
FIG. 55 STAGS model of Case 4: An example in which a nonlinear static STAGS run is followed by several nonlinear dynamic runs, followed by several more nonlinear static runs, followed by a final nonlinear dynamic run.



STAGS model of Case 4, Table 4: no Koiter, yes change imperfection, ICONSV = 1. Compare with Fig. 30. STAGS nonlinear dynamic run with load factor PA held constant at PA=1.08. This figure shows the deformed state at Step 1050, Time=0.0930187 seconds. The imperfection is shown in Fig. 49; amplitude, Wimp= -0.0625 inch.

FIG. 56 Elastic collapse of the imperfect cylindrical shell at the end of the nonlinear dynamic STAGS run.

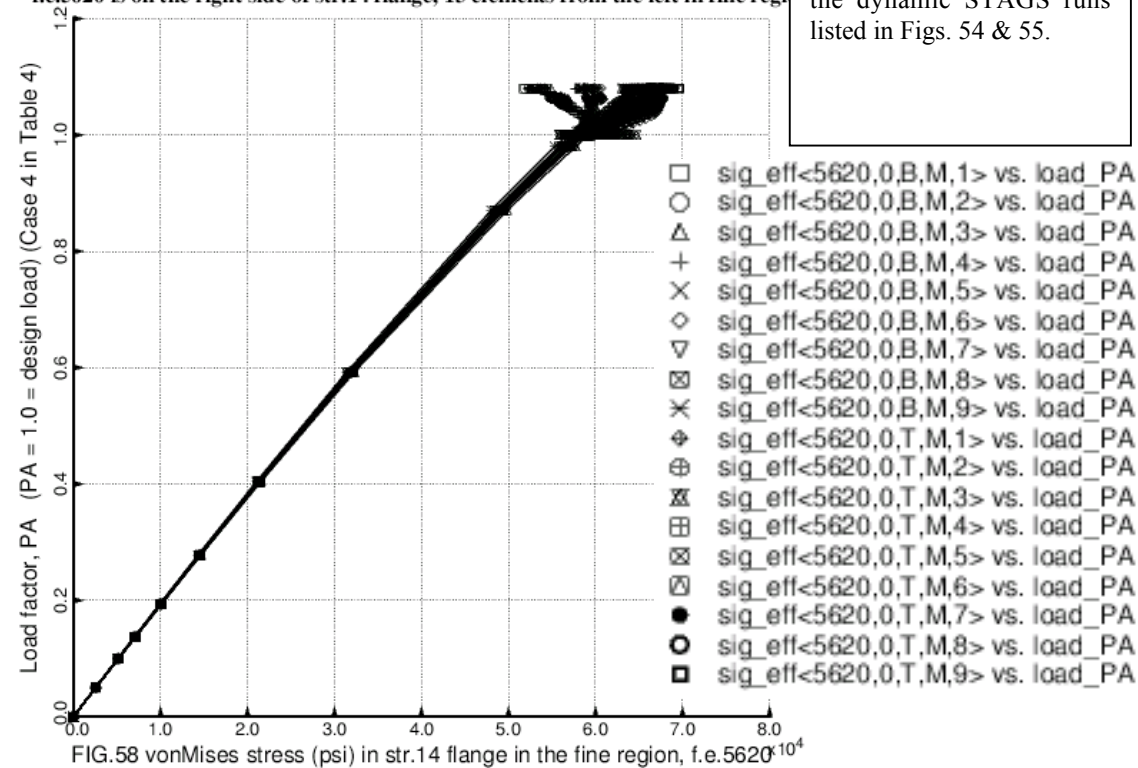
f.e.5135 is on the left side of str.12 flange, 14 elements from the left in fine region



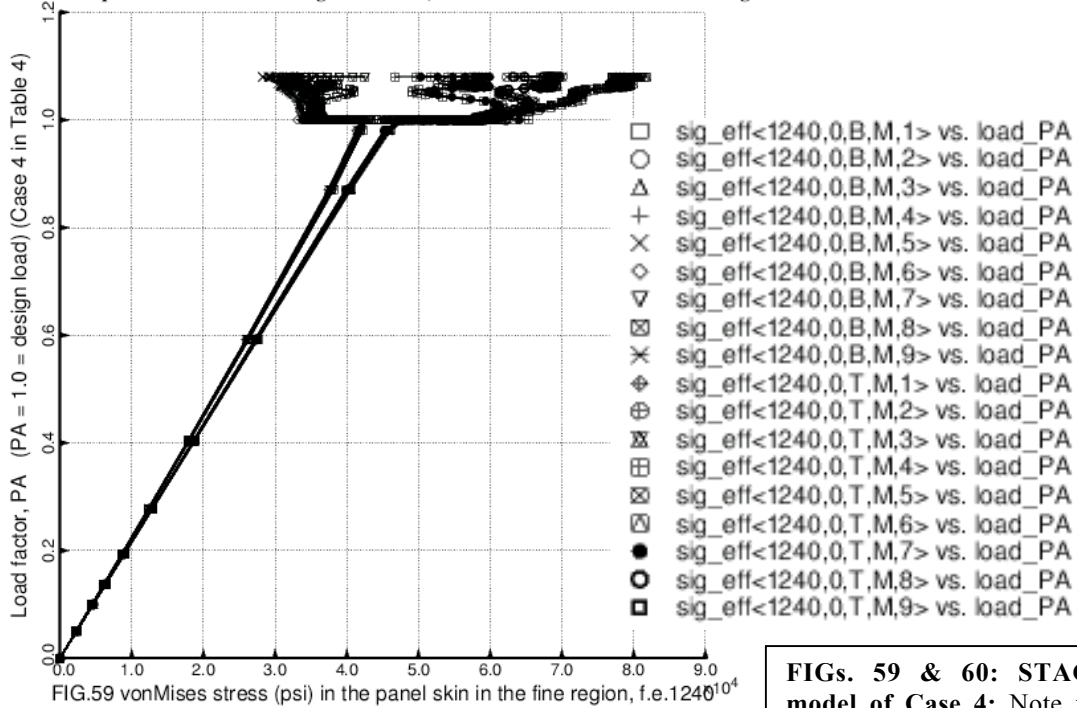
The maximum allowable effective stress is 60 ksi

FIGS. 57 & 58 STAGS model of Case 4: The imperfection shape is displayed in Fig. 49 with amplitude $W_{imp}=-0.0625$ inch. The horizontally arrayed data correspond to the dynamic STAGS runs listed in Figs. 54 & 55.

f.e.5620 is on the right side of str.14 flange, 13 elements from the left in fine region



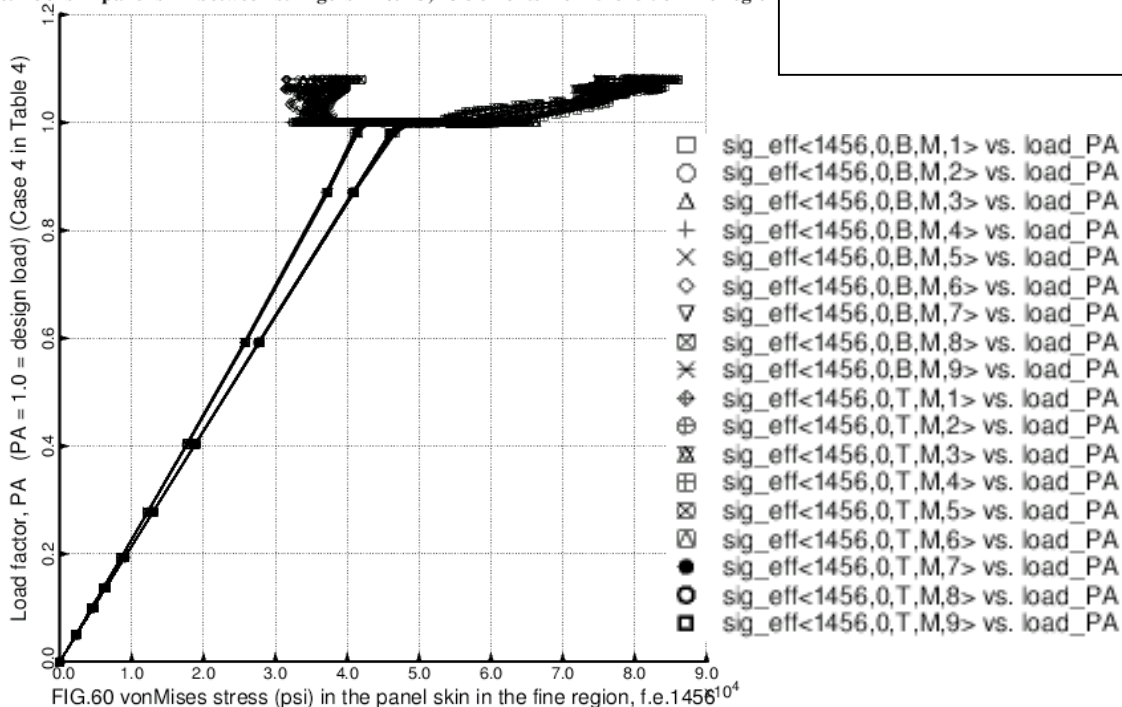
f.e.1240 is in panel skin between stringers 14 & 15, 12 elements from the left in fine region

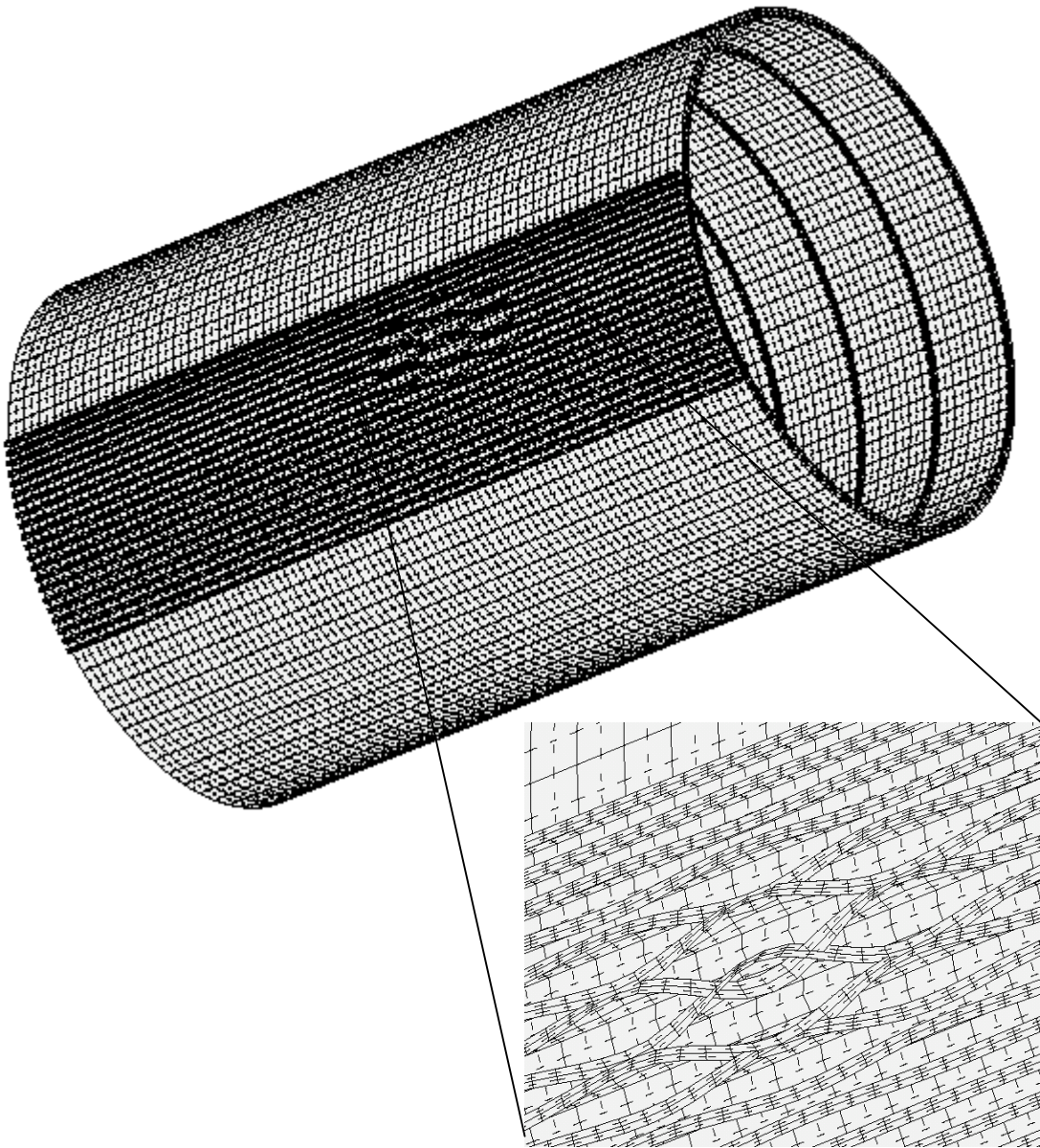


The maximum allowable effective (von Mises) stress is $\sigma_{\text{bar(allowable)}} = 60 \text{ ksi}$.

FIGS. 59 & 60: STAGS model of Case 4: Note the large increase in effective stress in the panel skin during the dynamic STAGS runs at load factor, PA = 1.0. This increase in effective stress is caused by local buckling of the type displayed in Figs. 4 and 48.

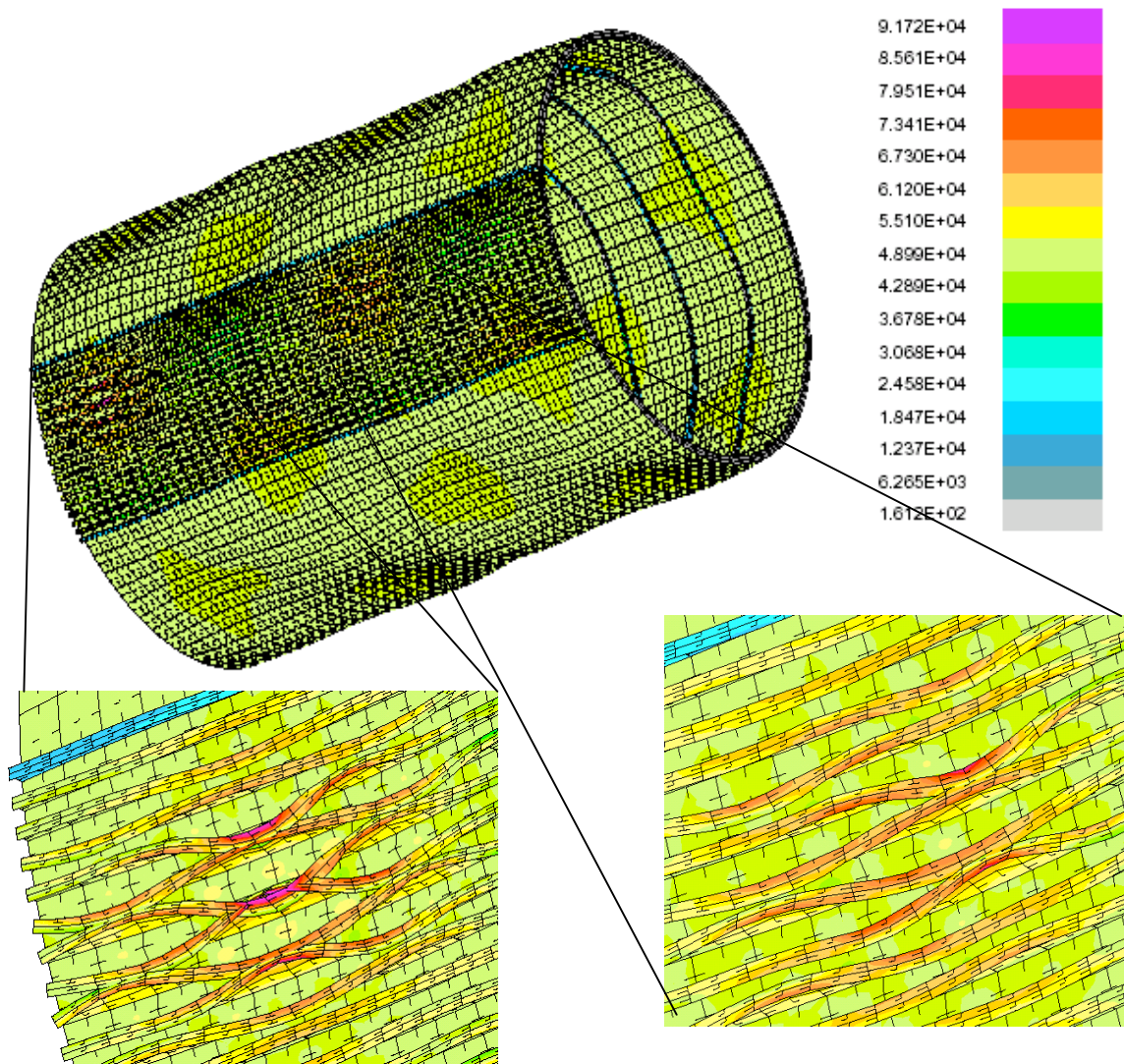
f.e.1456 is in panel skin between stringers 12 & 13, 18 elements from the left of fine region





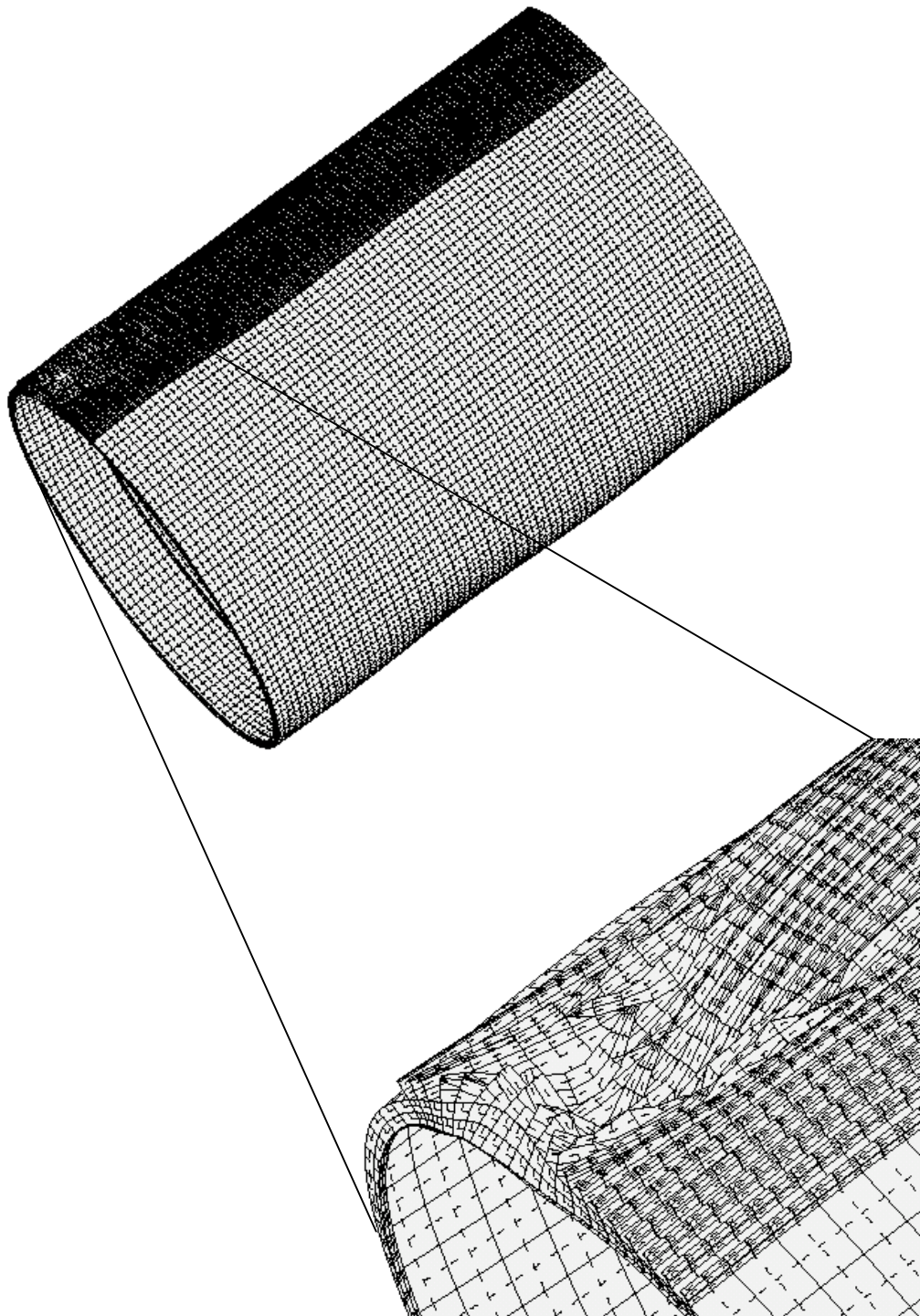
STAGS model of Case 4, Table 4: no Koiter, yes change imperfection, ICONSV = 1. STAGS nonlinear buckling mode at load factor, PA = 1.07084. There is one imperfection shape, shown in Figs. 1a,b, with amplitude, Wimp1=+0.0625 inch. The nonlinear buckling load factor from STAGS, pcr=1.1386; PANDA2 predicts a load factor, 1.0097, for the bending-torsion buckling mode of the imperfect shell as loaded by the design load, Nx= -3000 lb/in.

FIG. 61 NONLINEAR bending-torsion buckling mode from STAGS. This mode is used as a second imperfection shape with amplitude, Wimp2 = -0.0005 inch in a subsequent nonlinear STAGS run.



STAGS model of Case 4, Table 4: no Koiter, yes change imperfection, ICONSV = 1. Compare with Fig. 2. There are two imperfection shapes in the STAGS model: Fig. 1a with amplitude, Wimp1 = +0.0625 inch plus Fig. 61 with amplitude, Wimp2 = -0.0005 inch. This figure shows the nonlinear STABLE equilibrium state at the end of the nonlinear dynamic STAGS run: Time=0.04205 seconds. The load factor PA is held constant at PA = 1.078. The stringer at the top of the inserts has half the stiffness and half the load of its neighbors.

FIG. 62 STAGS prediction of outer fiber effective stress (psi) at axial load, Nx= -3000 x 1.078 lb/in.



STAGS model of Case 4, Table 4: no Koiter, yes change imperfection, ICONSV = 1. Compare with Fig. 56. The imperfect shell has the same two imperfections as described in Figs. 61 and 62. This figure shows the state of the imperfect shell at the end of a nonlinear dynamic STAGS run with load factor PA held constant at PA = 1.089. Time of collapse = 0.0481906 seconds, Step 530. The collapse load, collapse mode, and load factor PA at collapse agree with those for the 60-degree STAGS model, which validates the 60-degree model.

FIG. 63 Dynamic elastic collapse of the STAGS model shown in the previous figure.

Case4 dynamic response: Fig.1a Wimp=0.0625 plus Fig.61 Wimp2=-0.0005 inch

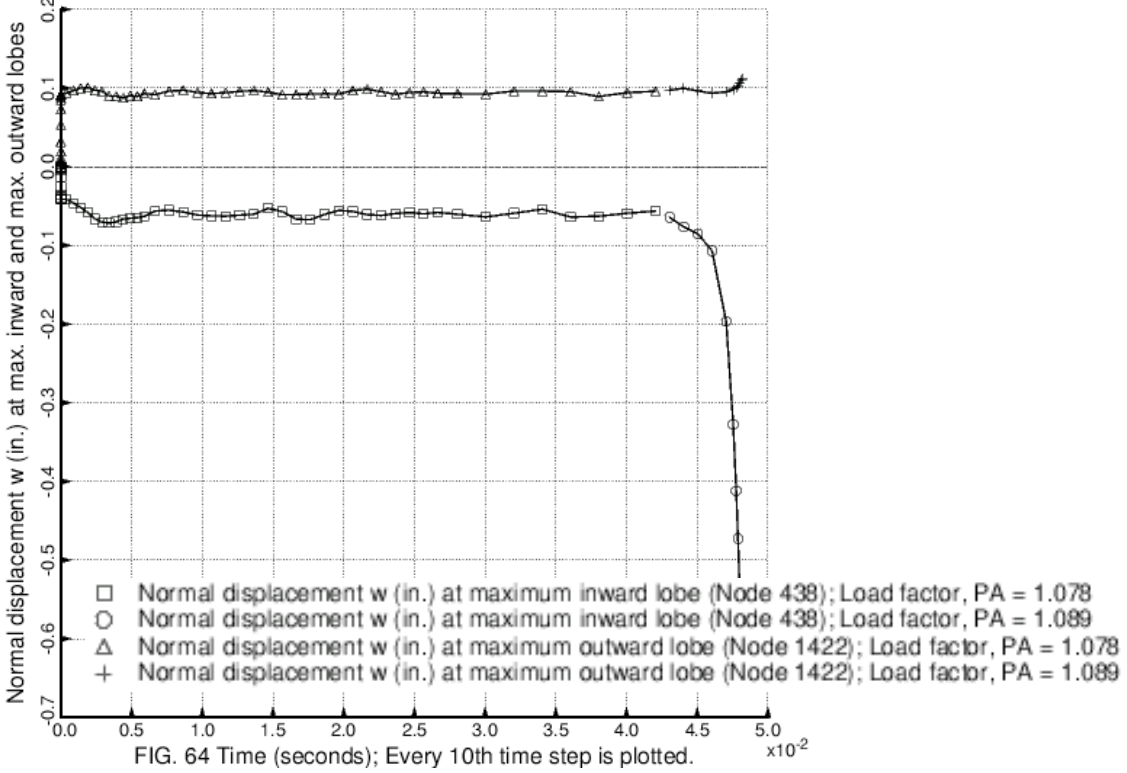


FIG. 64 Time (seconds); Every 10th time step is plotted.

FIGS. 64 & 65 STAGS model of Case 4: STAGS predictions of maximum normal displacement (FIG. 64) and effective stress (FIG. 65).

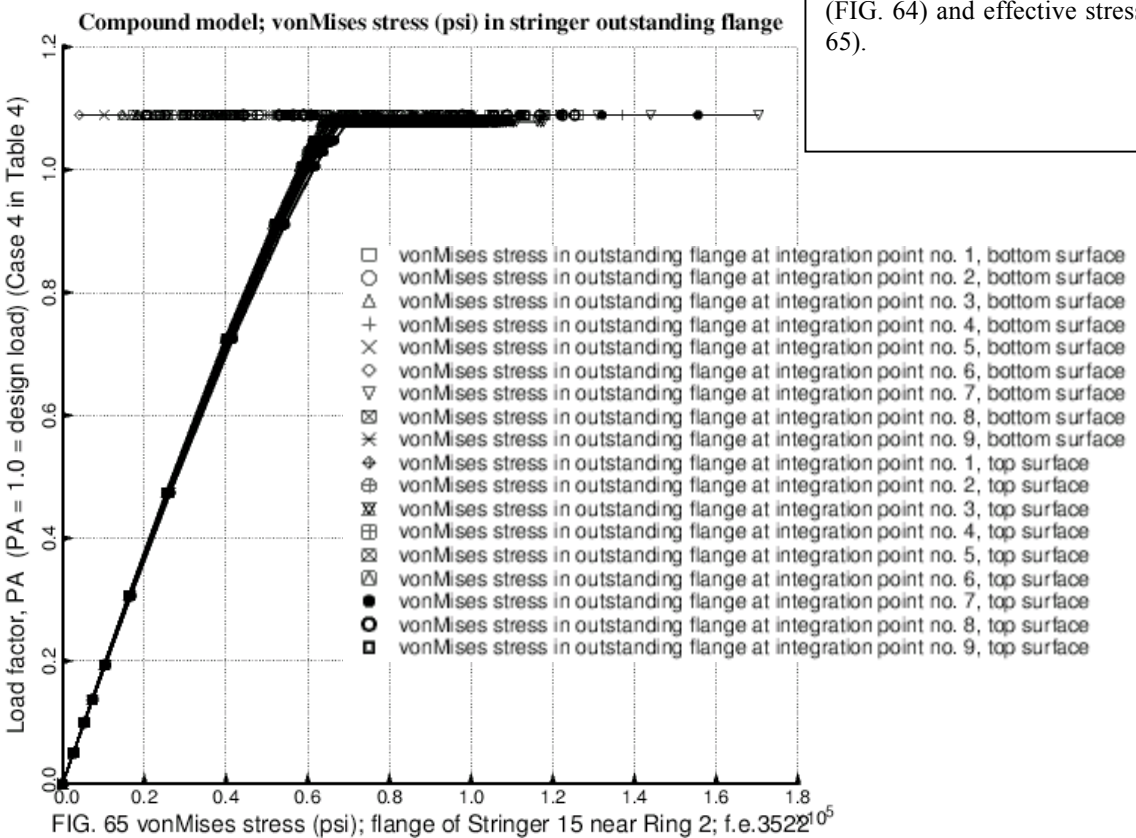
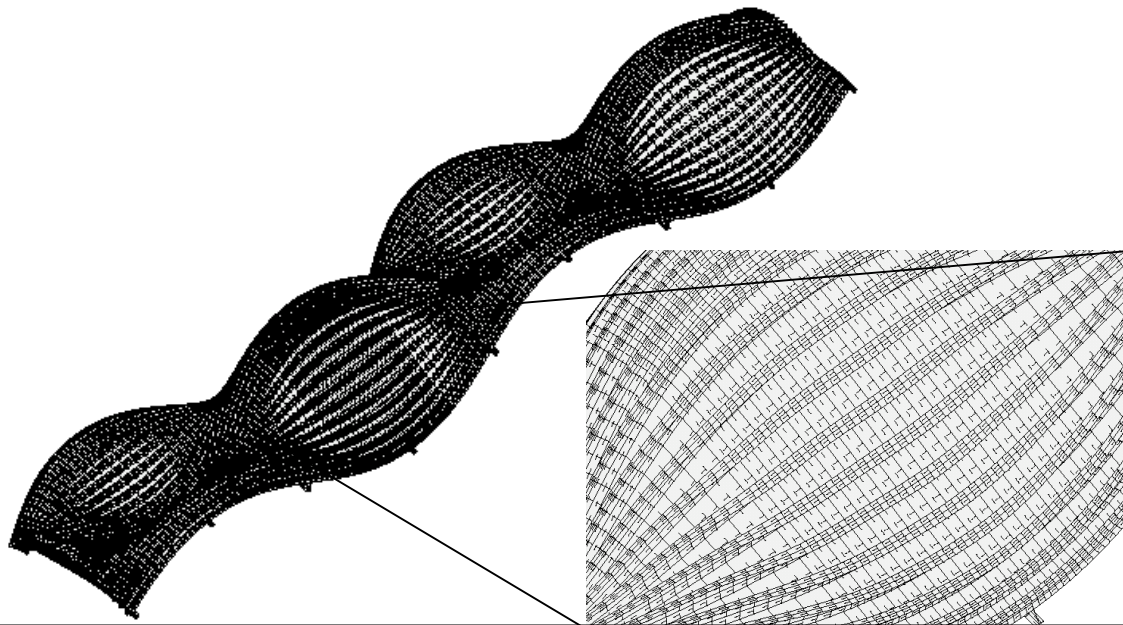
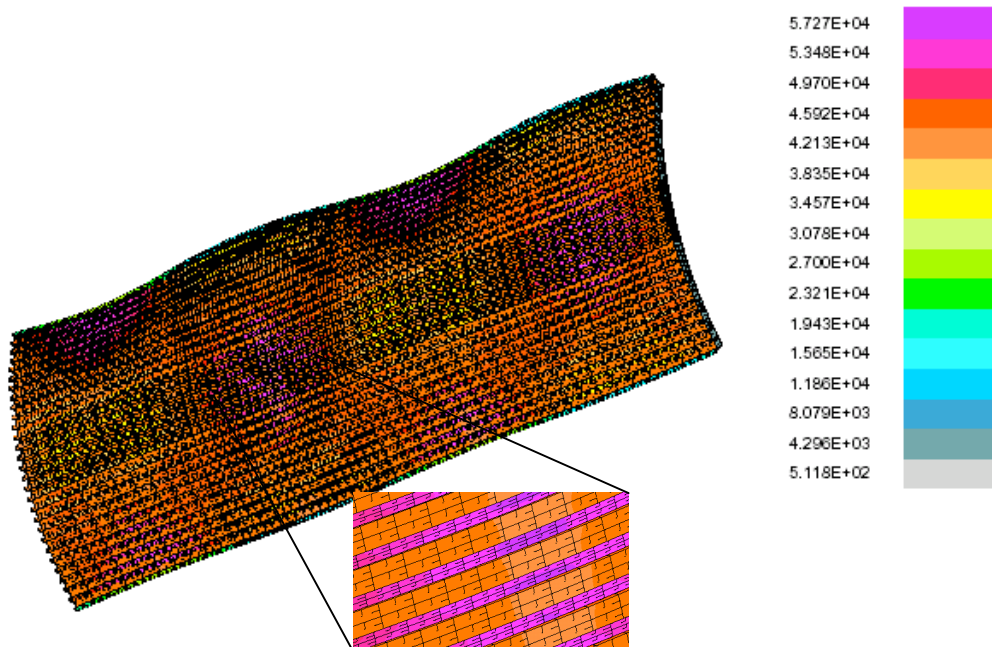


FIG. 65 vonMises stress (psi); flange of Stringer 15 near Ring 2; f.e.3522^{10⁵}



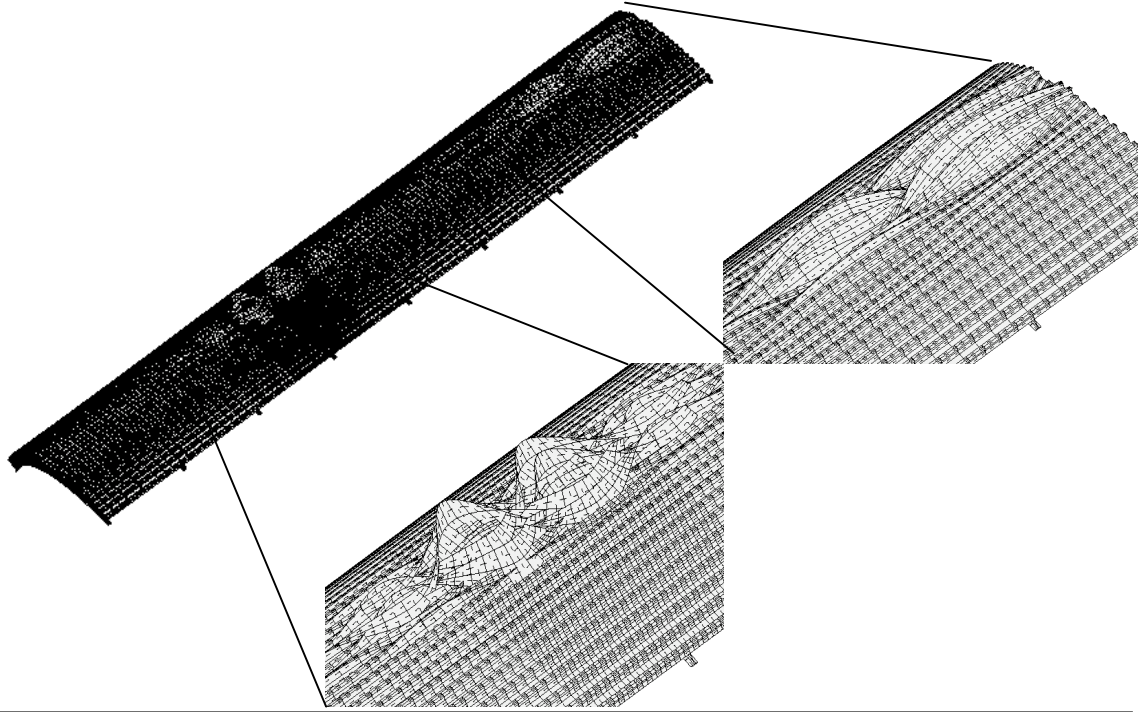
STAGS model of Case 5, Table 4: yes Koiter, yes change imperfection, ICONSV = 1. Compare with Fig. 49. STAGS Mode no. 564; buckling load factor, pcr=2.0155. PANDA2 predicts a load factor, 2.04, before application of the 3 knockdown factors identified in Fig. 37; 1.890 after application of the 3 knockdown factors. The expanded insert demonstrates that the general buckling mode is very “pure”, having no discernable local components of the sort clearly visible in the expanded insert in Fig. 49.

FIG. 66 Linear general buckling mode from the STAGS 60-degree model with a nonuniform mesh.



STAGS model of Case 5, Table 4: yes Koiter, yes change imperfection, ICONSV = 1. Compare with Fig. 50. There is one imperfection with the shape shown in Fig. 66, amplitude, Wimp= -0.0625 in. This figure shows the deformed state of the imperfect 60-degree STAGS model at load factor, PA = 1.0. Nodal mesh is concentrated in 2nd half of the 3rd and 1st half of the 4th ring bay. The maximum effective stress is lower than that in Fig. 50 because the general buckling modal imperfection is “pure”, as shown in Fig. 66, in contrast to the “impure” general buckling mode displayed in Fig. 49.

FIG. 67 STAGS prediction of outer fiber effective stress (psi) at axial load, Nx = -3000 x (PA=1.0) lb/in. The maximum effective stress is in the outstanding flange of one of the stringers in the region where the mesh density is greatest.



STAGS model of Case 5, Table 4: yes Koiter, yes change imperfection, ICONSV = 1. The single imperfection shape is shown in Fig. 66, amplitude, Wimp = -0.0625 inch. This nonlinear bending-torsion buckling mode is computed at load factor, PA = 1.14263. The nonlinear buckling load factor from STAGS, per = 1.1446. PANDA2 predicts a load factor, 1.131, for Load set 1, Subcase 1 for bending-torsion buckling of the imperfect shell.

FIG. 68 NONLINEAR bending-torsion buckling mode, Wimp2 in the STAGS 60-degree model.

Wimp2 is used as a second imperfection shape in further nonlinear STAGS runs of Case 5.

- Disp(26337,v,L) vs. load_PA, Sidesway of Stringer 14 in 3rd ring bay, 11 nodes from left of fine region
- Disp(27547,v,L) vs. load_PA, Sidesway of Stringer 15 in 3rd ring bay, 11 nodes from left of fine region

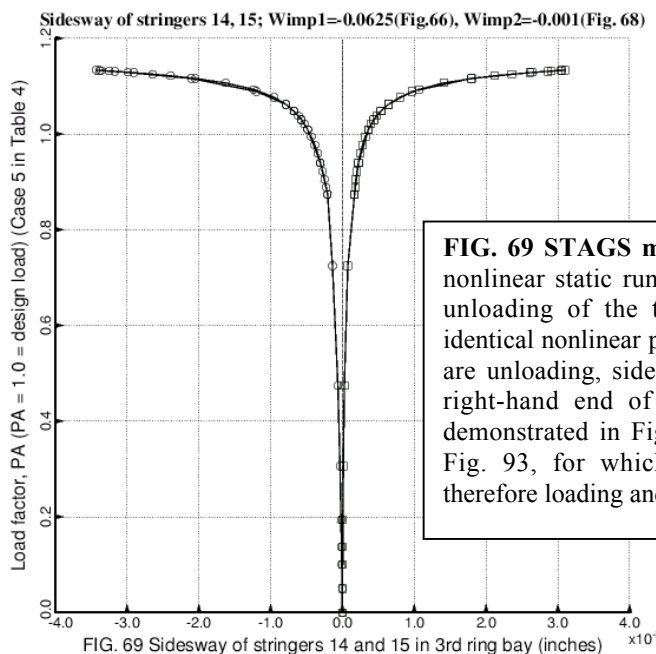
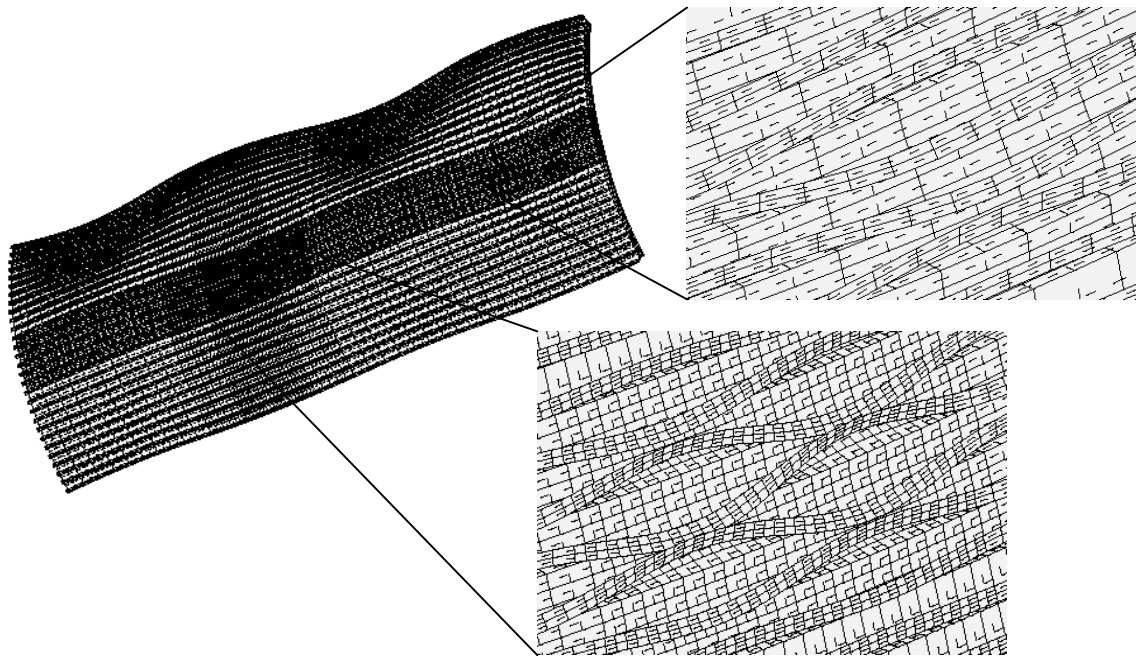
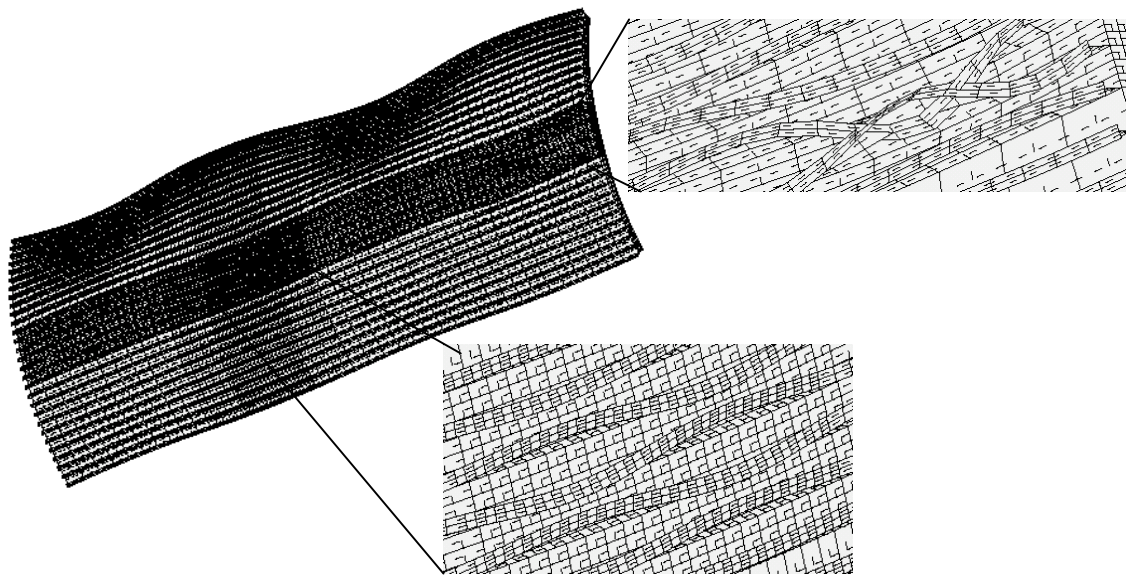


FIG. 69 STAGS model of Case 5: Results from a STAGS nonlinear static run. The elastic model predicts loading and unloading of the two stringers in Ring bay 3 along the identical nonlinear path. While the two stringers in Ring bay 3 are unloading, sidesway of the same two stringers near the right-hand end of the shell continues to increase, as is demonstrated in Figs. 70 and 71. Compare this figure with Fig. 93, for which irreversible plastic flow occurs and therefore loading and unloading occur along different paths.



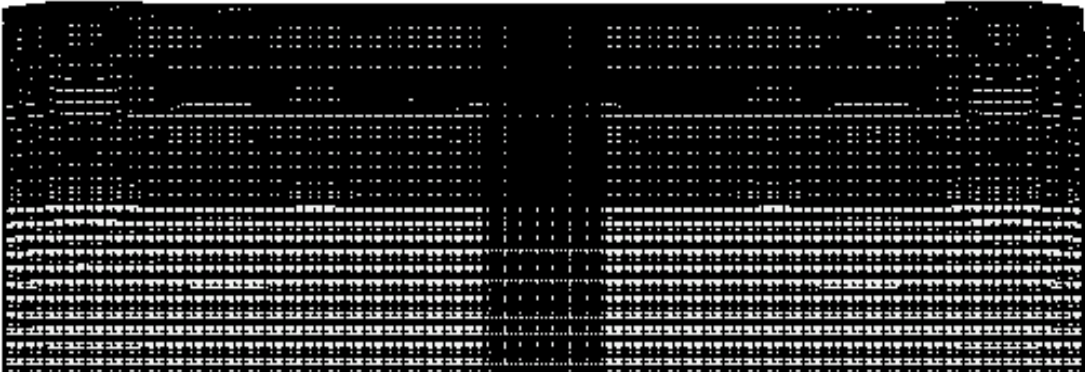
STAGS model of Case 5, Table 4: yes Koiter, yes change imperfection, ICONSV = 1. See Fig. 69 for stringer sidesway. There are two imperfections, Wimp1 = -0.0625 in. (Fig. 66), Wimp2= -0.001 in. (Fig. 68). The panel state displayed in this figure corresponds to the leftmost and rightmost data points in Fig. 69 (at load factor PA = 1.13344). There is much more sidesway in the region of dense mesh than in the neighborhood of the right end of the STAGS model.

FIG. 70 STAGS prediction of deformed panel showing stringer sidesway (Fig. 69) at the collapse load, PA = 1.13344.



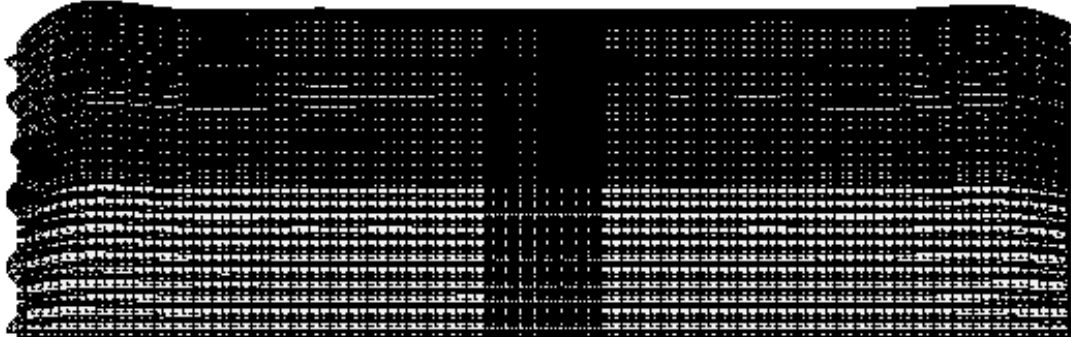
STAGS model of Case 5, Table 4: yes Koiter, yes change imperfection, ICONSV = 1. Compare with Fig. 70. There are two imperfections: Wimp1 = -0.0625 in.(Fig. 66); Wimp2 = -0.001 in. (Fig. 68). The stringers at the right end of the shell collapse while those in the region of dense mesh unload.

FIG. 71 STAGS prediction of the deformed panel showing stringer sidesway after elastic collapse at PA=1.13344.



STAGS model of Case 6, Table 4: no Koiter, perfect shell, $N_x = -6000$ lb/in, $s_{bar}(\text{allowable}) = 120$ ksi, $\text{ICONSV} = 1$. This deformed state is from the very early part of a nonlinear dynamic STAGS run. Note the beginning of axisymmetric edge collapse at the STAGS load factor, $PA = 1.0$, Time = 0.00025 seconds. (PA is held constant at 1.0 during the nonlinear dynamic run). This type of axisymmetric edge buckling cannot be predicted by the PANDA2 model. It is possible in the STAGS model because normal displacement $w = \text{constant}$ along the two curved edges, not zero.

Fig. 72 Axisymmetrically deformed panel very early in the nonlinear dynamic STAGS run during which the load is held constant at the design load, that is at the load factor, $PA = 1.0$.

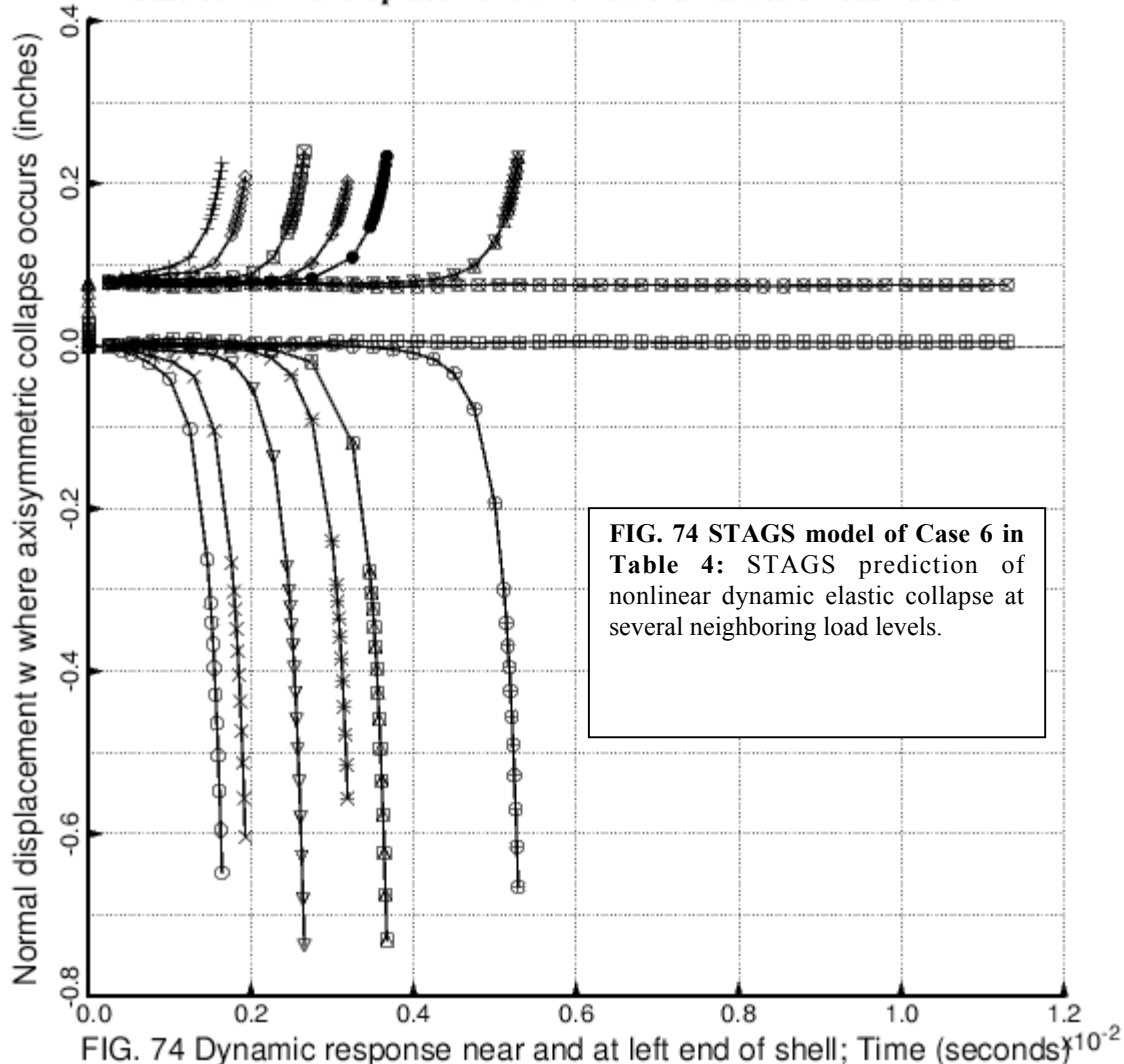


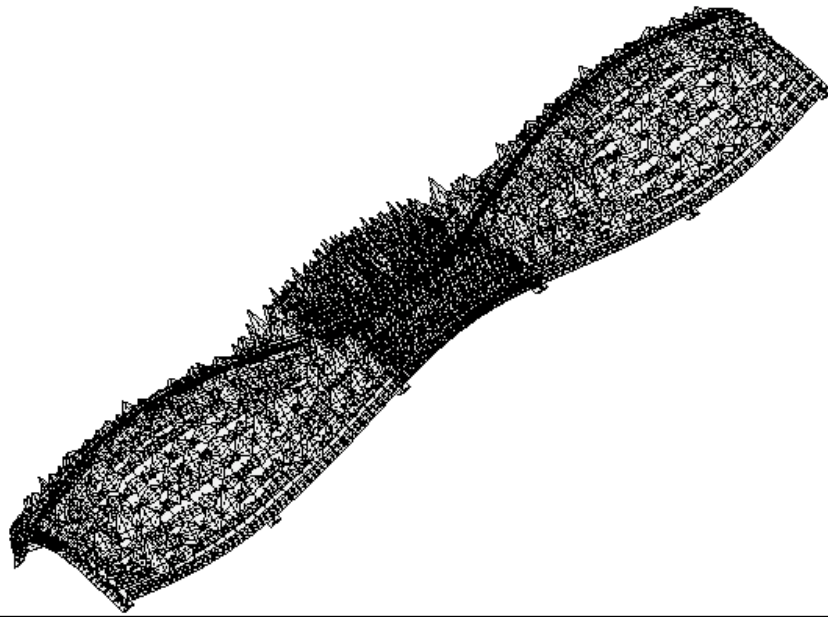
STAGS model of Case 6, Table 4: no Koiter, perfect shell, $N_x = -6000$ lb/in, $s_{bar}(\text{allowable}) = 120$ ksi, $\text{ICONSV} = 1$. PANDA2 cannot predict this almost axisymmetric behavior. The STAGS load factor PA is maintained at $PA = 1.0$ throughout the nonlinear dynamic run. The ring at the left-hand edge has buckled dynamically. The right edge is still almost axisymmetric. Actual shells will not buckle in this mode because of the presence of local reinforcement at the ends not accounted for in either the STAGS or the PANDA2 models.

FIG. 73 Advanced dynamic “axisymmetric” collapse with edge wrinkling at Time = 0.00164375 seconds in the nonlinear dynamic STAGS run.

- time vs. Disp(36,w,L), Static run: Normal displacement w at left edge, 14 nodes up in the fine region
- time vs. Disp(36,w,L), Dynamic run, PA=1.0: Normal displacement w at left edge, 14 nodes up, fine region
- △ time vs. Disp(684,w,L), Static run: Normal displacement w at outward bulge near the left edge
- + time vs. Disp(684,w,L), Dynamic run, PA=1.0: Normal displacement w at outward bulge near left edge
- × time vs. Disp(36,w,L), Dynamic run, PA=0.99: Normal displacement w at left edge, 14 nodes up, fine region
- ◊ time vs. Disp(684,w,L), Dynamic run, PA=0.99: Normal displacement w at outward bulge near left edge
- ▽ time vs. Disp(36,w,L), Dynamic run, PA=0.98: Normal displacement w at left edge, 14 nodes up, fine region
- ▣ time vs. Disp(684,w,L), Dynamic run, PA=0.98: Normal displacement w at outward bulge near left edge
- * time vs. Disp(36,w,L), Dynamic run, PA=0.975: Normal displacement w at left edge, 14 nodes up, fine region
- ◆ time vs. Disp(684,w,L), Dynamic run, PA=0.975: Normal displacement w at outward bulge near left edge
- ⊕ time vs. Disp(36,w,L), Dynamic run, PA=0.970: Normal displacement w at left edge, 14 nodes up, fine region
- ⊗ time vs. Disp(684,w,L), Dynamic run, PA=0.970: Normal displacement w at outward bulge near left edge
- time vs. Disp(36,w,L), Dynamic run, PA=0.965: Normal displacement w at left edge, 14 nodes up, fine region
- ▢ time vs. Disp(684,w,L), Dynamic run, PA=0.965: Normal displacement w at outward bulge near left edge
- ▢ time vs. Disp(36,w,L), Start at Step 11, PA=0.972964, Apply same PA in dynamic run: w at left edge
- time vs. Disp(684,w,L), Start at Step 11, PA=0.972964, Apply same PA in dynamic run: w at outward bulge

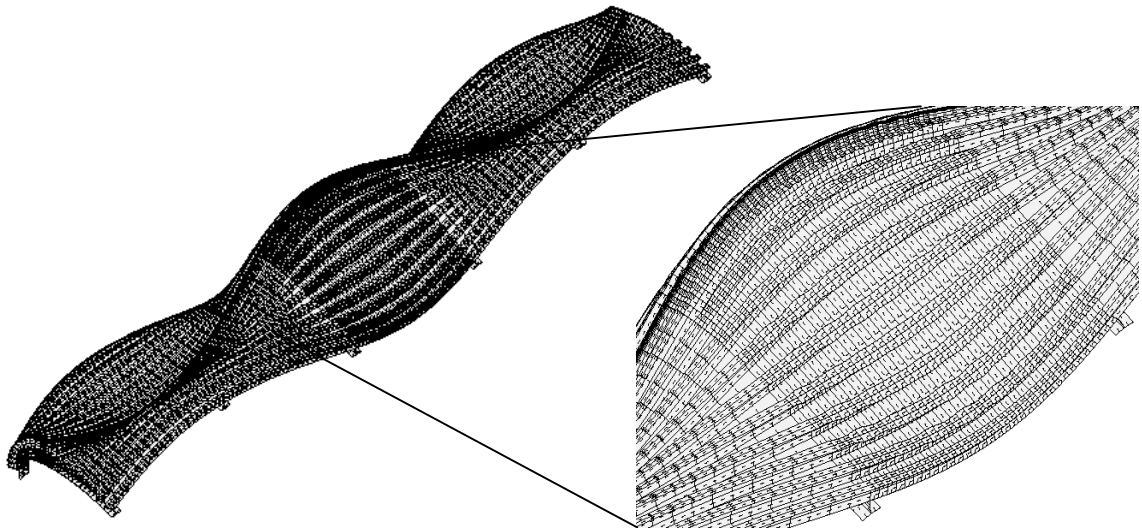
Case 6: Normal displacement w for several values of load factor PA





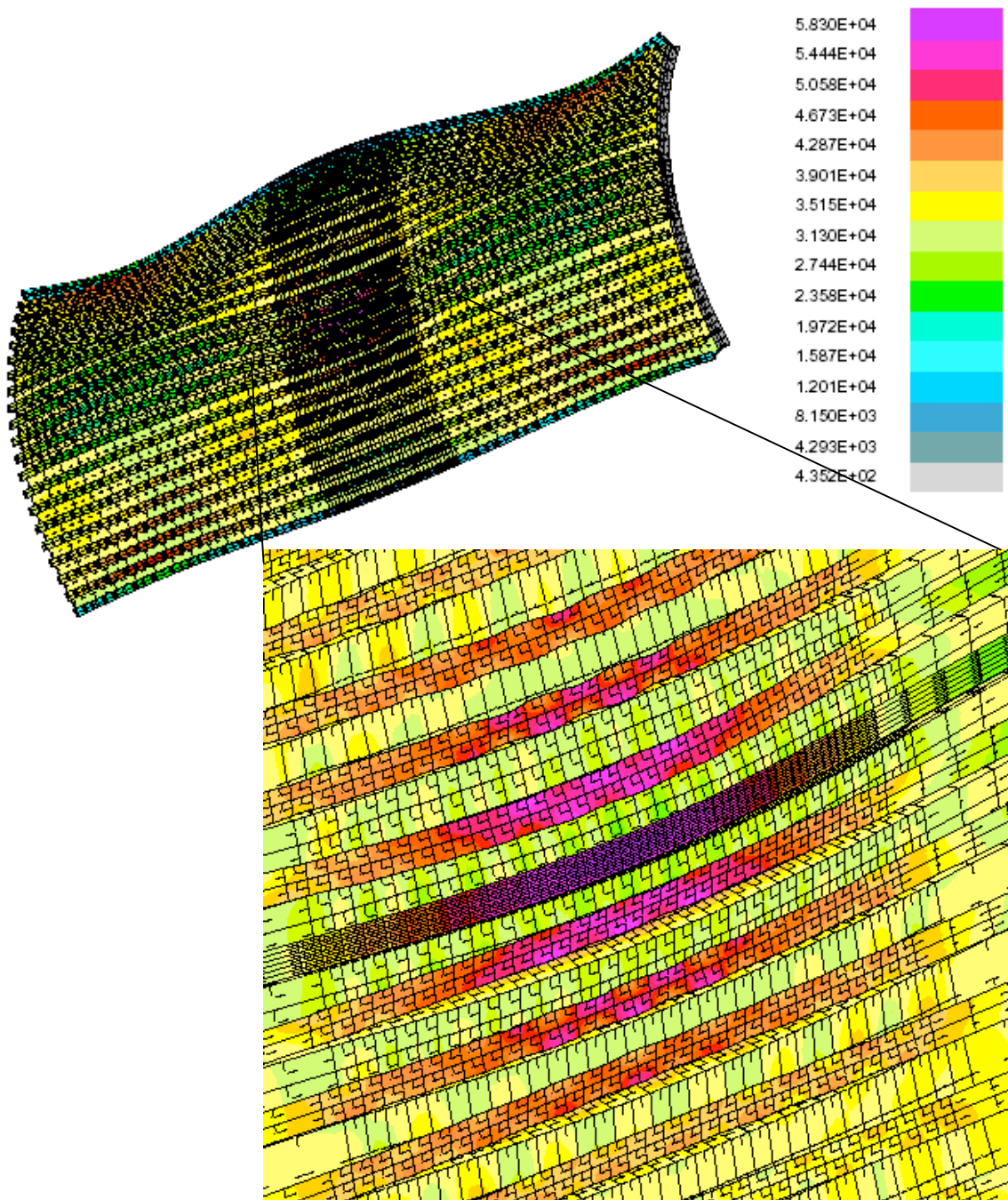
STAGS model of Case 7, Table 4: no Koiter, no change imperfection, ICONSV = 1. STAGS mode no. 1829, buckling load factor, pcr = 3.7470. This mode is not a suitable imperfection shape because of the large component of local deformation that “pollutes” the general buckling mode shape.

FIG. 75 General buckling mode shape computed with the STAGS control index, ILIN = 0, in every shell unit [20C]. Compare with Fig. 76.



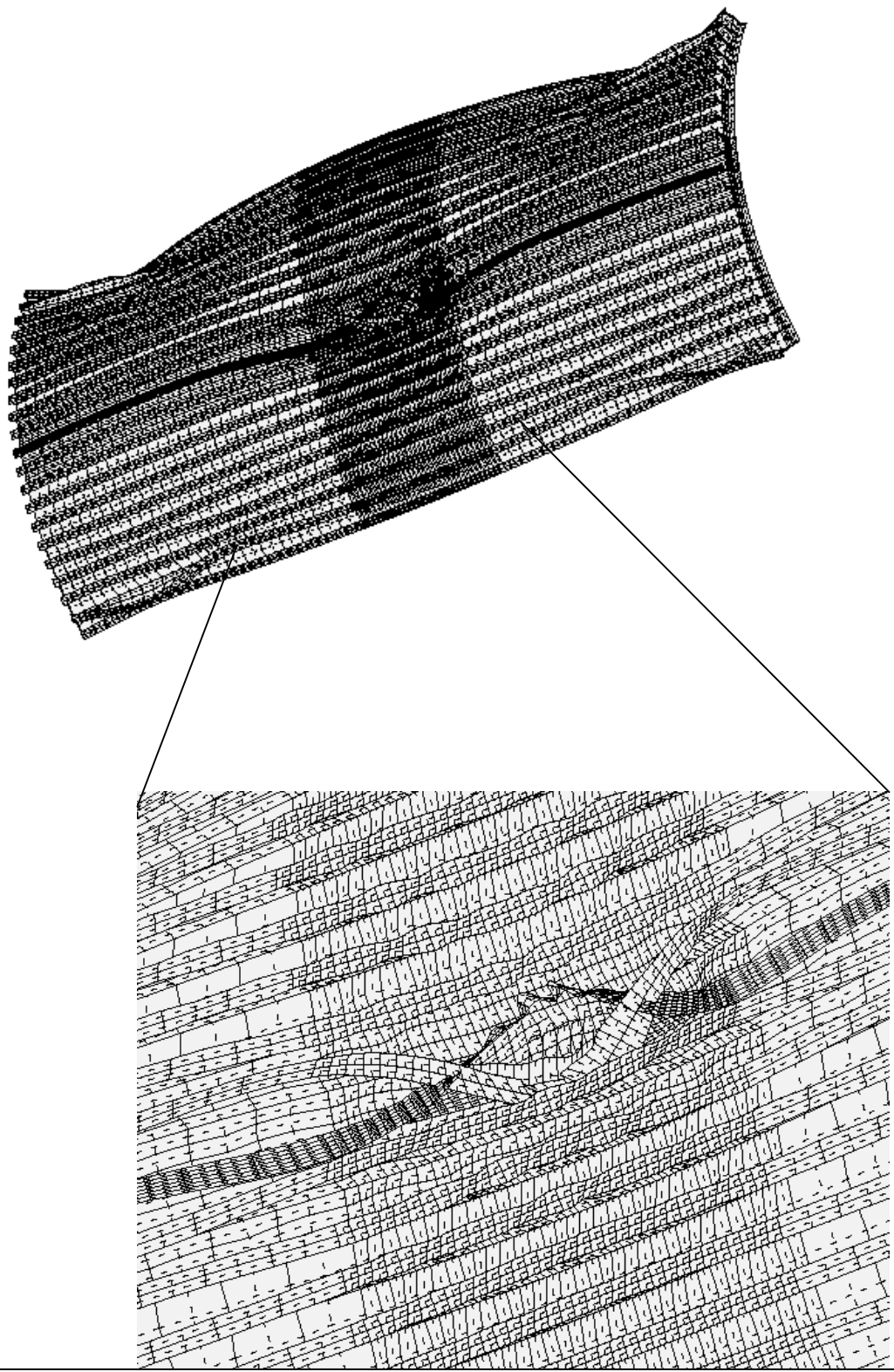
STAGS model of Case 7, Table 4: no Koiter, no change imperfection, ICONSV = 1. This mode is a suitable imperfection shape. Mode No. 427, STAGS load factor, pcr=3.7904; BIGBOSOR4 predicts a load factor, 3.7217, with $(m,n) = (3,5)$ waves. PANDA2 predicts a load factor, 4.01, before the application of the three knockdown factors identified in Fig. 37, and a load factor, 2.25, after application of the three knockdown factors. (With ICONSV=1 two of the knockdown factors are conservative: those for smearing stringers and for smearing rings).

FIG. 76 STAGS general buckling mode with a very small component of local deformation. This mode was computed with the STAGS control index ILIN = 1 [20C]. Compare with Fig. 75.



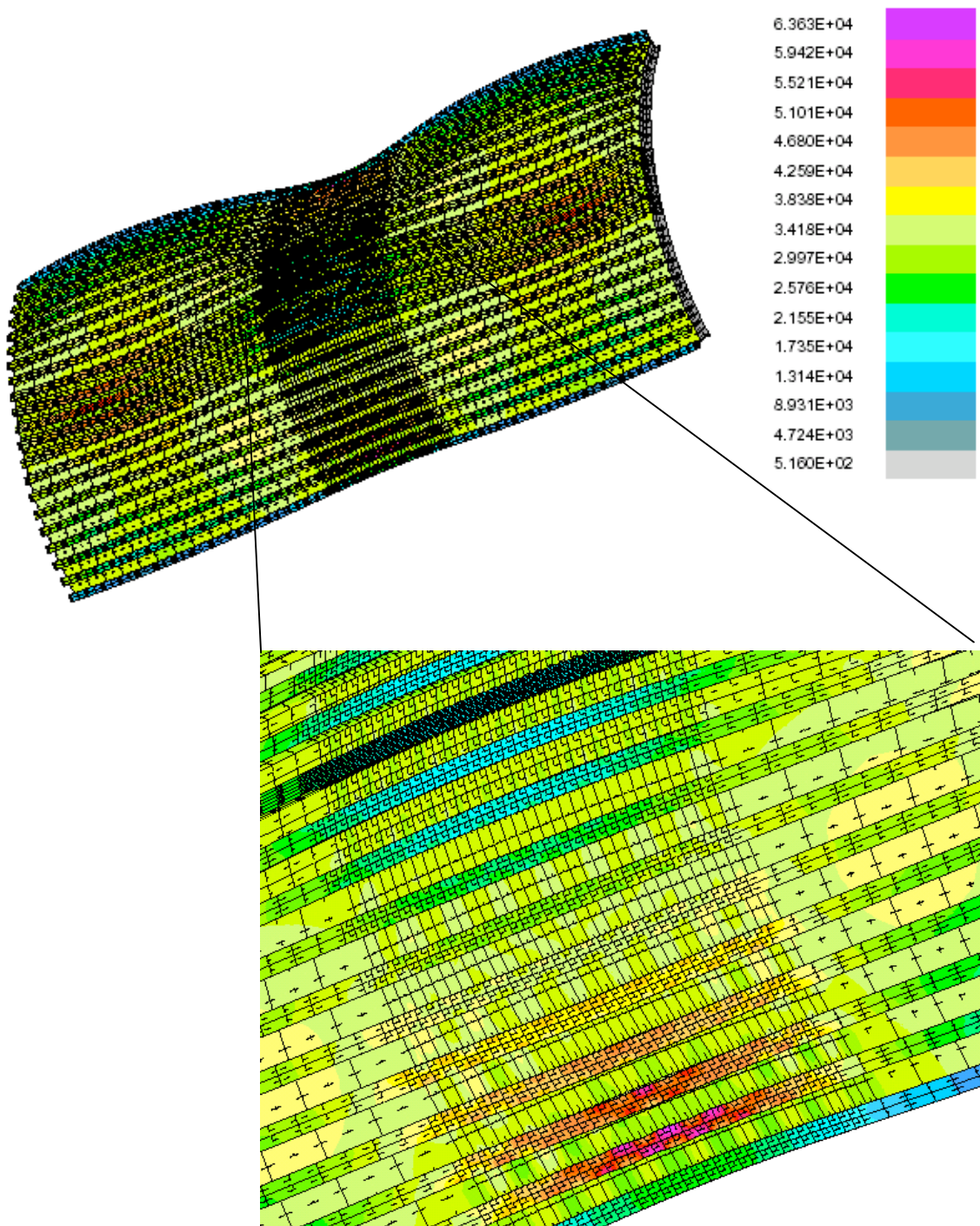
STAGS model of Case 7, Table 4: no Koiter, no change imperfection, ICONSV = 1. Compare with Fig. 79. The imperfect shell has one imperfection shape, that shown in Fig. 76 with an amplitude, Wimp = -0.25 inch. The nodal mesh is concentrated in the 3rd ring bay. Note the presence of short-wavelength deformation in some of the outstanding flanges of the stringers. This figure shows the deformed state of the imperfect STAGS 60-degree model at the load factor, PA = 1.0 (the design load).

FIG. 77 STAGS prediction of outer fiber effective stress (psi) at axial load, Nx = -3000 x (PA=1.0) lb/in. The maximum effective stress is in the outstanding flange of one of the stringers in the region where the mesh density is greatest.



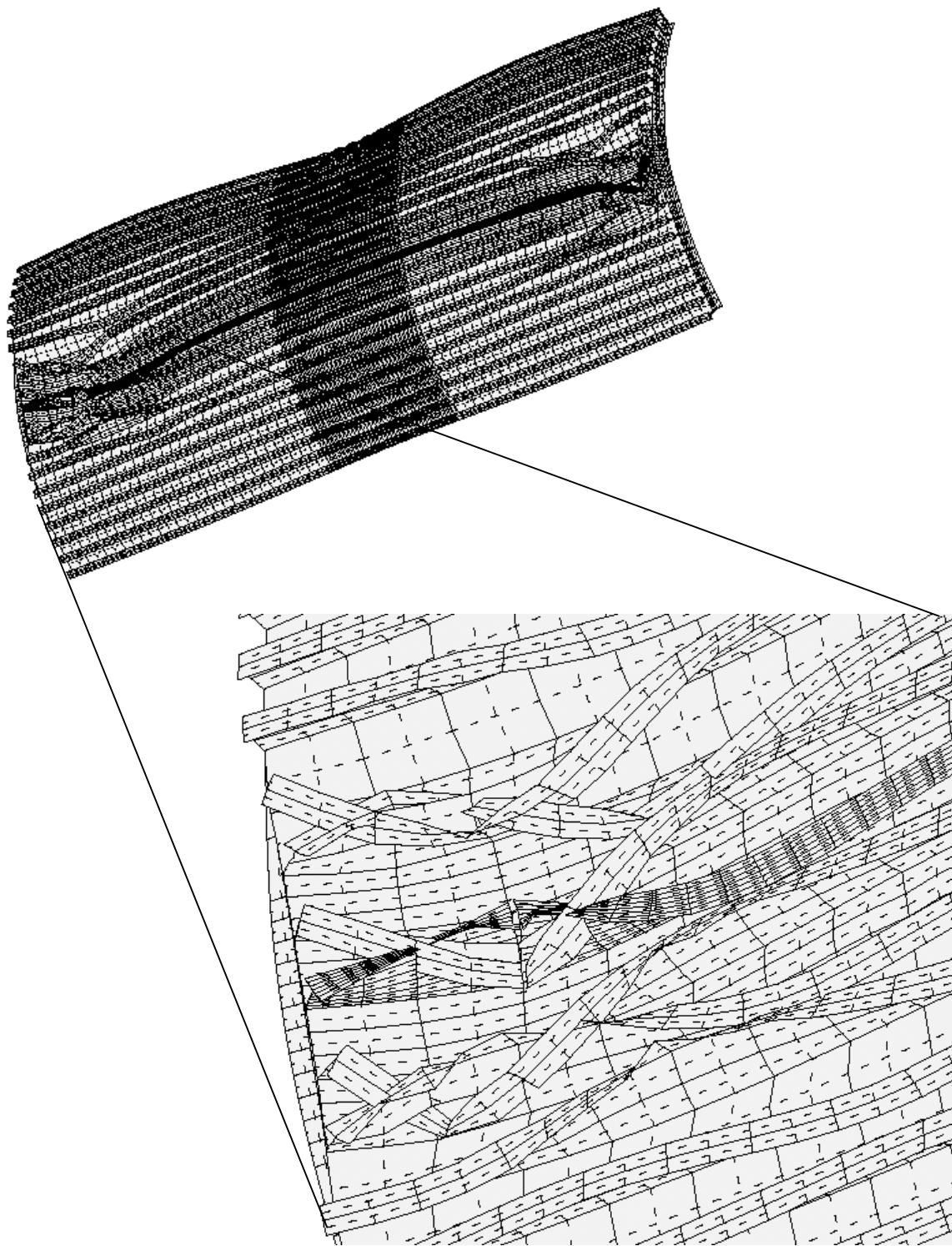
STAGS model of Case 7, Table 4: no Koiter, no change imperfection, ICONSV = 1. There are three imperfection shapes: Wimp1(general) = -0.25 inch; Wimp2(bending-torsion) = +0.005 inch; Wimp3(local) = +0.005 inch. [The imperfection shapes are not shown. They are similar to those displayed in Fig. 88(d) (Wimp2) and 88(c) (Wimp3).] Shown here is the deformed state obtained from a nonlinear dynamic STAGS run in which the load factor PA is held constant at PA = 1.22. Time of collapse=0.07185 seconds.

FIG. 78 Nonlinear dynamic elastic collapse of the STAGS model at load factor PA = 1.22.



STAGS model of Case 7, Table 4: no Koiter, no change imperfection, ICONSV = 1. Compare with Fig. 77. NOTE: The general buckling modal imperfection has the opposite sign from that shown in Fig. 77. The single imperfection shape is shown in Fig. 76. It has an amplitude, Wimp1(general) = +0.25 inch. The deformed state of the panel shown here corresponds to the STAGS load factor, PA = 1.0 (the design load). The stress in the outstanding stringer flange at the bottom edge of the STAGS model is much less than that in its neighbor above because the edge stiffener has half the stiffness and half the loading of the interior stiffeners, a characteristic of all STAGS models generated via STAGSUNIT.

FIG. 79 STAGS prediction of outer fiber effective stress (psi) at axial load, $N_x = -3000 \times (PA=1.0)$ lb/in.



STAGS model of Case 7, Table 4: no Koiter, no change imperfection, ICONSV = 1. Compare with Fig. 78. The single imperfection shape is shown in Fig. 76 and has amplitude Wimp = +0.25 inch. The results shown here are from a nonlinear dynamic STAGS run in which the load factor PA is held constant at PA = 1.15. Time of collapse=0.0929188 seconds.

FIG. 80 Dynamic elastic collapse of the STAGS model shown in the previous figure.

- Stress-strain curve used for STAGS runs in which plasticity is included
- Stress-strain curve for 7075-T6 aluminum at room temperature, compression
- Stress-strain curve for 7075-T6 aluminum at room temperature, tension
- Elastic material used in STAGS runs without plasticity

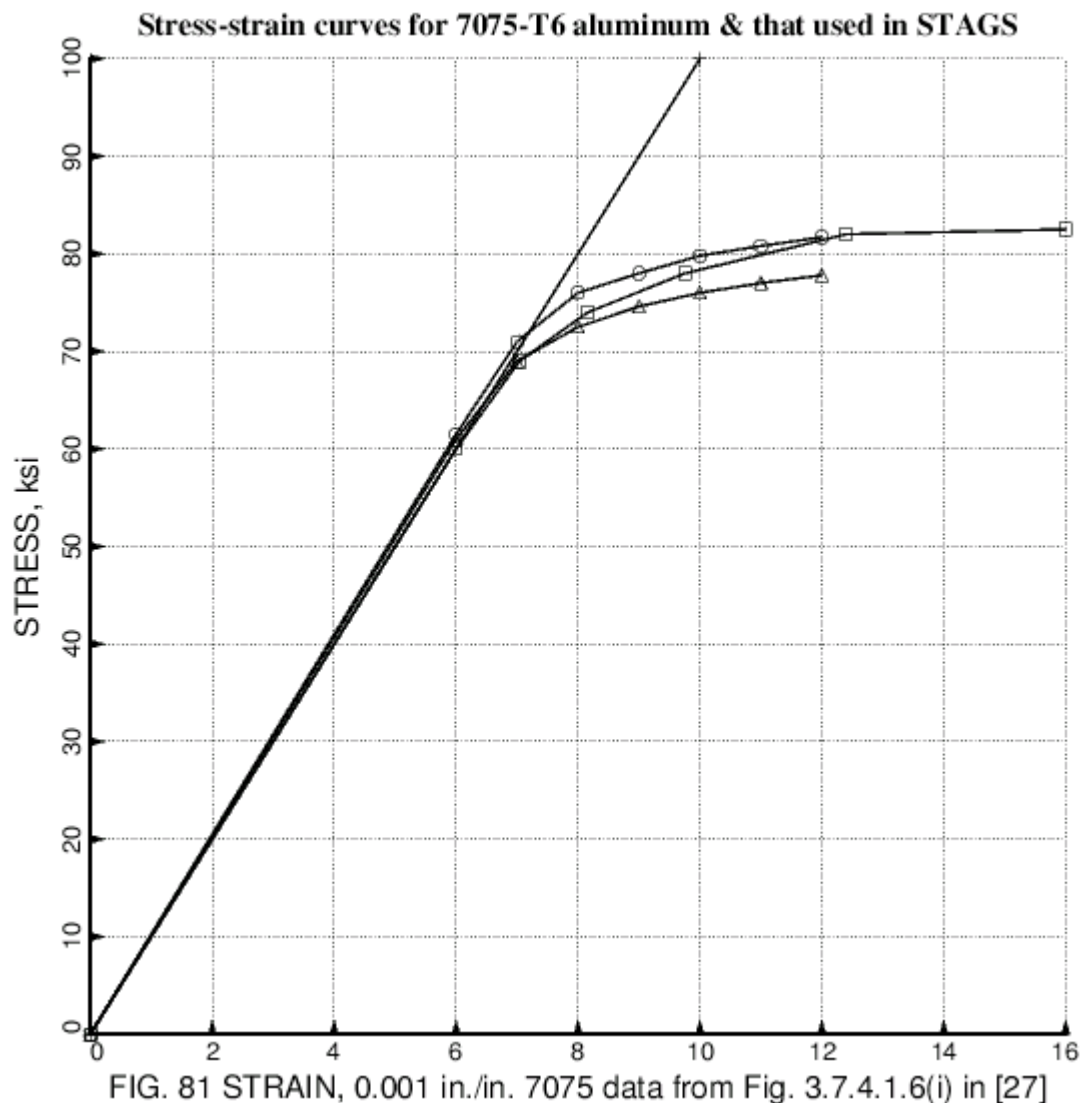


FIG. 81 STRAIN, 0.001 in./in. 7075 data from Fig. 3.7.4.1.6(i) in [27]

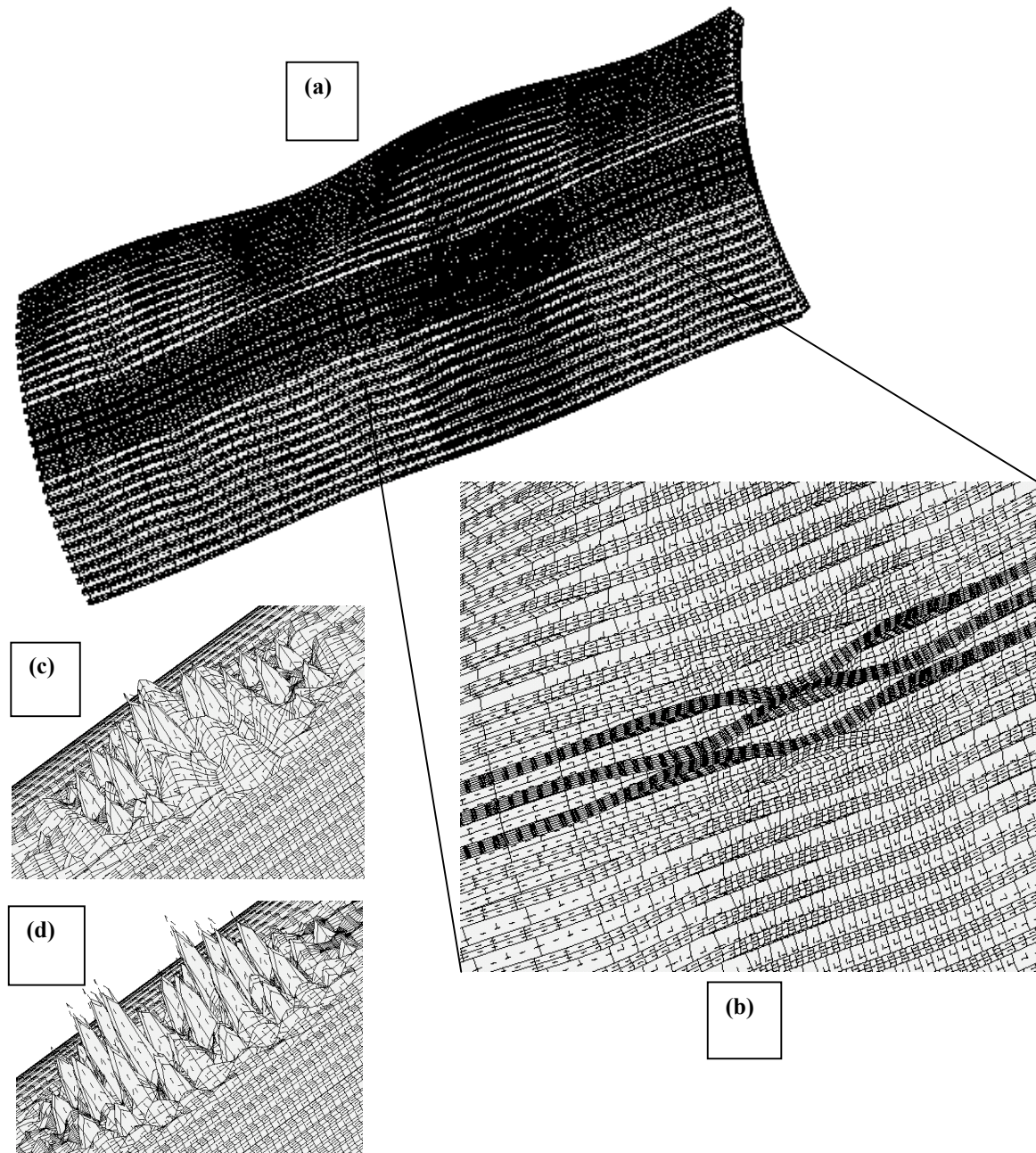


FIG. 82 STAGS model of Case 2, Table 4 with plasticity included (Fig. 81). (a,b) Deformed state at STAGS load factor, PA=1.019. There are three imperfection shapes: 1. general buckling modal imperfection shape similar to that in Fig. 24 with amplitude, Wimp1 = -0.0625 inch, 2. local/bending-torsion combined shape (c) with Wimp2 = +0.0005 inch, 3. local buckling mode shape (d) with Wimp3 = +0.0005 inch. Compare with Fig. 29. Compare (c) and (d) with Figs. 26 and 27, respectively.

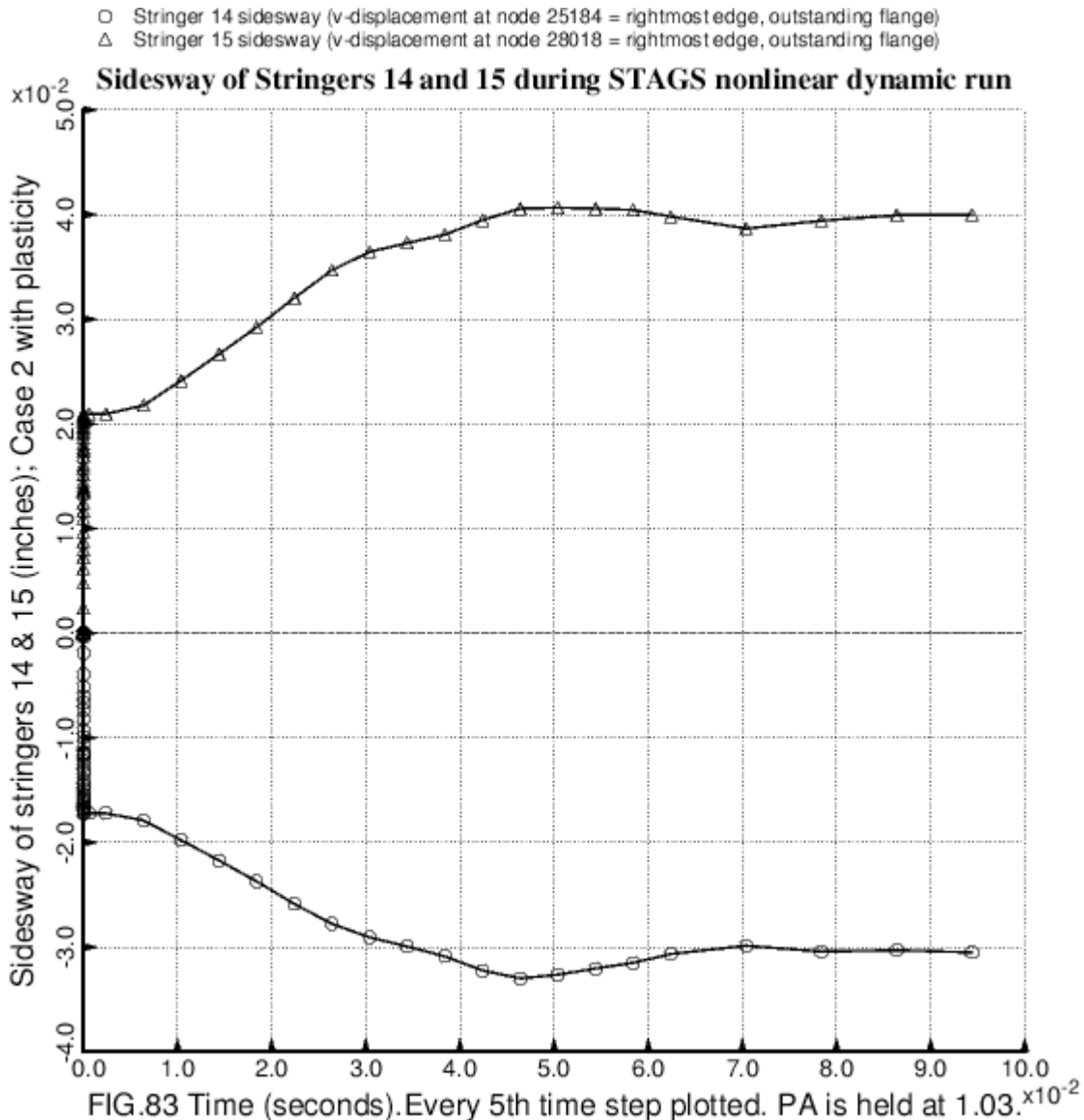


FIG. 83 STAGS model of Case 2 with plasticity. The maximum stringer sidesway is in Ring bays 5 and 6 (Fig. 24) where the nodal mesh is the most dense, as displayed in Fig. 82(b). The vertically arrayed data at Time = 0.0 are the results from the nonlinear static STAGS runs. In this nonlinear dynamic STAGS run the load factor is held constant at PA = 1.03. At Time = 0.095 seconds the stiffened cylindrical shell has come to rest at a new **stable** nonlinear equilibrium state with maximum stringer sidesway shown in the next figure. The deformed configuration resembles that shown in Fig. 82(b). However, there is now more stringer sidesway than that displayed in Fig. 82(b).

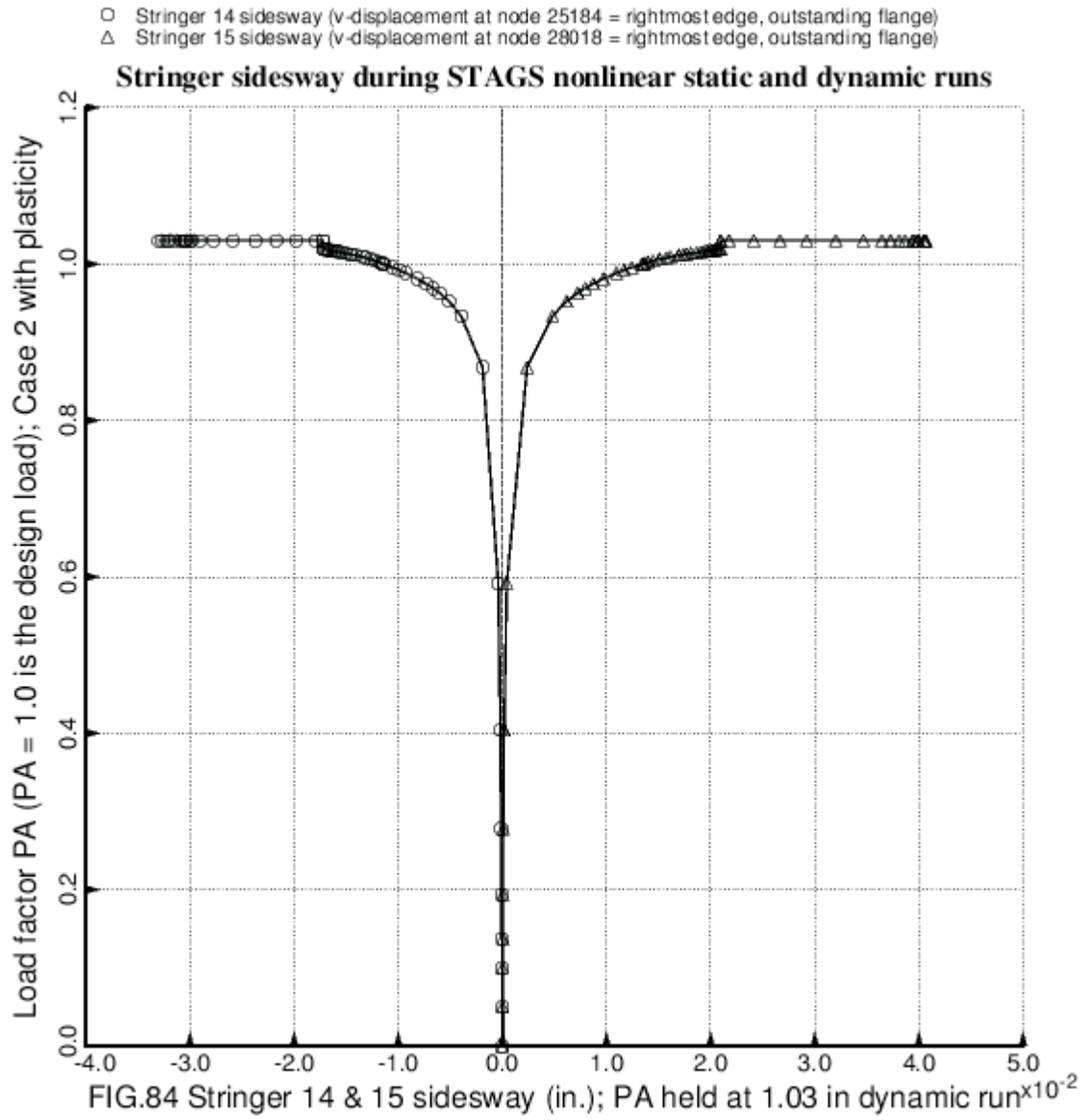


FIG. 84 STAGS model of Case 2 with plasticity. The maximum stringer sidesway is in Ring bays 5 and 6 (Fig. 24) where the nodal mesh is the most dense, as displayed in Fig. 82(b). The horizontally arrayed data at load factor PA = 1.03 are the results from the nonlinear dynamic STAGS run. At Time = 0.095 seconds the stiffened cylindrical shell comes to rest at a new **stable** nonlinear equilibrium state with maximum stringer sidesway shown in the previous figure. The deformed configuration resembles that shown in Fig. 82(b). However, there is now more stringer sidesway than that displayed in Fig. 82(b). The shell is stable but collapse is imminent.

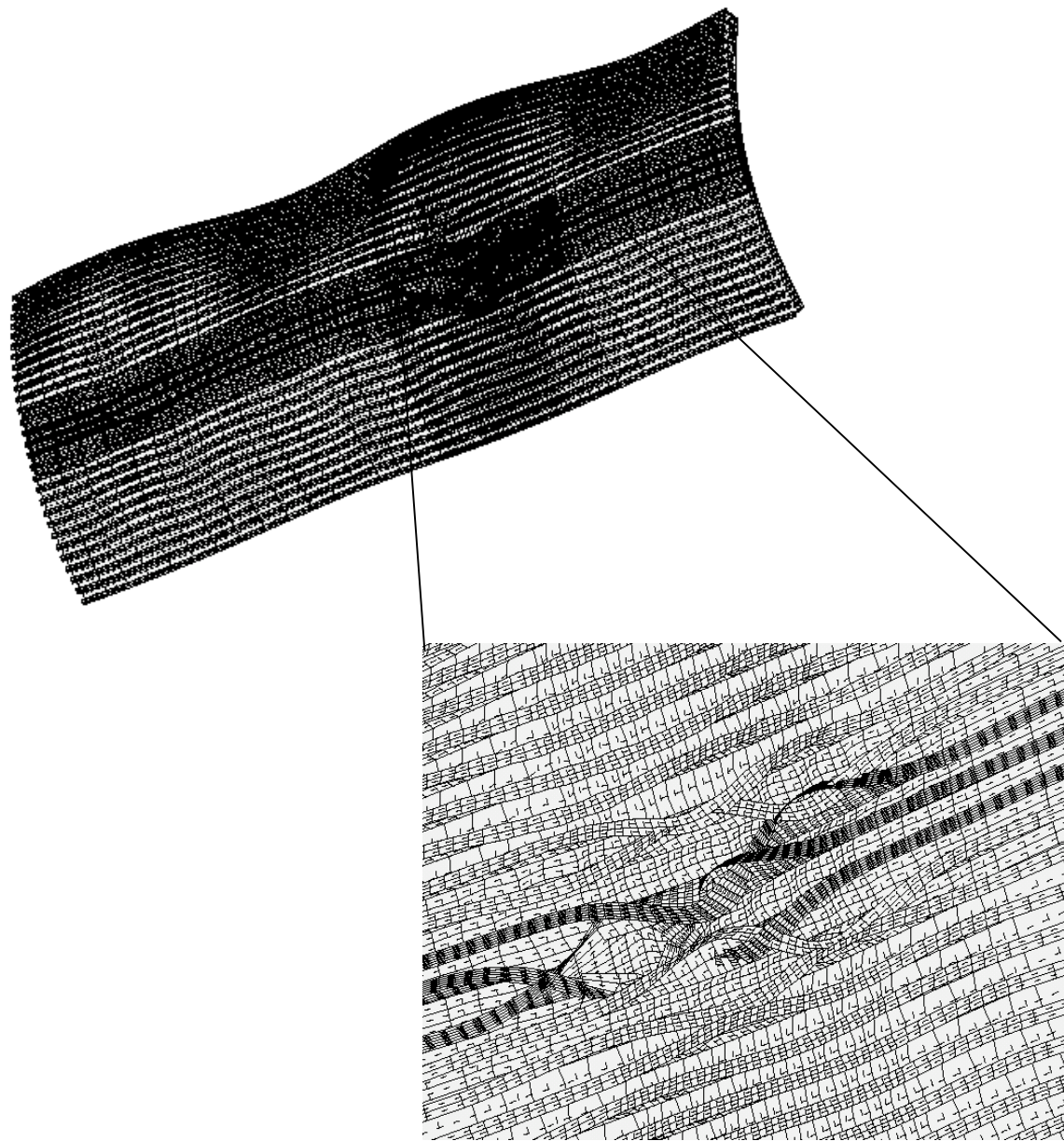


FIG. 85 STAGS model of Case 2, Table 4 with elastic-plastic material behavior accounted for.
Collapse of the imperfect cylindrical shell at STAGS load factor, PA = 1.04, Time = 0.055 seconds.
The imperfect shell has the same three imperfection shapes and amplitudes as those for the previous
three figures. Compare with Fig. 30.

- \square Normal displacement w in the panel skin at nodal point 3845 (8 i.e. up, 3 over, dense region)
- \circ Stringer 14 sidesway (v -displacement at node 25041 = rightmost edge, outstanding flange)
- Δ Stringer 15 sidesway (v -displacement at node 27875 = rightmost edge, outstanding flange)

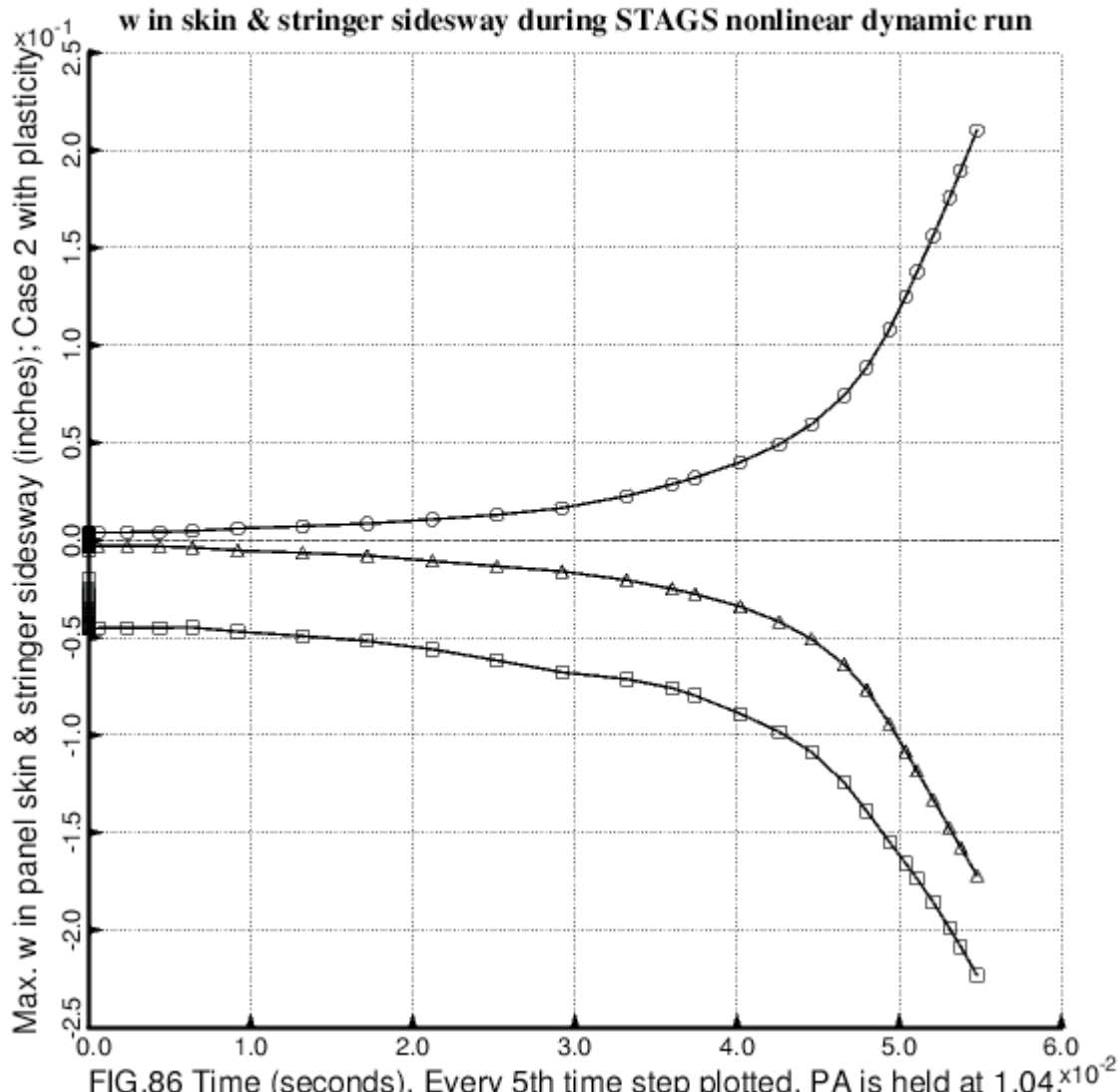


FIG.86 Time (seconds). Every 5th time step plotted. PA is held at 1.04×10^{-2}

FIG. 86 STAGS model of Case 2 with plasticity. The maximum stringer sidesway is in Ring bays 5 and 6 (Fig. 24) where the nodal mesh is the most dense, as displayed in the previous figure. The maximum normal displacement in the panel skin is inward and located between two stringers swaying toward each other. The vertically arrayed data at Time = 0.0 are the results from the nonlinear static STAGS runs. In this nonlinear dynamic STAGS run the load factor is held constant at PA = 1.04. Time = 0.055 seconds corresponds to the last time step archived during the STAGS run. The kinetic energy is high and increasing; the shell is collapsing in the mode displayed in the previous figure. Collapse occurs for load factor PA in the range $1.03 < PA < 1.04$, essentially the same as for the elastic STAGS model, but collapse occurs at an interior region, not near an end of the cylindrical shell as displayed in Fig. 30.

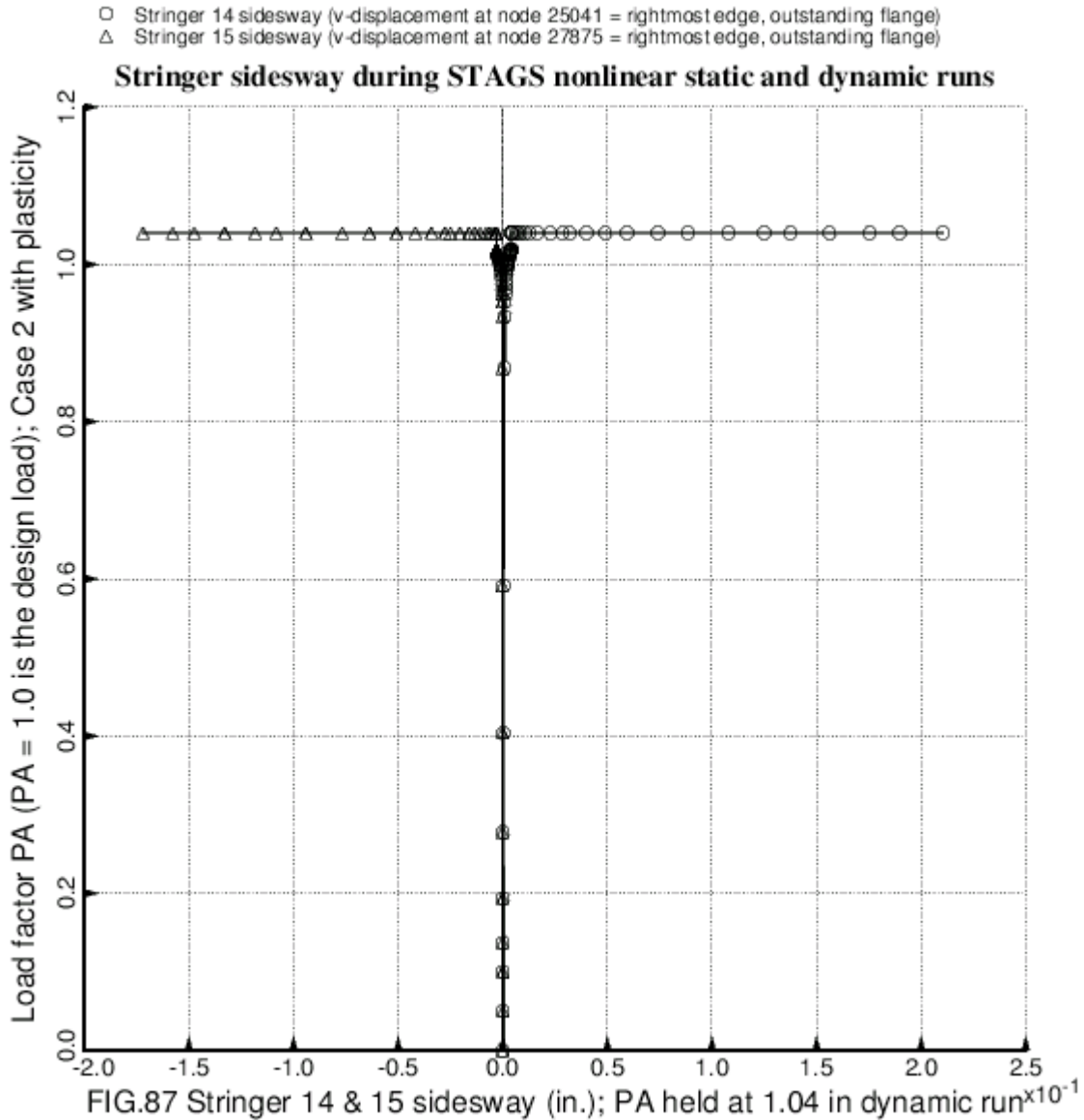


FIG. 87 STAGS model of Case 2 with plasticity. The maximum stringer sidesway is in Ring bays 5 and 6 (Fig. 24) where the nodal mesh is the most dense, as displayed in Fig. 85. The horizontally arrayed data at load factor PA = 1.04 are the results from the nonlinear dynamic STAGS run. The nonlinear dynamic run was terminated at Time = 0.055 seconds. At that time the kinetic energy is fairly large and increasing; the shell collapses in the mode shown in Fig. 85. Collapse occurs for load factor in the range $1.03 < PA < 1.04$ in an interior region. In the elastic STAGS model collapse occurs at the same load but at a different location. Compare Fig. 85 with Fig. 30.

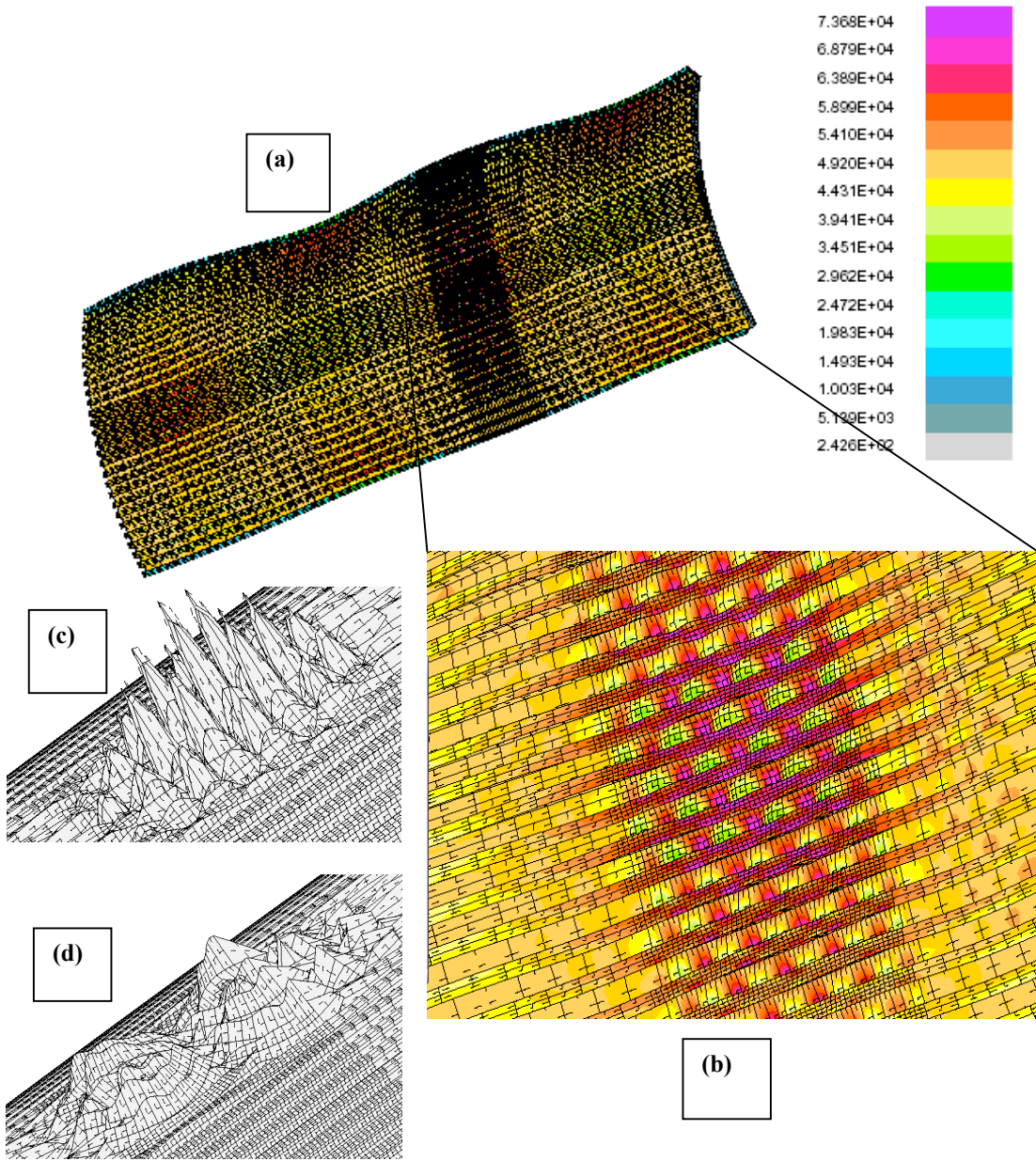


FIG. 88 STAGS model of Case 4, Table 4 with plasticity included (Fig. 81). Outer fiber effective stress (psi) at STAGS load factor, PA=1.05847. (a,b) show the deformed state at STAGS load factor, PA=1.05847. There are three imperfection shapes: 1.=Fig. 49 with amplitude, Wimp1 = -0.0625 inch; 2.=(c) with Wimp2=+0.0005; 3.=(d) with Wimp3=+0.0005 inch. Compare (b) with Fig. 53a. NOTE: Imperfections analogous to (c) & (d) were **not** used in the elastic STAGS model, results for which appear in Figs. 49-60. Instead, the local bending, obvious in Figs. 53a,b, developed “automatically” during the dynamic phase of the elastic STAGS analysis.

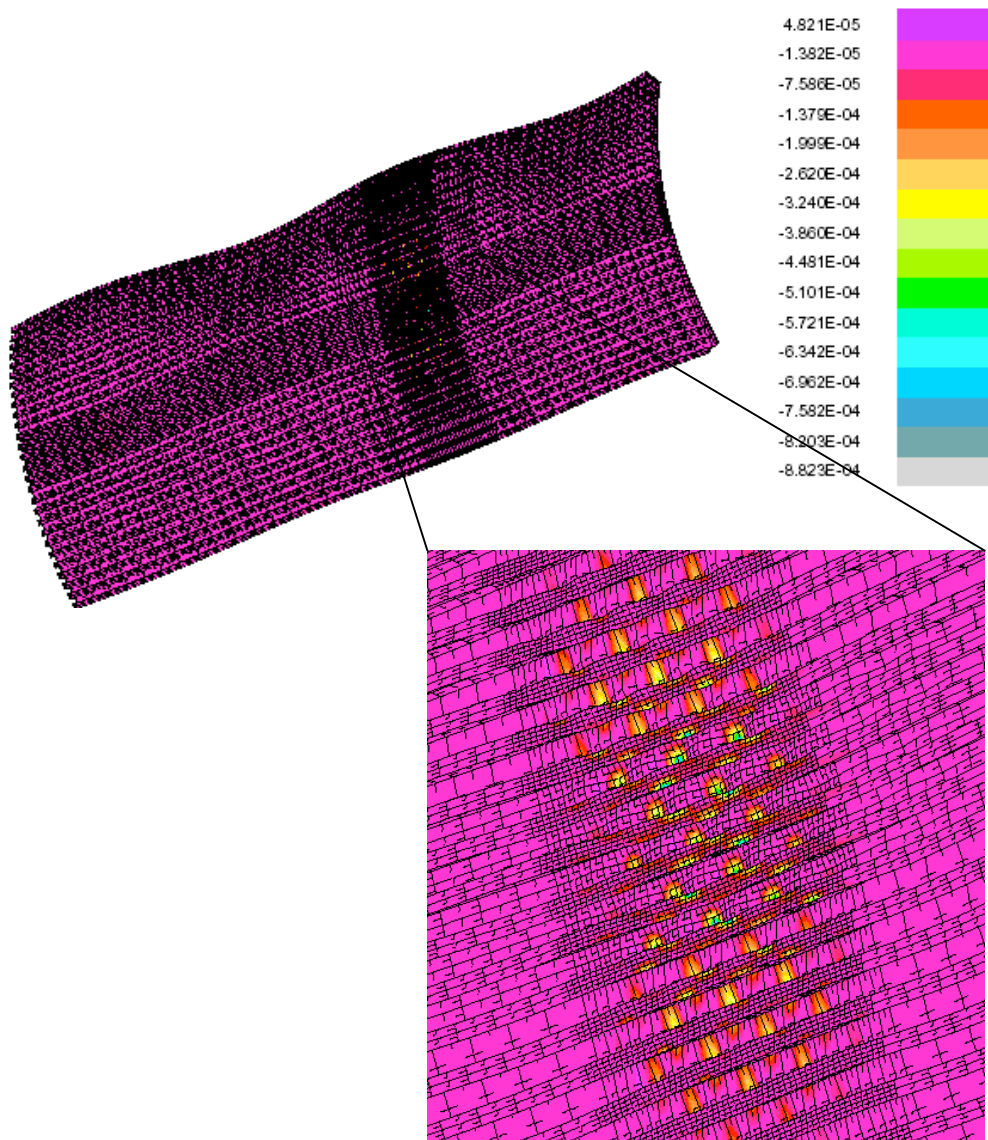


FIG. 89 STAGS model of Case 4, Table 4 with plasticity included. Outer fiber axial plastic strain at STAGS load factor, PA = 1.05847. The imperfect shell has the same three imperfection shapes as noted in the previous figure.

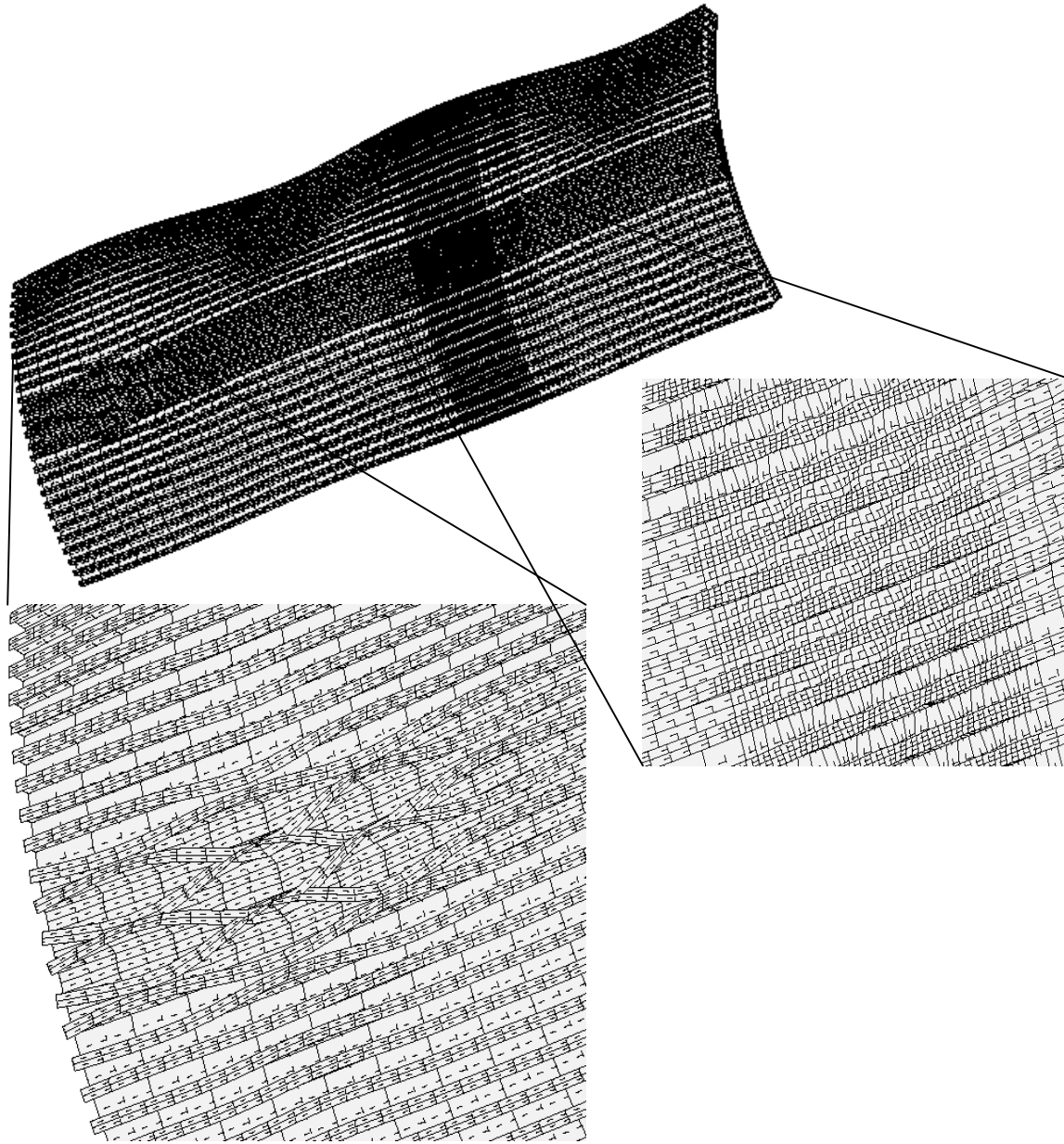


FIG. 90 STAGS model of Case 4, Table 4 with plasticity included. Dynamic collapse occurs at STAGS load factor, PA = 1.06, Time = 0.1 seconds due to sidesway of the stringers in Ring bay 1. Compare with Fig. 56.

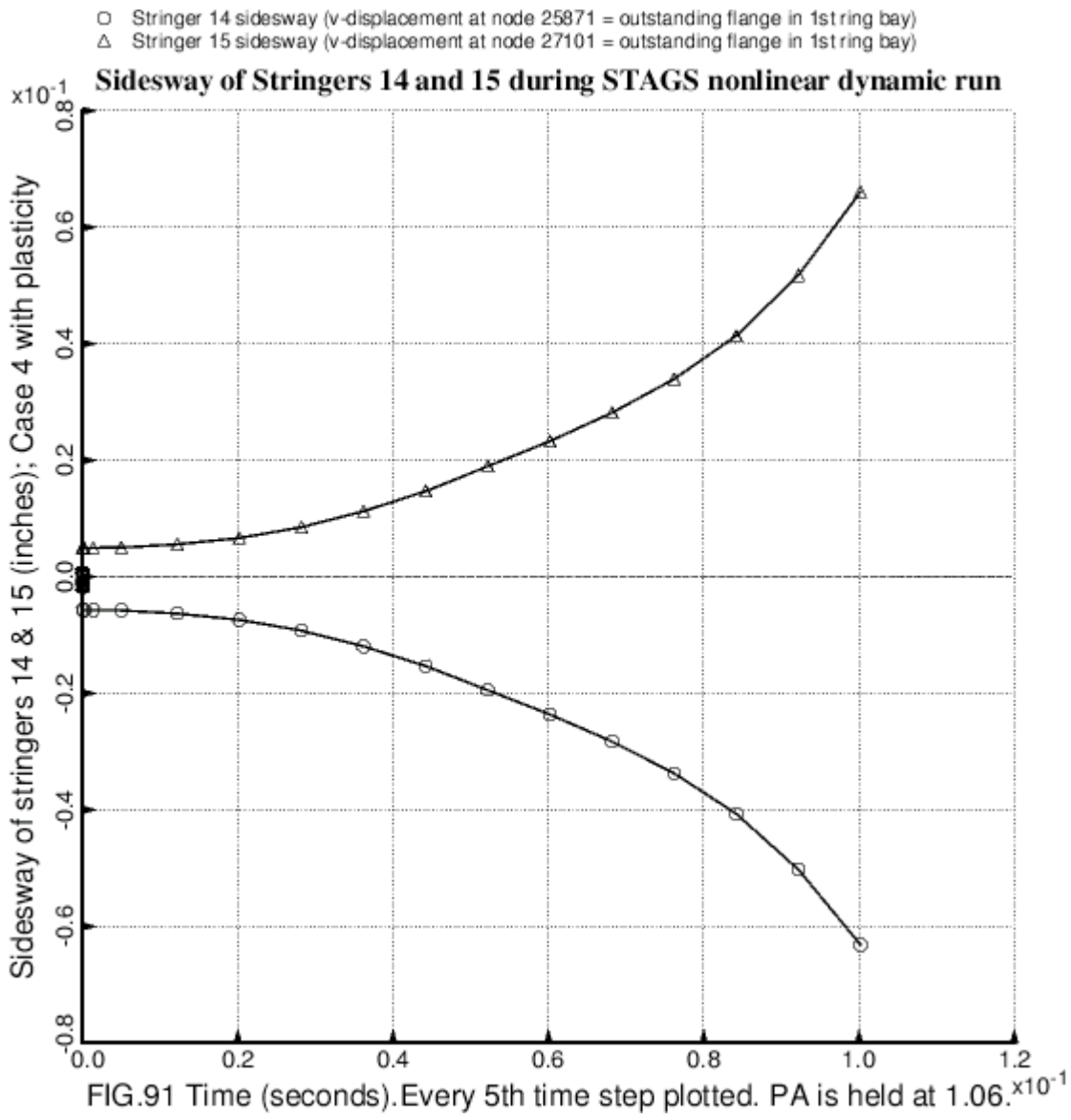


FIG. 91 STAGS model of Case 4 with plasticity. The maximum stringer sidesway is in Ring bays 1 and 2 (Fig. 49) near the left-hand end of the shell, as displayed in the previous figure. The vertically arrayed data at Time = 0.0 are the results from the nonlinear static STAGS run. In this nonlinear dynamic STAGS run the load factor is held constant at PA = 1.06. Time = 0.10 seconds corresponds to the last time step archived during the STAGS run. The kinetic energy is high and increasing; the shell is collapsing in the mode displayed in the previous figure. Collapse occurs for load factor PA in the range $1.05847 < PA < 1.06$, a slightly lower load than that at which the elastic STAGS model collapses, $1.06687 < PA < 1.08$, as shown in Figs. 54 and 55. The mode of collapse, end bay collapse, is similar in both the elastic and elastic-plastic models.

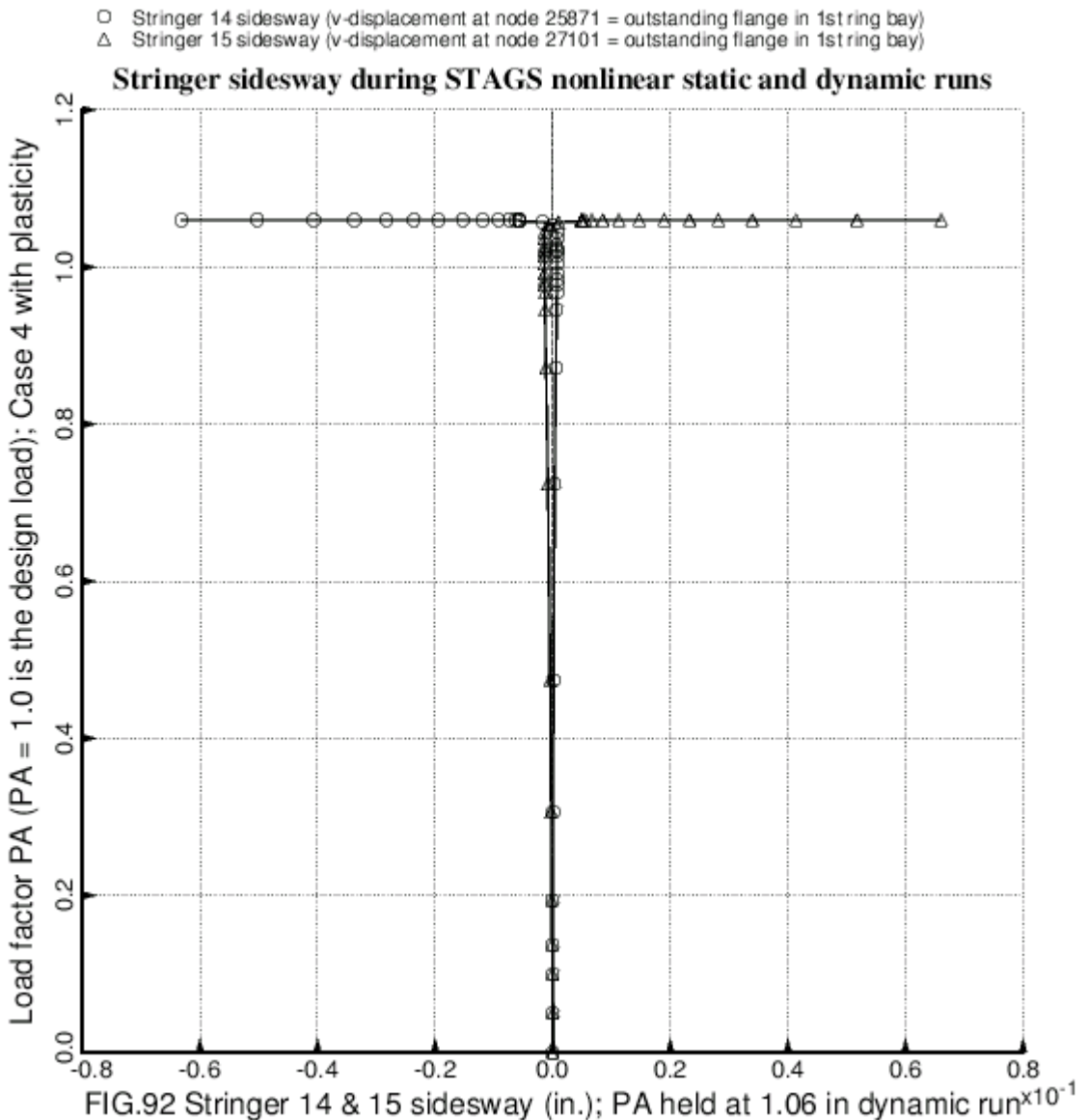


FIG. 92 STAGS model of Case 4 with plasticity. The maximum stringer sidesway is in Ring bays 1 and 2 (Fig. 49) near the left-hand end of the shell, as displayed in the Fig. 90. The horizontally arrayed data at $PA = 1.06$ are the results from the nonlinear dynamic STAGS run. In the nonlinear dynamic STAGS run the load factor is held constant at $PA = 1.06$. Time = 0.10 seconds corresponds to the last time step archived. The kinetic energy is high and increasing; the shell is collapsing in the mode displayed in Fig. 90. Collapse occurs for load factor PA in the range $1.05847 < PA < 1.06$, a slightly lower load than that at which the elastic STAGS model collapses, $1.06687 < PA < 1.08$, as shown in Figs. 54 and 55. The mode of collapse, end bay collapse, is similar to that for the elastic STAGS model.

- Stringer 15 sidesway (v -displacement at node 27637 = outstanding flange in 4th ring bay)
- Stringer 16 sidesway (v -displacement at node 28847 = outstanding flange in 4th ring bay)

Case 5: Sidesway of Stringers 15 & 16 during STAGS nonlinear static run

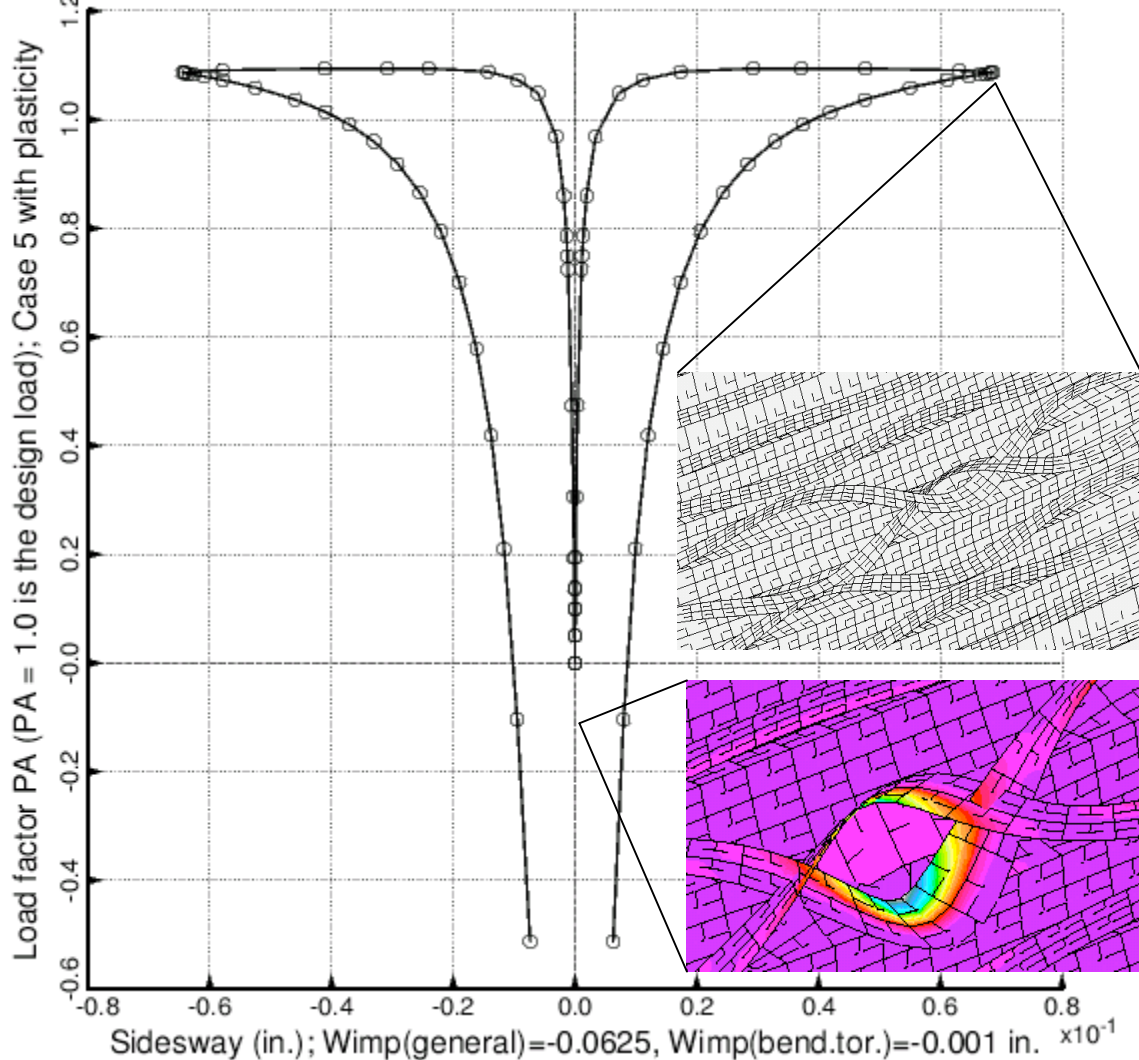


FIG. 93 STAGS model of Case 5, Table 4 with plasticity included. Nonlinear static elastic-plastic sidesway of Stringers 15 & 16 (numbering from the bottom in Figs. 66 & 67) in Ring bays 3 & 4 (Fig. 66). The imperfect shell has two imperfection shapes: 1. general buckling modal imperfection shape similar to that in Fig. 66 with amplitude, $W_{imp1} = -0.0625$ inch, and 2. bending-torsion buckling shape similar to that shown in the lower expanded insert in Fig. 68 with amplitude, $W_{imp2} = -0.001$ inch. In the bending-torsion imperfection shape in this elastic-plastic model there is no buckling modal deformation near the right-hand end of the shell. Compare with Figs. 69-71.

- Stringer 15 static sidesway (v-displacement at node 27637 = outstanding flange in 4th ring bay)
- △ Stringer 15 dynamic sidesway (v-displacement at node 27637 = outstanding flange in 4th ring bay)
- + Stringer 16 static sidesway (v-displacement at node 28847 = outstanding flange in 4th ring bay)
- ✗ Stringer 16 dynamic sidesway (v-displacement at node 28847 = outstanding flange in 4th ring bay)

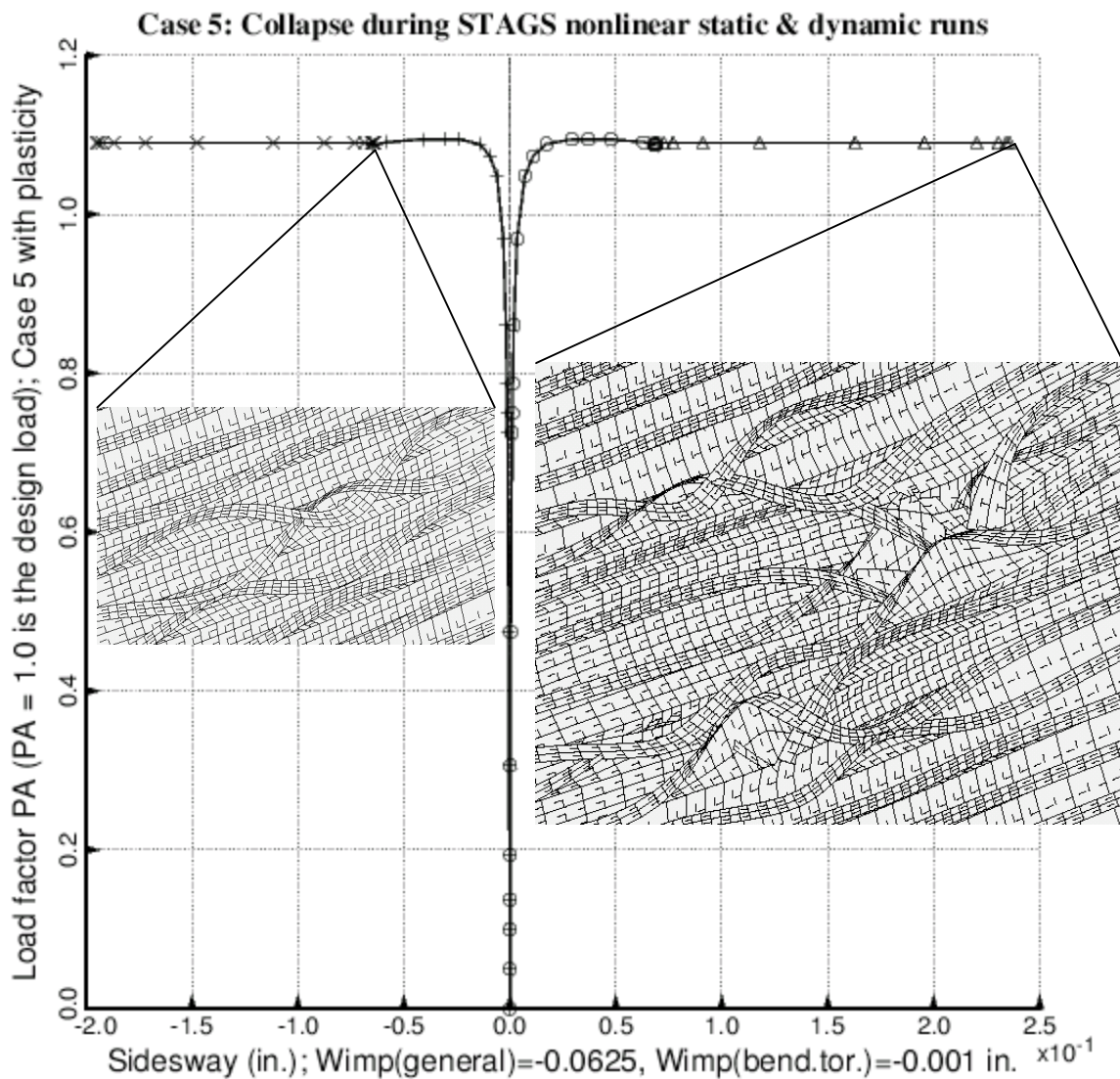


FIG. 94 STAGS model Case 5, Table 4 with plasticity included. Dynamic collapse at STAGS load factor, PA = 1.09, due to stringer sidesway in Ring bays 3 and 4 (Fig. 66). The imperfect shell has two imperfection shapes: 1. general buckling mode shape similar to that shown in Fig. 66 with amplitude, $W_{imp1} = -0.0625$ inch, 2. bending-torsion buckling mode similar to that in the left-most expanded insert in Fig. 68 with amplitude $W_{imp2} = -0.001$ inch. The expanded insert on the left-hand side shows the deformed state in Ring bays 3 and 4 at the last load step reached in the nonlinear static STAGS run. The expanded insert on the right-hand side shows the deformed state in Ring bays 3 and 4 at the end of the nonlinear dynamic STAGS run. During the nonlinear dynamic run PA is held constant at PA = 1.09.

- Stringer 11 static sidesway (v-displacement at node 21325 = outstanding flange in 3rd ring bay)
- △ Stringer 11 dynamic sidesway (v-displacement at node 21325 = outstanding flange in 3rd ring bay)
- + Stringer 12 static sidesway (v-displacement at node 23039 = outstanding flange in 3rd ring bay)
- × Stringer 12 dynamic sidesway (v-displacement at node 23039 = outstanding flange in 3rd ring bay)

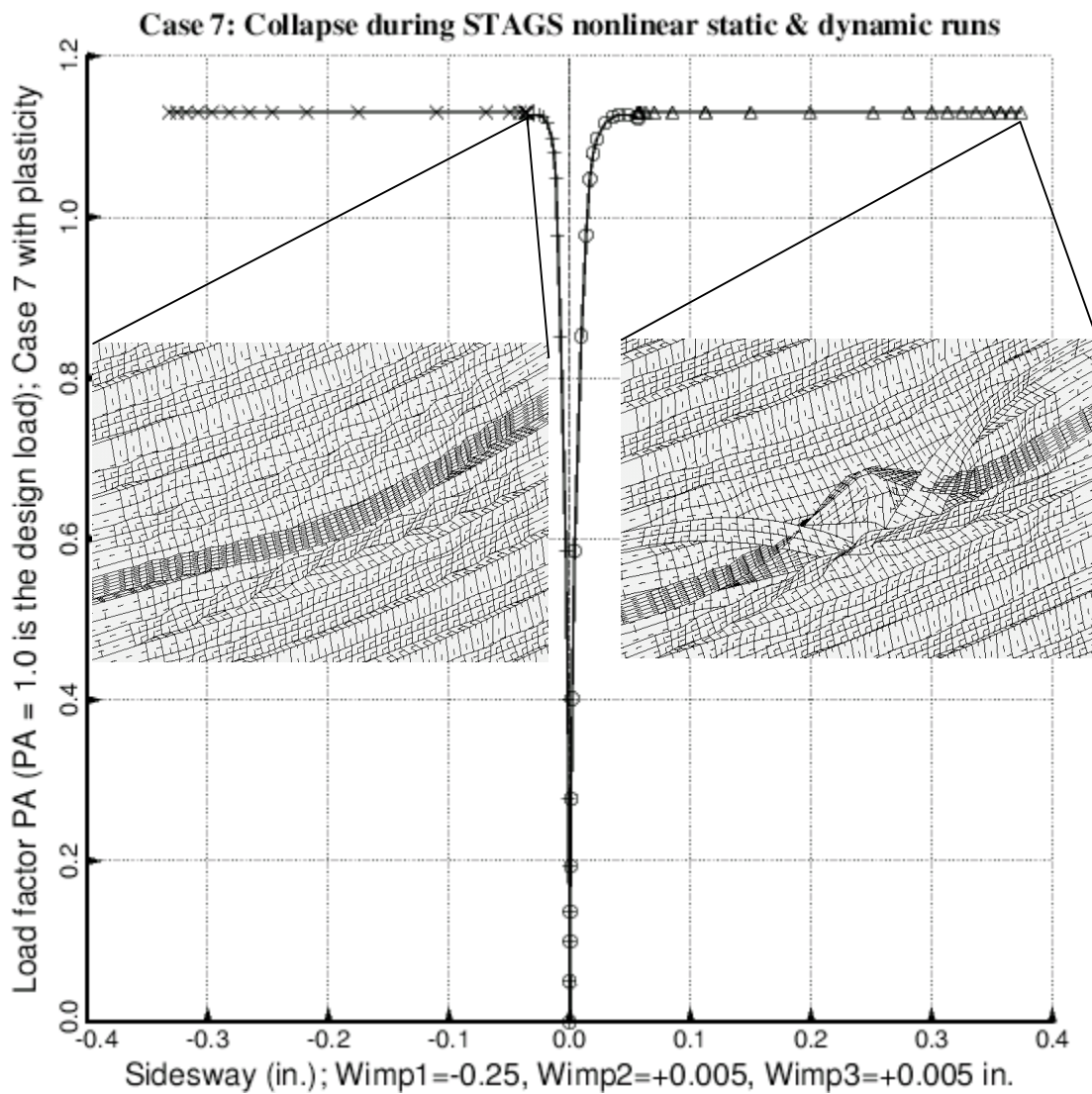


FIG. 95 STAGS model of Case 7, Table 4 with plasticity included. Dynamic collapse at STAGS load factor, PA = 1.13, due to stringer sidesway in Ring bay 3 (Fig. 76). The imperfect shell has three imperfection shapes: 1. general buckling mode shape similar to that shown in Fig. 76 with amplitude, Wimp1 = -0.25 inch, 2. bending-torsion buckling mode shape (not shown in this paper) with amplitude Wimp2 = +0.005 inch, 3. local buckling mode shape (not shown in this paper) with amplitude Wimp3 = +0.005 inch. The expanded insert on the left-hand side shows the deformed state in Ring bay 3 at the highest load reached in the nonlinear static STAGS run. The expanded insert on the right-hand side shows the deformed state in Ring bay 3 at the end of the nonlinear dynamic STAGS run. During the nonlinear dynamic run the load factor is held constant at PA = 1.13.

- 1.1.1 Local buckling: discrete model
- 2.1.1 Long-axial-wave bending-torsion buckling
- △ 3.1.1 eff.stress:matl=1; MID.
- + 6.1.1 m=? lateral-torsional buckling
- × 7.1.1 Inter-ring buckling, discrete model
- ◊ 8.1.1 eff.stress:matl=1,allnode,-MID.
- ▽ 9.1.1 buckling: stringer seg.3 . MIDLENGTH
- ▣ 10.1.1 buckling: stringer seg.4 . MIDLENGTH
- ✗ 11.1.1 buckling: stringer lssegs.3+4. MIDLENGTH
- ◆ 15.1.1 buckling: stringer seg.3 . NO POSTBK
- ⊕ 16.1.1 buckling: stringer seg.4 . NO POSTBK
- ☒ 17.1.1 buckling: stringer lssegs.3+4. NO POSTBK
- 21.1.1 buck(SAND)simp-support general buck; MIDLENGTH
- ▢ 24.1.1 buck(SAND)rolling only of stringers; MIDLENGTH
- ▢ 25.1.1 buck(SAND)hiwave roll. of stringers; MIDLENGTH
- 26.1.1 buck(SAND)rolling only of rings; MIDLENGTH
- 27.1.1 buck(SAND)hiwave roll. of rings; MIDLENGTH
- ▣ 28.1.1 buck(SAND)rolling only axisym.rings; MIDLENGTH

FIG. 96 PANDA2 model of Case 5: These results correspond to an **initial user-specified** imperfection amplitude, $W_{imp} = 0.5$ inch. These curves were generated with the “yes change imperfection” option. Curves such as these, which are obtained for several different **initial** imperfection amplitudes, are used to generate the “imperfection sensitivity” plots displayed in the next figure. The almost singular appearance of the curves near axial load $N_x = -2550$ lb/in is explained in the text (Section 15.0).

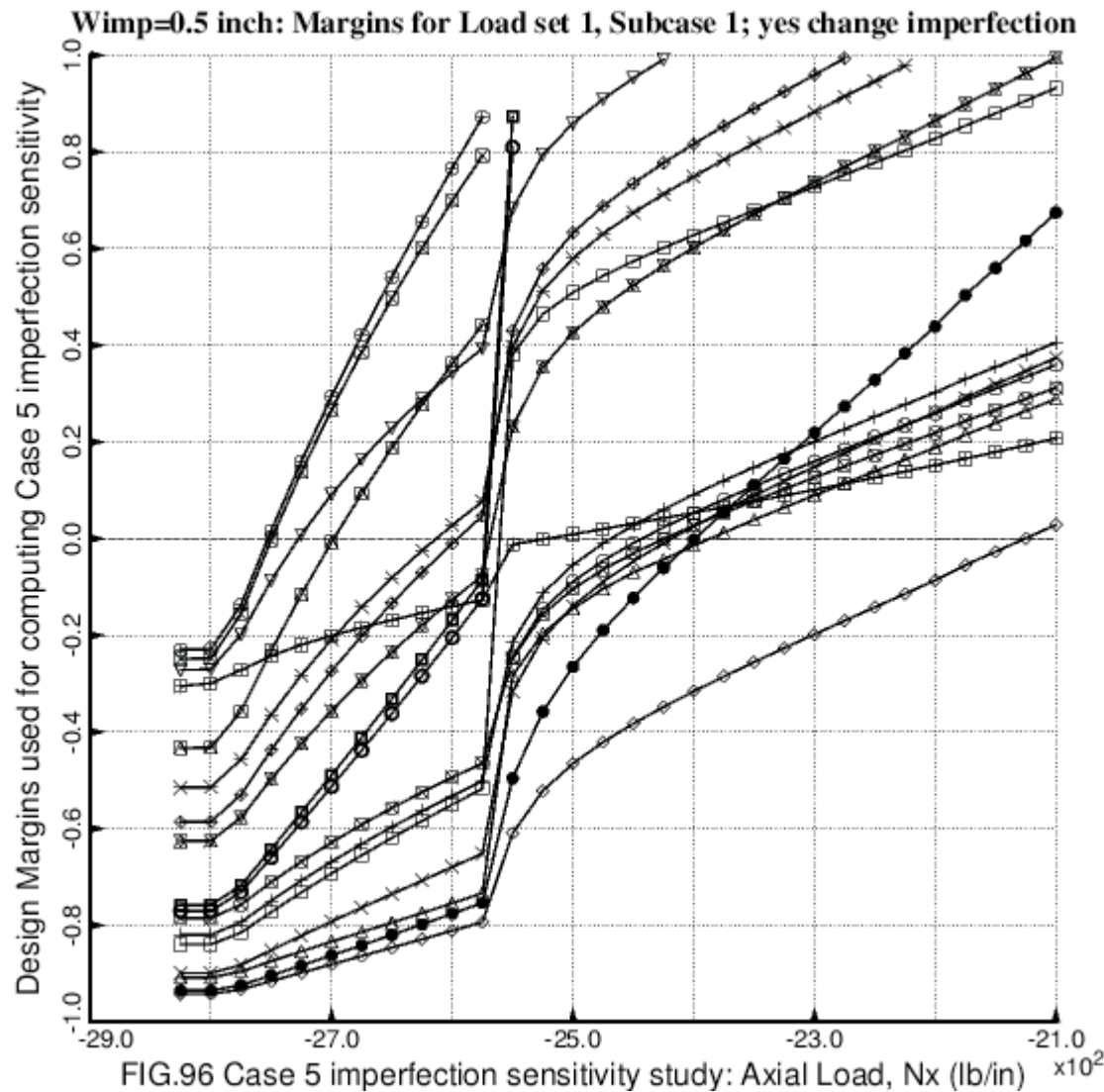
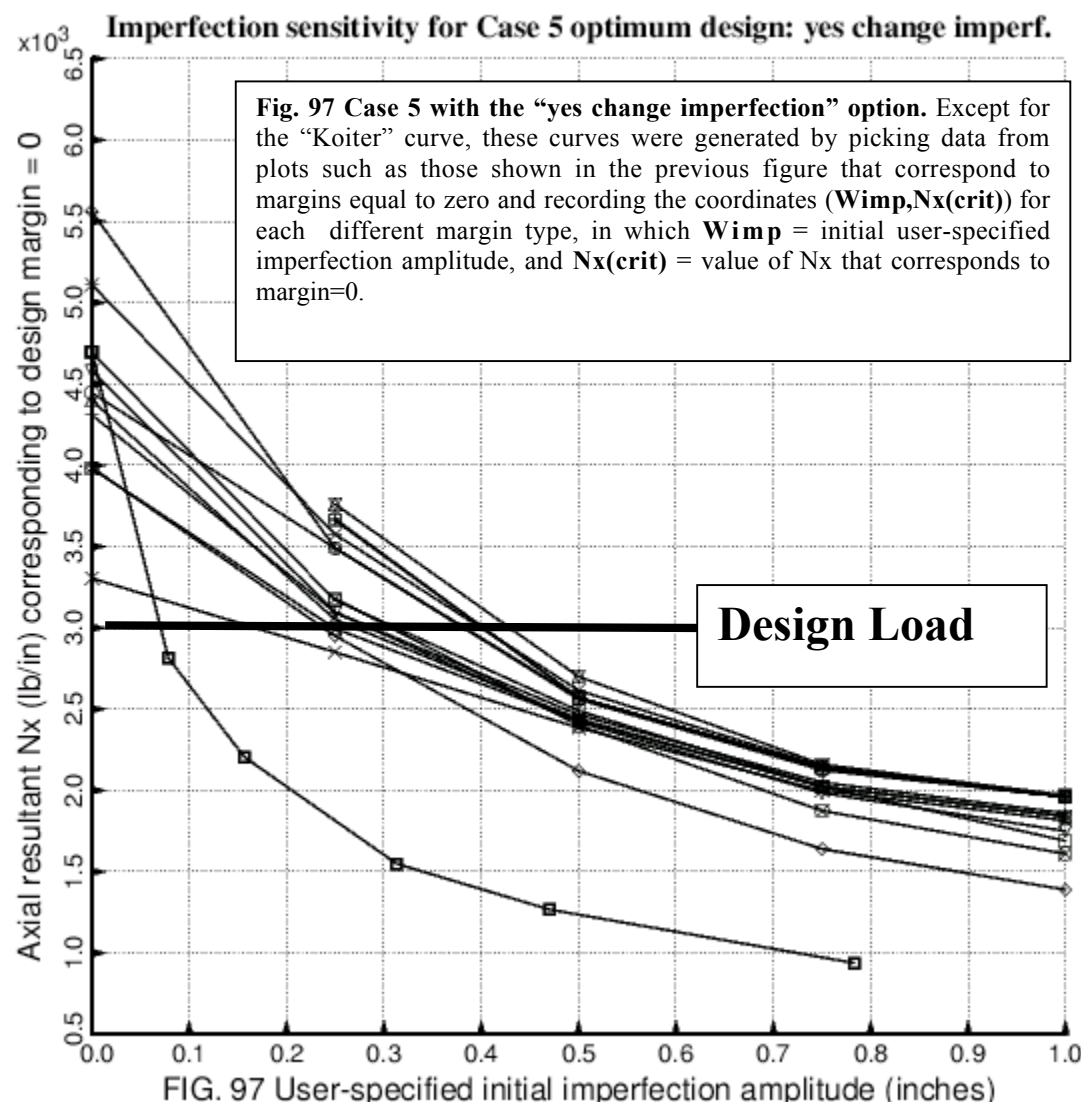
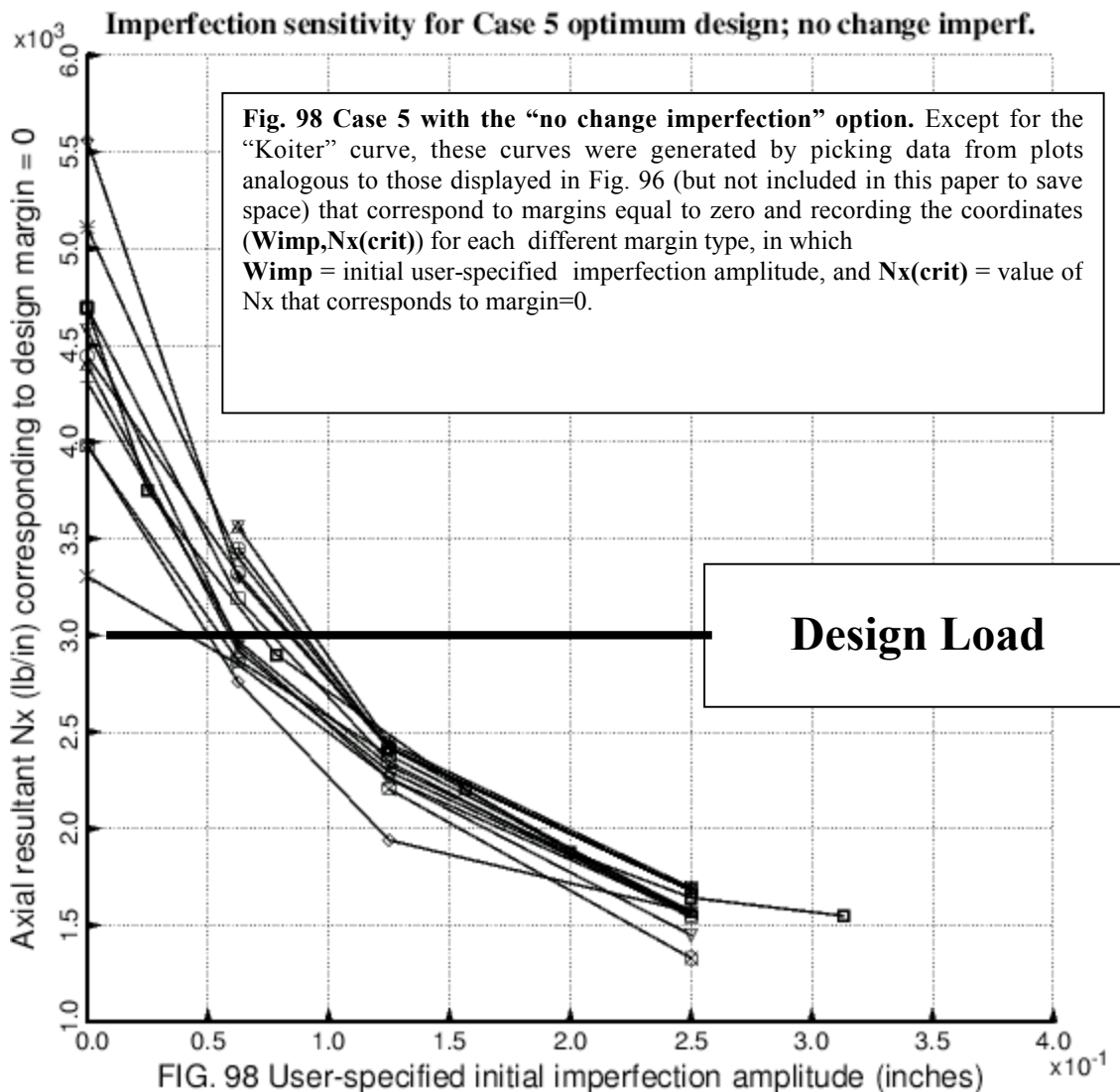


FIG.96 Case 5 imperfection sensitivity study: Axial Load, N_x (lb/in) $\times 10^2$

- "yes change imperfection" General buckling (PANDA-type model [1B])
- "yes change imperfection" Local buckling from discretized skin-stringer module model
- "yes change imperfection" Bending-torsion buckling from discretized skin-stringer model
- "yes change imperfection" Lateral-torsional buckling from discretized skin-stringer model
- "yes change imperfection" Effective stress from discretized skin-stringer module model(STRTHK)
- "yes change imperfection" Effective stress from SUBROUTINE STRCON (ring stress included)
- "yes change imperfection" Inter-ring buckling from discretized skin-smeared-stringer/ring model
- "yes change imperfection" Rolling only of stringers from PANDA-type model [1B]
- "yes change imperfection" Stringer segments 3+4 "MID" buckling (PANDA-type model [1B])
- "yes change imperfection" Stringer segments 3+4 "NOPO" buckling (PANDA-type model [1B])
- "yes change imperfection" Axisymmetric ring rolling from PANDA-type model [1B]
- "yes change imperfection" High-axial-wave stringer rolling from PANDA-type model [1B]
- "yes change imperfection" High-circumferential-wave ring rolling from PANDA-type model [1B]
- "yes change imperfection" Non-axisymmetric ring rolling from PANDA-type model [1B]
- Koiter special theory [28]. See Fig. 262 on page 297 of [8]



- "no change imperfection" General buckling (PANDA-type model [1B])
- "no change imperfection" Local buckling from discretized skin-stringer module model
- △ "no change imperfection" Bending-torsion buckling from discretized skin-stringer model
- + "no change imperfection" Lateral-torsional buckling from discretized skin-stringer model
- ◊ "no change imperfection" Effective stress from discretized skin-stringer module model(STRTHK)
- ◇ "no change imperfection" Effective stress from SUBROUTINE STRCON (ring stress included)
- ⊗ "no change imperfection" Inter-ring buckling from discretized skin-smeared-stringer/ring model
- ⊗ "no change imperfection" Rolling only of stringers from PANDA-type model [1B]
- ⊗ "no change imperfection" Stringer segments 3+4 "MID" buckling (PANDA-type model [1B])
- ⊕ "no change imperfection" Stringer segments 3+4 "NOPO" buckling (PANDA-type model [1B])
- ⊗ "no change imperfection" Axisymmetric ring rolling from PANDA-type model [1B]
- ⊗ "no change imperfection" High-axial-wave stringer rolling from PANDA-type model [1B]
- ⊗ "no change imperfection" High-circumferential-wave ring rolling from PANDA-type model [1B]
- ⊗ "no change imperfection" Non-axisymmetric ring rolling from PANDA-type model [1B]
- ▣ Koiter special theory [28]. See Fig. 262 on page 297 of [8]



- Local buckling from discrete model-1,M=9 axial halfwaves;FS=0.99
- Long-axial-wave bending-torsion buckling; M=2 ;FS=0.999
- △ eff.stress:matl=1,STR,Dseg=4,node=11,layer=1,z=-0.0114; MID.;FS=1.(SUBROUTINE STRTHK)
- + (m=2 lateral-torsional buckling load factor)/(FS)-1;FS=0.999
- × Inter-ring buckling, discrete model, n=49 circ.halfwaves;FS=0.999
- ◊ eff.stress:matl=1,RNG,Iseg=4,allnode,layer=1,z=0.0293;MID.;FS=1.(SUBROUTINE STRCON)
- ▽ buckling margin stringer Iseg.3 . Local halfwaves=13 .MID.;FS=1.
- ▣ buckling margin stringer Iseg.4 . Local halfwaves=13 .MID.;FS=1.
- * buckling stringer Isegs.3+4 together.M=13 ;C=0. ;MID.;FS=1.4
- ◆ buck.(SAND);simp-support general buck;M=4;N=6;slope=0.;FS=0.999
- ⊗ buck.(SAND);rolling only of stringers;M=18;N=0;slope=0.;FS=1.4
- ⊗ buck.(SAND);hiwave roll. of stringers;M=153;N=0;slope=0.;FS=1.2
- 田 buck.(SAND); STRINGERS: web buckling;M=13;N=1;slope=0.01;FS=1.

Case 4: Effect on margins of "conservativeness" index, ICONSV

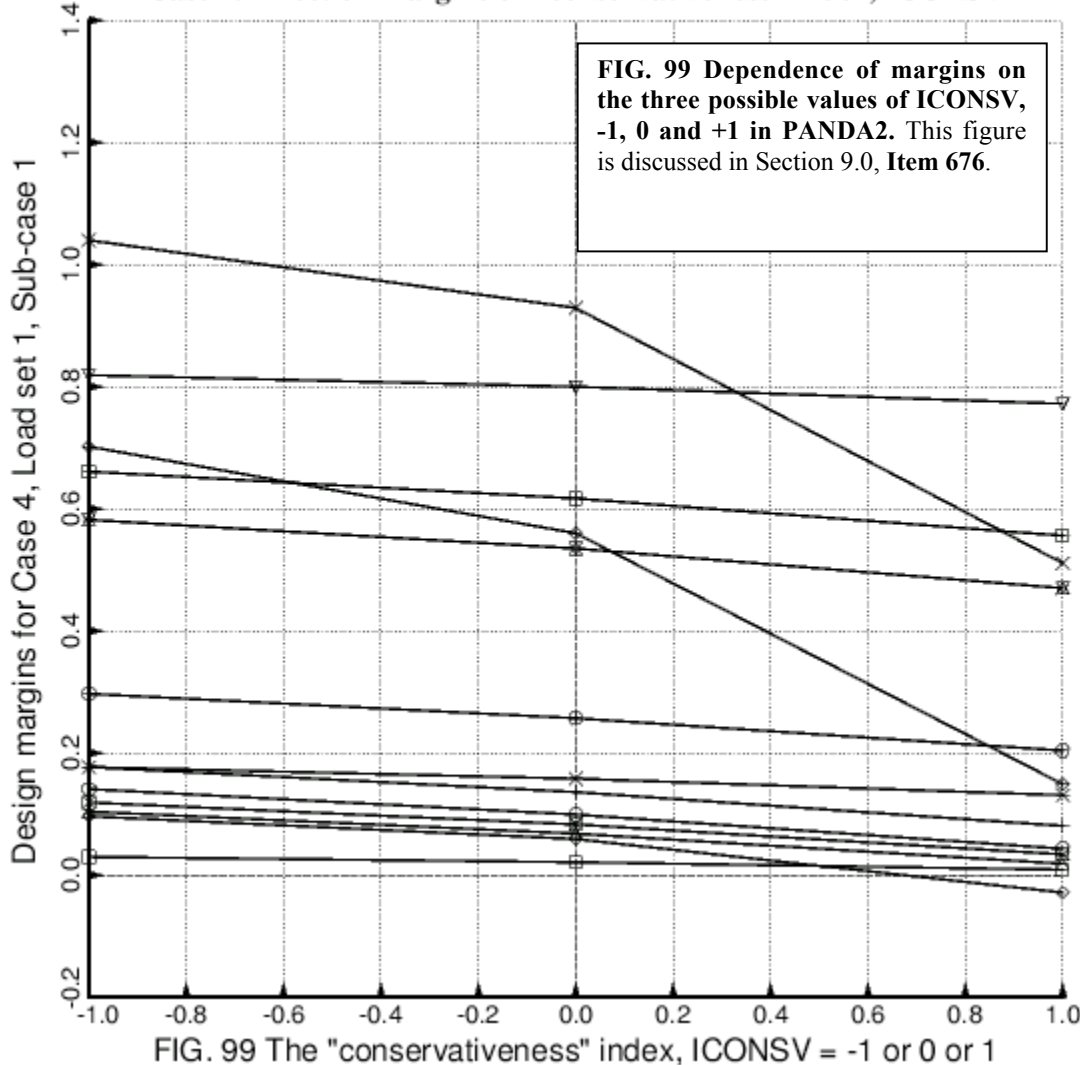


FIG. 99 The "conservativeness" index, ICONSV = -1 or 0 or 1

